PRACTICAL IMAGING OF COMPLEX GEOLOGICAL STRUCTURES USING SEISMIC PRESTACK DEPTH MIGRATION

JINMING ZHU

INFORMATION TO USERS

This manuscript has been reproduced from the microfilm master. UMI films the text directly from the original or copy submitted. Thus, some thesis and dissertation copies are in typewriter face, while others may be from any type of computer printer.

The quality of this reproduction is dependent upon the quality of the copy submitted. Broken or indistinct print, colored or poor quality illustrations and photographs, print bleedthrough, substandard margins, and improper alignment can adversely affect reproduction.

In the unlikely event that the author did not send UMI a complete manuscript and there are missing pages, these will be noted. Also, if unauthorized copyright material had to be removed, a note will indicate the deletion.

Oversize materials (e.g., maps, drawings, charts) are reproduced by sectioning the original, beginning at the upper left-hand corner and continuing from left to right in equal sections with small overlaps. Each original is also photographed in one exposure and is included in reduced form at the back of the book.

Photographs included in the original manuscript have been reproduced xerographically in this copy. Higher quality 6" x 9" black and white photographic prints are available for any photographs or illustrations appearing in this copy for an additional charge. Contact UMI directly to order.

UMI

A Bell & Howell Information Company
300 North Zeeb Road, Ann Arbor, MI 48106-1346 USA
313/761-4700 800/521-0600

PRACTICAL IMAGING OF COMPLEX GEOLOGICAL STRUCTURES USING SEISMIC PRESTACK DEPTH MIGRATION

by

Jinming Zhu

A dissertation submitted to the

School of Graduate Studies

in partial fulfillment of the

requirements for the degree of

Doctor of Philosophy

Department of Earth Sciences

Memorial University of Newfoundland

July 1997

St. John's Newfoundland

Abstract

This thesis develops innovative procedures to address problems in imaging multichannel reflection seismic data in regions of complex geology. Conventional common midpoint (CMP) based processing fails to produce adequate Earth images for complex geological structures with both vertical and lateral heterogeneities. This failure is due to the breakdown of assumptions such as common midpoint stacking and exploding reflector models. In these cases, seismic prestack depth migration is necessary since it can produce an accurate subsurface image — provided that a good estimate of the low wavenumber component of the velocity model is available. Two powerful prestack depth migration techniques are developed through the integral and finite-difference solutions of the wave equation.

I first develop a new, robust, and accurate traveltime calculation method which is essentially a wavefront tracing procedure. This is implemented as a combination of a finite-difference solution of the eikonal equation, an excitation of Huygens' secondary sources, and an application of Fermat's principle. This method is very general and can be directly applied to compute first arrival traveltimes of incident plane waves. These traveltimes are extensively used by the Kirchhoff integral method to determine the integral surface, and also by the reverse-time migration to determine imaging conditions.

The prestack Kirchhoff integral migration of shot profiles which is developed using

the WKBJ approximation to the Green's function is simply a summation of amplitudes of differential traces along an integral surface with amplitudes being modulated by certain geometrical functions. I demonstrate that this summation scheme along a general integral surface is the mathematically more rigorous extension of the summation scheme along diffraction surfaces and of the superposition scheme of aplanatic surfaces. With the utilization of efficient traveltime computations, the integral depth migration is very computationally effective. It can be easily used to perform target-oriented imaging tasks by migrating selective shots and traces.

In contrast to the Kirchhoff method, reverse-time migration is based on a direct solution of the wave equation by approximating the differential terms of the wave equation with finite differences. It is theoretically more accurate than the Kirchhoff method since it attempts to solve the wave equation without a high frequency approximation. In addition to such attractions as implicit static corrections and coherent noise elimination based on velocity information, I find that there exist self-healing mechanisms of the wavefield due to constructive interference during the reverse-time propagation of the unaliased wavefield. The self-healing ability of waves thus provides the basis of migrating sparsely and irregularly sampled unaliased recordings relative to a fine finite-difference grid without prior interpolation of missing traces. This is particularly valuable in migrating unaliased shot records with a gridded velocity model as fine as common depth point (CDP) bins with no explicit trace interpolation. As in the integral method, I implement the reverse-time migration directly from topography using the actual source and receiver positions.

Considering the nature of imaging in geologically complex areas, I view the geophysicists' goal of obtaining an accurate Earth image as an iterative interpretive imag-

ing procedure. This procedure consists of an initial velocity model building followed by iterative prestack depth migration, geological interpretation and velocity analysis. I formulate a very general prestack depth migration velocity analysis method with illustrations of both simple and complex examples. The evaluation of the performances of both the integral and the reverse-time migrations, especially through extensive application examples of both methods to geologically complex areas, demonstrates that the Kirchhoff integral scheme should be a better candidate for iterative imaging from the cost effectiveness viewpoint. Nevertheless, reverse-time migration is a valuable complement to Kirchhoff migration, since it can possibly produce a more accurate image of the Earth during the final imaging iterations. In this study, I extensively compare Kirchhoff and reverse-time migration procedures both on model data and an Alberta foothills real data set provided by Husky Oil Inc.

Acknowledgments

I thank Larry Lines for accepting me as his Ph.D. student, and giving me the opportunity to participate in the research activities within the Memorial University Seismic Imaging Consortium (MUSIC). I benefited tremendously through his lectures and seminars which are always full of refreshing ideas with numerous application examples. I greatly appreciate the numerous times of free exchange of ideas which Larry always encourages. I thank Jim Wright for his continuous interest in my thesis. His encouragement and financial assistance through my changing of the seismograph on weekends are a very important part of my graduate life at Memorial University. I appreciate the help of the Society of the Exploration Geophysicists for its generous support through a scholarship. I also acknowledge a graduate fellowship from Memorial University of Newfoundland.

I would like to thank all the sponsors of the MUSIC project for their great interest in this thesis work on prestack depth migration, and also for their financial support. Their keen interest is one of the main forces pushing me to the frontier of this research. Special thanks go to Larry Mewhort of Husky Oil and Christof Stork of Landmark Graphics for providing us with the Husky–Canadian foothills line; and to Andrea Ehinger of Institut Francais du Petrole for sending me a copy of the Marmousi data set.

The completion of this thesis research is partly due to the help of many of my

colleagues within MUSIC. I thank Tony Kocurko for his excellent maintenance of the computer systems. I would also like to thank Paul Fardy for allowing me to use the university's high performance computer clusters. Both Tony and Paul made my task of development of this work easier and more efficient than I originally thought. My office mate Andy Burton was always ready for discussion, advice, and help in seismic data processing. Bill Nickerson and Han-xing Lu, my former office mates, helped me in my early studies in MUSIC before departing for industrial jobs. I greatly appreciate the time I had with Jamie Jamison during my comprehensive exams. Jamie enhanced my understanding of thrust belt geology, which is critical in my application of the prestack imaging technology to the Canadian foothills. I also thank Richard Wright and Anna Smirnova for their drafting work.

Finally, I thank my parents, my grandmother, especially my wife, Liyan, and my son, Yangyang for their patience, love and understanding during my long time leave for my graduate studies.

CONTENTS

List of Tables

List of Figures

Chapter 1. Introduction

Exploration seismology is the most important tool in the search for oil and natural gas. It is carried out by producing seismic waves that propagate in the Earth, reflected from different geological formation boundaries and are recorded at the Earth's surface. These recorded signals are then processed at computer centres to produce seismic sections or velocity models which provide geologically meaningful images of the subsurface. Geological interpretations are routinely carried out at different stages parallel to or cascaded with such a processing stream.

Traditionally, seismic data processing is based on the concept of a common midpoint (CMP) gather which is a set of traces sharing a same midpoint between source and receiver (Sheriff, 1991, p46). The CMP based processing is strictly valid only for layered Earth models in which velocity varies only with depth. In such Earth models, stacking or summation of traces which share a single CMP position but have different source-receiver offsets significantly enhances the signal to noise ratio of the result. As the search for oil and gas moves into more and more geophysically difficult environments with very complicated geological structures, this simple CMP based method often fails to fulfill its designated tasks: producing approximate structural images and velocity estimations of the interest area. To confront such challenges, geophysicists must create more advanced processing schemes and apply them more wisely.

In this dissertation, I investigate two powerful prestack depth imaging methods which can accurately image complex geology with strong velocity variations both vertically and laterally. The Kirchhoff integral and the reverse-time migrations are based on the integral and finite-difference solutions to the acoustic wave equation respectively. By performing depth migration with prestack data, most independent processing steps in the CMP based processing system are included in a single prestack depth wavefield extrapolation and imaging procedure. This prestack depth processing scheme is no longer dependent upon such concepts as CMP gathers. It aims to remove the wavefield propagation effect taking place in a physical experiment such as a shot gather using wave equation solutions. The key to such a depth migration is an accurate velocity model. In this dissertation, I extensively demonstrate the effectiveness of both the Kirchhoff and the reverse-time migration techniques coupled with robust and general velocity analysis methods in imaging both model data and real data from geologically very complex areas.

1.1. A critical review of standard CMP based processing

A CMP gather is a group of traces which share the same midpoint between source and receiver. It is also called a common depth point (CDP) gather, though they are not exactly the same in dipping interface cases. If the Earth is horizontally layered, then a CMP gather is just a common reflection point (CRP) gather in which

each trace records reflections from the same subsurface position of a given reflecting surface. In such cases, a sum or stack of these CMP traces, after proper static and dynamic time corrections, will produce a better representation of the reflectivity for that CMP position, because of the stacked trace's drastically improved S/N ratio. The advent of velocity analysis methods based on the semblance or stacking power of CMP gathers (Taner and Koehler, 1969) marked the zenith of CMP based processing. The conventional CMP based processing procedure consisted of static and dynamic corrections, CMP sorting, velocity analysis, and stacking. This procedure, typically used in the 1960s, worked very well when the exploration target was of a simple layer-cake geology. With the addition of post-stack migration, this CMP method could even provide reasonably good images of the subsurface with some mild structural variations, though it was found that reflection points in a CMP gather were not common for dipping layers (Levin, 1971). This reflection point smearing problem can be removed by dip-moveout processing (DMO) (Deregowski, 1982; Hale, 1984) in media without lateral velocity variations. DMO is a process that creates apparent CRP gathers by a convolution applied to adjacent CMP gathers. After DMO, the normal moveout for reflections from a dipping bed no longer depends on the dip angle. Figure 1.1 is a simplified flowchart of this processing scheme based on the CMP concept. In practice, this flowchart is often augmented with additional quality control components. Here I will review some of the key steps in this procedure.

1.1.1. Static and dynamic corrections

Two time corrections have to be applied to each trace before CMP stacking. This will ensure that each trace in a CMP gather records the reflections from the CMP

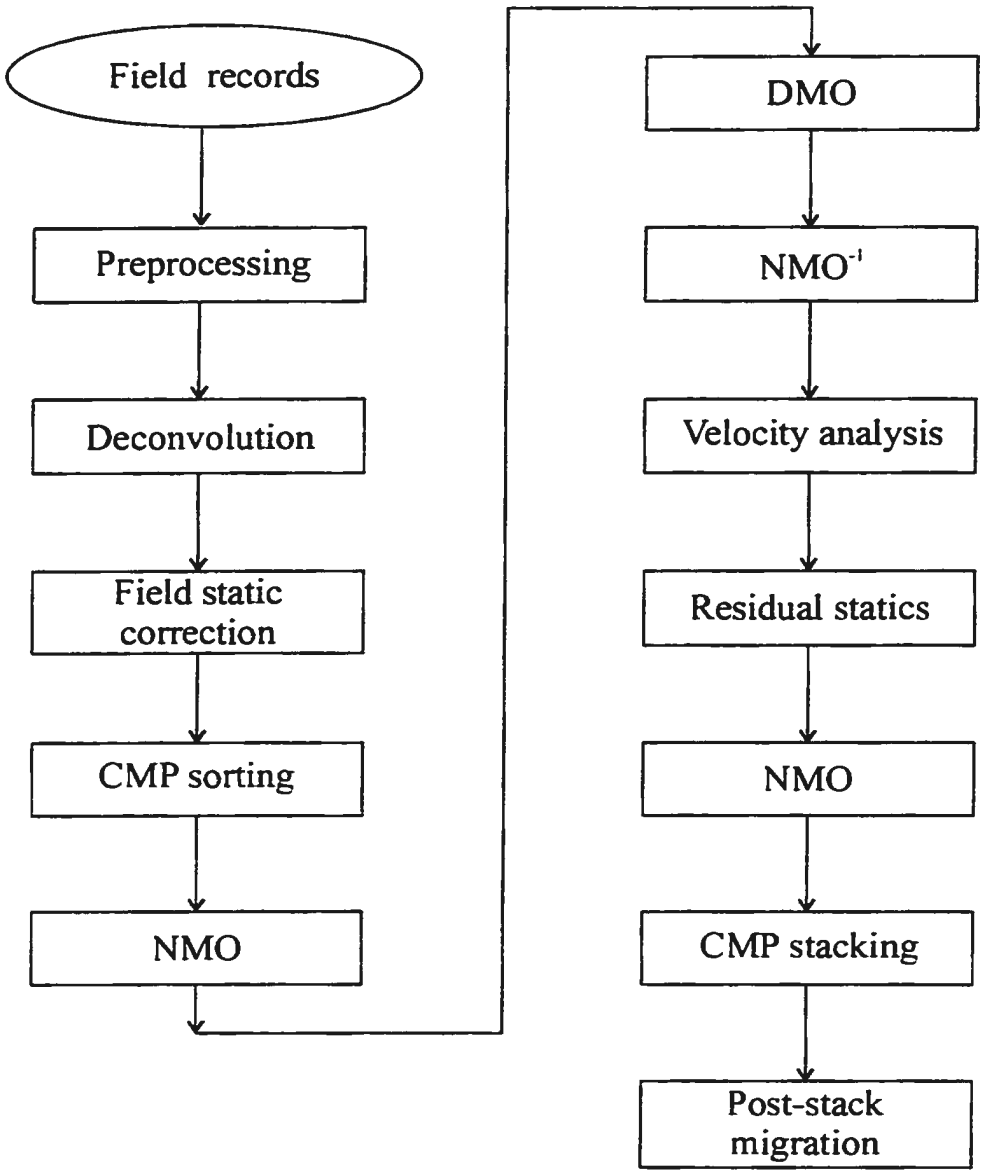

Figure 1.1: Standard CMP based processing flowchart.

with nearly the same travel time in a layer-cake Earth model, and thus stacking is coherent.

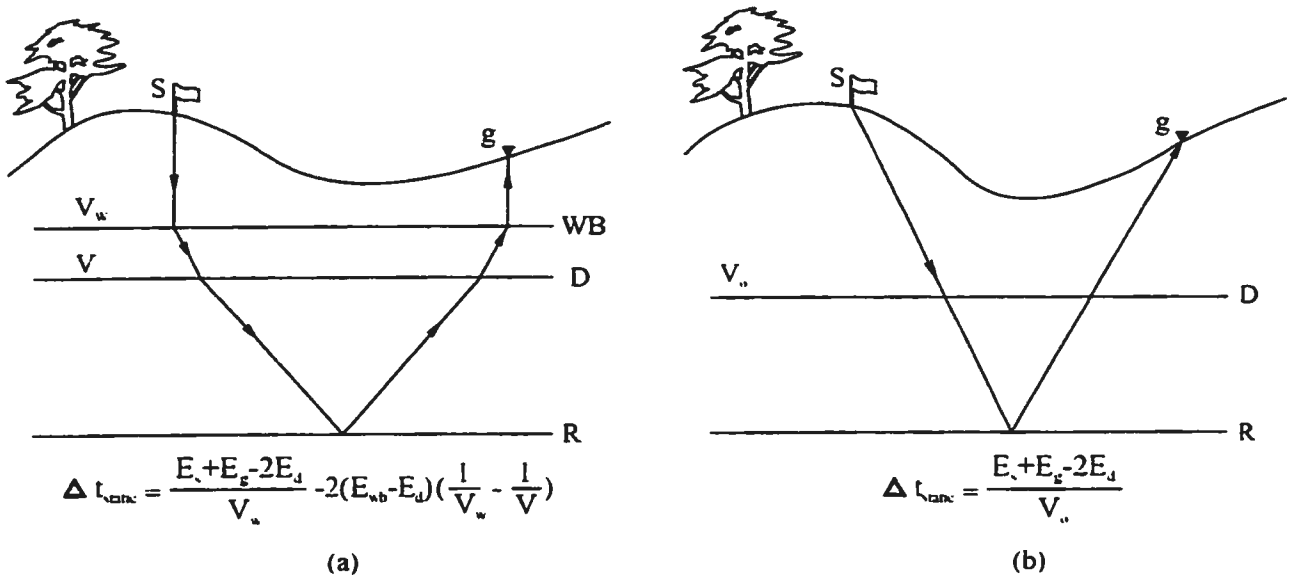

Figure 1.2: (a) Conventional statics model works well with Earth models covered by a low velocity layer where emergent rays are nearly vertical. (b) The model is a poor approximation for cases with high velocity layer coverage where rays bend away from vertical.

Static corrections compensate for traveltime anomalies caused by source and/or receiver elevations and near surface heterogeneity. Thus in their simplest form. static corrections are essentially a geometrical re-datuming process which maps recordings from the Earth's surface to some reference level. This geometrical approach is a good approximation as long as rays travel nearly vertically between the topography and the datum (Figure 1.2a). In most sedimentary basins where there exists a low velocity layer at the Earth's surface, raypaths are nearly vertical near the surface. However, there still exist many geological areas where high velocities exist at the

Earth's surface. A good example is the Alberta foothills where thrust faults placed high velocity rocks at the surface. In such cases, raypaths significantly deviate from the vertical, as shown in Figure 1.2b, and the conventional static correction is thus not appropriate (Lines et al., 1996).

The dynamic, or normal moveout (NMO) correction aims to remove the offset dependency of traveltimes in a laterally invariant medium. Using small offset/depth ratio assumption, traveltimes are often approximated by (Dix, 1955),

$$t^2(x) = t^2(0) + \frac{x^2}{v_{rms}^2} \tag{1.1}$$

This is equivalent to the assumption that the reflection traveltimes follow hyperbolic trajectories. Such a treatment is acceptable when offset is limited. However, as greater source–receiver offsets become common, traveltimes at far offsets, especially for shallow reflectors, can never be properly described by equation (1.1). A good example is the Husky–Alberta foothills line which I will use extensively in this thesis where the maximum offset is greater than 6 km while the exploration target is only about 3 km in depth.

1.1.2. DMO and stacking

The NMO correction removes only the offset dependence of traveltimes. In the case of a dipping interface as shown in Figure 1.3a, source-receiver pairs sharing a common midpoint will generally record reflections from different segments of the reflector. Hence the sorted CMP gathers are no longer equivalent to CRP gathers. Such reflection point smearing is particularly deleterious for shallow dipping formations, a common feature in mountainous areas. In fact, even with horizontal interfaces, there

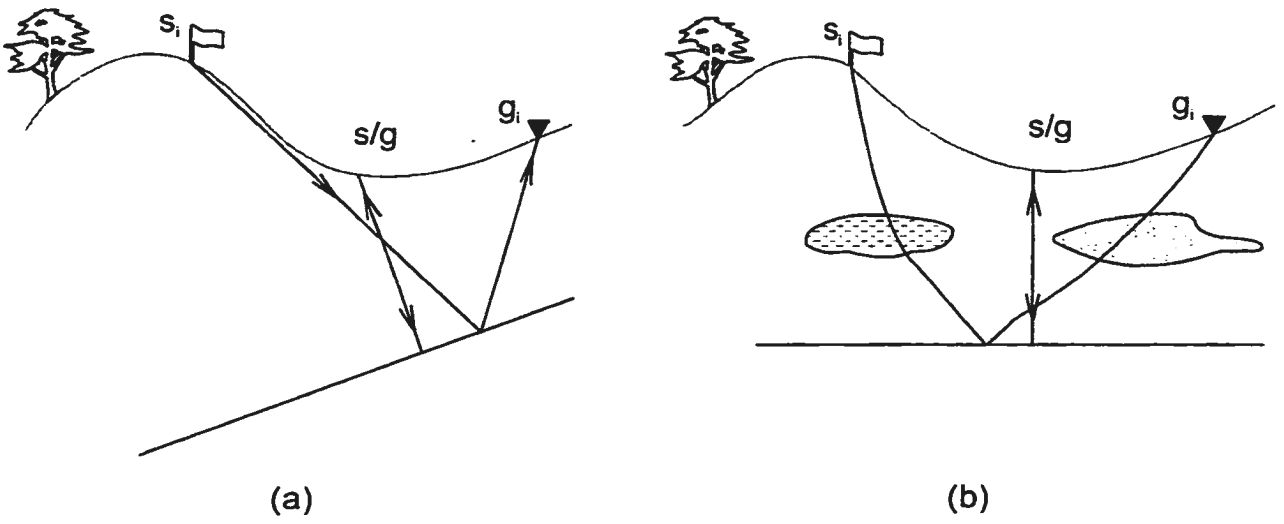

Figure 1.3: Reflections from a given reflector in a CMP are not from a common reflection point. Such reflection smearing can be due to dipping interfaces (a), or lateral heterogeneities (b). DMO can only remove the dipping layer effect in (a). s/g represents an identical source-receiver position.

is still the possible problem of reflection smearing due to lateral velocity variations, as shown in Figure 1.3b. In addition to smearing, there is another component of traveltime variations due to the dipping effect. DMO is designed to solve both problems of the reflection point smearing and the time dependence on dips (Hale, 1984; Deregowski, 1986). However, DMO can only solve the problem shown in Figure 1.3a. The problem in Figure 1.3b is essentially a depth migration issue.

DMO, combined with NMO, thus can effectively transform each offset trace into a zero-offset one. This implies that after DMO, a CMP gather essentially contains reflections from a CRP. Stacking these DMO corrected traces is thus truly CRP stacking which should be coherent after NMO. In areas with lateral variations and/or strong vertical variations, DMO is, nevertheless, not totally effective.

1.1.3. Post-stack migration and the exploding reflector model

Migration is the mathematical process of moving reflection and diffraction events to their true originating places. Post-stack migration is based on the assumption that a stacked section is equivalent to a zero-offset section. How good is this assumption? We actually only record signals without zero-offset components due to the field difficulties of placing a detector at the same place as the source. The process of "$NMO + DMO + stacking$" which I just described transforms the non-zero offset sections into a zero offset one based on the assumption of hyperbolic trajectories of the reflections. As I reviewed above, such a hyperbolic assumption is not valid for cases with large offset/depth ratios. It introduces a significant error in areas with strong lateral velocity variations. As will be seen in the later chapters, such violations of the assumption exist in the Husky–Alberta foothills data. In these cases, it is impossible to expect post-stack migration to do a good imaging job, as migration cannot recover the loss of information due to the inadequacies of time corrections, DMO and stacking.

In addition to the hyperbolic approximations, post-stack migration is also based on an imaginative model — the exploding reflector model. Instead of placing sources and receivers at identical positions at the Earth's surface, the model assumes that sources are excited in unison on impedance interfaces and reflections are then picked up by receivers at the surface. To make the sections time comparable, we can either halve the velocities, or halve the size of the velocity model in proportion, or just double the traveltime. The exploding reflector model is very powerful for both simulation and migration. However, it still cannot predict all the wave phenomena in the zero

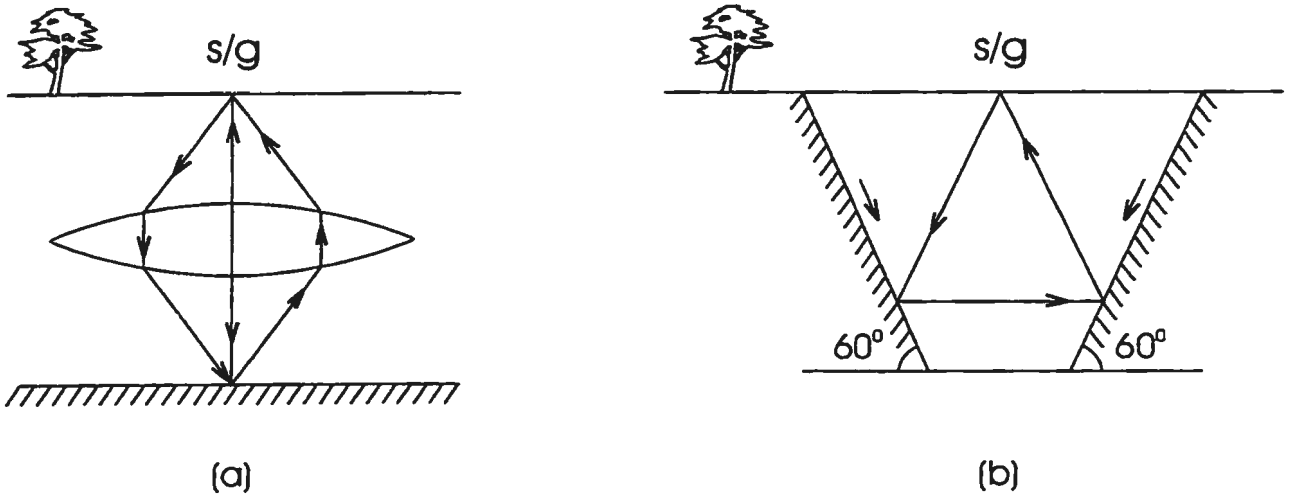

Figure 1.4: Two examples of zero-offset sections where received reflections do not follow the travel-paths of the downgoing waves due to the effects of a low velocity lens (a), and a combination of antithetic faults (b). s/g represents an identical source-receiver position.

offset section. As pointed out by Claerbout (page 11, 1985), there are at least three occasions where the reflector model fails. The first is in its inability to predict some events which appear in a zero-offset section. Figure 1.4a illustrates that many non-perpendicular reflections, in addition to the perpendicular one, could be reflected from the reflecting horizon and arrive at the same surface position as the source position due to the highly focusing function of the low velocity lens in a high velocity environment. These non-perpendicular raypaths are nevertheless not described by the reflecting model. Figure 1.4b shows another example of such non-perpendicular reflections bouncing between steeply dipping antithetic faults. Secondly, the exploding reflector model only predicts multiples that strike the Earth's surface with odd numbers, which implies that about half of the multiple family is not properly included by the exploding

reflector model. A third mismatch of the exploding reflector model with a zero-offset section lies in the polarity of reflections from an interface. According to the exploding reflector model, interfaces will emit waves to both sides with the same polarity while the reflection law actually dictates that these reflections should be of opposite polarity. In addition, the amplitudes predicted by the exploding reflector model are different from those in a zero-offset experiment. This is due to the different transmission effects and geometrical divergence as a result of halving the propagation procedure.

From all the above analysis, it is apparent that in geologically complex areas, a CMP gather is no longer equivalent to a CRP gather; the conventional static corrections model and the exploding reflector model break down; and DMO fails in lateral velocity variation areas. Therefore, there is no doubt that the standard CMP based processing scheme cannot produce a good subsurface image in these complex geological environments.

1.2. Prestack depth migration: its promises and premises

A critical review of the CMP based processing strategy indicates that it cannot properly handle the problem of imaging steeply dipping reflections, especially those far offset components. Neither can it be applied to areas with strong lateral heterogeneity. The failure is basically due to the breakdown of the hyperbolic approximation of reflections. Thus, even prestack time migration cannot properly image subsurface

with such strong lateral variations as it is also based on the same hyperbolic assumption described by a single velocity — the RMS velocity. In fact, as the CMP based procedure of "NMO + DMO + stacking + post-stack migration" is approximately equivalent to prestack time migration if the vertical velocity variation is not too drastic (page 337, Yilmaz, 1987), it is not surprising that prestack time migration will also fail in areas with lateral velocity variations.

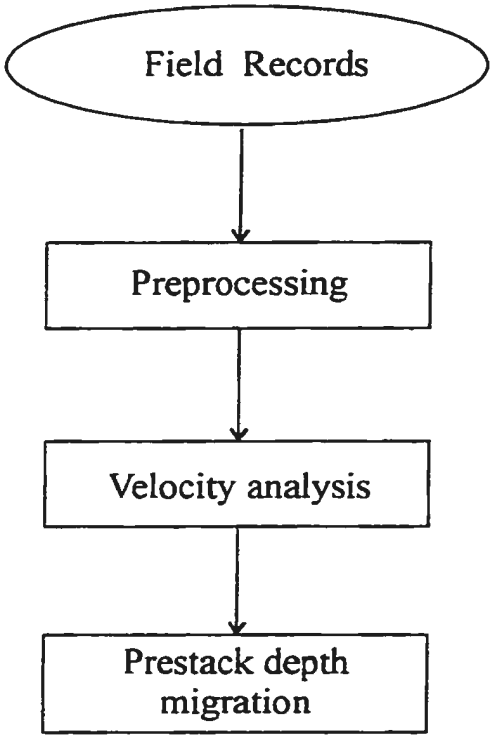

Figure 1.5: Schematic flowchart for prestack depth processing.

Prestack depth migration is promising for such situations. This migration, as is theoretically expected, uses a physically meaningful velocity — the interval velocity model of the Earth — to backward propagate the recorded seismic signals at the Earth's surface to their true originating places in depth. Figure 1.5 schemati-

cally illustrates the key processing components in a prestack depth processing procedure. Comparison of Figure 1.5 with Figure 1.1 clearly demonstrates the simplicity of prestack depth processing. Thus, a wave equation based prestack depth imaging process such as the Kirchhoff integral or the reverse-time migration method which I will discuss in later chapters provides the following promises:

· Migration is directly based on solutions of the wave equation of the true physical process without the use of such concepts as CMP and the exploding reflector model.

· Independent processes such as statics, NMO, DMO, and migration in a CMP based processing strategy are automatically included in the sole prestack depth migration program, making the whole processing procedure more compact. This single program is even capable of filtering selectively, and interpolating missing traces of unaliased seismic data.

· Migration will be theoretically accurate with no restriction on the nature of the structure and velocity variations of the earth. Thus, diffractions will be fully focused to their true diffractor locations; dip reflections will truly move to their true spatial positions.

· Migration will be directly applicable to topographic areas with strong vertical and lateral velocity variations as migration uses the true source and receiver positions.

· Migration can be highly target-oriented as it is performed on shot gathers. If the integral method is used, we can even select only a portion of traces in a gather. Such shot gather migration also significantly simplifies the data management and processing without the need to sort to other data structures. Such profile migration is naturally tailored to parallel processing.

· Migration only uses one velocity function, the interval velocity in contrast to sev-

eral different velocity functions for each processing step in the CMP based method. Though many different velocity tools are available in the CMP based system, using the rock velocity as a single necessary velocity function makes the procedure more physically interpretable and theoretically simpler. In addition, migration itself provides a theoretically more accurate domain and data set for rock velocity analysis.

· Migration provides a depth section of reflectivity, stacked over a range of illuminated angles, which is a directly interpretable geological section. This section contains no vertical and lateral exaggerations.

· Migration provides a more accurate estimation of reservoir locations and reservoir volumes.

Therefore, prestack depth migration should be theoretically performed whenever possible to achieve all the above benefits. Nevertheless, such benefits can only be achievable with the following two premises:

· Very powerful computing resources are available, as prestack depth migration generally requires huge amounts of computation for wavefield extrapolation. Previously, this was the bottleneck in the implementation of prestack depth migration. With the drastic increase of computational powers in the past few years, this constraint is becoming less critical.

· A reasonably good estimate of the interval velocity model is available. As such a velocity model is used for the wavefield propagation purposes, a macro model with the low wavenumber components of the velocity field often suffices for this purpose (Berkhout, 1984). Theoretically, this model is progressively approachable by velocity analysis after prestack depth migration itself. An approximate starting model is often provided by the CMP based processing flowchart, as no prestack depth migration is

attempted without preliminary CMP processing.

It is seen that prestack depth migration offers great promise to improve imaging in complex geological settings. I will layout the overview of the two approaches to accomplish the imaging task: prestack Kirchhoff and reverse-time depth migrations.

1.3. Overview of the dissertation

This thesis develops two powerful prestack depth migration techniques to image complex geological structures using seismic data. Seismic imaging is fully based on wave equation solutions of wave propagation in true physical processes. Such prestack depth imaging is nevertheless computationally highly intensive. The ultimate objective of this dissertation is to develop an accurate imaging strategy for seismic data acquired from very complex geological areas using prestack depth migrations with reasonably inexpensive computations.

For this objective, a new, efficient, and robust traveltime calculation method is first developed by tracing propagating wavefronts. This method is used for a prestack Kirchhoff migration method, which is developed in Chapter 3. Though the Kirchhoff method has been around for about 2 decades, I have made several innovations to make the technology more widely applicable and more efficient. The technique is now applicable to any heterogeneous media for any recording geometry. In the prestack reverse-time migration, I find its implicit interpolation mechanism during its back-

ward wavefield extrapolation. I demonstrate that this mechanism makes it possible to migrate irregularly and sparsely spaced unaliased seismic data directly without explicit trace interpolation. Both the prestack Kirchhoff and the reverse-time migrations are extensively compared from both theoretical and application perspectives. It is one of the first such comparisons in the area of prestack depth migrations. The prestack migration moveout theoretical derivations are totally new, and also more general than any previous publications. Because of the difficulty of obtaining an accurate velocity model, the imaging of complicated geological structures is completed by an iterative interpretive imaging procedure which I develop in this thesis. This imaging strategy of complex geological settings is certainly innovative. In addition, I have extensively applied the developed prestack Kirchhoff and reverse-time imaging techniques to produce improved images of both complex model and real seismic data.

Throughout this dissertation, I will extensively use a synthetic seismic data set — the Marmousi model (Versteeg, 1993), and a real seismic data set from the Alberta foothills—the Husky–Alberta foothills line. Figure 1.6 shows the Marmousi velocity model. It is based on a geophysical model from the Cuanza Basin of Angola. The basin is dominated by growth faults due to salt creep (Bevc, 1997). Figure 1.7 is the final velocity model of the Husky–Alberta foothills line. The Alberta foothills line entails many geological features such as rough topography and shallow steeply dipping formations due to thrust faulting that make seismic imaging difficult (Skuce, 1995). The migration methods developed in this thesis will be tested on these two difficult data sets. Figure 1.8 is the final geological interpretation of the Husky–Alberta foothills data using the iterative interpretive imaging strategy developed in this thesis. This interpretation outlines the geological formations in the subsurface.

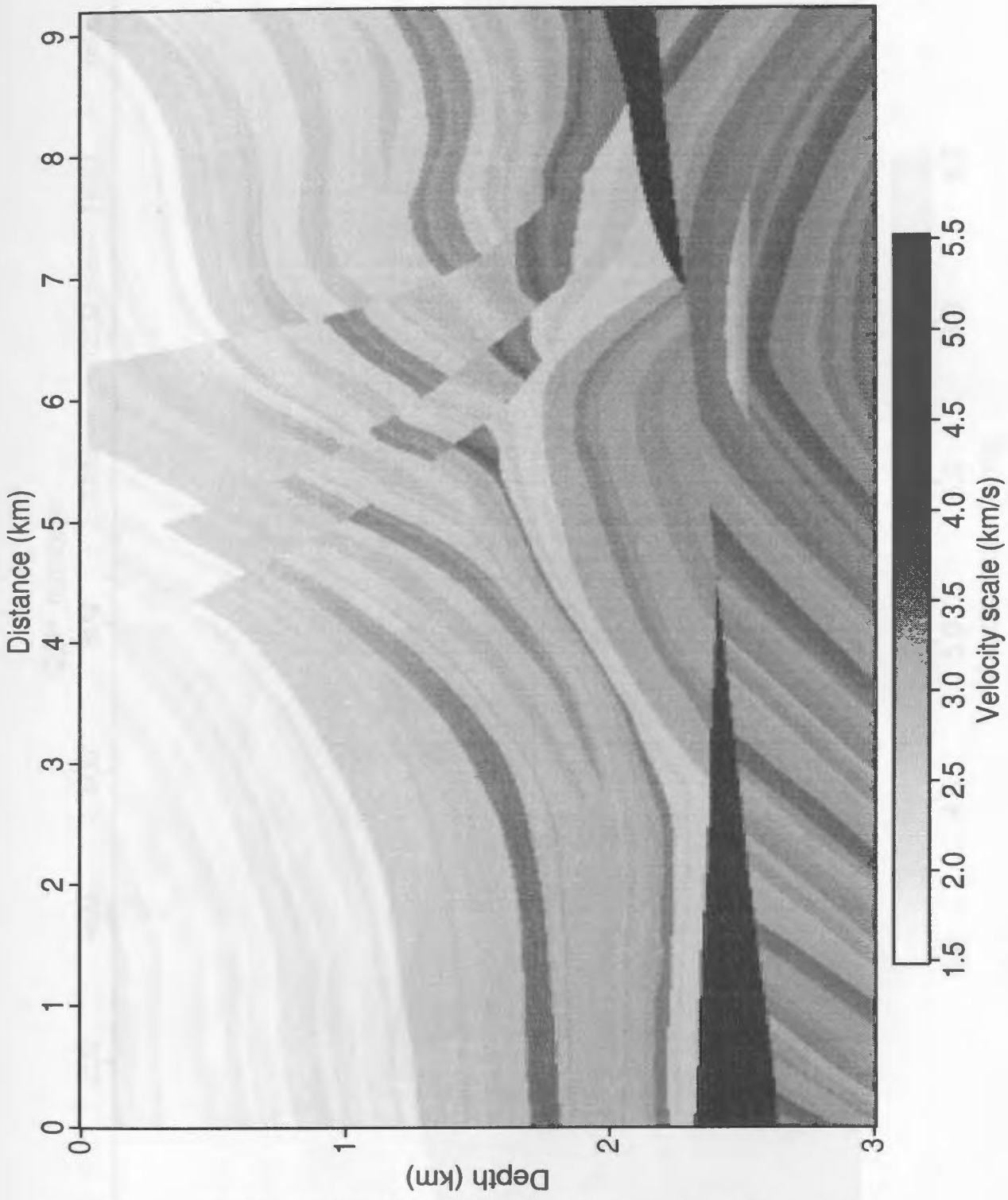

Figure 1.6: The Marmousi velocity model.

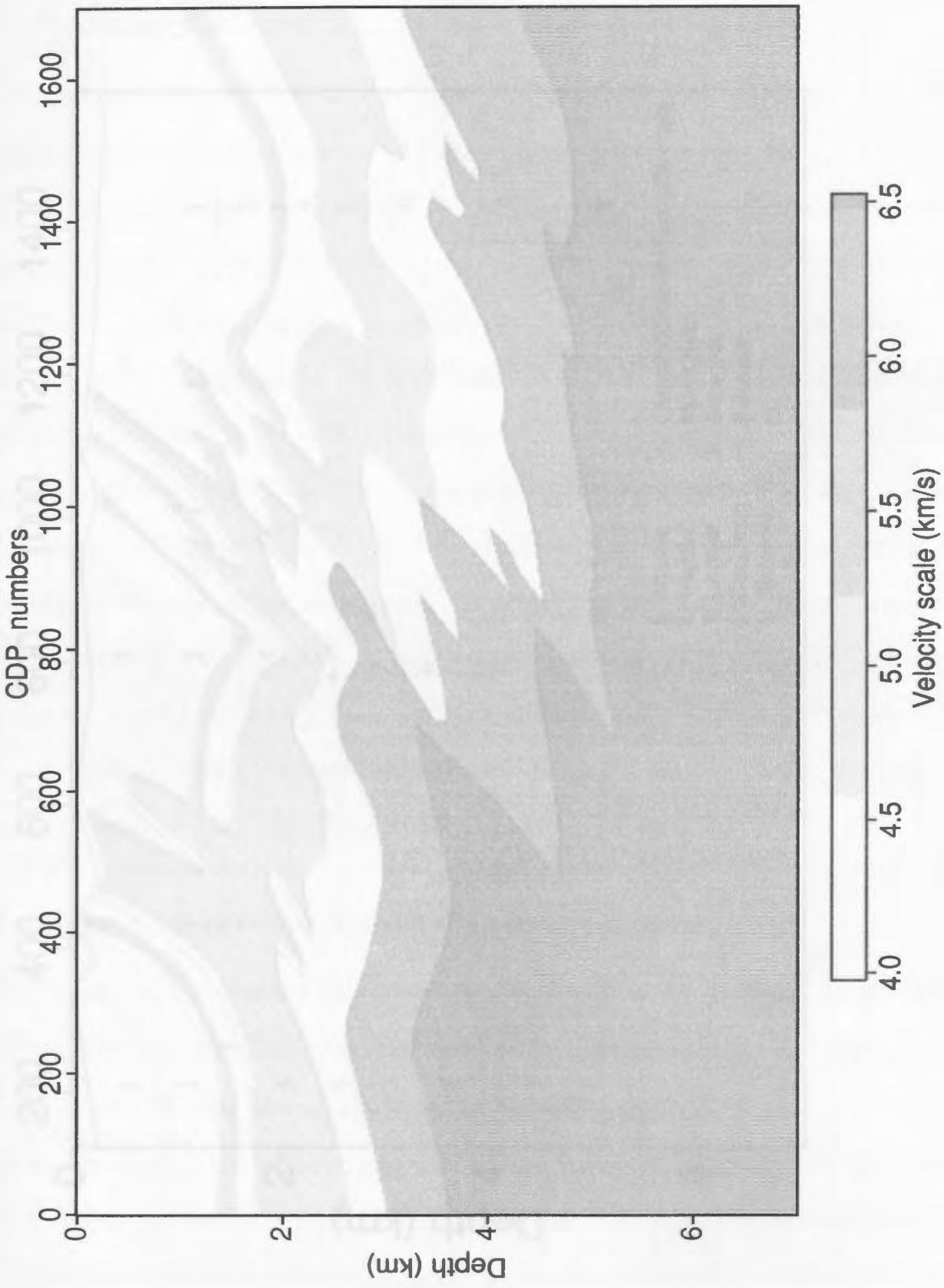

Figure 1.7: Velocity model of the Husky–Alberta foothills line.

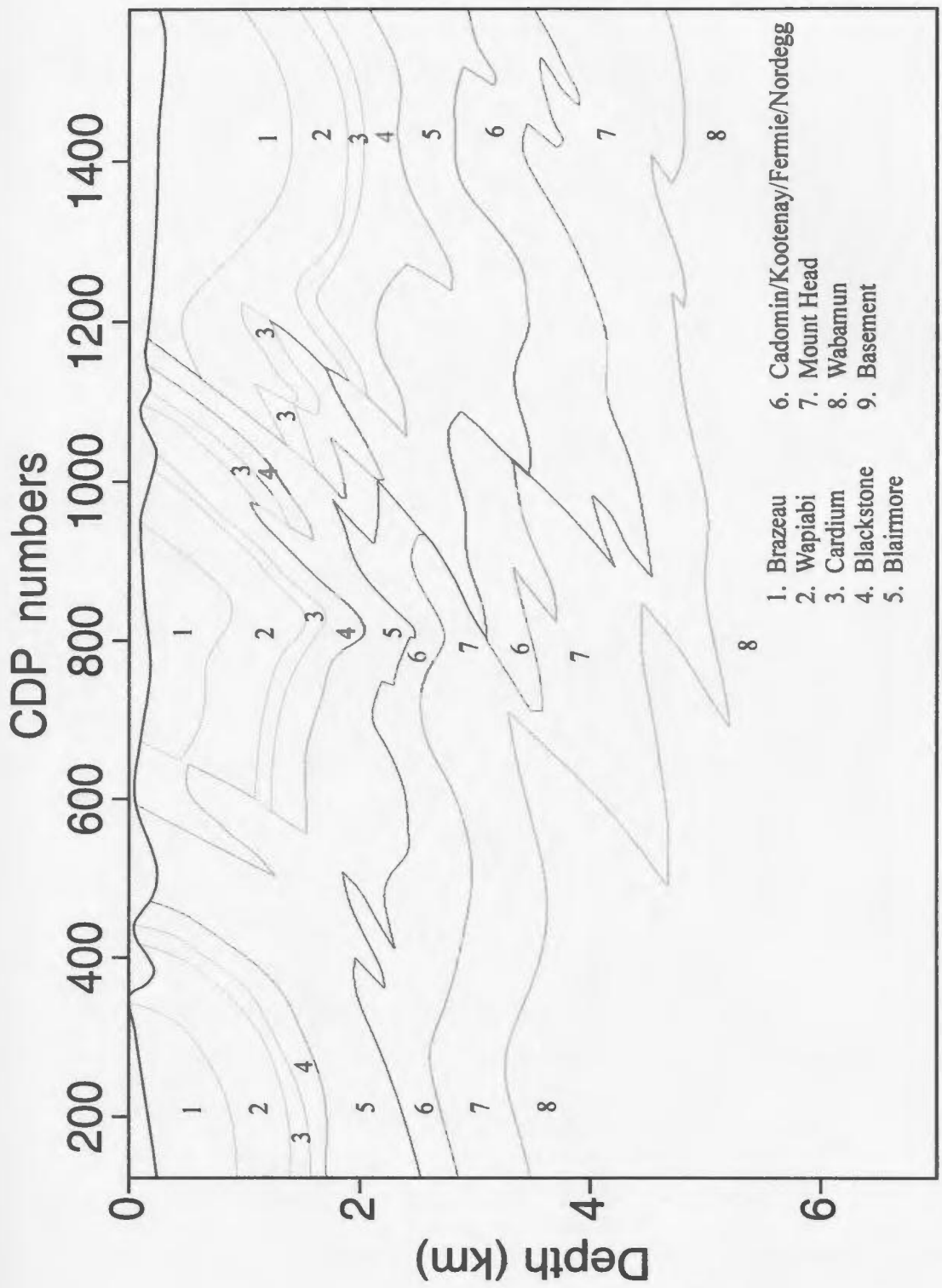

Figure 1.8: Geological interpretation of the Husky–Alberta foothills line.

1.3.1. Wavefront tracing

Seismic traveltime is one of the most fundamental parameters in exploration geophysics. Ray tracing via solutions to the eikonal equation is a standard technique for traveltime determination. The eikonal equation describes a relationship between the gradient of the traveltime field and the medium velocity. The finite difference solution method provides another alternative for solving the eikonal equation.

In Chapter 2, I formulate a comprehensive algorithm for traveltime calculations by tracking wavefronts in complicated media. This method combines the finite difference solution of the eikonal equation, excitation of Huygens' secondary wavelets, and the application of Fermat's principle. The method is in fact a unified algorithm for computations of first arrival traveltimes. It is directly applicable to tracking plane waves. Its accuracy and robustness are demonstrated through examples of complicated Earth models with very high velocity contrast both vertically and laterally. Examples show that first arrivals are properly tracked for direct waves, transmitted waves, head waves, and even diffracted waves.

1.3.2. Imaging via prestack Kirchhoff depth migration

In Chapter 3, I present a unified integral formulation for prestack depth migration of common shot gathers acquired with any recording geometry in structurally complex areas. Firstly, the classic summation method along hyperbolae and the superposition method of circular wavefronts are shown to be extendible for use in variable velocity areas by replacing the hyperbolic diffraction trajectories and circular wavefront patterns with generalized hyperbolic curves and aplanatic surfaces

which define isochrons of possible diffraction/reflection points for a given source and receiver pair. These extensions are useful for imaging complex structures if amplitude information is not critical. Using the WKBJ approximation to the Green's function, I then derive several migration integral equations which are termed Kirchhoff integrals. These integrals are very general and are applicable to any recording pattern over complex structures. The general Kirchhoff integral is shown to be a simple summation of amplitudes of differential traces along an integral surface with amplitudes being modulated by certain geometrical functions.

Using the stationary phase concept, I derive an integral equation for migrating data acquired along a line instead of over an area. The integral over a line is more complicated than its 3D counterpart. It is essentially a curvilinear integral of differential trace amplitudes affected by some geometrical factors. The determination of the integral curve, along with the weighting factors, constitutes the main challenge to the calculation of this integral. The implementation of such an integral using traveltimes provided by the wavefront tracing method of Chapter 2 proves to be viable. The chapter concludes with application examples of the general integral implementation to the Marmousi model where very complicated geological structures exist, and to the Husky–Alberta foothills line with rough topography and strong near surface heterogeneities due to thrust fault movement.

1.3.3. Imaging irregular data via prestack reverse-time migration

Reverse-time migration, currently the most accurate migration method applicable to both 2D and 3D surveys, is investigated in Chapter 4. In addition to its intrinsic advantages, such as simultaneous static correction and selective filtering based on the

velocity model, I find that it also has the inherent interpolation mechanism which results from the wavefield self-healing ability via interference of waves during the reverse–time propagation procedure. However, such mechanisms function properly only when the original records are not both temporally and spatially aliased. Snapshots taken during reverse-time migration of the Marmousi synthetic data and a line of the Husky–Alberta foothills data clearly demonstrate the wavefield self-healing procedures. These tests provide the experimental results for migrating unaliased seismic data, either stacked or prestack, without the need of prior interpolation of missing traces. In fact, by treating recordings as distributed sources on the recording surface, the wave equation can directly be driven backward in time with these distributed sources acting continuously. Thus migration of unaliased data without interpolation of missing traces is also developed. However, such an implicit interpolation mechanism is very difficult to explain from the boundary value viewpoint of the recordings.

The self-healing mechanism of the wavefield thus provides the basis for directly migrating sparsely spaced unaliased data. This is especially important in prestack cases where there is seldom one trace per grid point on the recording surface if a grid model with the mesh size as fine as the CDP bin size is used. This implementation of reverse-time migration has been extensively applied to data sets both of stacked and shot gathers acquired over structurally very complex areas. The imaging of the Husky–Alberta foothills line, where traces are generally sparse and irregularly spaced relative to the fine finite-difference grid, demonstrates a successful example of this reverse-time migration implementation on unaliased data, without the need for interpolating the missing traces in advance.

1.3.4. Iterative interpretive imaging

In Chapter 5, I move one step further in trying to propose an ambitious imaging system which will solve the imaging problem in a reasonably accurate and efficient way. For that development, I first make a comparison of two of the most widely used prestack depth migration methods — the Kirchhoff integral and the reverse-time techniques discussed in Chapters 3 and 4. Theoretical insights tell us that both are wave equation based methods applicable to very complex geological areas even with rough topographies. Both are good candidates for algorithm optimization through several levels of parallelization and vectorization. However, the integral scheme is trace based processing, and thus can migrate data selectively for some pre-specified targets. On the other hand, reverse-time migration is theoretically more accurate. Its high accuracy is achieved at the expense of significantly more computation. The application of both methods to the Husky–Alberta foothills line demonstrates that the Kirchhoff method can produce a migration image nearly as accurate as the reverse-time migration method, with much less computational effort. This is due to our inability to obtain an exact interval velocity model in the real data case. From such comparisons, I conclude that the Kirchhoff method should be the primary migration technique in the process of the iterative interpretive imaging strategy, with the reverse-time migration being applied at the last iterations to possibly provide a better image.

The interval velocity model determination is both our goal and also an assumed input for this imaging scheme. This appears to be a dilemma. As prestack depth migration itself is very sensitive to velocity errors, common image gathers (CIGs) formed from prestack depth migration results are shown to be an effective domain

for analyzing and updating velocity. However, interval velocity should be updated with proper geological input, otherwise significant errors could be introduced into the velocity model due to improper definition of formations. For more efficient and accurate determination of the interval velocity field, I propose to use as many parallel means as possible during the process of this iterative interpretive imaging.

1.4. Summary

The thrust of this thesis is to use solutions to the wave equation, both via Kirchhoff integrals and finite-difference schemes, to perform a general prestack depth migration. This procedure greatly simplifies the standard CMP based processing scheme, while maintaining validity in structurally complex settings. Both the prestack Kirchhoff and reverse-time migrations are incorporated into an iterative interpretive imaging procedure which consists of initial velocity model setup, prestack depth migration. geological interpretation of migrations sections and velocity analysis. The final result of such an interpretive imaging procedure produces not only improved images of the subsurface, but also a detailed interval velocity model. The consistent results of the migration image and the velocity model are very helpful in structural interpretation and reservoir analysis.

Chapter 2. Traveltime determination by tracing of wavefronts

Seismic traveltimes are the primary data recorded in geophysical applications ranging through locating earthquake epicenters, seismic modeling, seismic tomography, and seismic migration and inversion. Traditionally, theoretical traveltimes have been computed with ray tracing methods. The ray equations are derived from the eikonal equation whose solutions are raypaths or characteristic curves of the eikonal equation. Physically, rays are the trajectories along which high frequency energy transports. A number of efficient methods for solving the ray equations have been developed in the past two decades (Langan et al., 1985; Cerveny, 1987)

In contrast to tracing rays, graphic methods were proposed for tracing wavefronts in simple models, and were computerized and further generalized to layered media. Reshef and Kosloff (1986) first formulated a finite difference scheme to solve the eikonal equation for traveltimes on a uniform grid by depth extrapolating the gradient of the traveltime field, followed by a depth integration of the gradient field. Subsequently, Vidale (1988) proposed a very general and efficient quasi-wavefront tracing algorithm directly based on a finite difference scheme for the eikonal equation. Based on the assumptions of local plane or circular wavefronts, Vidale solves the eikonal equation by progressively extrapolating the traveltime field of the first arrival waves

outward from an "expanding square" centered at the point source. However, Vidale's original method often fails in geologically complex settings where large velocity contrasts exist.

In this chapter, I will first examine the intrinsic assumptions in the derivation of the eikonal equation which helps give a better appreciation of the validity of applying the eikonal equation in the real geophysical world. Then I will formulate a scheme for extrapolating wavefronts of first arrivals in a very general sense. The scheme is essentially a combination of the finite difference solution of the eikonal equation, the excitation of Huygens' secondary sources, and application of Fermat's principle. This formulation is applicable to calculating traveltimes from any shape of the initial wavefront.

2.1. The eikonal equation and its ray solution

Current seismic data processing practices are mainly structured on the acoustic wave equation. Using a high frequency approximation, the eikonal equation is derived which describes the relationship between the traveltime gradient field and the velocity distribution of the medium. In this section, a solution of the eikonal equation is formulated as a ray tracing system using the traveltime as the independent integral variable. By tracing a fan of rays from the distributed source, it is shown that this is equivalent to tracing the wavefronts.

The heterogeneous acoustic wave equation governs wave propagation in a general acoustic medium (Kelly et al., 1982):

$$\nabla^2 u - \frac{1}{c^2}\frac{\partial^2 u}{\partial t^2} = \nabla \ln \rho \cdot \nabla u, \tag{2.1}$$

where $c = \sqrt{K/\rho}$ is the propagation velocity of the compressional waves in the media. It is generally a function of space, i.e., $c = c(\vec{r}) = c(x_1, x_2, x_3)$. ρ is the mass density; and K is the compressional modulus of the medium, i.e., the reciprocal of compressibility. u is either the acoustic pressure or the rate of particle displacement. From both acoustic and elastic wave propagation studies (Alford et al., 1974; Kelly et al., 1976; and Wapenaar and Berkhout, 1989), it is seen that a vertically oriented seismometer primarily records compressional waves, especially when the recorder is not far away from the source. As the current seismic industry is still dominated by vertical component seismometers, this scalar wave equation would thus be an appropriate substitute for the elastic wave equation.

From (2.1) it is apparent that the influence of an inhomogeneous density distribution on the compressional wave propagation is simply to introduce an extra source term whose strength is dependent on both the gradient field of the pressure and the gradient of the density function. Hence, in a homogeneous medium where $\nabla\rho = 0$. the wave equation simplifies to

$$\nabla^2 u - \frac{1}{c^2}\frac{\partial^2 u}{\partial t^2} = 0. \tag{2.2}$$

Equation (2.2) is the starting point for geophysical applications and analysis. In fact, it can be validly used if the following condition holds (Berkhout, 1982),

$$|\nabla \ln \rho| \ll k, \tag{2.3}$$

or,

$$\frac{|\nabla \rho|}{\rho} \ll \frac{2\pi}{\lambda}, \tag{2.4}$$

where k is the wavenumber; λ is the wavelength. This condition simply states that the relative variation of the density is far smaller than 2π within the distance of a single wavelength. This condition is true for most geological formations, especially under the assumption of the high frequency approximation which is widely used in seismology.

Even in the normal seismic frequency band (10 — 100 Hz), there are good reasons to drop the density term acting as a source. Claerbout (1985, p48-49) gives two explanations for this approximation: the relative difficulty in obtaining a good density information, and for ease of mathematical treatment of the wave equation. For example, spatial Fourier transforms will be applicable to (2.2), greatly simplifying the solution procedure. In fact, dropping the source term due to the density heterogeneity does not simply mean we neglect the density function altogether in the wave equation. In reality its main influence is properly included in the description of wave propagation by both the velocity and the impedance which is the product of density and velocity.

Now assume equation (2.2) has the following Fourier series trial solution (Berkhout, 1982, p85),

$$u(\vec{r}, t) = \sum_i A_i(\vec{r}) e^{-j\omega_i[t-\tau_i(\vec{r})]}. \tag{2.5}$$

For this trial function, we have

$$\nabla^2 u = \sum_i \left(\left[-\omega_i^2 A_i (\nabla \tau_i)^2 + \nabla^2 A_i \right] + j\omega_i \left[2\nabla A_i \cdot \nabla \tau_i + A_i \nabla^2 \tau_i \right] \right) e^{-j\omega_i[t-\tau_i(\vec{r})]} \tag{2.6}$$

$$\frac{\partial^2 u}{\partial t^2} = -\sum_i \omega_i^2 A_i e^{-j\omega_i[t-\tau_i(\vec{r})]}. \tag{2.7}$$

Substituting the above expressions into (2.2) leads to

$$\sum_i \left\{ \left[-\omega_i^2 A_i \left((\nabla \tau_i)^2 - \frac{1}{c^2} \right)^2 + \nabla^2 A_i \right] + j\omega_i \left[2\nabla A_i \cdot \nabla \tau_i + A_i \nabla^2 \tau_i \right] \right\} e^{-j\omega_i [t - \tau_i(\vec{r})]} = 0. \tag{2.8}$$

Thus both the real and the imaginary parts should be zero

$$\nabla^2 A_i - \omega_i^2 A_i \left((\nabla \tau_i)^2 - \frac{1}{c^2} \right) = 0; \tag{2.9}$$

$$2\nabla A_i \cdot \nabla \tau_i + A_i \nabla^2 \tau_i = 0. \tag{2.10}$$

Equation (2.10) is the transport equation. In the case of high frequency content or spatially slowly varying wave amplitudes, it follows that

$$\nabla^2 A_i \ll \frac{\omega_i^2}{c^2} A_i, \tag{2.11}$$

and (2.9) simplifies to (Bleistein, 1984, p258),

$$(\nabla \tau_i)^2 = \frac{1}{c^2}. \tag{2.12}$$

Equation (2.12) is the well-known eikonal equation. That is, traveltime τ is the solution of the eikonal equation. This formulation clearly indicates that the traveltime field $\tau(\vec{r})$ is independent of frequency provided that condition (2.11) holds.

As $\nabla \tau_i = 0$, or $\tau_i = const$ represents a wavefront where all the waves are in phase. condition (2.11) implies that there is little amplitude variation along the wavefront or the waves are of very high frequency. That is, when the frequencies of the waves studied are high, or the amplitudes change little along the wavefront even with frequency band-limited content, the wave propagation can be mathematically described by the eikonal equation.

After the traveltime field $\tau(\vec{r})$ is obtained, it can be used to calculate the amplitude information using the transport equation (2.10).

Now we will seek a solution of the eikonal equation by ray tracing. First we will rewrite the eikonal equation as

$$p_1^2 + p_2^2 + p_3^2 = p^2, \tag{2.13}$$

where $p_j = \frac{\partial \tau}{\partial x_j}, j = 1,2,3$, and $p = \frac{1}{c}$. p is called slowness, while $\vec{p} = (p_1, p_2, p_3)$ is named the slowness vector. The characteristics of first-order nonlinear differential equations (Bleistein, 1984, p12-18) can be expressed as

$$\begin{aligned} \frac{dx_j}{d\sigma} &= \lambda p_j, & j = 1,2,3 \\ \frac{dp_j}{d\sigma} &= \lambda p \frac{dp}{dx_j}, & j = 1,2,3 \\ \frac{d\tau}{d\sigma} &= \lambda p^2 \end{aligned} \tag{2.14}$$

where λ is a parameter. If we specifically choose $\lambda = c^2$, then $\frac{d\tau}{d\sigma} = 1$. So this choice of λ corresponds to specifying the traveltime itself as the independent parameter σ along the ray. In this special case, (2.14) becomes

$$\begin{aligned} \frac{dx_j}{d\tau} &= c^2 p_j, & j = 1,2,3 \\ \frac{dp_j}{d\tau} &= c \frac{dp}{dx_j}, & j = 1,2,3. \end{aligned} \tag{2.15}$$

This is a ray tracing system which is a system of ordinary differential equations with traveltime τ itself as the independent variable. This system can be easily solved by standard integration algorithms. One good candidate for this solution, if proper initial conditions can be formulated, is provided by the fourth-order Runge-Kutta method. The most natural way of specifying the initial conditions is using the source position $\vec{r_o} = (x_1^0, x_2^0, x_3^0)$ and the ray directivity $\vec{p^0} = (p_1^0, p_2^0, p_3^0)$ corresponding to the take off angle at the source position where $\tau = 0$. The solution of this system

not only determines the raypaths emanating from the source, it also automatically locates the wavefronts during outward propagation if we simultaneously shoot a beam of rays from the source.

To demonstrate these principles, Figure 2.1 shows an example of ray tracing

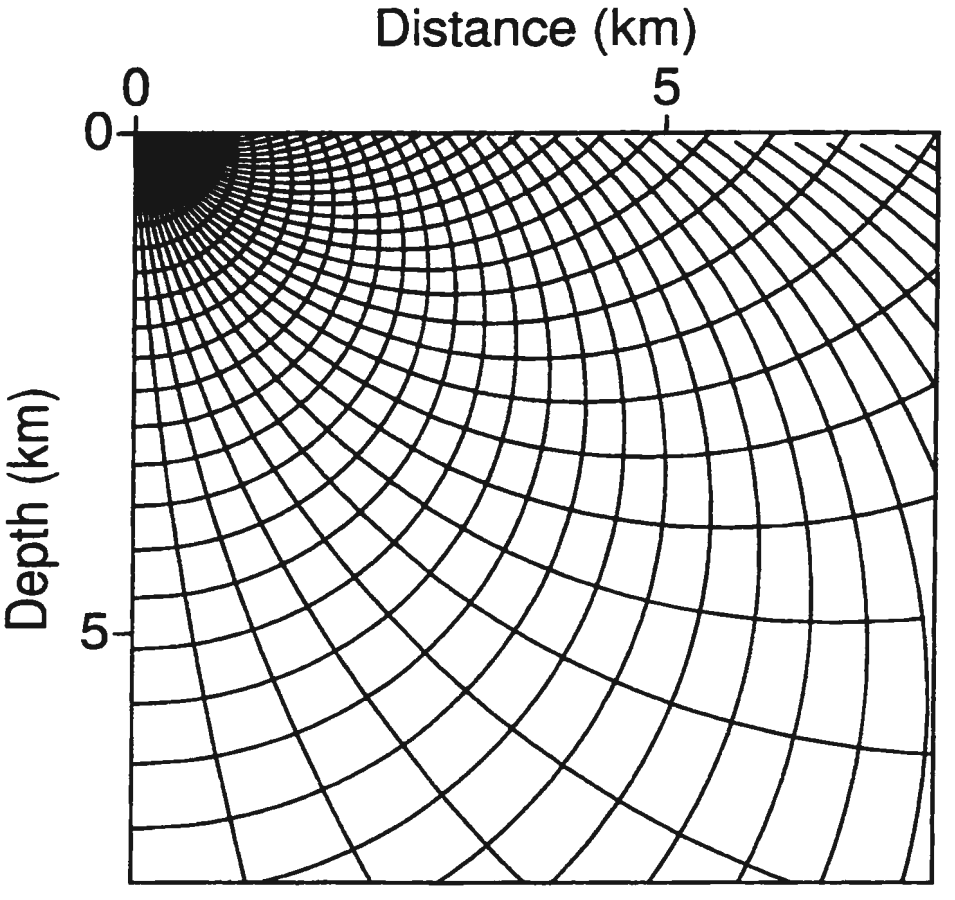

Figure 2.1: Traveltimes calculated from ray tracing systems. The velocity of the model is simply a linear function of depth, $v(z) = v_0 + az$ with $v_0 = 1500\ m/s$ and $a = 0.75\ s^{-1}$. The rays are traced from the surface source at (x_s, z_s) =(0.0, 0.0) m. The wavefronts are at intervals of 200 ms.

through a medium where the velocity changes vertically, $v(z) = v_0 + az$ with $v_0 = 1500\ m/s$ and $a = 0.75\ s^{-1}$. A total of 30 rays have been traced from the surface

source at $(x_s,\ z_s) = (0.0,\ 0.0)\ m$. The wavefronts simultaneously traced are at intervals of 200 ms.

It is seen that the ray tracing scheme works well in this simple situation. However, as we will see in the next section, the simple ray tracing solution of the eikonal equation breaks down in situations often encountered in the real Earth.

2.2. Finite difference calculation of the first arrival traveltimes by wavefront tracing

Although the ray tracing method in the last section works quite well for models with moderate velocity variations, it has significant drawbacks. These arise from the fact that waves propagate not only in normal continuous forms, but also in discontinuous ways. What the ray tracing systems describe corresponds to the normal portion. which is clearly explained by the validity condition (2.11) in the last section. Shadow zones occur where wavefield discontinuities exist. Vidale's (1988) finite difference solution of the eikonal equation alleviates the shadow zone problem. However it does not solve the problem totally. The use of the finite difference technique does not change the nature of the physics described by the eikonal equation, but only provides more efficient and possibly more accurate solutions, as the finite difference solution still assumes that a single wavefront is intrinsically propagating through the Earth.

Thus, to fully describe the traveltime field, the discontinuous portion of the wavefield should be properly taken into account. Theoretically there should be waves propagating in the shadow zone. These waves come from discontinuities which scatter secondary wavelets, or diffraction waves, according to the Huygens' principle. So, a combination of the finite difference solution and the excitation of Huygens' secondary sources would be a reasonable solution to find the traveltimes of first arrivals in every corner of the Earth.

2.2.1. General formulations and a numerical test

To formulate the method, the slowness field s(x, y) is first discretized into identical cells with size of h_x by h_z, the grid spacings horizontally and vertically respectively. The slowness s(x, y) here is fixed for each grid point, while the slowness $\vec{p}$ in the last section is a vector and is related to a ray. The slowness in each cell of the mesh is assumed to be constant, and its value is assigned to the upper left grid point as shown in Figure 2.2. Other choices of discretization could be substituted.

Now, suppose that in one cell, we already know the traveltime at three corners, say A, B, C as shown in Figure 2.3. If there is any geometrical ray traveling to D in a direction between arrows 1 and 2, then this ray can be described by the eikonal equation (2.12). Using a finite difference stencil centered at the mesh center, and averaging the first order difference at the opposite sides, we obtain the following second-order finite difference approximations

$$\frac{\partial t}{\partial x}\Big|_0 = \frac{1}{2h_x}\left[(t_D - t_C) + (t_B - t_A)\right], \tag{2.16}$$

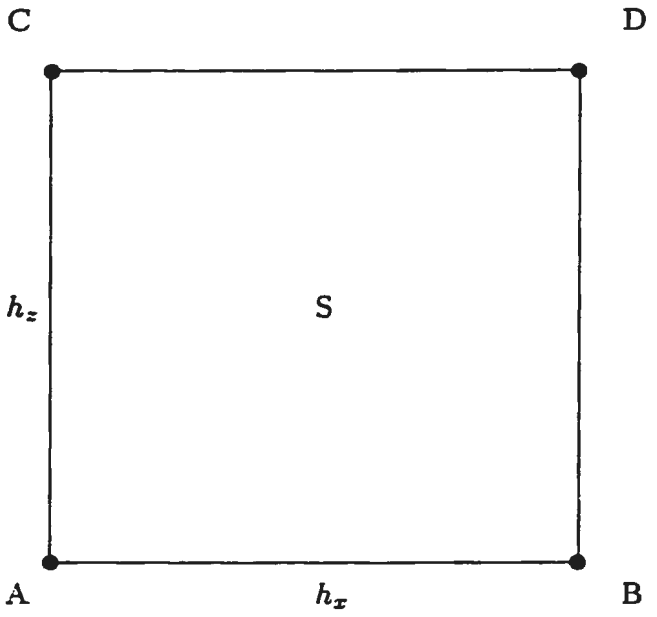

Figure 2.2: Discretization of the model. The model is uniformly discretized into cells with size of h_x by h_z. The slowness in each cell is constant. Its value is registered at the upper left corner C of the cell.

or,

$$\frac{\partial t}{\partial z}|_0 = \frac{1}{2h_z}\left[(t_D - t_B) + (t_C - t_A)\right]. \tag{2.17}$$

Substituting equations (2.16) and (2.17) into the eikonal equation (2.12), however, will generally produce a second order algebraic equation which involves five multiplications, one division and one square root operation. In contrast, in the extreme case of $h_x = h_z$ the computation reduces significantly to two multiplications and one square root operation,

$$t_D^0 = t_A + \sqrt{2h^2s^2 - (t_B - t_C)^2}. \tag{2.18}$$

Thus the finite difference solution of the eikonal equation simplifies to the evaluation of only an analytic expression (2.18).

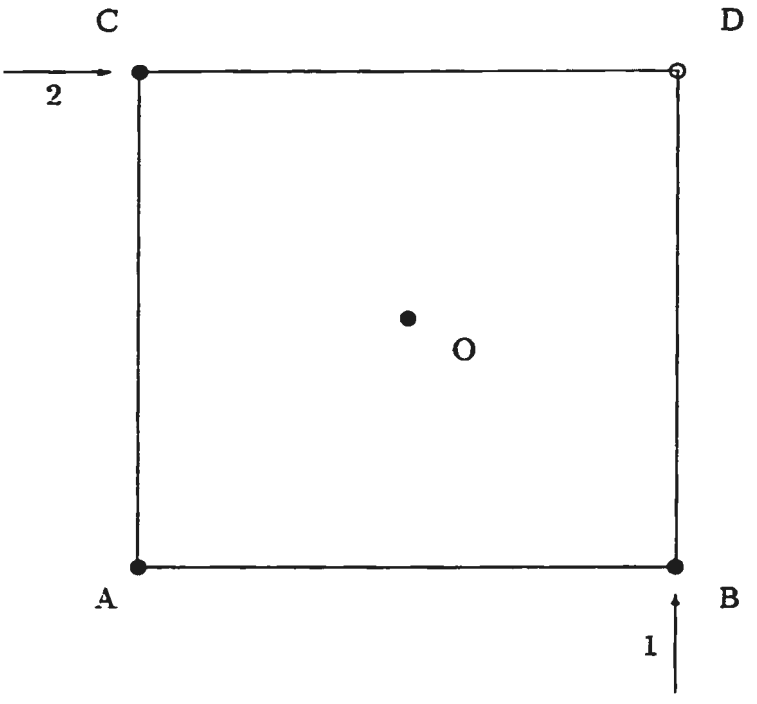

Figure 2.3: Finite difference stencil at cell center O. Traveltime at D is calculated from traveltimes at A, B, C, if there is a transmitted wave propagating in within the two directions 1 and 2.

To implement Huygens' principle, we only need to remember that the timed points A, B, C (Figure 2.3) where waves have already reached will scatter secondary wavelets which are not regular solutions of the eikonal equation. So, we will calculate the possible diffraction arrivals, as shown in Figure 2.4. Arrows denote direction of propagation. In the case of the discretized model, if the discretization is fine enough (Nickerson, 1994), then there are only five candidates in the cell. As the velocity in every cell is constant, we simply have

$$\begin{aligned} t_D^C &= t_C + h \cdot min(s,\ s'_C), \\ t_D^B &= t_B + h \cdot min(s,\ s_D), \end{aligned} \tag{2.19}$$

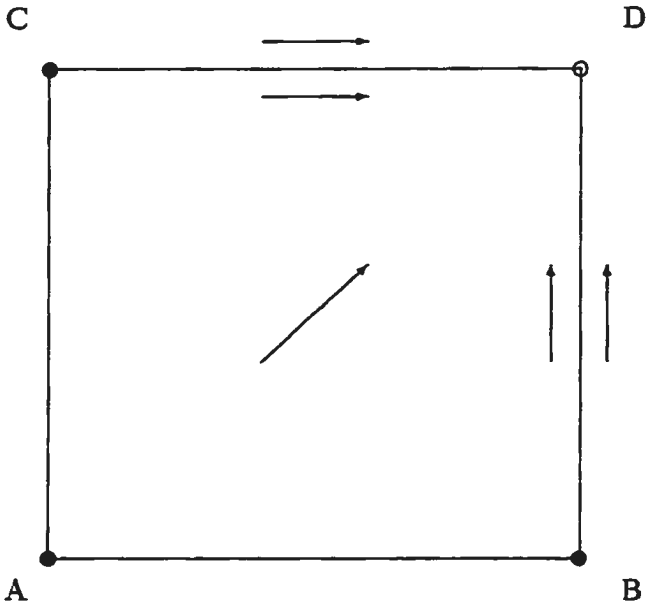

Figure 2.4: Arrivals due to Huygens' secondary wavelets. Five candidates for arrivals are examined at D due to the scattering of the secondary sources at A, B, and C. Arrows denote possible directions of travel for first arrivals.

$$t_D^A = t_A + \sqrt{2}hs,$$

where s_D is the slowness assigned to grid point D, while s'_C is the slowness in the cell just above the CD edge. The first arrival to D is just the least of the traveltimes of all the possible waves

$$t_D = min(t_D^0,\ t_D^A,\ t_D^B,\ t_D^C). \tag{2.20}$$

Thus, the total scheme for the single square is a combination of the finite difference solution of the eikonal equation, the scattering of the secondary sources and the application of Fermat's principle.

Based on this scheme, the traveltime calculation of first arrivals from a point source can be outlined as follows (see Figure 2.5):

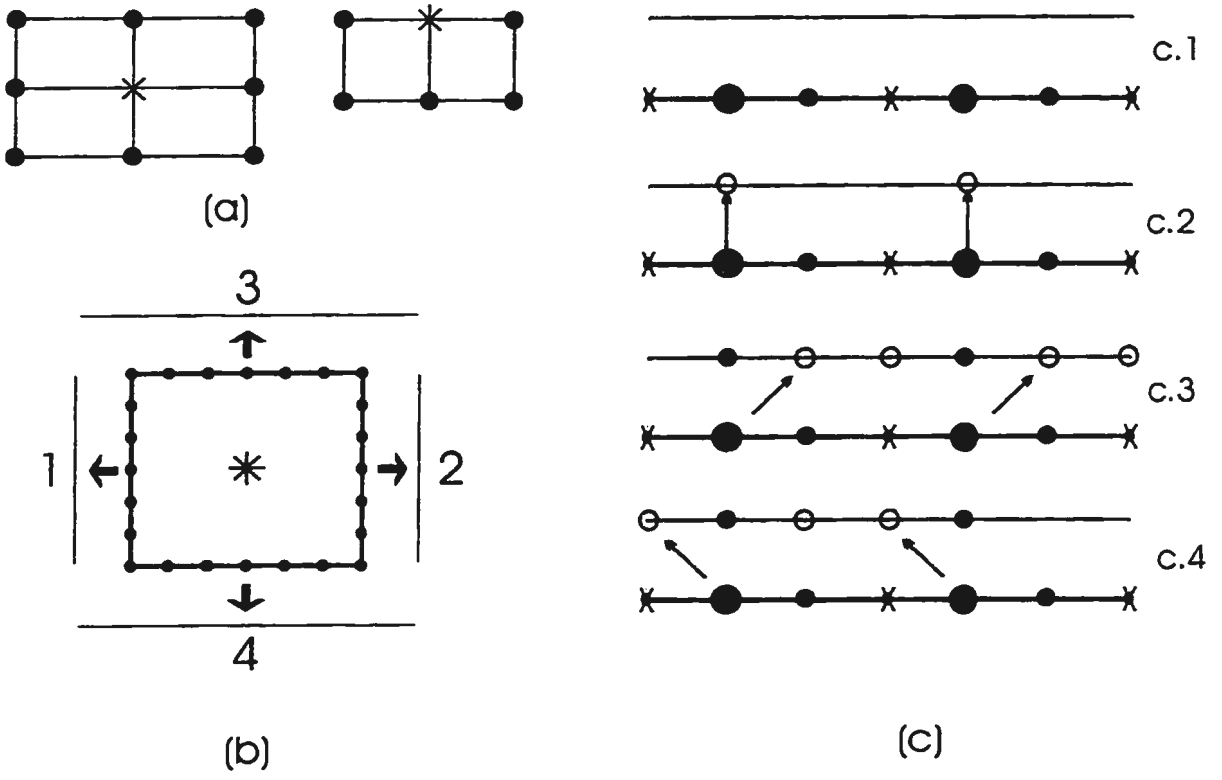

Figure 2.5: Illustration of extrapolation procedures. (a) illustrates that the initialization can be either over the squared ring around the source(left), or over a half-squared ring (right) if the source is on or close to a model boundary. In (b), the expanding quasi-wavefront has already reached the inner square with seven points on each side. The traveltimes at the solid dots and inside the inner square have been determined. The traveltimes on the outside ring are to be determined by sweeping the four sides sequentially as labeled. Four steps are used to extrapolate one inner side outward. (c) illustrates this extrapolation for a side. Here large solid dots denote local minimum points; a cross (X) denotes a local maximum point; small solid dots denote points where traveltimes have been computed; and a hollow circle (o) represents a point where traveltime is being computed at the current step.

A. Initialization of traveltimes at the source point and its close neighbors. These neighbors can be just a square ring around the source, or even several rings or quasi-rings (Figure 2.5a).

B. From the outermost ring of the initialization, traveltimes are extrapolated one ring outward by calculating traveltimes from side to side (Figure 2.5b).

C. For each edge of the ring, outward extrapolation is executed in the following manner. First the traveltime extremes are detected by computing the product of $t_{i+1} - t_i$ and $t_i - t_{i-1}$. If the product is not positive, then point i is an extremum. From the extrema, we can then find the position of local traveltime minima and maxima (Figure 2.5c.1). By Fermat's principle, the traveltime minima define first arrivals for a wavefront hitting a row of grid points. These points act as Huygens' secondary sources for arrivals as shown in Figure 2.5c. These local minimum points are thus first extrapolated one row outward to compute the traveltimes at the corresponding points of the outer row(Figure 2.5c.2). To compute the arrival times at other points in the outer row as shown in Figure 2.5c.3 and Figure 2.5c.4, we use the traveltime computation method described in Figure 2.3 and Figure 2.4. In order to compute the set of possible traveltimes, we have to sweep right (as in Figure 2.5c.3) and sweep left (as in Figure 2.5c.4) in the direction from a relative minimum to a relative maximum, and apply the computational formulae (2.18) and (2.19). We then compare the times computed from Figure 2.5c.3 and Figure 2.5c.4, and take the minimum time at each grid point, thereby defining arrival times in the outer row.

D. The last two procedures are repeated throughout the total model.

To illustrate the effectiveness and robustness of the proposed scheme, I design a model with a very high velocity contrast which is shown in Figure 2.6. This model is

certainly not geologically plausible. It nevertheless presents a good challenge to the traveltime calculation algorithms. Most of the current available methods, including Vidale's (1988) original method fail to handle a model with such high velocity contrasts (Nickerson, 1994). Figure 2.6 also shows the traveltime contours of the first arrivals. The source is positioned at the center of the upper surface. We can see that there are very few geometrical rays penetrating the first interface. Note the development of head waves in both sides of the top layer due to the first interface of high velocity contrast. The waves in the second, third, and fourth layers are almost all diffracted waves by the secondary sources excited at the upper interface of the corresponding layer. I name these diffractions the first, second and third order diffractions as they have been diffracted sequentially with corresponding times. However, in the bottom layer, due to its extremely low velocity, its upper boundary acts as an excellent lens which focuses the diffracted ray arrivals. The focused rays in the bottom layer are essentially straight rays, similar to formal geometrical rays, but with little energy.

This example clearly shows that all the possible waves are properly considered for the purpose of determining first arrivals. These first arrivals can be of either transmitted waves, head waves, or even diffracted waves.

2.2.2. Application to the Marmousi model

Now I will show applications of this wavefront tracing technique to a very complicated velocity model, the Marmousi model. The Marmousi model, as described by Versteeg (1993), has become a well known test model for seismic imaging algorithms throughout the industry. Figure 2.7 shows the computed traveltime contours from the

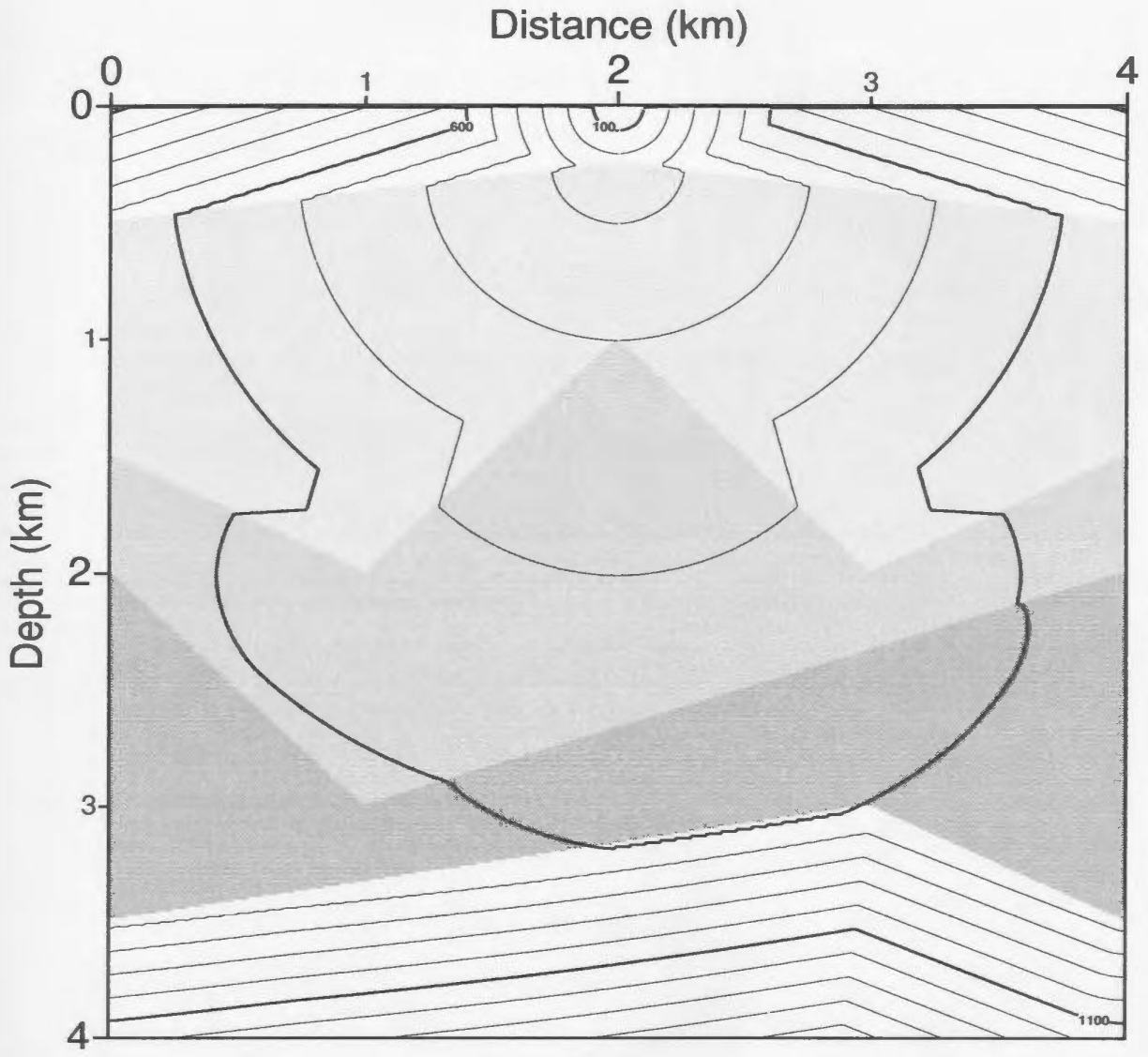

Figure 2.6: Traveltimes in a model of a very high velocity contrast. Velocities in the five shaded blocks are 1, 5, 10, 15, and 1 km/s respectively from top to bottom. The traveltime contours correspond to a source at the center of the upper surface. Traveltimes are of intervals of 100 ms.

Marmousi velocity model with the source positioned at (2000, 0.0) m. The velocity model is overlain with the traveltime field. This traveltime field is very complicated, possibly just as complicated as the model itself. Nevertheless, the waves in the right side of the model are mainly non-geometrical waves. For example, in the upper right part, waves are mostly head waves, while around the bottom right corner, waves are mainly diffracted in nature. Figure 2.8 shows the wavefronts from the point source at (6000, 0.0) m which lies in the central part of the model where complicated steep dip faulting and salt creep exist. The traveltime field is also very complicated. However, waves in one narrow curved band are easily identified as diffracted waves which can be approximately traced from (4500, 1000) m to the left edge with coordinate (0.0, 1800) m. Different types of waves develop during the propagation through the model. A characteristic in common with the previous example is the occurrence of turned rays, the result of head waves or diffractions, especially in one or both sides of the model.

This test confirms that the innovative approach to solving for the wavefronts and traveltimes for first arrivals is effective and stable even in very complicated settings. where most previous formulations have failed or are deficient in describing all of the components of the first arrivals: direct, transmitted, diffracted, or head waves.

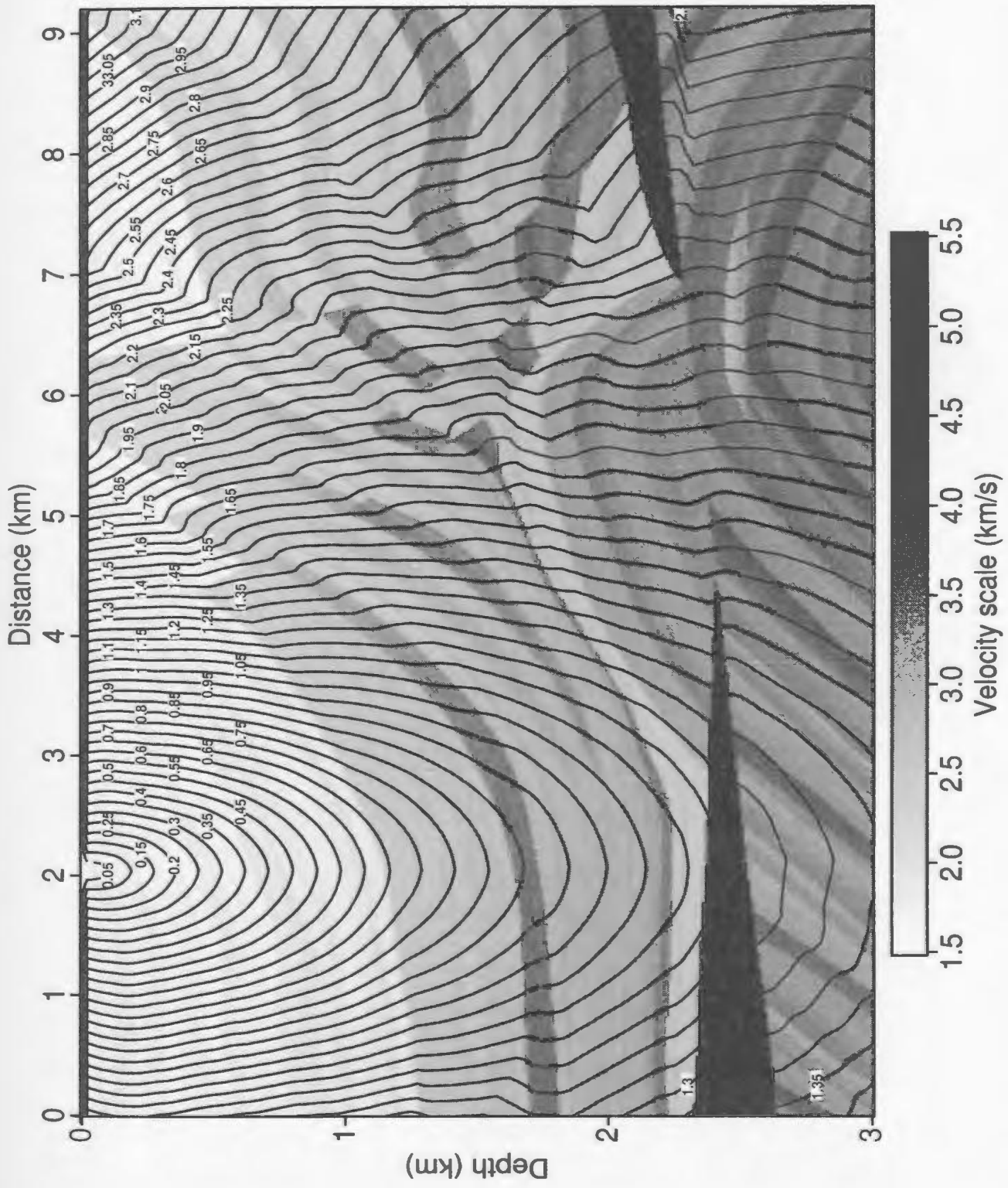

Figure 2.7: Traveltime contours in the Marmousi model with the source position at (2000, 0.0) m. The velocity model is overlaid with the traveltime contours in seconds.

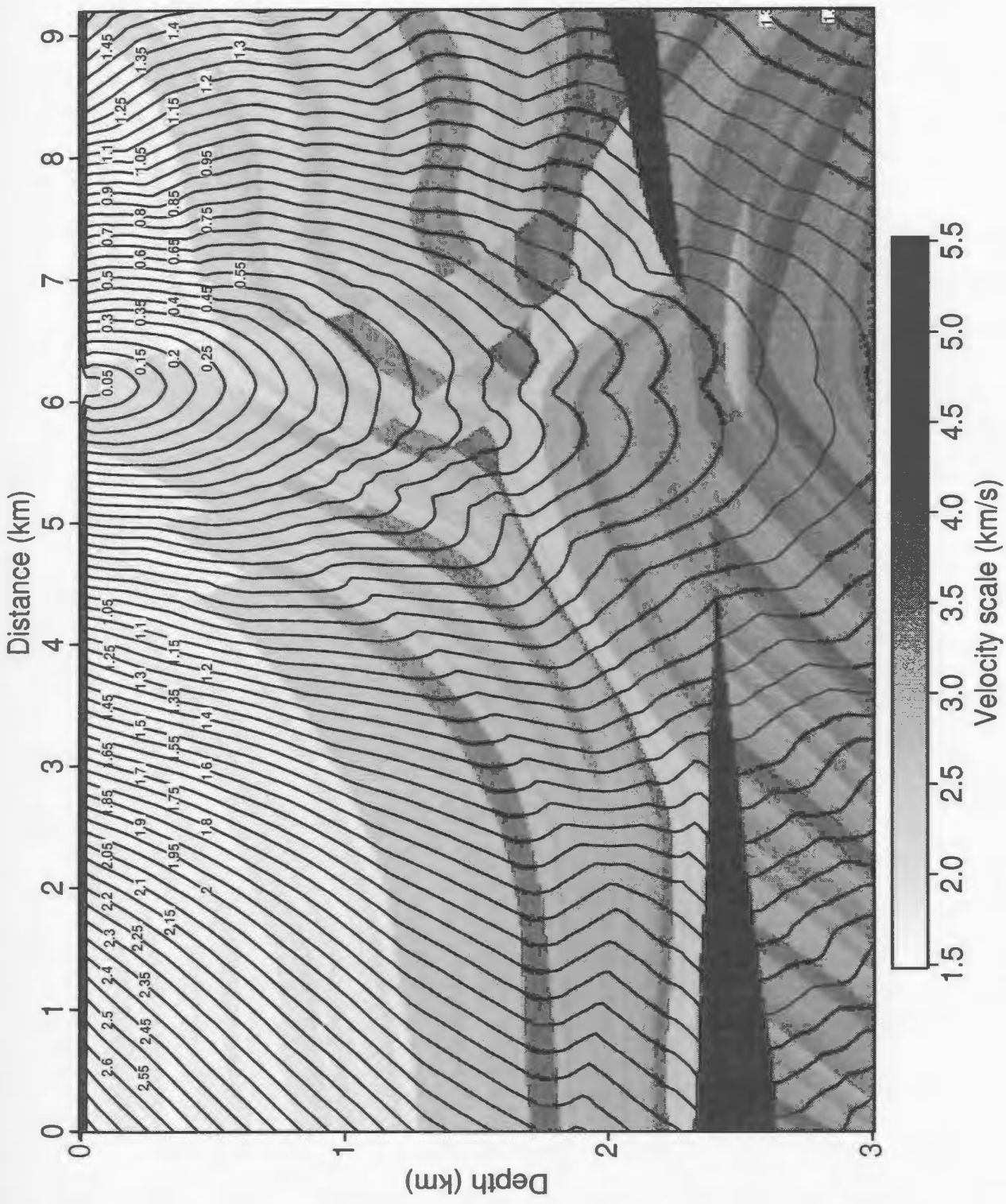

Figure 2.8: Traveltime contours in the Marmousi model with the source position at (6000, 0.0) m. The velocity model is overlaid with the traveltime contours in seconds.

2.3. Unification of the finite difference traveltime computations and plane wave traveltimes

In the last section, I proposed a finite difference scheme for traveltime computations from a point source. The procedure is similar to Vidale's (1988) original method with the inclusion of exciting Huygens' secondary wavelets. Huygens' principle is used by Qin et al. (1992) to improve the accuracy of traveltimes around the source point in their method of expanding the "actual" wavefronts instead of rings. There are still problems of stability due to the square root of negative values which occur in complicated models (Nickerson, 1994). In addition, there are other problems such as sacrifice of efficiency, difficulty of vectorization, and increased use of computer memory for tracking the"actual" wavefronts. Schneider et al. (1992) use a mapping procedure to calculate traveltimes. Their formulation of the problem is of a more mathematical nature. Their mapping scheme is basically equivalent to the application of Huygens' principle with the inclusion of Fermat's principle to select the first arrivals. To make the method robust, they have to sweep the model twice, in different directions. Thus the number of computations are about twice that of Vidale's. In addition, their calculations are still of first order accuracy. Nevertheless, this method should be a good candidate for application to problems with complicated velocity models where robustness is often of first concern. Podvin and Lecomte (1991) implement a parallel approach for traveltime calculations based on the explicit application of Huygens' principle. Their expanding strategy is along rings in 2D or cubes in 3D,

which is the same as Vidale's (1988, 1990). Their scheme is nevertheless of first order of accuracy. Compared to Vidale's method, their method has proven to be robust at the expense of less accuracy.

My proposed systematic application of finite difference solutions of the eikonal equation, excitation of Huygens' secondary sources, and the application of Fermat's principle is more general than the above cited algorithms. I see it as a unified algorithm for first arrival traveltimes that is in fact very general in the nature of its application. In the last section, it was shown that the algorithm can compute traveltimes from point sources.

The method can be extended to calculate the traveltimes of incident plane waves by considering a plane wave impinging along one edge of the model with its wavefront making an angle θ with the model edge (Figure 2.9). There are two possible methods for calculating the traveltimes in the model due to this incident plane wave.

The first method treats the first point excited by the plane wave in the model as a point source, and expands the quasi-wavefronts by quarter rings (upper panel of Figure 2.9). The extrapolation procedure is almost the same as that described in the last section, with the exception that the application of Fermat's principle at the upper surface, AB, should include one more term due to the direct arrival from the plane wave. This scheme takes proper account of head waves produced in the near field.

The second method is to use the direct arrival traveltimes at the upper surface as initialized traveltimes (lower panel of Figure 2.9). The initial datum acts as a computerized "wavefront". The wavefront at the upper surface will extrapolate the traveltime field into the model row by row using the procedures illustrated in Figure

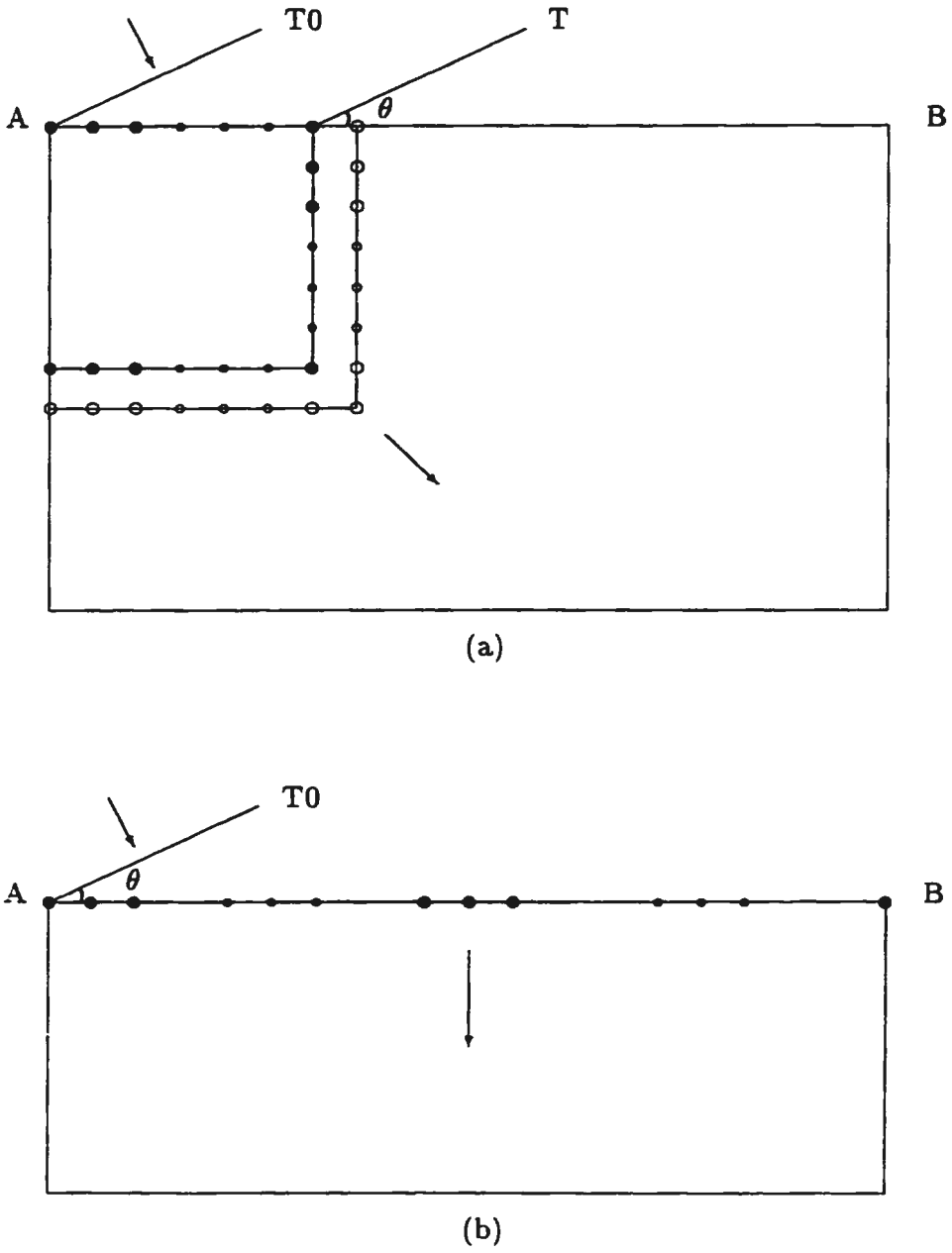

Figure 2.9: Two computational methods for calculating plane wave traveltimes. The plane wave is impinging on the upper surface. The wavefront forms an angle of θ with the upper surface AB. The first scheme (a) treats the first point excited by the plane wave in the model as a point source, and expands the quasi wavefront by quarter rings. The second method (b) uses the direct arrival times at the surface as initialized traveltimes. This computerized "wavefront" at the interface AB will be extrapolated into the model according to the procedures illustrated in Figure 2.5c.

2.5c. This treatment is generally simpler than the first scheme as it involves only one edge. In very complex velocity models, it would be preferable to follow the downward extrapolation procedure by a second sweep but with reverse direction to include first arrivals corresponding to turned rays (Schneider et al., 1992).

These two methods of computing plane wave traveltimes by finite difference schemes produce almost identical first arrival traveltimes in most geological models. The first scheme is both physically more sound and mathematically more complete. However, it often requires 50 % more computational effort.

Now I will show two examples of traveltime computations in the case of plane wave incidence. Figure 2.10 shows the propagating wavefronts in a model which is the same as that used in Figure 2.1, which is a vertically variant velocity model with constant velocity gradient. The incident wavefront is parallel to the upper surface of the model. In this case the wavefront keeps its original orientation as it moves from top to bottom, consistent with Snell's law. In contrast, Figure 2.11 plots the wavefronts in the same model with the incident wave plane impinging at an angle of 45^0 to the upper surface of the model. It shows that the traveltime contours, i.e., the wavefronts, experience drastic changes during the propagation through the model. In fact, near the upper right side of the model, the wavefronts indicate that the rays there are turned rays. In the deeper part of the model, the wavefronts do not correspond to geometrical waves. For the current velocity model, $v(z) = 1500.0 + 0.75z$, and initial incident ray angle, $\theta = 45^0$, the ray corresponding to the incident plane wave has its deepest penetration of $Z_D = 828.28m$ (Slotnick, 1974, p205-211). Thus, there will be no arrivals found if standard geometrical ray tracing is used.

In summary, this finite difference traveltime algorithm also provides an efficient

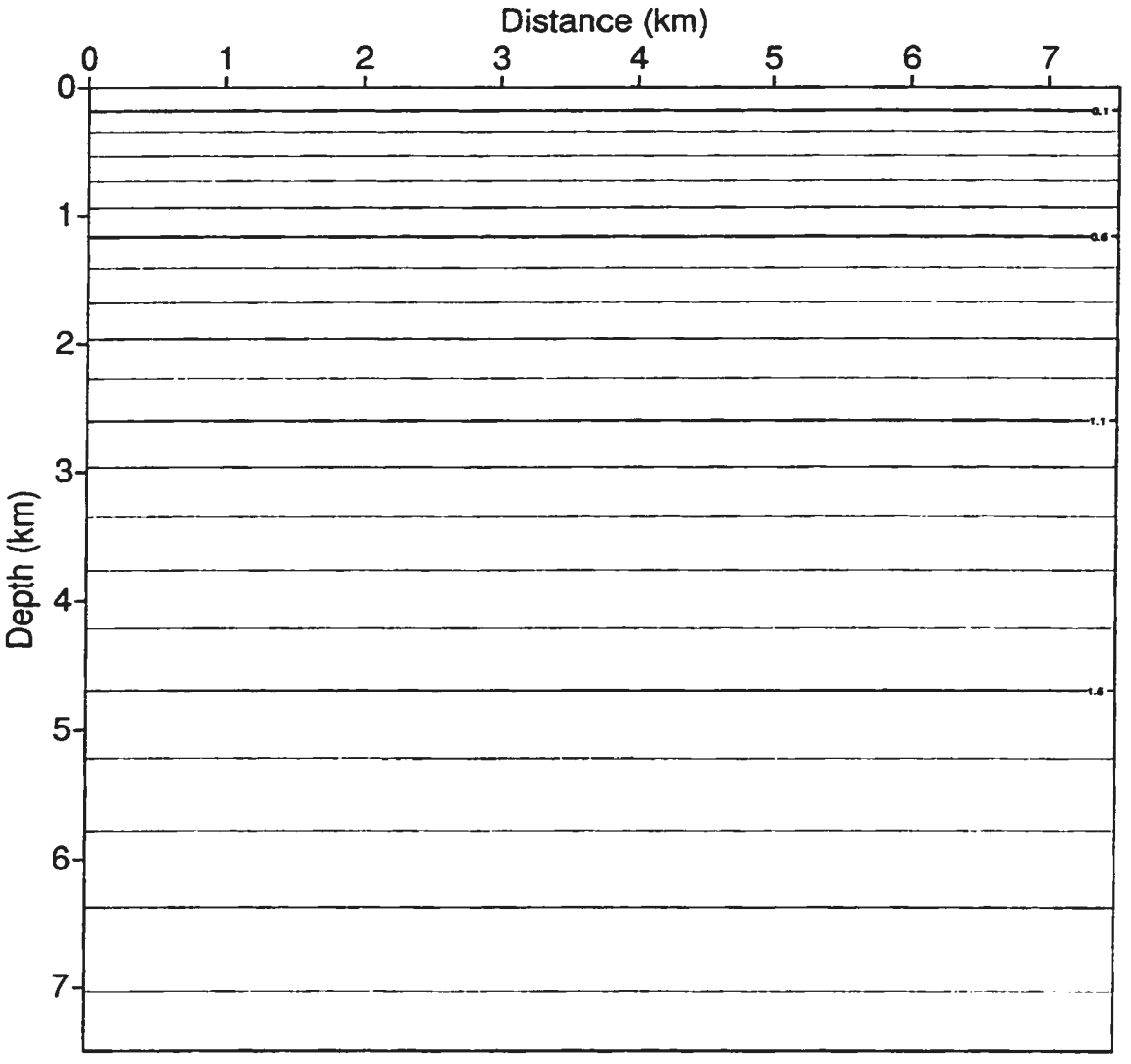

Figure 2.10: Propagation wavefronts in a v(z) velocity model with a vertically incident plane wave. The velocity function is $v(z) = 1500.0 + 0.75z$.

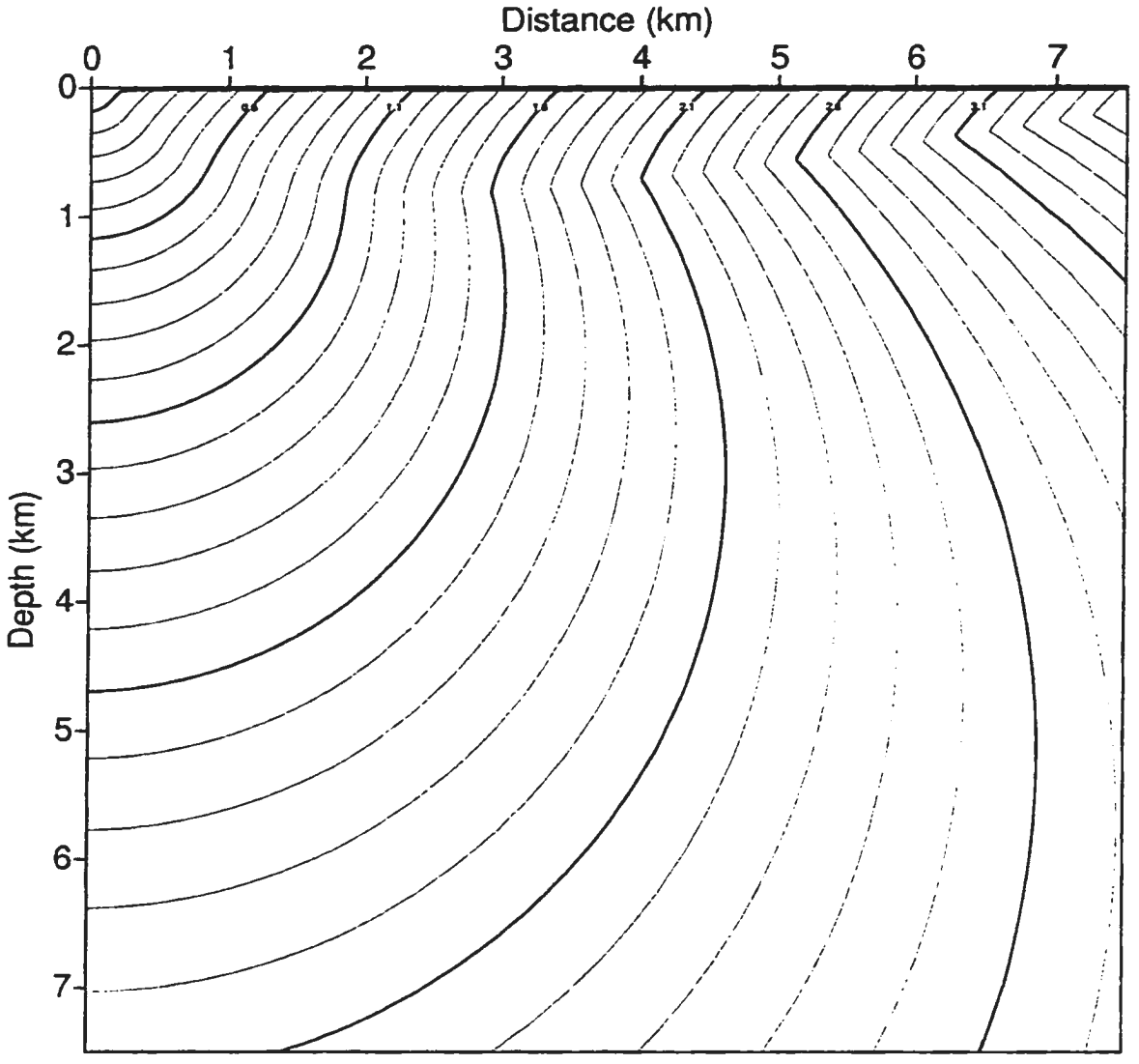

Figure 2.11: Propagation wavefronts in a v(z) velocity model with an obliquely incident plane wave. The velocity function is $v(z) = 1500.0 + 0.75z$. The plane wave impinges on the upper surface with an incident angle of 45^0.

and robust traveltime calculation method for plane waves. This method parallels the ray tracing scheme described by Whitmore (1995); however, my algorithm is much more efficient and complete. Its only drawback is the lack of availability of raypaths, a drawback common to all finite-difference traveltime computation methods. This problem is often obviated by using the steepest descent method to derive the raypaths (Vidale, 1988).

Chapter 3. Imaging of complex geological structures by prestack Kirchhoff depth migration

Historically, the conventional summation method along hyperbolae and superposition of circular wavefronts were the first numerical migration schemes which had their physical basis in the scalar diffraction theory of Huygens' and Fresnel (Schneider, 1971, 1978; French, 1975). The basic geometric migration theory was excellently dealt with by Hagedoorn (1954) in terms of wavefronts and diffraction charts. Schneider (1978) first mathematically formulated migration as a solution to the acoustic wave equation in the form of a Kirchhoff integral where the surface recordings were the known boundary values. Though Schneider (1978) derived the Kirchhoff integral for migration based on a homogeneous medium and planar recording geometry, the basic idea is directly applicable to any geometry, and even heterogeneous media if geometrical ray theory is a reasonable approximation. However, a difficulty arises in the efficient and accurate determination of the integral surface which is defined by the traveltimes.

In this chapter, I will first extend the classic summation and superposition schemes to the variable velocity case for any recording geometry, by replacing hyperbolic

diffractions and circular wavefronts with general hyperbolae and aplanatic surfaces. Then, I will derive several migration integrals which are applicable to any heterogeneous media for any recording geometry, by application of the WKBJ approximation of the Green's function to the Kirchhoff integral solution for the acoustic wave equation. These integrals are all accurate under the WKBJ theory, and are shown to be very similar to each other, and can thus be unified by a single integral formula. This general migration integral is simply a summation of differential traces along some integral surface with the amplitudes being modulated by certain geometrical functions. A differential trace is a trace derived from the recorded one by a differential operator of $\frac{d^m}{dt^m}$, where $m = \frac{1}{2}$ for 2D case while $m = 1$ for 3D case. The determination of the integral surface, nevertheless, constitutes the computational kernel of this general Kirchhoff migration.

3.1. Superposition of aplanatic surfaces versus summation along diffraction surfaces

Maximum convexity migration and superposition of amplitudes along "aplanatic surfaces" of equal travel times are the first digital migrations which were mathematically developed by Hagedoorn (1954). They are also the most comprehensible of all available migration methods. Though the methods were originally described in terms of circular wavefronts and hyperbolic diffraction curves, the basic principle of

the method still applies to any recording geometry in any geology. However, in the case of variable velocity media, the wavefronts and the diffraction hyperbolae have to be replaced by the general aplanatic and diffraction curves which are now of any shape.

Figure 3.1 illustrates the summation method along diffraction curves. Point D denotes a diffractor in the Earth. The media are considered to be variable both vertically and laterally. Any diffraction excited at the diffractor D by the direct wave from the source S, and received at R, does not necessarily follow a straight line. In fact, the travel path could be of any shape. I use dashed lines to represent any such complicated paths for simplicity. In the same figure, I have plotted the diffraction curve due to the excitation of the source at S. Thus, for the diffractor point, the vertical axis is depth; while for the diffraction curve, the vertical axis is defined in time. The diffraction curve is no longer hyperbolic, nor is its apex laterally coincident with the diffractor. The apex could be anywhere along the curve, determined by the velocity structure and the excitation and recording geometry of the diffraction. Figure 3.2 is one such computed diffraction curve in the Marmousi velocity model for a diffractor at $(x, z) = (4.0, 1.5)$ km corresponding to a surface source at x=6.0 km. This diffraction curve is significantly deviated from a hyperbola. The use of hyperbolic summation is definitely deemed to be in significant error. Nevertheless, the first step of the classical summation method, in which amplitudes are summed along the diffraction curve, is still applicable in this general case. However, the second step, putting the summed amplitude at the lateral position of the diffraction apex D' is no longer valid. Instead, the sum should directly be placed onto the diffractor D itself.

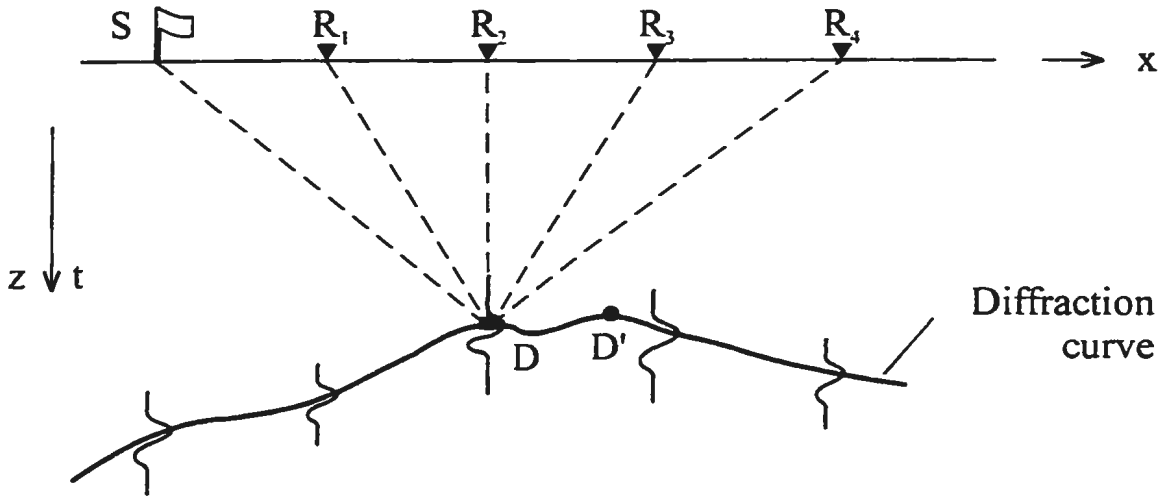

Figure 3.1: Migration by summation along diffraction curves. The diffraction curve is either determined by ray tracing or finite difference solutions of the eikonal equation. The sum of the input amplitudes along the diffraction curve is put at the position of the diffractor D instead of the apex of the diffraction curve, D'.

The above procedure for a single diffractor is essentially the reverse procedure of diffraction which can be clearly explained by Huygens' principle. Thus, if D is a real diffractor, a large sum will be produced at the position of D in the migrated section. This diffraction point certainly works for any continuous reflector, as such a reflector can be considered of a continuum of diffractors. The images of all these individual diffractors will finally merge to be a smooth, continuous reflector (Schneider, 1971).

Thus the classical summation method is easily extended to variable velocity media. Its kernel computation is the determination of the diffraction curve. This could be carried out by either ray tracing or any solution of the eikonal equation. I will return to comment on this point later when I make a simple comparison between this summation scheme and the the superposition method of aplanatic curves.

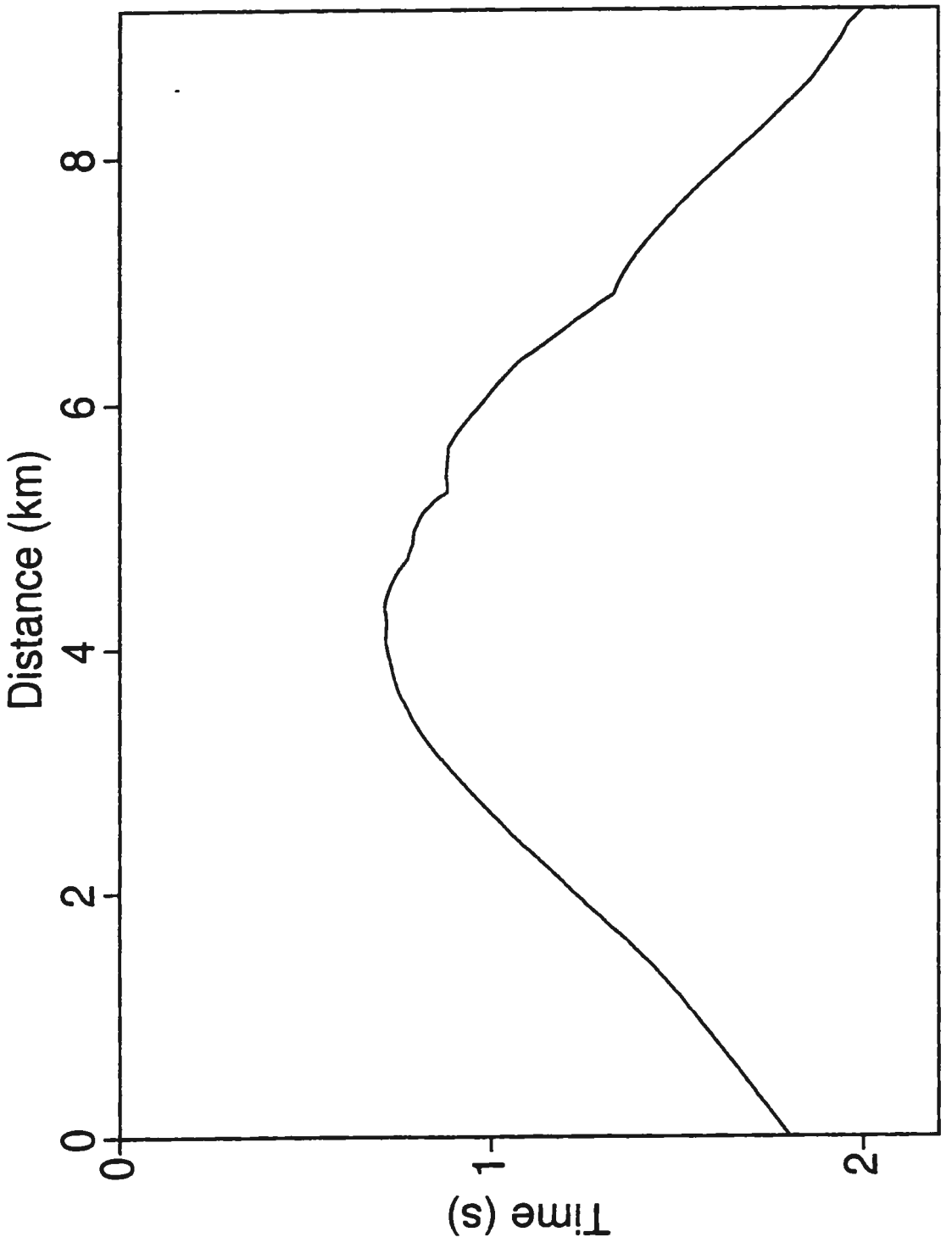

Figure 3.2: A diffraction curve in the Marmousi model. It corresponds to a diffractor at $(x, z) = (4.0, 1.5)$ km with a surface source at x=6.0 km.

Similarly I can extend the classical wavefront migration to any recording geometry in variable velocity media. Figure 3.3 illustrates the migration of two samples in a single trace along two aplanatic curves. For each trace at R, due to a source at S, its amplitude at time T could come from any possible diffractor D along the aplanatic curve, which is the locus of equal traveltimes from S to D, then from D to R. In the case of constant velocity, these aplanatic curves are simply ellipses with the foci at the source point S and receiver position R. In general cases, these aplanatic curves have to be explicitly determined by setting up two traveltime tables, using either ray tracing or eikonal equation solutions twice, once for the source, the other for the receiver. The collection of points with the same sum of the two traveltime tables essentially defines the aplanatic curve for that specific time. Migration can thus be effectively performed by scattering the amplitude at time T onto the corresponding aplanatic curve. In Figure 3.3, I have illustrated the migration procedure for two samples of the trace at R. Though a single aplanatic curve is not a useful image itself, the linear superposition of all such aplanatic curves will produce a useful subsurface image. At positions where a reflector or diffractor exists, these aplanatic curves will intersect. Thus the amplitudes will constructively interfere, producing a high superposition amplitude. On the other hand, at places without reflecting or diffracting bodies, the amplitudes on different curves will destructively interfere, resulting in a null or small amplitude (Schneider, 1971).

In the above, I have shown that the determination of the diffraction curves, or the aplanatic curves, is the essential part of migration methods in variable media. I use the method I have developed in Chapter 2 for determining these diffractions. However there are some differences in the determination of these curves. For a model of N_x by

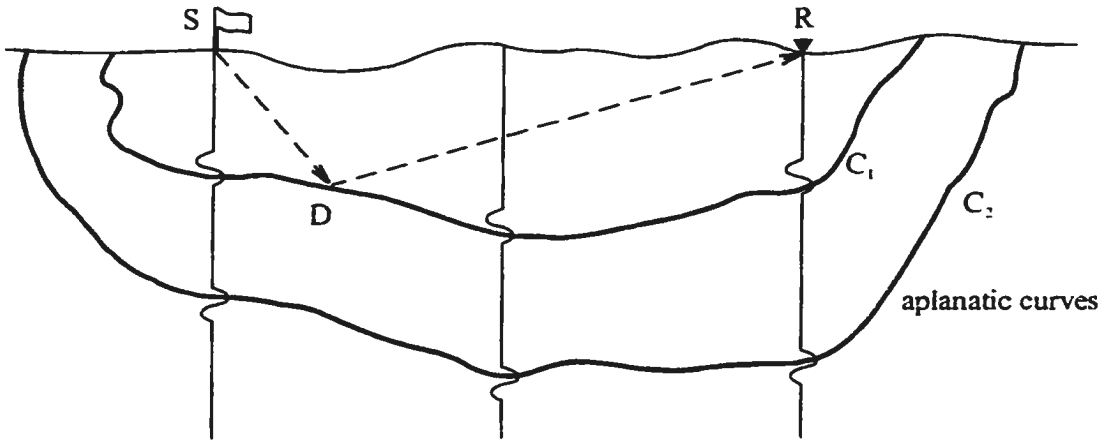

Figure 3.3: Migration by superposition of aplanatic curves. C_1 and C_2 are two aplanatic curves corresponding to two samples of a trace at R due to a source at S. The dashed path S-D-R symbolically represents a general raypath of any shape. Each amplitude at every trace is thrown onto its corresponding aplanatic curve. The linear superposition principle indicates that the superposition result is essentially the final migration image of the subsurface.

N_z, the determination of the aplanatic curves needs solutions of the eikonal equation only about N_x times. However, for the summation method, theoretically it requires $N_x \cdot N_z$ times of similar solutions. An alternative is available to reduce the solution times to N_x also. But much more effort is needed to rearrange the time table according to each individual grid point. The most significant difference is that summation along diffraction curves operates on many input traces simultaneously, while superposition of aplanatic curves operates trace by trace, which makes the latter ideal for parallel processing. In most cases, single trace processing is preferred to the multichannel processing in implementation. I have thus employed the superposition method of aplanatic curves for most of the applications included in this thesis. As illustrated

by Robinson and Treitel (1980, p385), both methods are equivalent in principle. The choice of the superposition scheme is for ease of implementation and illustration.

Figure 3.4 shows a suite of aplanatic charts corresponding to a surface source position at $x = 2000$ m, and a surface receiver position at $x = 6000$ m in the Marmousi velocity model. In this plot, none of the aplanatic curves is similar to either an ellipse or a circular arc. Their shapes are totally determined by the recording geometry and traveltimes. The latter in turn are determined by the velocity distribution. Figure 3.5 shows the final migrated section of the Marmousi model data by simple superposition of aplanatic surfaces. The Marmousi model is based on a geological model from the Cuanza Basin of Angola. The model seismic data set contains 240 shot records, each with 96 traces. It is computed using a finite difference solution to the acoustic wave equation. Even in this simple migration, the main features of the the structures such as the steep faults are reasonably well imaged. There are even some indications of the positions of the reservoir in the subsalt anticline at a depth of about 2.6 km and lateral extent of $6.0 \sim 7.5$ km. In this model data migration, the biggest difference from the accurate reverse-time migration result which I will describe in Chapter 4 probably lies in the change of phase signature. This phase variation is well known to be related to neglecting the differential operation's effect on the input data before migration, which I will elucidate in section 3.3.

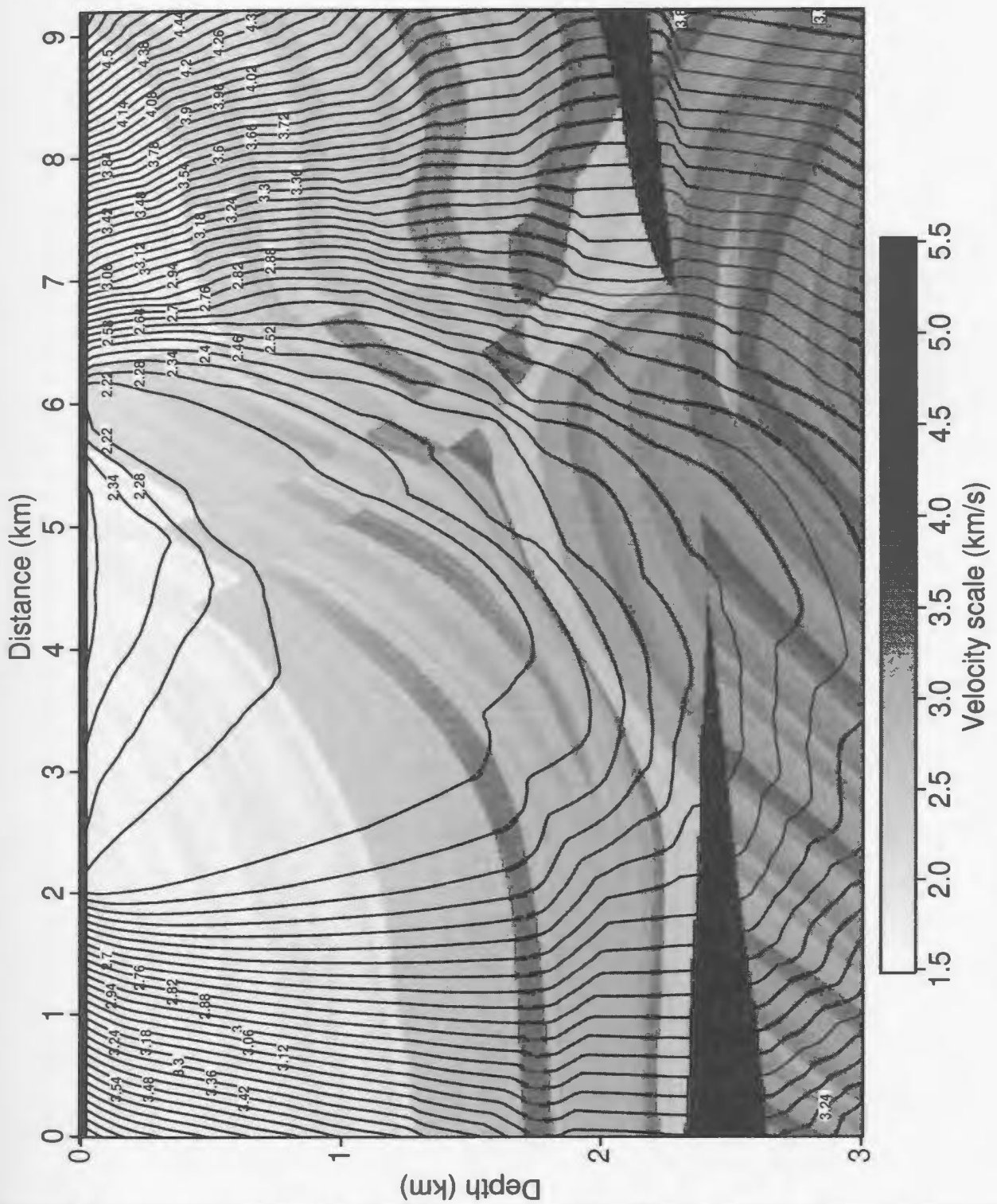

Figure 3.4: Aplanatic curves in the Marmousi model. The aplanatic charts correspond to a surface source position at $x = 2000\ m$, and a surface receiver position at $x = 6000\ m$.

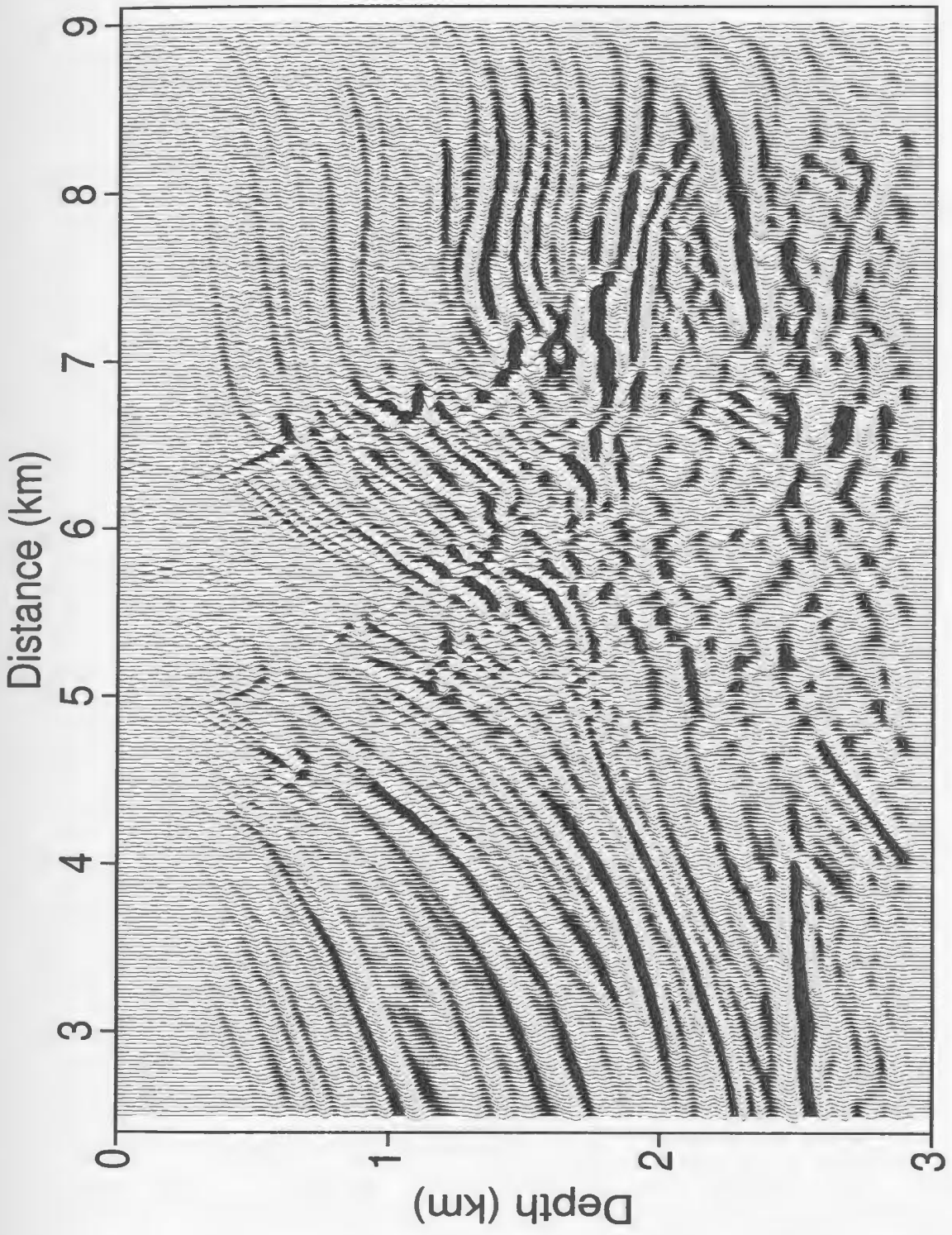

Figure 3.5: Migration section of the Marmousi data by prestack superposition of aplanatic curves.

3.2. A unified integral migration formulation in heterogeneous media

Migration consists of two connected parts: wavefield extrapolation and the application of an imaging principle. The natural way of deriving a migration formula is thus to first obtain the wavefield extrapolator, the equation necessary to express the wavefield in the interior of the Earth from the surface recordings.

Suppose we have an array of recordings on the Earth's surface S_0 in a single physical experiment as shown in Figure 3.6. The natural choice for this experiment is a shot gather. The recordings of this experiment are the result of wave propagation down from the source and then scattered up to the surface by discontinuities of the Earth. This physical phenomenon of wave propagation is mathematically formulated by the acoustic wave equation

$$\nabla^2 u(\vec{x},t;\vec{x_s}) - \frac{1}{c^2(\vec{x})}\frac{\partial^2 u(\vec{x},t;\vec{x_s})}{\partial t^2} = -\delta(\vec{x}-\vec{x_s})\delta(t), \tag{3.1}$$

where $\vec{x_s}$ denotes the position of the source. $u(\vec{x},t;\vec{x_s})$ is the wavefield at time t at position $\vec{x}$ due to a point source at $\vec{x_s}$. As I explained in Chapter 2, this acoustic wave equation is only an approximation for the real wave propagation problem. However, as pointed out by Kelly et al. (1982), such an acoustic approximation matches very well with real synthetic seismograms in many applications while at the same time avoiding the complexity of the full elastodynamic wave equations.

Temporally Fourier transforming this equation leads to the Helmholtz equation

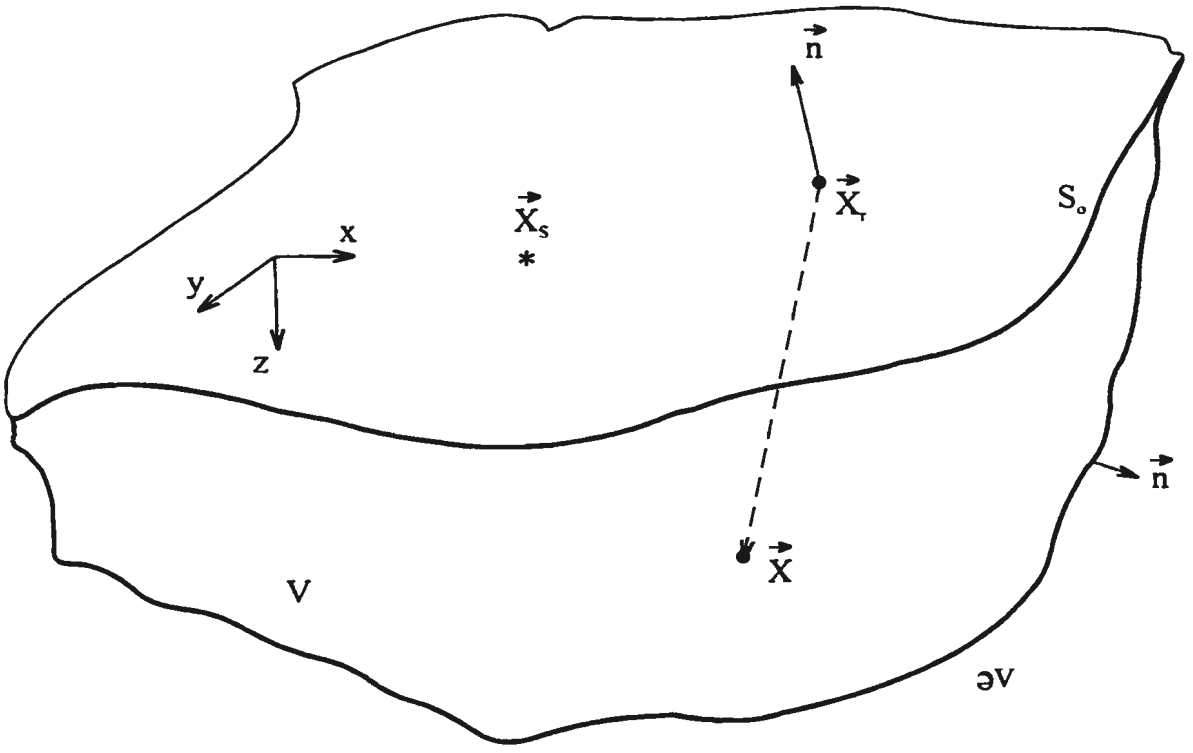

Figure 3.6: Integral geometry for the Kirchhoff equation (3.5).

(Bleistein, 1984, p92),

$$\nabla^2 u(\vec{x},\omega;\vec{x_s}) + k^2(\vec{x})u(\vec{x},\omega;\vec{x_s}) = -\delta(\vec{x}-\vec{x_s}), \tag{3.2}$$

where ω is the temporal frequency and $k = \frac{\omega}{c(\vec{x})}$ is the wavenumber. In the interior of the Earth, $\vec{x} \in (V - \partial V)$, equation (3.2) reduces to

$$\nabla^2 u(\vec{x},\omega;\vec{x_s}) + k^2(\vec{x})u(\vec{x},\omega;\vec{x_s}) = 0, \tag{3.3}$$

where ∂V is the boundary of volume V.

The Green's function, $G(\vec{r},\omega;\vec{x})$, representing the wavefield at $\vec{r}$ due to a point impulse at $\vec{x}$, satisfies the wave equation

$$\nabla^2 G(\vec{r},\omega;\vec{x}) + k^2(\vec{r})G(\vec{r},\omega;\vec{x}) = -\delta(\vec{r}-\vec{x}). \tag{3.4}$$

Now applying Green's second theorem (Goodman, 1968, p34) to the scattered wavefield $u(\vec{x},\omega;\vec{x_s})$ and the Green's function $G(\vec{x_r},\omega;\vec{x})$ in the volume V with a tiny volume around $\vec{x}$ being excluded to avoid singularities, we have (Goodman, 1968, p37),

$$u(\vec{x},\omega;\vec{x_s}) = \oint_{\partial V}\left\{u(\vec{x_r},\omega;\vec{x_s})\frac{\partial G(\vec{x_r},\omega;\vec{x})}{\partial n} - G(\vec{x_r},\omega;\vec{x})\frac{\partial u(\vec{x_r},\omega;\vec{x_s})}{\partial n}\right\}ds. \qquad (3.5)$$

This is an exact expression regardless of the complexity of the Earth model. This integral equation relates the scattered wavefield in the Earth's interior to its values on the surface. Nevertheless, this relation involves both the wavefield itself, and its normal derivative component which is not usually recorded in seismic exploration.

In exploration seismology, we generally record the wavefield on the Earth's surface: our recordings never cover the whole Earth surface. However, as long as the wavefield u satisfies the Sommerfeld radiation condition (Bleistein, 1984, p182)

$$\begin{aligned} Ru(\vec{x},\omega;\vec{x_s}) &\longrightarrow 0, \qquad as \qquad R\to\infty; \\ R\left(\frac{\partial u(\vec{x},\omega;\vec{x_s})}{\partial n} - jk(\vec{x})u(\vec{x},\omega;\vec{x_s})\right) &\longrightarrow 0, \qquad as \qquad R\to\infty. \end{aligned}$$

where R is the distance between $\vec{x}$ and $\vec{x_s}$, the integral (3.5) is still a very good approximation to the wavefield in the Earth, with the surface of integration consisting of the recording surface S only.

To simplify the integral, I suppose that there is a totally identical half space above the Earth's surface which forms a symmetrical image of the actual subsurface. Furthermore, I consider a Green's function which is the result of two monopoles with opposite sign situated symmetrically on either side of the Earth's surface (Figure 3.7). As long as the recording surface is planar, the Green's function will be zero any-

where at the surface, as each monopole will contribute exactly the same propagation wavefields but opposite signs, i.e.,

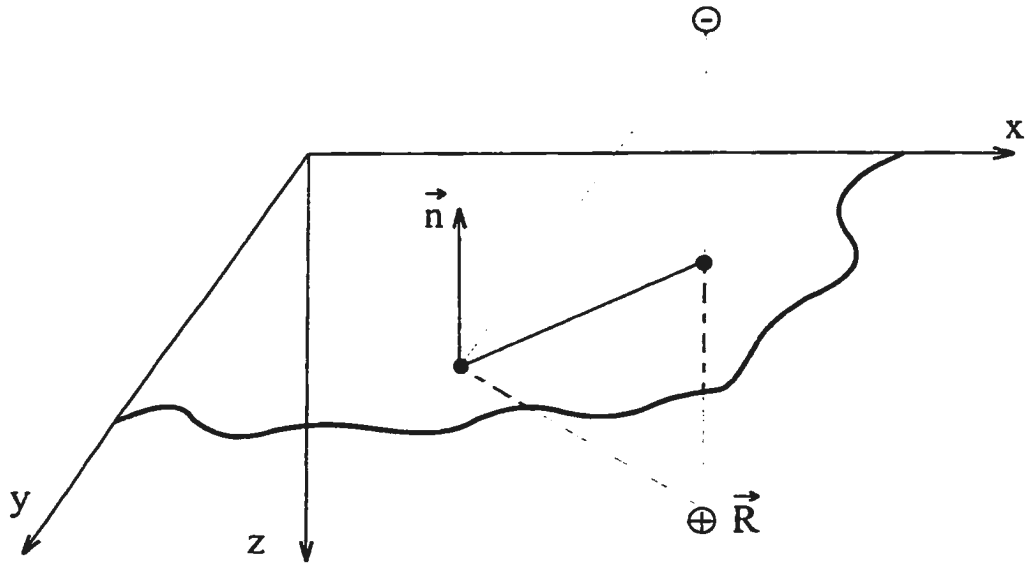

Figure 3.7: Green's function for the Rayleigh integral. It is the responses of two monopoles of opposite sign symmetrically at opposite sides of the Earth's surface.

$$G(\vec{x_r},\omega;\vec{x}) = G^+(\vec{x_r},\omega;\vec{x}) + G^-(\vec{x_r},\omega;\vec{x}) = 0, \tag{3.6}$$

where $G^+(\vec{x_r},\omega;\vec{x})$ obeys equation (3.4) in the lower half space. To write the normal derivative of the Green's function. we can extrapolate easily from the homogeneous case,

$$\frac{\partial G(\vec{x_r},\omega;\vec{x})}{\partial n} = 2\frac{\partial G^+(\vec{x_r},\omega;\vec{x})}{\partial n}. \tag{3.7}$$

Using this definition of the Green's function and following the same lines as in the derivation of (3.5), I obtain the general Rayleigh integral (Berkhout, 1985, p145)

$$u(\vec{x},\omega;\vec{x_s}) = 2\int_S \frac{\partial G^+(\vec{x_r},\omega;\vec{x})}{\partial n} u(\vec{x_r},\omega;\vec{x_s})d\vec{x_r}. \tag{3.8}$$

This integral applies to most complex media as well. Its validity is only challenged when the recording surface is extremely rough which includes topographies with both

very large elevation variations and large spatial wavenumber components. Figure 3.8 schematically illustrates that the Rayleigh integral (3.8) is in significant error when the recording surface is rough. In these cases, the general Kirchhoff integral (3.5) should be used.

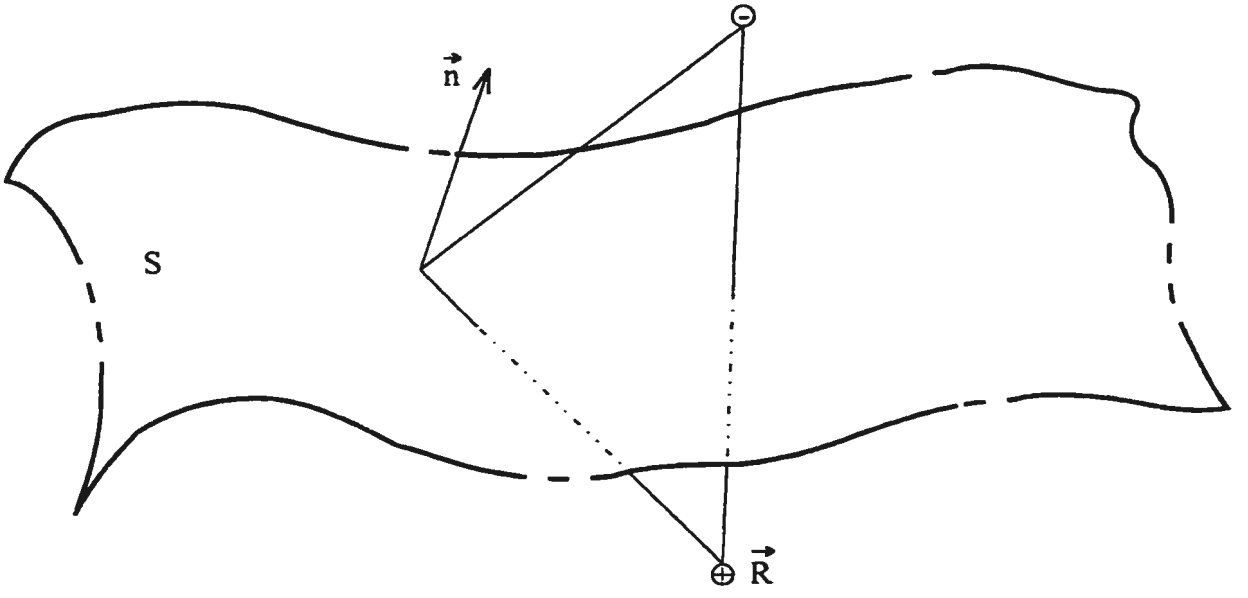

Figure 3.8: The error of the Rayleigh integral in areas of non-planar topography. In rough topographic areas, the Green's function due to two contrasting monopoles is no longer zero at the surface. The full Kirchhoff integral should be used.

Equation (3.8) generally formulates the scattered wavefield in the heterogeneous Earth based on recordings on the surface of the Earth in cases for which surface roughness is negligible. Now I will expand this formulation using the WKBJ theory (Aki and Richards, 1980, p415-419). The WKBJ approximation of the Green's function $G^+(\vec{x_r}, \omega; \vec{x})$ can be expressed as

$$G^+(\vec{x_r}, \omega; \vec{x}) = A_G(\vec{x_r}; \vec{x}) e^{-i\omega\tau_G(\vec{x_r};\vec{x})}, \tag{3.9}$$

where A_G is the amplitude and τ_G is the traveltime related to phase. The normal derivative term of the Green's function is

$$\frac{\partial G^+(\vec{x}_r,\omega;\vec{x})}{\partial n} = \vec{n}\cdot\left\{\nabla A_G(\vec{x}_r;\vec{x}) - i\omega A_G(\vec{x}_r;\vec{x})\nabla\tau_G(\vec{x}_r;\vec{x})\right\}e^{-i\omega\tau_G(\vec{x}_r;\vec{x})}. \qquad (3.10)$$

Under the high frequency approximation, the first term of the normal derivative is of lower order in frequency, thus the above equation can be approximated by its leading term in ω

$$\frac{\partial G^+(\vec{x}_r,\omega;\vec{x})}{\partial n} = -i\omega\vec{n}\cdot\nabla\tau_G(\vec{x}_r;\vec{x})A_G(\vec{x}_r;\vec{x})e^{-i\omega\tau_G(\vec{x}_r;\vec{x})}. \qquad (3.11)$$

In fact, this is a good approximation of the normal derivative of the Green's function even with low frequency content, as the following condition

$$\|\nabla A_G(\vec{x}_r;\vec{x})\| \ll \|A_G(\vec{x}_r;\vec{x})\| \qquad (3.12)$$

holds for most exploration problems. This condition is simply the assumption that the amplitude changes slowly spatially.

Substituting (3.11) into (3.8) leads to

$$u(\vec{x},\omega;\vec{x}_s) = -2i\omega\int_S \vec{n}\cdot\nabla\tau_G(\vec{x}_r;\vec{x})A_G(\vec{x}_r;\vec{x})u(\vec{x}_r,\omega;\vec{x}_s)e^{-i\omega\tau_G(\vec{x}_r;\vec{x})}d\vec{x}_r. \qquad (3.13)$$

The corresponding time domain expression is

$$u(\vec{x},t;\vec{x}_s) = 2\int_S \vec{n}\cdot\nabla\tau_G(\vec{x}_r;\vec{x})A_G(\vec{x}_r;\vec{x})u'(\vec{x}_r,t+\tau_G(\vec{x}_r;\vec{x});\vec{x}_s)d\vec{x}_r. \qquad (3.14)$$

where u' is the time derivative of u.

For migration purposes, we need to extrapolate the source wavefield too. The source wavefield $D(\vec{x},t;\vec{x}_s)$ is reconstructed with the assumption that it consists of any direct arrivals from the source at $\vec{x}_s$ without any secondary scattered energy.

Under this assumption, $D(\vec{x}, t; \vec{x}_s)$ is simply a Green's function $G^+(\vec{x}, t; \vec{x}_s)$

$$D(\vec{x}, t; \vec{x}_s) = G^+(\vec{x}, t; \vec{x}_s). \tag{3.15}$$

Using the WKBJ approximation, the source wavefield takes the form of equation (3.9) but with a phase advance instead of delay

$$D(\vec{x}, \omega; \vec{x}_s) = A_G(\vec{x}; \vec{x}_s) e^{i\omega\tau_G(\vec{x}; \vec{x}_s)}. \tag{3.16}$$

Now, we are ready to evaluate the acoustic impedance discontinuities. The first measure of these discontinuities is the illuminated reflectivity at $\vec{x}$ which is defined to be the ratio of the scattered to the source wavefields at that position

$$R(\vec{x}, \omega; \vec{x}_s) = \frac{u(\vec{x}, \omega; \vec{x}_s)}{D(\vec{x}, \omega; \vec{x}_s) + \epsilon}. \tag{3.17}$$

This formulation also has a time domain definition first proposed by Claerbout (1971). The inclusion of the small constant ϵ is to improve stability by avoiding division by zero. This formulation properly describes the angular reflectivity function of the subsurface. Using (3.13) and (3.16), we obtain

$$R(\vec{x}, \omega; \vec{x}_s) = -2i\omega \int_S \vec{n} \cdot \nabla \tau_G(\vec{x}_r; \vec{x}) \frac{A_G(\vec{x}_r; \vec{x})}{A_G(\vec{x}; \vec{x}_s) + \epsilon} u(\vec{x}_r, \omega; \vec{x}_s) \epsilon^{-i\omega\left(\tau_G(\vec{x}_r; \vec{x}) + \tau_G(\vec{x}; \vec{x}_s)\right)} d\vec{x}_r. \tag{3.18}$$

By recognizing that the traveltimes $\tau_G(\vec{x}_r; \vec{x})$ and $\tau_G(\vec{x}; \vec{x}_s)$ correspond to the traveltimes from the interior point $\vec{x}$ to the receiver position $\vec{x}_r$, and from the source position $\vec{x}_s$ to $\vec{x}$ respectively.

$$\begin{aligned} \tau_s(\vec{x}; \vec{x}_s) &= \tau_G(\vec{x}; \vec{x}_s); \\ \tau_r(\vec{x}_r; \vec{x}) &= \tau_G(\vec{x}_r; \vec{x}). \end{aligned}$$

(3.18) can be rewritten as

$$R(\vec{x},\omega;\vec{x_s}) = -2i\omega \int_S \vec{n}\cdot\nabla\tau_r(\vec{x_r};\vec{x})\frac{A_G(\vec{x_r};\vec{x})}{A_G(\vec{x};\vec{x_s})+\epsilon}u(\vec{x_r},\omega;\vec{x_s})e^{-i\omega\left(\tau_s(\vec{x};\vec{x_s})+\tau_r(\vec{x_r};\vec{x})\right)}d\vec{x_r}. \tag{3.19}$$

By integrating through the whole frequency band, we have the following angular reflectivity

$$R(\vec{x};\vec{x_s}) = 2\int_S \vec{n}\cdot\nabla\tau_r(\vec{x_r};\vec{x})\frac{A_G(\vec{x_r};\vec{x})}{A_G(\vec{x};\vec{x_s})+\epsilon}u'(\vec{x_r},\tau_s(\vec{x};\vec{x_s})+\tau_r(\vec{x_r};\vec{x});\vec{x_s})d\vec{x_r}. \tag{3.20}$$

This is the generalized Kirchhoff migration integral for prestack depth imaging. It indicates that the migration of a single physical experiment can be effectively performed by summing the differential traces along the traveltime curve $\tau_s(\vec{x};\vec{x_s})+\tau_r(\vec{x_r};\vec{x})$ with the amplitudes modulated by the geometrical divergence factor $\frac{A_G(\vec{x_r};\vec{x})}{A_G(\vec{x};\vec{x_s})+\epsilon}$, the corresponding obliquity $\cos\theta_r$ and velocity c_r at the receiver position $\vec{x_r}$, as $\vec{n}\cdot\nabla\tau_r(\vec{x_r};\vec{x}) = \frac{\cos\theta_r}{c_r}$.

As I mentioned above, the computation of this angular reflectivity using (3.20) requires some measure in advance for stability. In fact, in migration, we are more interested in the qualitative description of discontinuities than the reflectivity values. A common definition of migration is the cross-correlation of source and scattered wavefields (Claerbout, 1971)

$$R^c(\vec{x},\omega;\vec{x_s}) = u(\vec{x},\omega;\vec{x_s})D^*(\vec{x},\omega;\vec{x_s}), \tag{3.21}$$

where D^* is the complex conjugate of D. This definition gives a measure of the relative reflectivity. It can be expressed as

$$R^c(\vec{x};\vec{x_s}) = 2\int_S \vec{n}\cdot\nabla\tau_r(\vec{x_r};\vec{x})A_G(\vec{x_r};\vec{x})A_G(\vec{x};\vec{x_s})u'(\vec{x_r},\tau_s(\vec{x};\vec{x_s})+\tau_r(\vec{x_r};\vec{x});\vec{x_s})d\vec{x_r}. \tag{3.22}$$

It is apparent that this expression has a very similar form to the angular reflectivity (3.20) with the only difference appearing in the geometrical spreading term. There no longer exists the problem of instability as in equation (3.20).

In many implementations of migration, especially in reverse-time migration which I will discuss in Chapter 4, another definition of migration imaging is often used. It simply takes the scattered wavefield at the excitation time of position $\vec{x}$ as the measure of the relative reflectivity

$$R^r(\vec{x};\vec{x_s}) = u(\vec{x}, t = \tau_s(\vec{x};\vec{x_s});\vec{x_s}), \tag{3.23}$$

where $\tau_s(\vec{x};\vec{x_s})$ is the excitation time of position $\vec{x}$ due to a point source at $\vec{x_s}$ (Chang and McMechan, 1986). Using equation (3.14), it can be directly written as

$$R^r(\vec{x};\vec{x_s}) = 2\int_S \vec{n}\cdot\nabla\tau_r(\vec{x_r};\vec{x})A_G(\vec{x_r};\vec{x})u'(\vec{x_r},\tau_s(\vec{x};\vec{x_s})+\tau_r(\vec{x_r};\vec{x});\vec{x_s})d\vec{x_r}. \tag{3.24}$$

By comparing this formula with (3.22), it is evident that this excitation-time imaging formulation is a special case of the angular reflectivity formulation when

$$A_G(\vec{x};\vec{x_s}) = 1. \tag{3.25}$$

This corresponds to assuming that the amplitude of the source wavefield function is unit everywhere in the Earth.

Equations (3.20), (3.22) and (3.24) are three very general migration integrals which can all be termed as Kirchhoff integrals. They are all directly applicable to variable velocity media. They can essentially be unified using a general integral

$$R(\vec{x};\vec{x_s}) = 2\int_S \vec{n}\cdot\nabla\tau_r(\vec{x_r};\vec{x})A(\vec{x_r};\vec{x};\vec{x_s})u'(\vec{x_r},\tau_s(\vec{x};\vec{x_s})+\tau_r(\vec{x_r};\vec{x});\vec{x_s})d\vec{x_r}, \tag{3.26}$$

with the amplitude correction due to wavefront spreading being generalized to be $A(\vec{x_r};\vec{x};\vec{x_s})$. Almost all Kirchhoff migration methods available can be explained by this general formulation (Schneider, 1978; Keho and Beydoun, 1988; Docherty, 1991).

By combining all individual angular reflectivity functions provided by each separate shot,

$$R(\vec{x}) = \sum_{\vec{x_s}} R(\vec{x};\vec{x_s}), \tag{3.27}$$

we should be able to obtain a relatively good estimate of the discontinuities in the Earth, as long as these shots provide a symmetric coverage of illumination including wide angles.

3.3. 2.5D prestack depth migration integrals

In the last section, I obtained three integral formulations for prestack depth migrations. These formulations are uniquely represented by a more general integral equation. This migration equation can theoretically be applied to any velocity model and recording topography. However, its application requires the availability of an areal coverage of records. At present, most seismic data are still acquired along lines using point sources. Prestack depth migrations are thus required for such data from geologically complex areas. As the data are limited to a single line, migration is thus based on the assumption that the Earth is uniform perpendicular to the seismic line, which is essentially a 2.5D problem. The term of 2.5D refers to 3D wave propagations

in a medium varying only along the seismic line (Bleistein, 1984). I will show that the 2.5D integral migration equation is much more complicated than its 3D counterpart. This reflects the fact that the natural way is usually the simplest, both physically and mathematically.

To derive the 2.5D integrals for migration, I follow Bleistein (1984) to integrate the x_2 part by means of the stationary phase method. First I will rewrite equation (3.26) as follows,

$$R(\vec{x};\vec{x_s}) = 2\int -i\omega d\omega I(\vec{x};\vec{x_s};\omega), \tag{3.28}$$

where,

$$I(\vec{x};\vec{x_s};\omega) = \int d\xi_1 \int \vec{n}\cdot\nabla\tau_r(\vec{x_r};\vec{x})A(\vec{x_r};\vec{x};\vec{x_s})u(\vec{x_r},\omega;\vec{x_s})e^{-i\omega\phi}d\xi_2, \tag{3.29}$$

where $\vec{\xi} = (\xi_1,\xi_2)$ is the surface position parameter to represent $\vec{x_s}$ and $\vec{x_r}$, and ϕ is the total travel time,

$$\phi = \tau_s(\vec{x};\vec{x_s}) + \tau_r(\vec{x_r};\vec{x}). \tag{3.30}$$

Its first derivative with respect to ξ_2 is,

$$\frac{\partial\phi}{\partial\xi_2} = \frac{\partial\tau_s(\vec{x};\vec{x_s})}{\partial\xi_2} + \frac{\partial\tau_r(\vec{x_r};\vec{x})}{\partial\xi_2}. \tag{3.31}$$

Using the definition that

$$\nabla\tau = \vec{p} = (p_1,p_2,p_3), \tag{3.32}$$

where $p = 1/c(\vec{x})$ is the slowness, we have

$$\frac{\partial\phi}{\partial\xi_2} = p_2^s(\vec{x};\vec{x_s}) + p_2^r(\vec{x_r};\vec{x}). \tag{3.33}$$

Now using the fact that velocity $c(\vec{x})$ is independent of x_2, or ξ_2, we have,

$$\frac{dp_2}{d\sigma} = 0, \tag{3.34}$$

from the second equation of (2.18). Thus, without loss of generality, p_2 can be expressed as (Bleistein, 1986)

$$p_2 = \frac{1}{c(\vec{\xi})} \sin\alpha \sin\beta, \tag{3.35}$$

where α, β are two parameters describing the direction of the ray.

Similarly, from the first equation of (2.18), we obtain,

$$\xi_2 = p_2 \sigma. \tag{3.36}$$

Note that I have here used $\lambda = 1$ in the above expression.

At the stationary phase position, $\partial\phi/\partial\xi_2 = 0$, that is,

$$p_2^s(\vec{x}; \vec{x_s}) + p_2^r(\vec{x_r}; \vec{x}) = 0 \tag{3.37}$$

or, using $p_2 = \xi_2/\sigma$ from equation (3.36),

$$\xi_2 \left(\frac{1}{\sigma_s} + \frac{1}{\sigma_r} \right) = 0. \tag{3.38}$$

Thus, $\xi_2 = 0$. That is, the stationary phase occurs at the plane $\xi_2 = 0$.

To carry out a stationary phase analysis, we have to compute the second derivative of the phase function,

$$\frac{\partial^2\phi}{\partial\xi_2^2} = \frac{\partial p_2^s(\vec{x}; \vec{x_s})}{\partial\xi_2} + \frac{\partial p_2^r(\vec{x_r}; \vec{x})}{\partial\xi_2}. \tag{3.39}$$

Using the relation between ξ_2 and p_2 in equation (3.36), we have,

$$d\xi_2 = p_2 d\sigma + \sigma dp_2. \tag{3.40}$$

At the stationary point where $p_2 = 0$, this results in

$$\frac{dp_2}{d\xi_2} = \frac{1}{\sigma}. \tag{3.41}$$

Thus,

$$\frac{\partial^2 \phi}{\partial \xi_2^2} = \left(\frac{1}{\sigma_s} + \frac{1}{\sigma_r}\right). \tag{3.42}$$

It is apparent that,

$$sgn\left(\frac{\partial^2 \phi}{\partial \xi_2^2}\right) = 1. \tag{3.43}$$

Now the integral (3.29) can be evaluated by the contribution in the plane $\xi_2 = 0$, using the stationary phase formulation (Bleistein, 1984, p108)

$$I = \int d\xi_1 \left(\frac{2\pi}{|\omega|}\right)^{\frac{1}{2}} \vec{n} \cdot \nabla \tau_r(\vec{x_r}; \vec{x}) A(\vec{x_r}; \vec{x}; \vec{x_s}) u(\vec{x_r}, \omega; \vec{x_s}) \frac{1}{\sqrt{\sigma_s^{-1} + \sigma_r^{-1}}} e^{-i\omega\left(\tau_s(\vec{x};\vec{x_s}) + \tau_r(\vec{x_r};\vec{x})\right)} e^{i\frac{\pi}{4} sgn\omega}. \tag{3.44}$$

Thus, the in-plane reflectivity can be expressed as,

$$R = 2 \int\int \sqrt{-i\omega}\sqrt{2\pi} \vec{n} \cdot \nabla \tau_r(\vec{x_r}; \vec{x}) A(\vec{x_r}; \vec{x}; \vec{x_s}) \frac{1}{\sqrt{\sigma_s^{-1} + \sigma_r^{-1}}} u(\vec{x_r}, \omega; \vec{x_s}) e^{-i\omega\left(\tau_s(\vec{x};\vec{x_s}) + \tau_r(\vec{x_r};\vec{x})\right)} d\omega d\xi_1, \tag{3.45}$$

or, using the fact that $\vec{x_r}$ is uniquely determined by ξ_1,

$$R = 2 \int \vec{n} \cdot \nabla \tau_r(\vec{x_r}; \vec{x}) A(\vec{x_r}; \vec{x}; \vec{x_s}) \frac{1}{\sqrt{\sigma_s^{-1} + \sigma_r^{-1}}} \left(\frac{du}{dt}\right)^{\frac{1}{2}} (\vec{x_r}, \tau_s(\vec{x}; \vec{x_s}) + \tau_r(\vec{x_r}; \vec{x}); \vec{x_s}) d\vec{x_r}. \tag{3.46}$$

Note that I have omitted a constant of $\sqrt{2\pi}$ in the above expression. In this expression, the vectors $\vec{x_r}, \vec{x}, \vec{x_s}$ are only two dimensional. This is the general migration equation based on the assumption that the seismic records are only available on a line which itself is the result of 3D wave propagation from a point source. That is, it is a migration for 2.5D imaging. This formulation essentially shows that migration of a single line can be accomplished by summation of differential trace amplitudes along

complicated diffraction curves with the amplitudes being modulated by both the in plane geometrical spreading and the obliquity before summation (Figure 3.9). Compared to its corresponding 3D equation, this is somewhat more complicated. This is a very good example of the common observation that problems from nature are often the simplest.

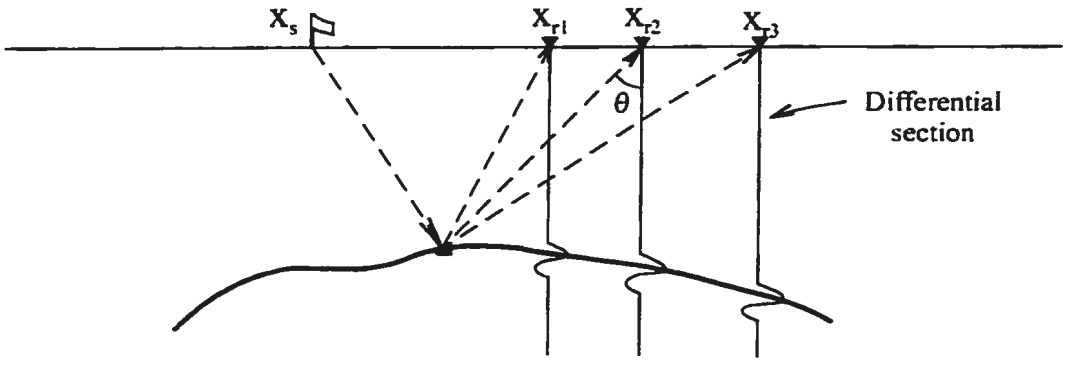

Figure 3.9: 2.5D migration by the prestack integral scheme. Migration of a gather is accomplished by summing amplitudes of the differential traces along diffraction trajectories. The differential amplitudes are modulated by a plane geometrical spreading and obliquity before migration. The obliquity is the cosine of the emergent angle θ.

I will now consider the special case of constant velocity, $c(\vec{x}) = c_0$ for equation (3.46). In this case, we have,

$$\tau_s = \frac{|\vec{x} - \vec{x_s}|}{c_0}, \qquad \sigma_s = c_0|\vec{x} - \vec{x_s}|; \tag{3.47}$$

$$\tau_r = \frac{|\vec{x_r} - \vec{x}|}{c_0}, \qquad \sigma_r = c_0|\vec{x_r} - \vec{x}|, \tag{3.48}$$

and,

$$\nabla\tau_r = \frac{1}{c_0}\frac{\vec{x}-\vec{x_r}}{|\vec{x_r}-\vec{x}|}. \tag{3.49}$$

With these specializations, equation (3.46) reduces to,

$$R = 2\int \frac{\cos\theta}{\sqrt{c_0}} A(\vec{x_r};\vec{x};\vec{x_s})\sqrt{\frac{|\vec{x}-\vec{x_s}||\vec{x_r}-\vec{x}|}{|\vec{x}-\vec{x_s}|+|\vec{x_r}-\vec{x}|}}\left(\frac{du}{dt}\right)^{\frac{1}{2}}(\vec{x_r},\tau_s(\vec{x};\vec{x_s})+\tau_r(\vec{x_r};\vec{x});\vec{x_s})d\vec{x_r}. \tag{3.50}$$

This equation is now familiar. As the general amplitude term $A(\vec{x_r};\vec{x};\vec{x_s})$ of the Green's function can also be explicitly expressed as functions of $|\vec{x_r}-\vec{x}|$, and/or $|\vec{x}-\vec{x_s}|$, this integral can simply be implemented on input traces without the need for determining the integral curve which is the most time consuming and also difficult in general cases. Two fundamental operations are involved here. First, each trace is half differentiated in time . Then a summation of the differentiated amplitudes along a hyperbolic trajectory with its apex at the lateral position $\vec{x}$, is implemented. The amplitudes on each trace are modulated by both the emergent angle θ at the receiver's position, and also a geometrical function which is now an analytic function of distances traveled, $|\vec{x_r}-\vec{x}|$ and $|\vec{x}-\vec{x_s}|$.

3.4. Prestack migration examples of complex structures by the Kirchhoff method

In the last section. I derived the 2.5D Kirchhoff migration integral (3.46). Two main constituents of that equation are the determination of the diffraction curves and the in-plane geometrical spreading factors. Both of them can be computed by dynamic ray tracing (Cerveny. 1987) or paraxial ray tracing (Beydoun and Keho. 1987). processes involving significant computations. I have effectively used the Vidale-type solution of the eikonal equation which I developed in Chapter 2 for the purpose of determining the traveltimes. These traveltimes correspond to first arrival times. As questioned by Geoltrain and Brac (1993). such arrivals possibly are not the arrivals which carry the most energy. In such cases. the use of the first arrival times would probably not get the best image (Gray and May. 1994: Nichols. 1996). Nevertheless. these calculated traveltimes determine the integral curve for the Kirchhoff migration. This drastically enhances computational efficiency. Though Vidale and Houston (1990) show that geometrical amplitudes can be computed using eikonal traveltimes. it is nevertheless less accurate than those calculated by dynamic ray tracing. In addition. the determination of emergence angles using such eikonal traveltimes lacks accuracy. although this determination is possible. Based on these observations and the relative success of imaging the Marmousi data with the simple superposition method of aplanatic curves as shown in section 3.1. I use an approximation to the geometrical spreading factors based on some average measurement of the Earth model. This approximation is very similar to that of Gray and May (1994) in their

migration of the Marmousi data. Such an approximation is mainly based on the following observations. First, a knowledge of the arrival time of an event, coupled with a general amplitude of that event, is often adequate for preliminary interpretation (Kelly et al., 1982). Second, the input for migration is seldom of true amplitude, as such processes as FK filtering and AGC are often applied before migration. The third is the observation that the migration result of the Husky-Alberta foothills line from such an approximation for the Kirchhoff method is almost the same as that of the reverse-time migration which is theoretically accurate. As summation along diffractions is equivalent to superposition of aplanatic curves which I elucidated in the first section of this chapter, I have implemented the migration in the mode of aplanatic superposition.

3.4.1. Prestack Kirchhoff migration of the Marmousi model data

I will show in this section a migration example of a standard test data set, the Marmousi model. This model test illustrates the accuracy and effectiveness of the above scheme.

The Marmousi model data has served as an excellent testbed for both prestack depth migration and velocity analysis since its creation (Versteeg, 1993). It is based on a geophysical model from the Cuanza Basin of Angola. The model is created using a high order finite difference solution of the acoustic equation. Figure 3.10 shows the velocity model. The structure of the basin is dominated by steep growth faults which arise from salt creep (Bevc, 1997). The reservoir in the subsalt anticline around a depth of 2.6 km and laterally at 6.0 $\sim$ 7.5 km is one of the exploration targets and thus an imaging objective. The whole synthetic data set consists of

96 traces. Figure 3.11 is the near offset section which shows a significantly distorted model structure. In fact, in areas of complex structures with significant velocity heterogeneity like the Marmousi model, prestack depth migration is a necessity for a proper imaging (Versteeg, 1993; Gray and May, 1994). Figure 3.12 shows the final migration stack of the Marmousi data by the prestack depth Kirchhoff migration that I formulated in this chapter. In this migrated section, it is evident that most of the salient features of the model have been properly imaged. The growth faults are well resolved. Even the subsalt anticline is imaged. However, it seems that the reservoir interfaces are not imaged clearly. This could be due to several causes. One is the approximation in the amplitude calculation of the Green's functions. Another possibility is the fact that the Kirchhoff migration method assumes a zero phase signature while the input can be of minimum phase due to the effect of deconvolution. The use of first arrivals instead of most energetic arrivals could be another possible factor also (Geoltrain and Brac, 1993; Gray and May, 1994; Nichols, 1996). Regardless of these possibilities, overall, the migration as shown in Figure 3.12 gives an image very close to the model within the seismic resolution.

3.4.2. Kirchhoff Migration from topography of the Husky–Alberta foothills line

The Husky–Alberta foothills line is an open file of real seismic data which is anticipated to serve as an excellent test data for imaging complicated structures with rough topography. The Alberta foothills are generally characterized by overthrust structures of steep dip and considerable lateral variation. The line is of excellent signal quality (Stork et al., 1995). Figure 3.13 shows one near offset section with

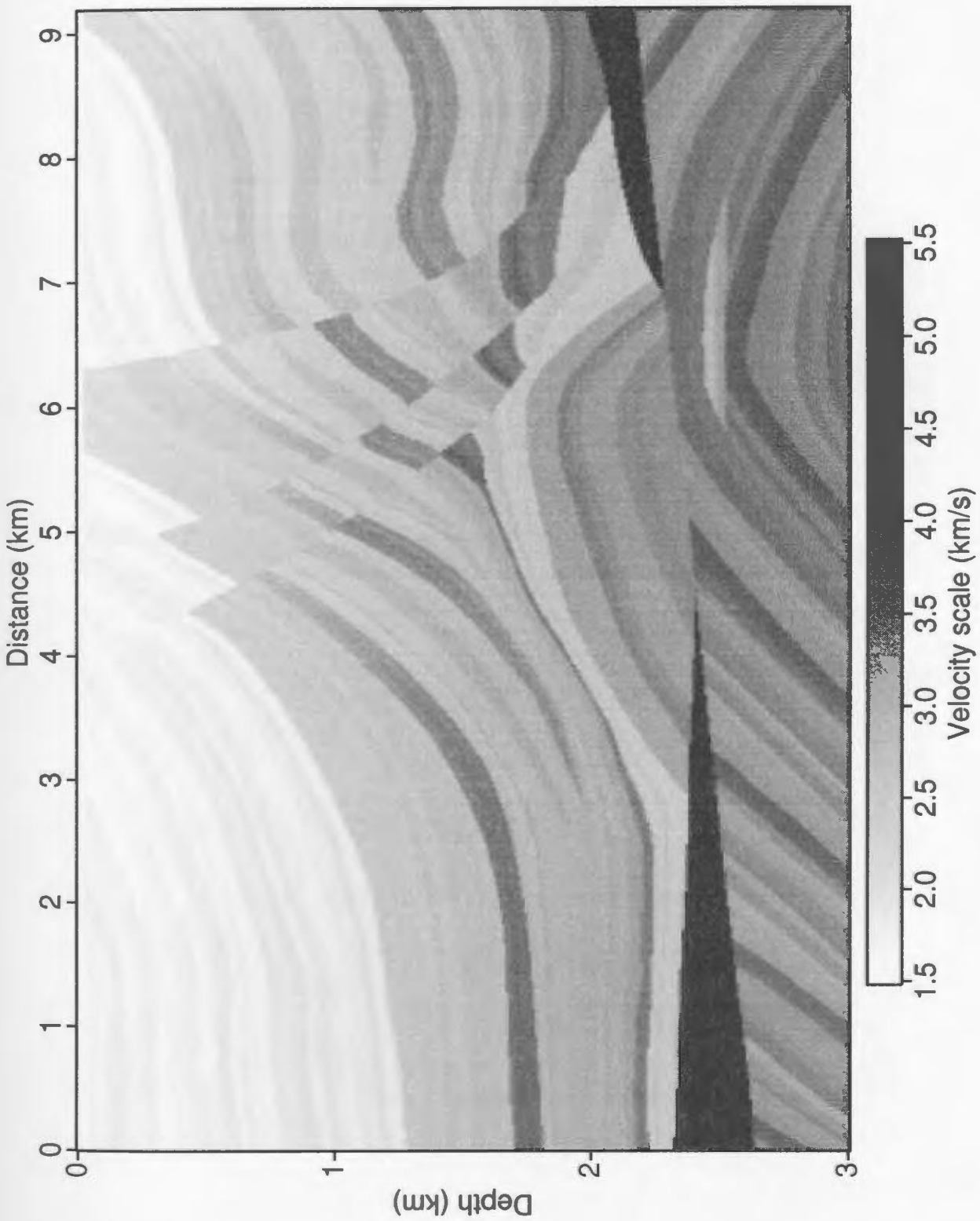

Figure 3.10: The Marmousi velocity model.

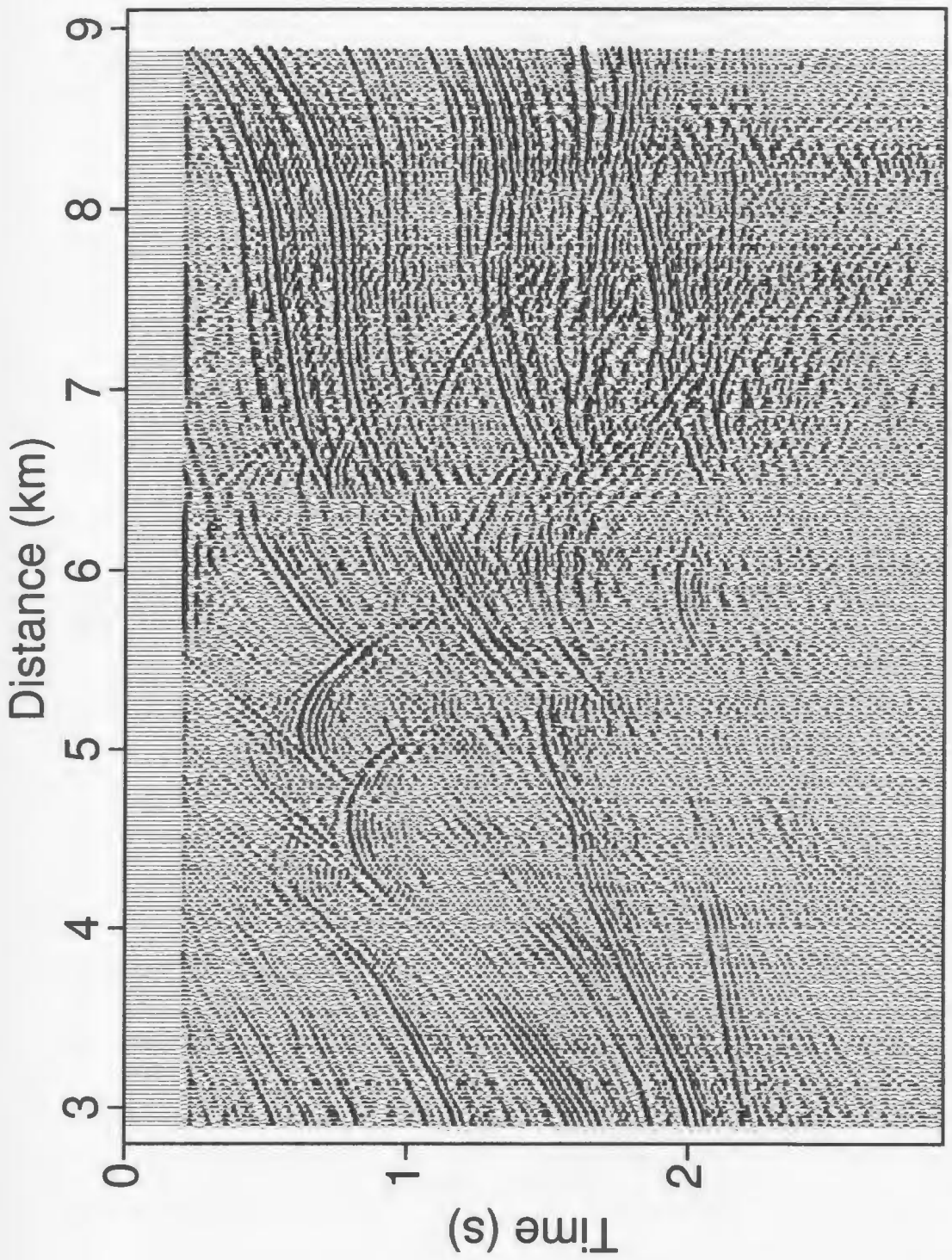

Figure 3.11: Near offset (200 m) section of the Marmousi data set.

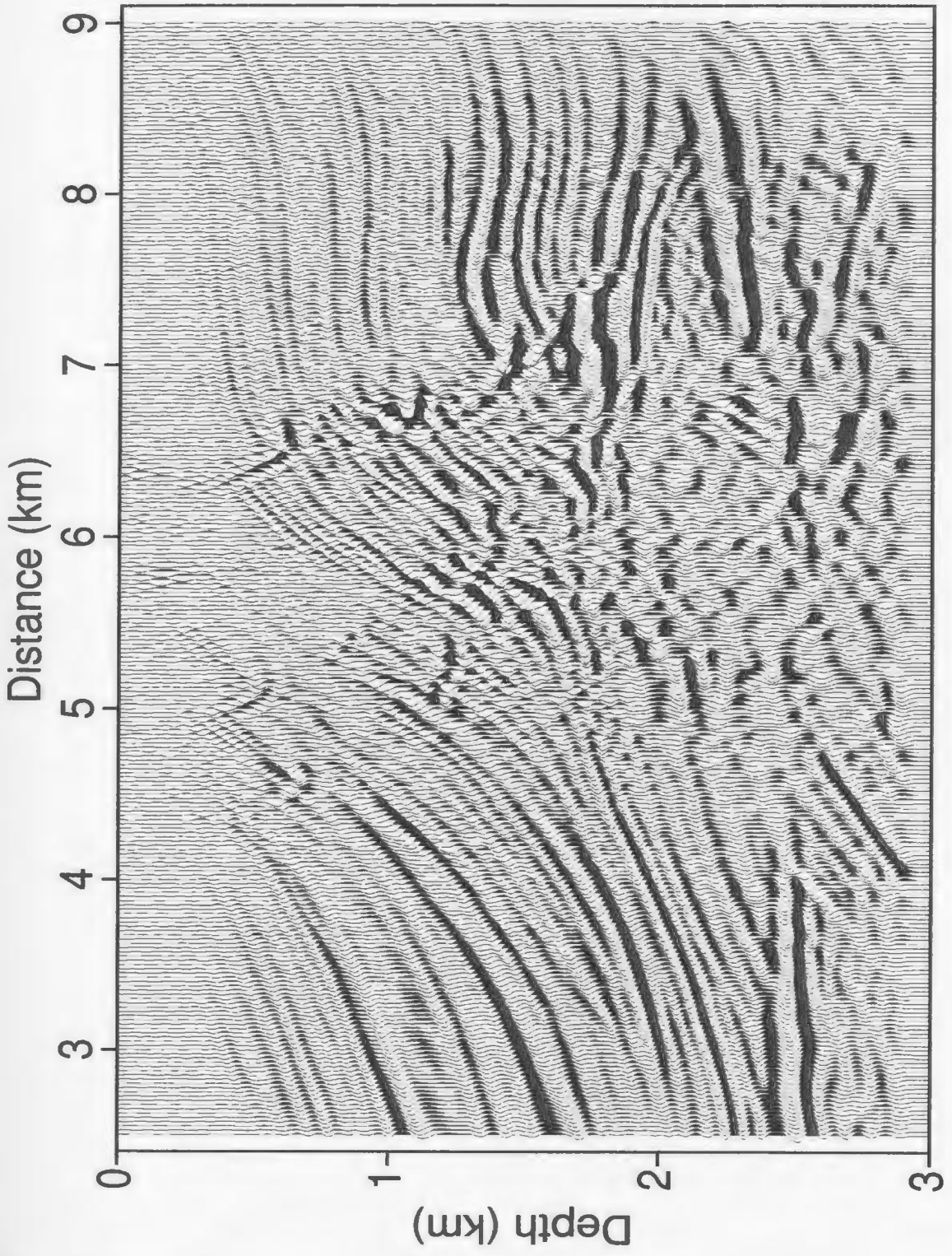

Figure 3.12: Migration section of the Marmousi data set by prestack Kirchhoff depth migration. The migration is based on a velocity grid of 12.5 m by 12.5 m.

offset of 60 m, which in many cases can be taken as a good approximation of the zero offset section. Figure 3.14 shows a similar near offset section with negative offset of 60 m, basically illustrating similar problems to those in Figure 3.13. By comparing these two near offset sections, it is apparent that the Earth is definitely not of layer cake structure with vertical variations only. These sections suggest that there exist significant lateral inhomogeneities.

For migration purposes in such mountainous areas, the integral migration should theoretically be done with the Kirchhoff integral by calculating the amplitudes of the Green's functions and the related geometrical factors from the actual source and receiver positions. For computing economy as described earlier this chapter, I have used the Rayleigh integral for migration here. By computing the aplanatic surfaces using the finite difference traveltime computation methods which I developed in Chapter 2, the total line is imaged by migration from topography (Lines et al., 1996). Using a velocity model (Figure 3.15) developed through an iterative interpretive depth imaging procedure (Zhu and Lines, 1996; Wu et al., 1996) which I will dissect in detail in Chapter 5, I obtain the migration result shown in Figure 3.16. In this migration image, the shallow dipping formations at the upper left side of the section are clearly imaged. Two main thrust faults are well defined approaching the surface, around CDP numbers of 580 and 810 respectively. Overall, this prestack Kirchhoff depth migration provides a very encouraging result. Its geological interpretation is essentially the same as the velocity model, because they are consistent with each other in many respects at this final stage of the iterative interpretive depth imaging procedure. This indicates that even this approximate solution of integral migration works very well as long as migration is implemented from the topography in a single unified procedure.

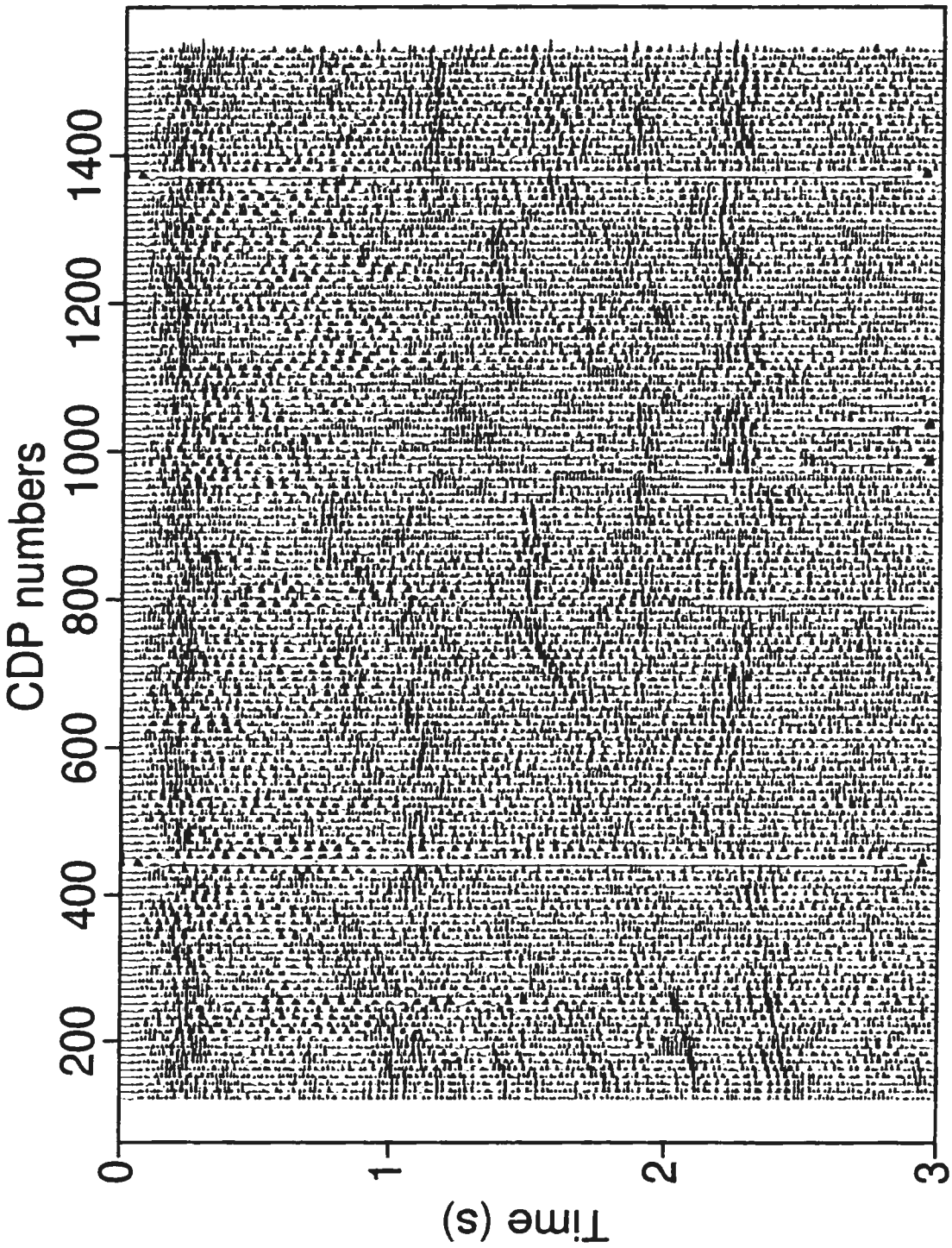

Figure 3.13: Near offset (60 m) section of the Husky–Alberta foothills line.

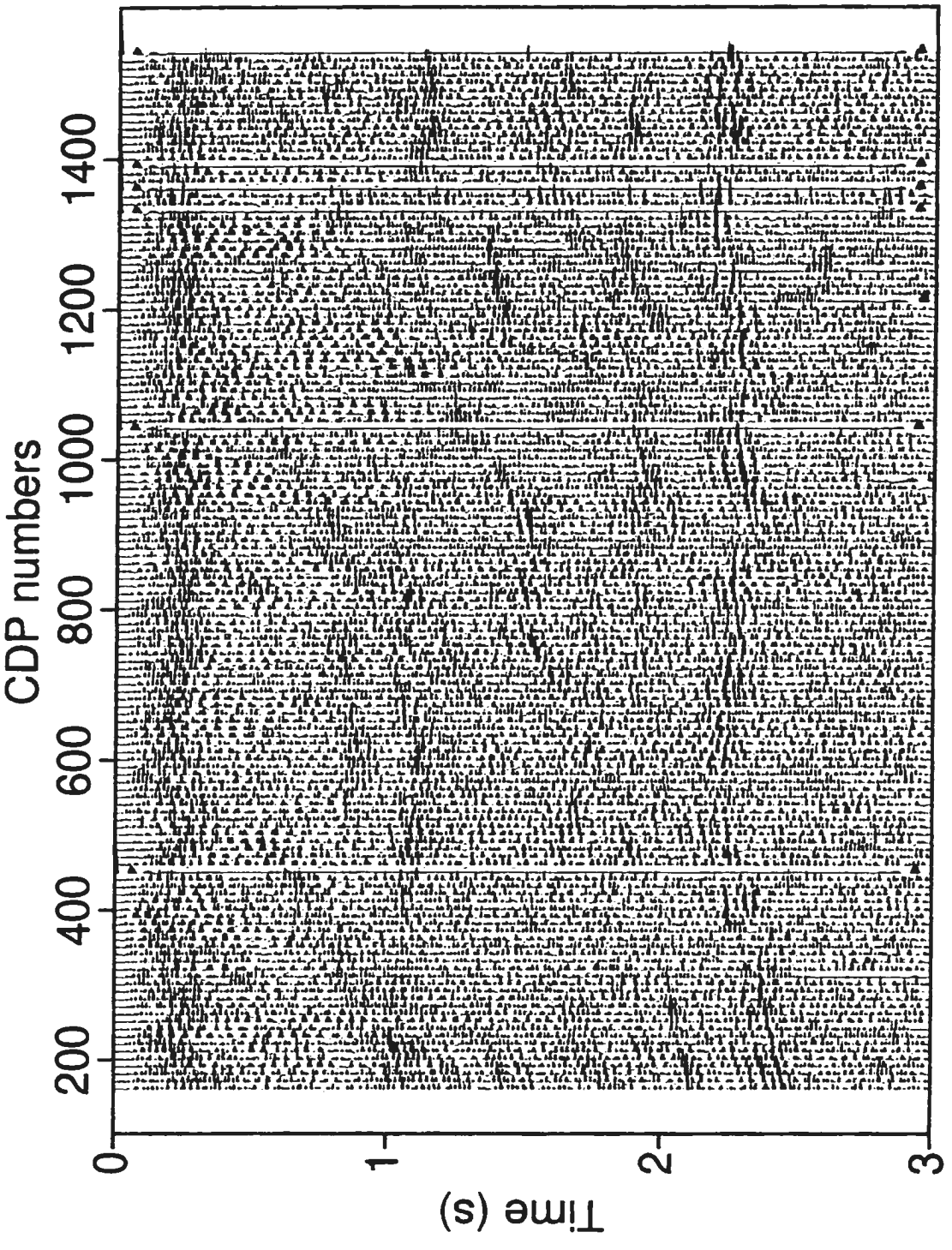

Figure 3.14: Near offset (-60 m) section of the Husky–Alberta foothills line.

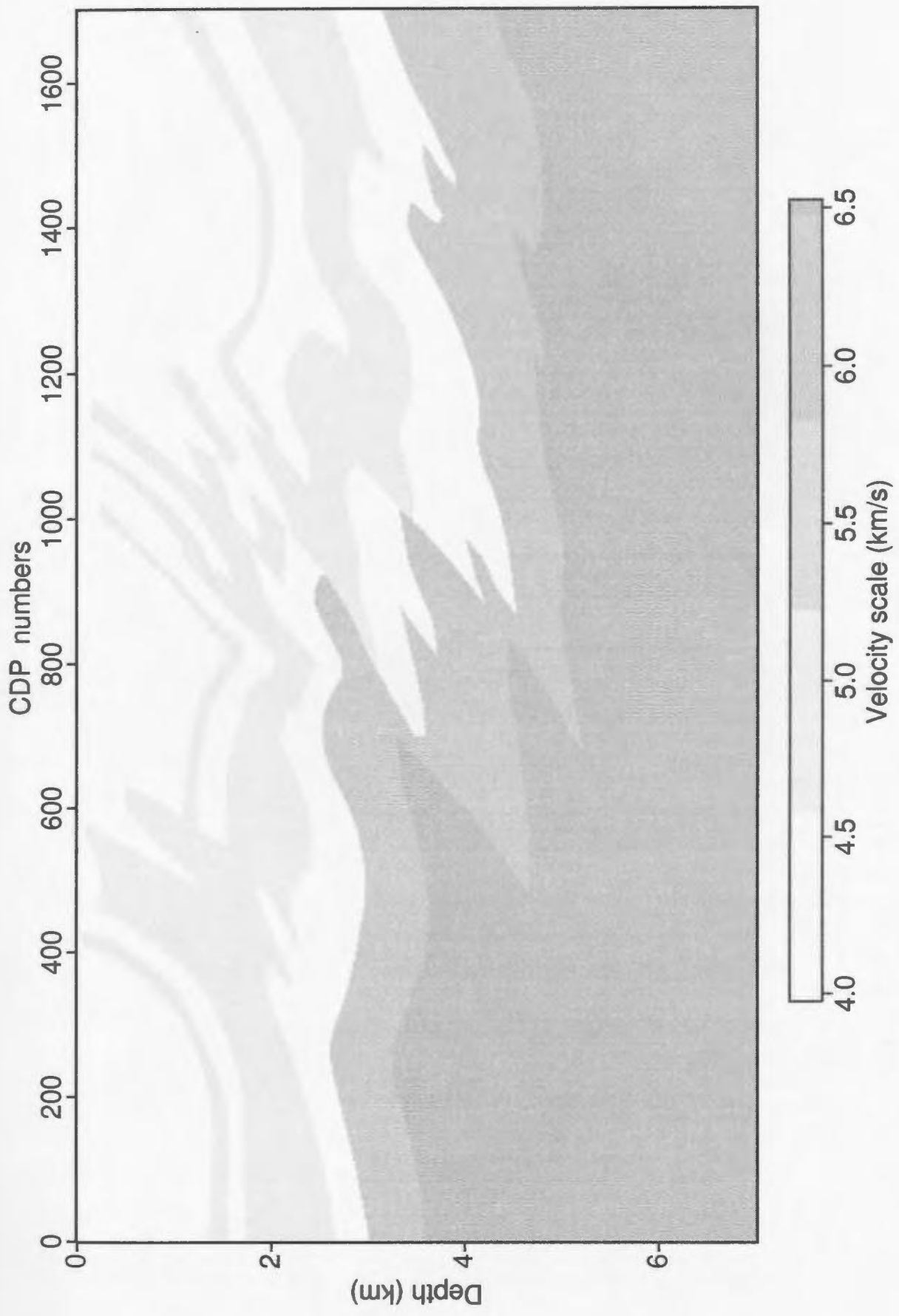

Figure 3.15: Velocity model of the Husky–Alberta foothills line.

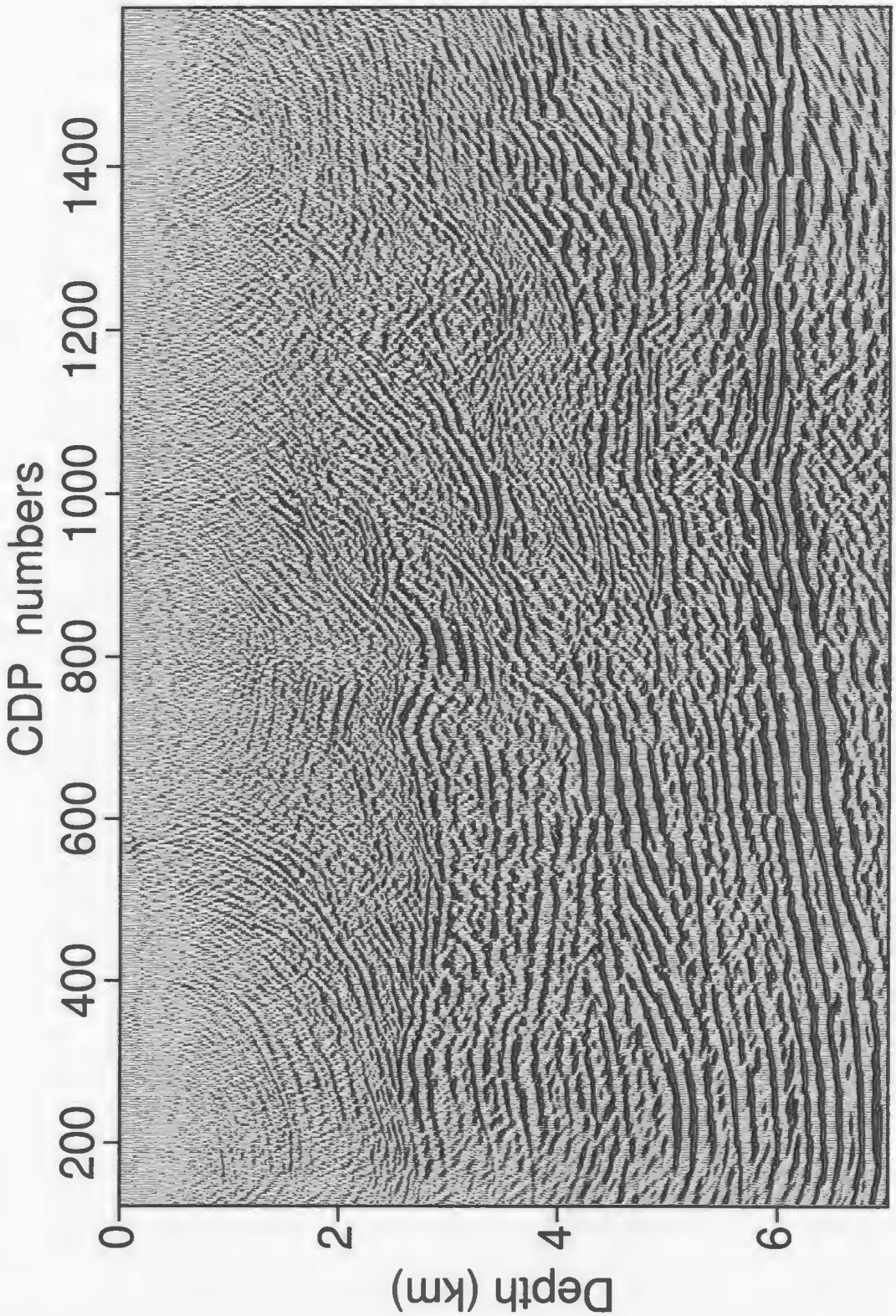

Figure 3.16: Migrated section of the Husky–Alberta foothills line by the Kirchhoff technique. Prestack depth migration is implemented on a fine grid of 10 m by 10 m.

3.5. Summary

The classic summation along hyperbola and superposition of circular wavefronts were extended to variable velocity media for any recording geometry. Based on the WKBJ approximation of the Green's function to the acoustic wave equation, I obtained several migration integrals. These integrals were unified by a single integral formula. I demonstrated that this general integral is simply a summation of differential trace amplitudes along an integral surface. The determination of the integral surfaces was shown to be the primary computations in this general Kirchhoff migration. The migration example of the Marmousi model illustrated the effectiveness of the method in imaging very complex geological structures including steep dip faults. The method was successfully applied to imaging the Husky–Alberta foothills line by migration from topography.

Chapter 4. Prestack reverse-time migration of sparse and irregular data

Compared to the integral migration method studied in the last chapter, reverse-time migration is a relatively new technique. The idea of using finite-difference wave equation solutions for reverse-time migration was originally published in a paper "Equations d'onde et modeles"(Hemon, 1978). Hemon did not emphasize the potential applications. At about the same time, Whitmore (1982) had extensively used the method, but did not publish results of the method until his participation in the 52nd SEG annual meeting's migration workshop. During the next year, a number of reverse-time migration papers appeared including the independent pioneering work of Baysal et al. (1983), Loewenthal and Mufti (1983), McMechan (1983) and Whitmore (1983). These papers established reverse-time migration as a very general imaging tool for seismic reflection data. It is solely based on the symmetry of the acoustic wave equation in time, which makes it possible to use basically the same finite-difference code for extrapolating the recorded wavefields backward in time as in forward modeling.

Nevertheless, reverse-time migration is computationally very expensive. In addition to its expense, it generally has more restrictions on the sampled seismic data. It was commonly assumed that the input traces in a record had to be equally spaced

on a relatively fine grid. However, many recent advances in reverse-time migration demonstrate that most of these restrictions can be removed without detrimental effects on the final migration results (Mufti et al., 1996; Zhu and Lines, 1997), especially for stacked data. Mufti et al. (1996) have shown that interpolation of traces can be eliminated by using relatively large horizontal grid steps compared to the fine vertical ones. Their method works whenever horizontal spatial wavenumbers are much smaller than the vertical wavenumbers. Their treatment is based on the insight that reflected waves mostly propagate vertically in the stacked section so that the dispersion horizontally is minimal compared to that vertically. Nevertheless, due to the nature of seismic acquisition and irregular data sampling relative to a finely spaced finite-difference mesh, such treatment will be very difficult. For prestack data where waves travel in nearly all directions, Mufti et al.'s method (1996) will generally not be applicable.

In this chapter, I will first illustrate that the reverse-time wave equation extrapolation procedure also has the capability of implicitly interpolating missing traces, whenever unaliased input records are considered to be sparsely and irregularly sampled. The interpolation is essentially based on the ability of the wavefield to heal itself due to constructive wavefield interference during propagation. Then I will show applications of this new treatment to the Marmousi and the Husky–Alberta foothills data. These applications demonstrate that reverse-time migration can be directly applied to sparsely and irregularly sampled records without any interpolation of missing traces in advance. The missing traces are simultaneously reconstructed during the migration by constructive interference.

4.1. Principles of reverse-time migration

Migration is the mathematical procedure which maps reflections and diffractions in time to their corresponding reflectors and diffractors in depth. It essentially consists of two closely connected steps: reverse propagation and imaging. The reverse propagation step tries to drive the recorded waves back into the Earth along the paths they originally traveled. It thus is basically a de-propagation procedure. The imaging step determines when the backward propagating energy represents the relative reflectivity of the Earth.

As I have discussed in Chapter 3, wave propagation phenomena can be accurately described by the wave equation. In 2D form,

$$\frac{\partial^2 u(x,z,t)}{\partial x^2} + \frac{\partial^2 u(x,z,t)}{\partial z^2} - \frac{1}{c^2(x,z)} \frac{\partial^2 u(x,z,t)}{\partial t^2} = -f(x,z,t), \qquad (4.1)$$

describes wave propagation in (x, z)–plane of a 3D medium excited by a line source, $f(x,z,t)$, distributed parallel to the y-axis along which the medium is uniform. As the source used in practice is often a point source, the recorded data thus have to be amplitude corrected in order to use equation (4.1). Theoretically, the spherical wave amplitude is inversely proportional to the distance the wave traveled, while the cylindrical wave amplitude is inversely proportional to the square root of the distance (Sheriff, 1991, p277). Thus, multiplication of each sample with the square root of the distance traveled would compensate for the most important factor of the amplitude due to the point source. This compensation makes the recorded amplitudes as if it were acquired with a line source. In practice, there are many factors contributing to

amplitude decay and seismograms are generally corrected with some type of amplitude balancing that provides energy balancing over chosen data windows (Robinson and Treitel, 1980).

Because of the second order differentiation of the wavefield u with respect to time t, and also of the time independence of the coefficients in equation (4.1), (4.1) also describes wave propagation backward in time. Mathematically it can be easily proven that, if $u(x, z, t)$ is a solution to (4.1), then $u(x, z, T - t)$ will also be a solution for any constant T.

To backward propagate the recorded wavefields using equation (4.1), a finite-difference approximation is employed to solve (4.1). Figure 4.1 shows a finite-difference mesh overlying a geological model. The mesh consists of uniform cells with lateral and vertical spacings of Δx and Δz respectively. Any point P with coordinates (x, z) in the model can be represented by an indexed integer pair (m, n), where $x = (m-1)\Delta x, z = (n-1)\Delta z$. Any physical property, say the velocity, at the point P, can thus be represented as $c(m, n)$, or, $c_{m,n}$. If the geological model considered is spatially limited, its gridded velocity model can be represented by a velocity matrix, say $C(M, N)$ with M, N representing the lateral and vertical ranges of the mesh. Similarly, we introduce the index l to represent the time instants such that instant $t = (l-1)\Delta t$. With these discretizations of the Earth model and time, the wavefield u at time $t = (l-1)\Delta t$ and point $P(x, z)$ can be discretely represented by $u(m, n, l)$, or $u^l_{m,n}$.

Now I will approximate the differential terms of equation (4.1) based on Taylor Series expansion. The time differential term is approximated by a second order central

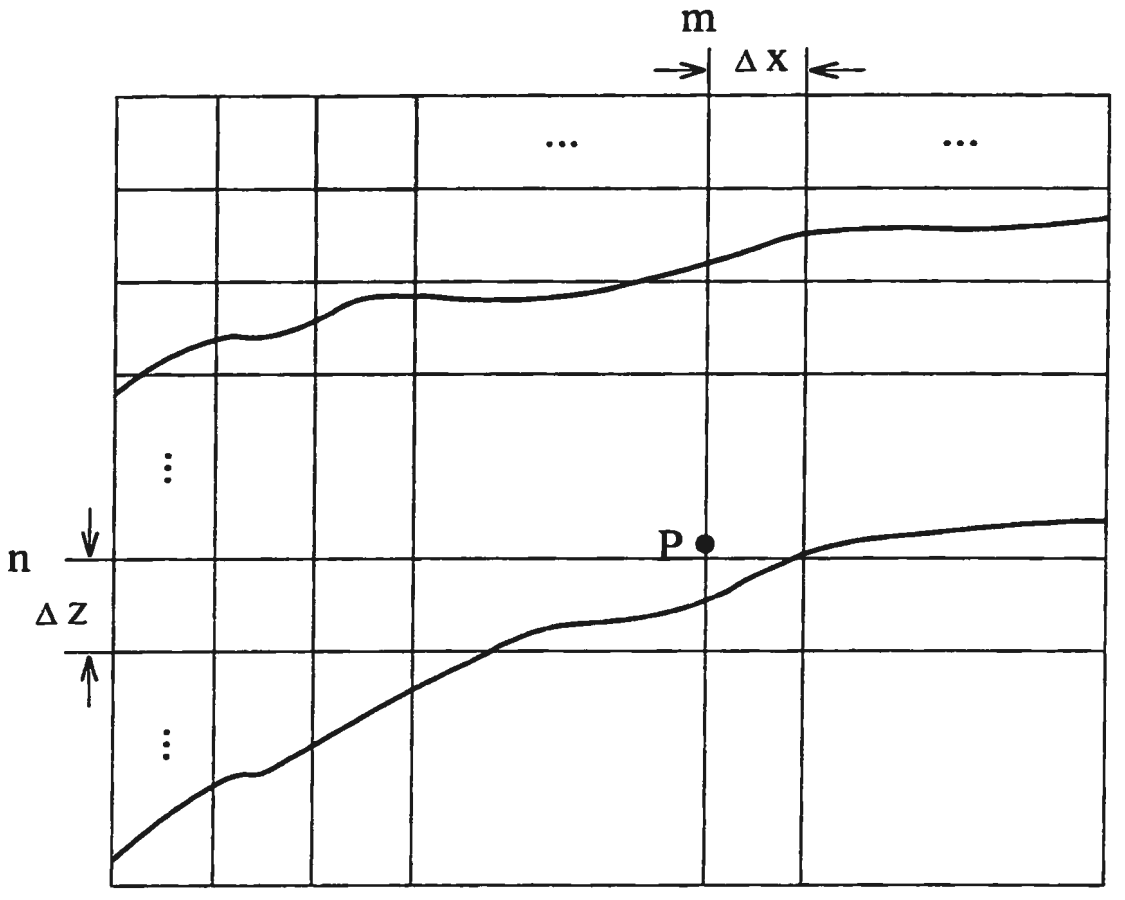

Figure 4.1: The finite-difference mesh for reverse-time migration. A uniformly gridded mesh overlies the geological model consisting of two curved reflectors. Each cell is of the same size with lateral and vertical length of Δx and Δz.

finite-difference scheme,

$$\frac{\partial^2 u(m,n,l)}{\partial t^2} = \frac{1}{\Delta t^2}[u^{l+1}_{m,n} - 2u^{l}_{m,n} + u^{l-1}_{m,n}] + O(\Delta t^2). \tag{4.2}$$

This approximation often is accurate enough as Δt is very small in exploration seismology. The spatial differential terms, however, generally need higher order differencing approximations. This is partially due to the need to reduce spatial dispersion effects which could otherwise be very disturbing (Alford et al., 1974; Dablain, 1986).

Though much higher order finite-difference schemes can be used, I found the fourth order scheme often provides the best cost effective results. The x, z derivatives are approximated as,

$$\frac{\partial^2 u(m,n,l)}{\partial x^2} = \frac{1}{12\Delta x^2}[16(u^l_{m+1,n} + u^l_{m-1,n}) - (u^l_{m+2,n} + u^l_{m-2,n}) - 30u^l_{m,n}] + O(\Delta x^4) \tag{4.3}$$

$$\frac{\partial^2 u(m,n,l)}{\partial z^2} = \frac{1}{12\Delta z^2}[16(u^l_{m,n+1} + u^l_{m,n-1}) - (u^l_{m,n+2} + u^l_{m,n-2}) - 30u^l_{m,n}] + O(\Delta z^4) \tag{4.4}$$

Substituting (4.2) - (4.4) into (4.1) leads to ,

$$\begin{aligned} u^{l-1}_{m,n} = \quad & -\tfrac{1}{12}\{ \quad \left(\frac{c_{m,n}\Delta t}{\Delta x}\right)^2 \left[(u^l_{m+2,n} + u^l_{m-2,n}) - 16(u^l_{m+1,n} + u^l_{m-1,n}) + 30u^l_{m,n}\right] \\ & + \quad \left(\frac{c_{m,n}\Delta t}{\Delta z}\right)^2 \left[(u^l_{m,n+2} + u^l_{m,n-2}) - 16(u^l_{m,n+1} + u^l_{m,n-1}) + 30u^l_{m,n}\right]\} \\ & +2u^l_{m,n} \quad -u^{l+1}_{m,n} + f(m,n,l) + O(\Delta x^4, \Delta z^4, \Delta t^2). \end{aligned} \tag{4.5}$$

This is a very general reverse-time extrapolation formulation for any rectangular gridded model, with each rectangle of the size of Δx by Δz. It can be generally expressed as the following recursive matrix formulation,

$$\mathrm{U}^{\,l-1} = \mathrm{A} \; + 2\mathrm{U}^{\,l} - \mathrm{U}^{\,l+1}, \tag{4.6}$$

if we omit the source term. A represents the spatial differential function of the wavefield which is basically a spatial filter, as differentiation is equivalent to high pass filtering (Berkhout, 1984, p30-36). This expression is a backward recursive formulation which enables one to compute the wavefields at the $(l-1)th$ step from its values at the lth and $(l+1)th$ steps. This will drive the wavefields at two later time instants $t = l\Delta t, (l+1)\Delta t$ to its past ones at $t = (l-1)\Delta t$. In the special case

of a square gridded mesh. $\Delta x = \Delta z$, equation (4.5) is simplified to.

$$\begin{aligned} u^{l-1}_{m,n} &= (2 - 5p^2)u^l_{m,n} - u^{l+1}_{m,n} + f(m,n,l) \\ &- \frac{p^2}{12}\Big[\Big(u^l_{m+2,n} + u^l_{m-2,n} + u^l_{m,n+2} + u^l_{m,n-2}\Big) \\ &- 16\ \Big(u^l_{m+1,n} + u^l_{m-1,n} + u^l_{m,n+1} + u^l_{m,n-1}\Big)\Big] + O(h^4, \Delta t^2). \end{aligned} \tag{4.7}$$

where $p = \frac{c_{m,n}\Delta t}{h}$, and $h = \Delta x = \Delta z$. This is well known (Alford et al., 1974). Comparing this simplification with equation (4.5), it is clear that (4.7) involves only 4 multiplications for every grid point at each extrapolation step, while (4.5) needs at least 7 multiplications. In addition, (4.5) requires one more additional 2D array to store the precomputed constants. The computational effort for equation (4.5) is almost twice that of equation (4.7) for a same size geological model, making (4.7) much more attractive. It is for this reason that equation (4.7) is used more often than equation (4.5) in seismic modeling and imaging.

With equation (4.7), reverse-time migration can now be illustrated by a single point diffractor model as shown in Figure 4.2. The wavefield extrapolation is performed in a gridded velocity model based on geological and geophysical information. At every extrapolation step, a constant time strip of amplitudes in the record are simultaneously imposed on the recording surface, either planar or topographic. The finite-difference stencil (4.7) then drives the recorded wavefields backward into the Earth model by computing the wavefields at earlier time instants from their present and future instant values.

During this backward propagation procedure, reflected and diffracted waves move along their original travel paths back into the Earth. They will focus at the spatial

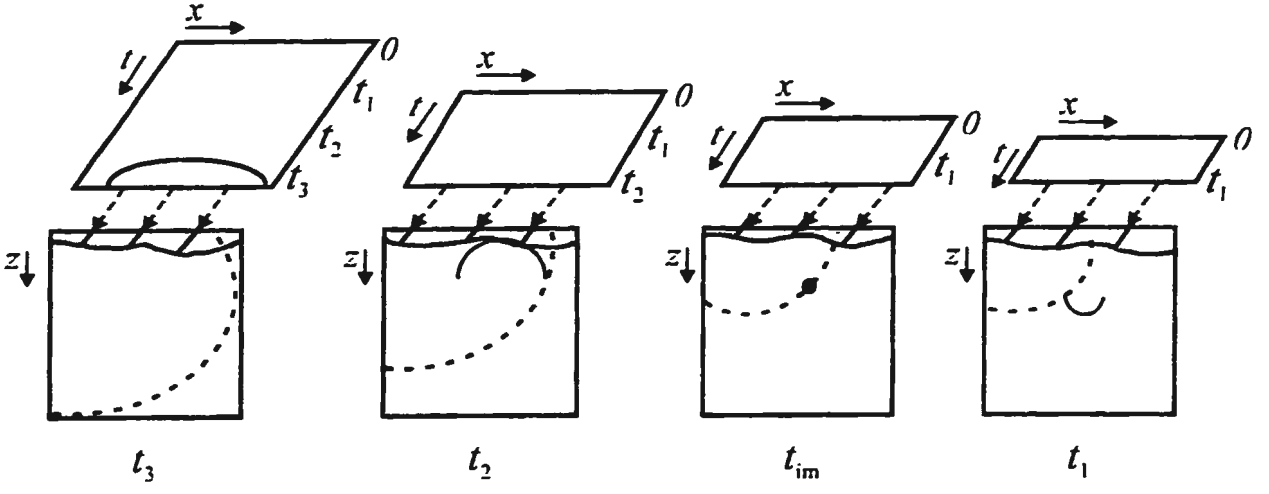

Figure 4.2: Prestack reverse-time migration principles. At each backward extrapolation step, the amplitudes at that time slice of the recordings are simultaneously acting on the recording topography. The wave equation solution then drives the wavefields into the Earth model by computing the wavefields at earlier instant from the corresponding later instants. The backscattered waves (solid curves) will gradually focus to the diffractor point at the imaging time t_{im}, and then defocus thereafter. The dashed curves define the trajectories of points which satisfy the imaging condition. Adapted from McMechan, 1989.

positions where they originate at the arrival time of incident waves (see the third panel of Figure 4.2). The focusing time is called "excitation time" by Chang and McMechan (1986). It is determined by the finite-difference solution of the eikonal equation discussed in Chapter 2. At every extrapolation step, the wavefields at the spatial locations of the wavefront of the incident waves are extracted from the backward extrapolated snapshot to fill the corresponding locations of the image space,

$$R^r(x,z) = u\Big(x,z,t=\tau_s(x,z)\Big), \tag{4.8}$$

where $\tau_s(x,z)$ is the excitation time of point (x,z). This imaging step in the reverse time migration is mathematically identical to the imaging procedure of the Kirchhoff scheme (3.24). In the case of the point diffractor as shown in Figure 4.2, the backward extrapolated energy focuses at the point diffractor position at the time of t_{im}, with t_{im} being the excitation time of the point diffractor corresponding to the incident wavefront which is shown in dashed curves in Figure 4.2. With time moving further backward, the extrapolated energy is defocused again. Nevertheless, as we are mainly interested in the combination of the imaged wavefront positions, only the focused energy at the extrapolation step t_{im} gives us the reflectivity information. When the reverse-time extrapolation proceeds back to the initial time of the shot, the complete shot image space will be filled. This shot image represents a partially illuminated reflectivity of the Earth.

The above illustration is simple as it only considers a single point diffractor with one shot. Nevertheless, as any complicated Earth model can be described as a continuum of diffractors, this simple illustration does represent our ability to process such complexity. The main point to be stressed is that each shot illuminates only

part of the model, and thus we need to optimally define this illuminated range. A proper definition is very important: a too narrow window will result in loss of reflectivity imaging, especially for steep reflectors; a too wide window will introduce extra computations. I use sliding image windows to help minimize computations while still retaining the migration aperture wide enough. Each sliding window is of the same depth range as the imaging depth interval. However, the lateral extent of each window is relatively difficult to determine, as it is dependent on the recording geometry of the shot, and especially on the velocity model. One ideal way to do this would be by using ray tracing to determine the possible reflection loci for the current shot; however, this is very expensive and impractical. I have found it practical to delimit the lateral extent based on personal insight and a rough ray tracing test. In general, the lateral extent of a migration shot should at least be wide enough to include the shot position and all the receiver positions. For areas where structural dips do not exceed 30 degrees, it is often good enough to pad 500 m on both sides of the current shot recording extent. For structurally more steep cases, it would be necessary to pad 100 m or even more on either side. In the case of the Husky–Alberta foothills case, I padded 800 m on each side. Figure 4.3 shows two such sliding windows (A_1–A_2 and B_1–B_2) for two neighboring shots A and B. The windows are of transparent boundaries laterally. A_1, A_2 delimit the lateral range of the migration shot A, while B_1, B_2 delimit the image space of B laterally. These neighboring windows generally share a considerable overlap and the final migration is simply a superposition of all such migration sliding windows.

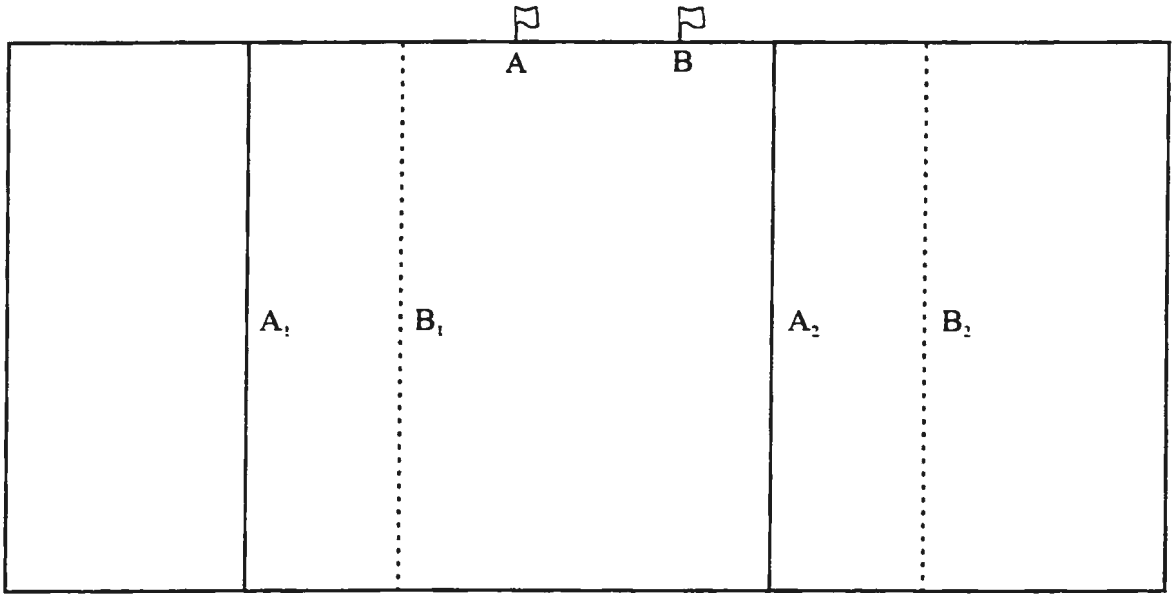

Figure 4.3: Sliding migration shot windows. Each window defines the image space of one shot gather.

4.2. Implicit interpolation of reverse-time migration

In the last section, I have shown that reverse-time migration essentially involves two steps: the reverse-time wavefield extrapolation and the subsequent imaging. The wavefield extrapolation is effectively provided by the finite-difference solution of the wave equation. This solution allows us to solve the past time instant wavefields from the future ones in a time backward sequence, as easily as solve the forward modeling problem in a time forward manner. During this extrapolation procedure, the recorded traces act as either known boundary conditions or source distributions to drive the finite-difference mesh. In this section, I will further demonstrate that the reverse-time extrapolation procedure also has the capability of interpolating the missing traces if the unaliased recordings are considered to be sources.

However, there is a stringent restriction on the recorded traces if the recordings are considered to be known boundary values: there is one trace at each grid point on the recording surface. Due to the nature of seismic acquisition, there are many cases where traces are missing, or not uniformly spaced along the recording topography. What is even more common is that the computational grid is much smaller than the recorded trace spacing, as the grid size is determined by the resolution requirement. In either of the above two cases, it is necessary to interpolate the missing traces at the surface grid positions using the original recordings. Figure 4.4 illustrates this practice of reverse-time migration by treating the recordings as known boundary conditions. Here a shot gather consisting of traces in heavy curves is displayed. This original record is both sparsely spaced with respect to the computational grid, and irregularly distributed as

the traces are not uniformly sampled on the recording topography. From this original configuration, the missing traces, shown as light curves, are interpolated. Commonly used interpolation techniques are simple linear interpolations, F–X interpolations (Spitz, 1991), and τ – p or τ – x methods (Claerbout and Nichols, 1991; Claerbout, 1992). Nevertheless, there are many cases where such interpolation schemes do not work well to create the missing traces.

In contrast to the above treatment of recordings, I take the recordings as known distributed sources to drive the wave equation backward in time, while the recording topography is still subject to its proper boundary conditions of a free surface. In this perspective, the original recordings are directly applied at the recording surface as distributed sources, which does not require that there be one trace at every grid point on the recording surface. Thus, there is no need for explicit trace interpolation — provided the record is originally not spatially aliased. This treatment is thus more like a wave equation modeling procedure using a finite-difference technique. The difference is that the source function now is time reversed and its duration is the total reverse-time extrapolation period. In fact, by using the finite-difference method, the reverse-time extrapolation itself will automatically build the missing traces. This interpolation of missing traces is simultaneously done by the wave equation during the reverse-time extrapolation of the gather. The traces are essentially created by saving the backward extrapolated wavefields at every grid point on the surface in each extrapolation step. Figure 4.4 schematically illustrates this new practice. Instead of interpolating the missing traces (light curves), the recorded traces (heavy curves), are directly applied to the recording surface as distributed sources, with each trace reversing its sample orders in advance. The missing traces are simultaneously

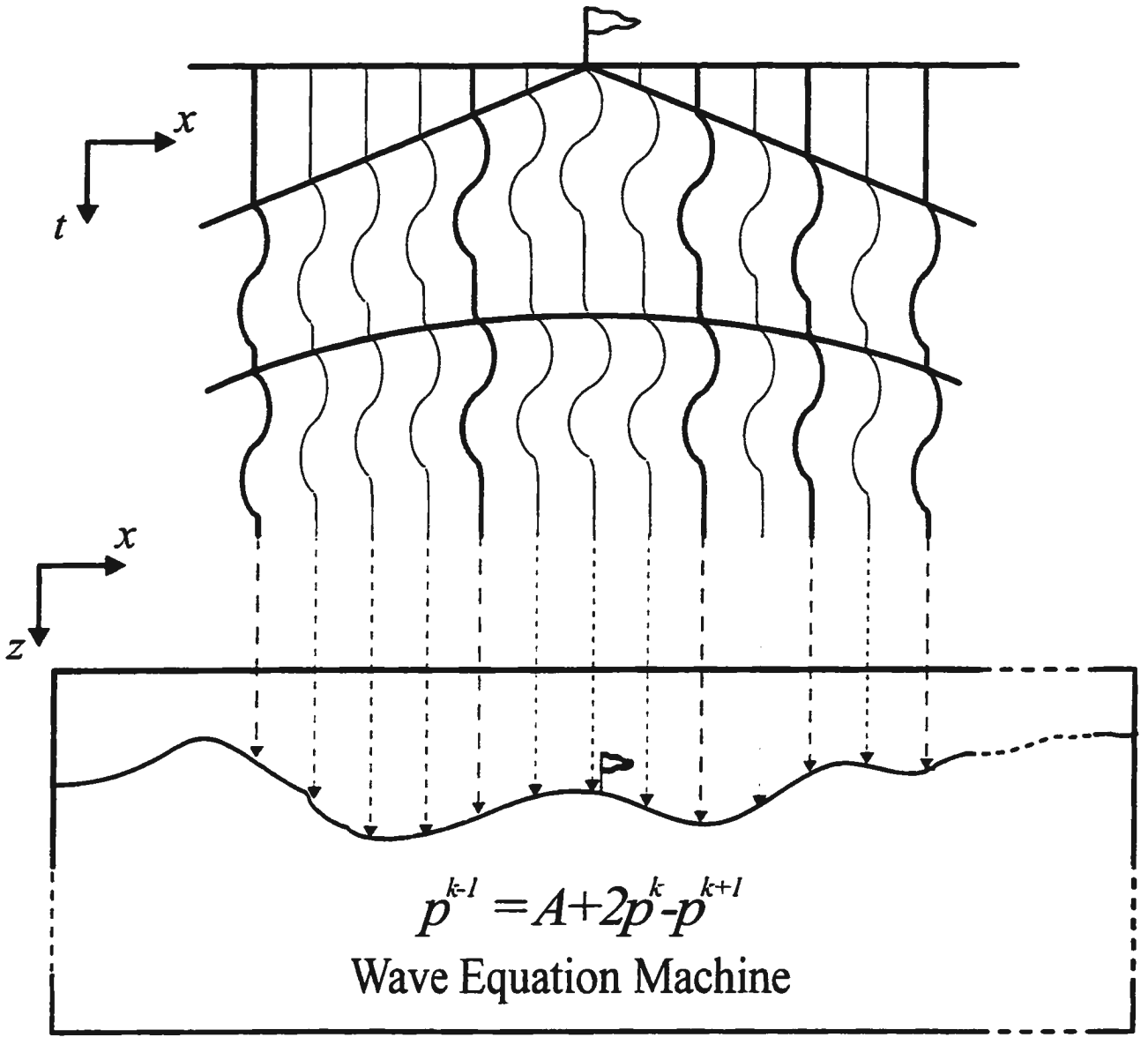

Figure 4.4: Two implementations of reverse-time migration. The original shot gather consists of traces in heavy curves which are sparse and irregular relative to the fine computational grid. The common solution is to interpolate the missing traces, in light curves, from the recordings, then apply the total data as known boundary values for migration. In contrast, the recordings can be directly applied as distributed sources at the recording topography, with the missing traces being built by the finite-difference solution of the wave equation itself during reverse-time extrapolation.

interpolated by the wave equation during the reverse-time extrapolation procedure.

To better illustrate this interpolation mechanism of the reverse-time migration, I take one specific shot, shot No.120, from the Marmousi model data set (Versteeg, 1993). This shot lies at the central part of the model where complicated faulting overlies a salt creep. It is evenly spaced with 25 m trace spacing. Five traces are randomly removed in order to make the record variably spaced. Figure 4.5 is the record for the migration input. This shot is migrated on a gridded velocity model of 12.5 m by 12.5 m. Figure 4.6 shows some selected snapshots taken during the reverse-time extrapolation of the record. As the snapshots show, at extrapolation time of 2.47 s (Figure 4.6a), the wavefields are limited to the upper central area of the section, while the recorded traces act as sources to drive the Earth model. As time steps backward, the recorded traces act as sources to propagate the wavefields to greater depths. At the time of 1.3 s (Figure 4.6d), the front of these excited wavefields has already reached every corner of the model. From this point on, though the recordings are still continuously acting on the surface, the characteristics of the wavefields become very complicated, mainly because of the complex nature of the Earth model and the corresponding complex interference patterns related to the wave propagations.

The migrated shot image is shown in Figure 4.7 which is almost the same as that produced when an interpolated shot gather of the filtered original is used as the input to the reverse-time migration program. Figure 4.8 shows the interpolated shot gather when the sparsely and unevenly spaced shot gather (Figure 4.5) is used as input. This gather is created by saving the extrapolation wavefield on each surface grid point in every backward extrapolation step. Comparing Figure 4.8 with Figure

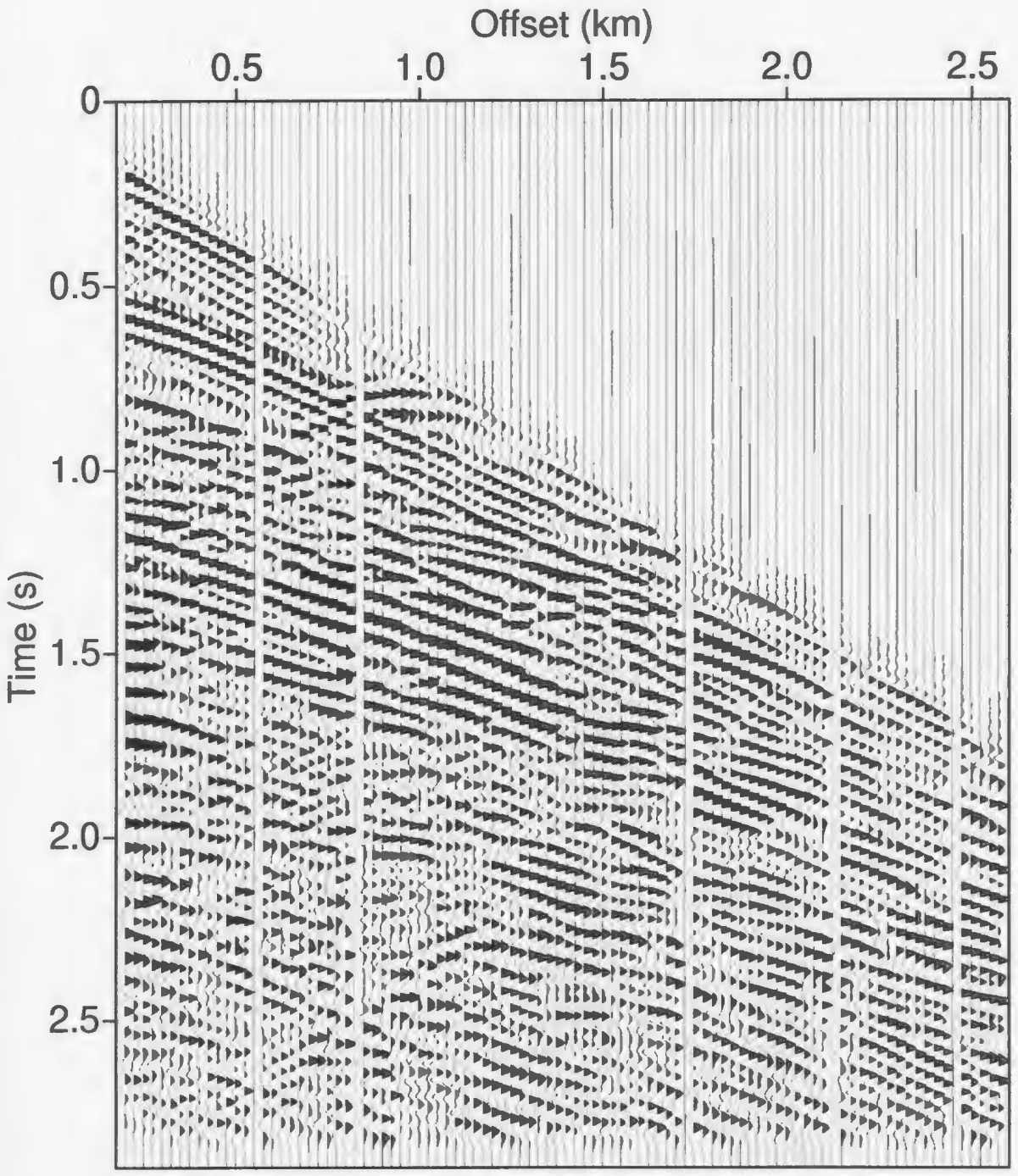

Figure 4.5: Shot record No.120 of the Marmousi model data with 5 traces randomly removed. The shot point is located at 6 km away from the left edge of the model (Figure 3.10), near the central part of the model where complicated faulting overlies salt creeping.

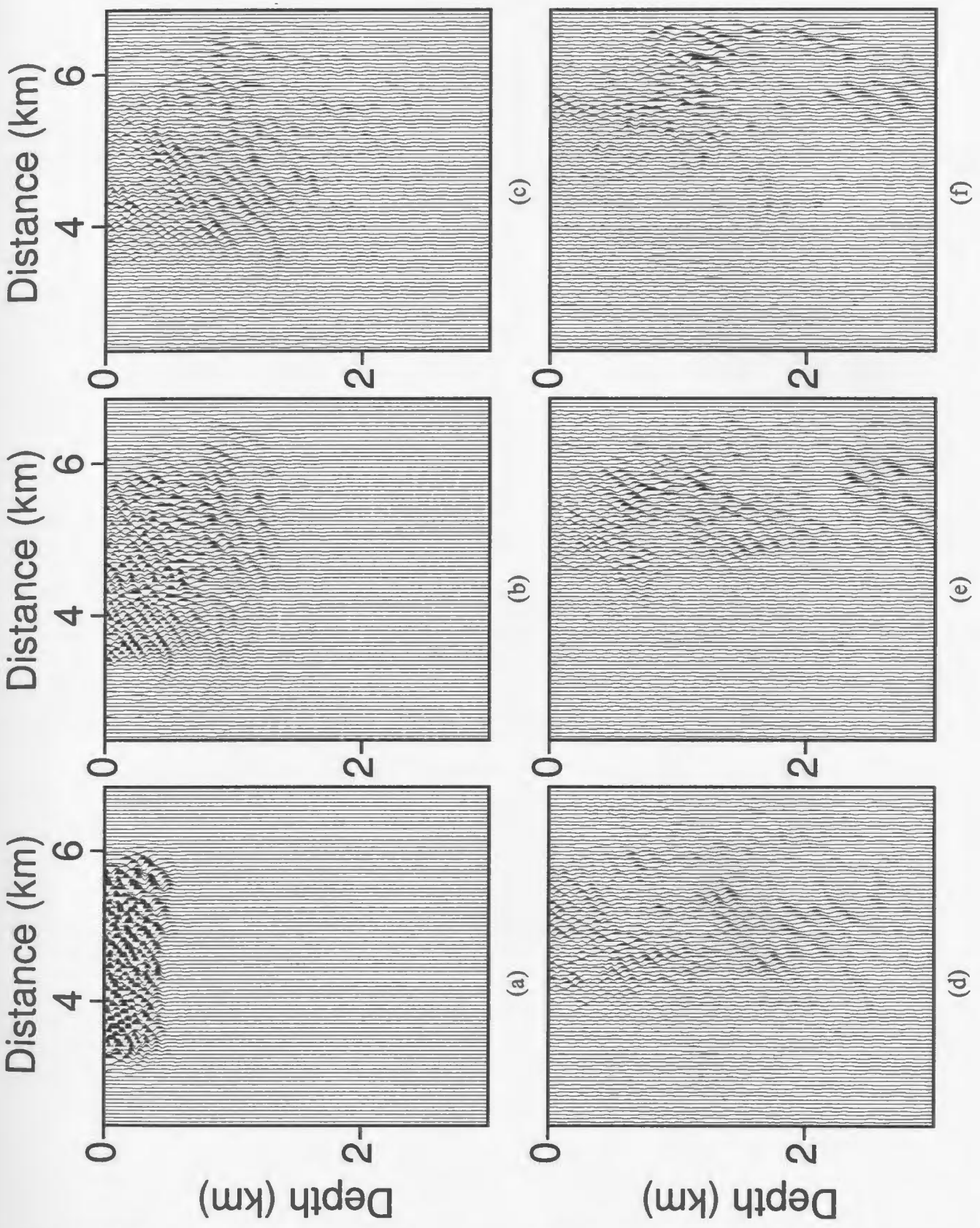

Figure 4.6: Selected snapshots taken during the reverse-time migration of the record No.120. The snapshots are sequentially taken at time of 2.47 s (a), 2.08 s (b), 1.69 s (c), 1.30 s (d), 0.91 s (e), and 0.52 s (f).

4.5, it is observed that the shot gathers are essentially identical. The only difference is that the trace spacing now is halved, and there is noise introduced prior to the first arrivals. This noise arises from numerical errors in discretization, the limited recording aperture, and also due to the finite length of computer words. From the above comparisons, it is clearly demonstrated that trace interpolation of the input gather is already implicitly included in the reverse-time migration just as is the static correction (McMechan and Chen, 1990; Reshef, 1991).

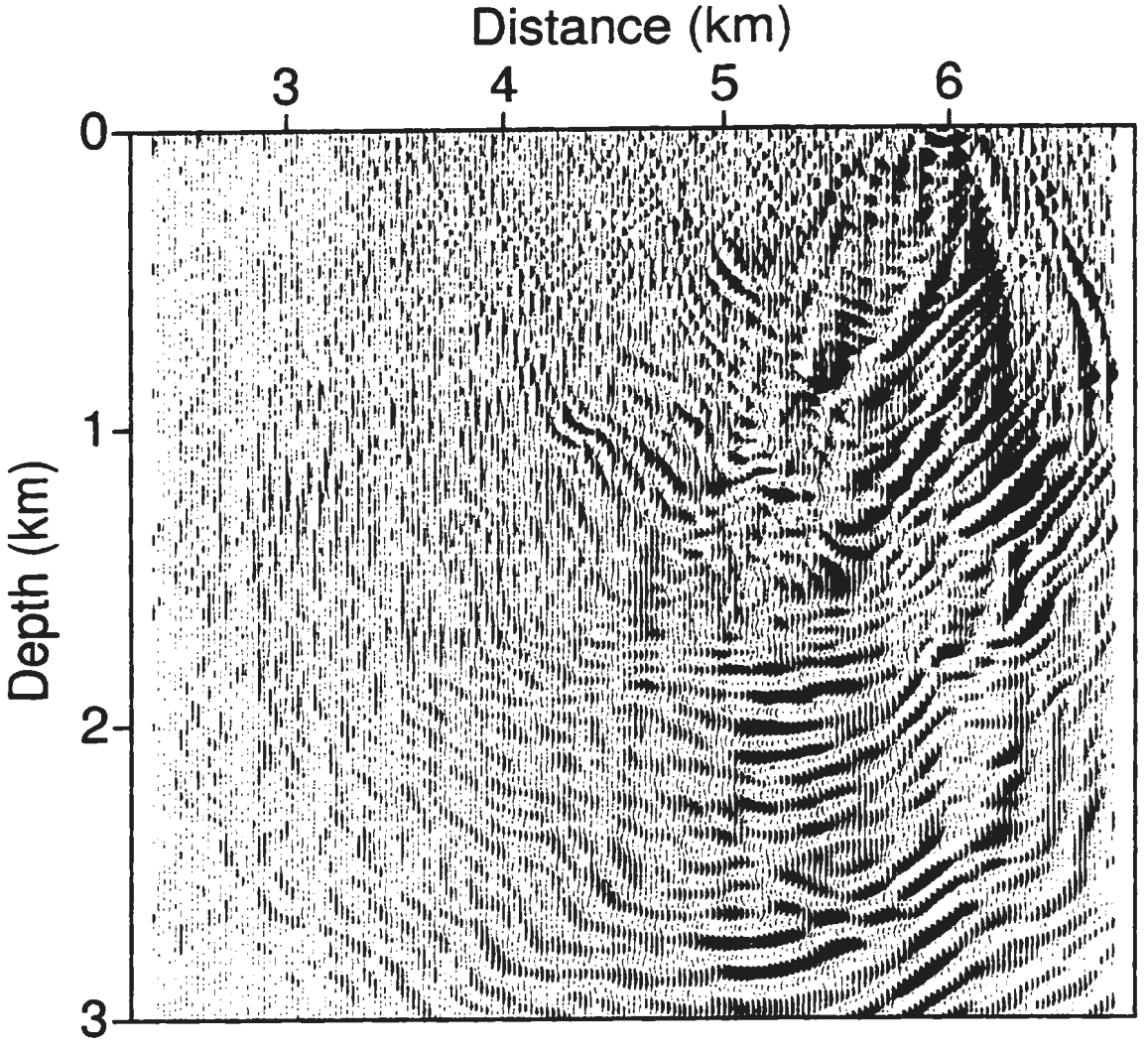

Figure 4.7: Migration shot image of the record No.120 from the Marmousi model.

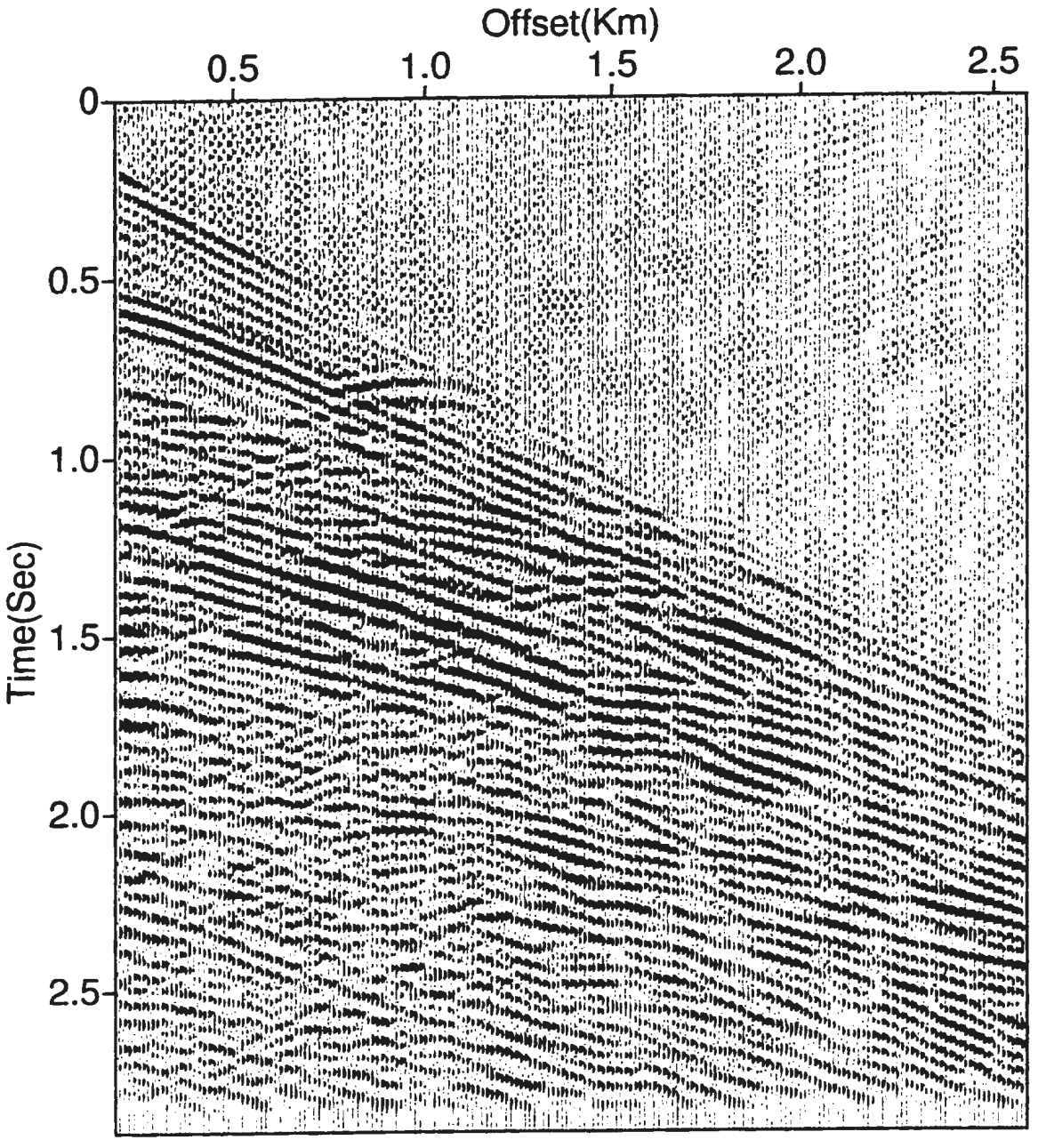

Figure 4.8: The interpolated shot record No.120 created by the reverse-time migration itself.

The above model data example demonstrates very well the mechanism of the interpolation implicit in the reverse-time migration. Now I will show a real data example, the Husky–Alberta foothills line. The data is acquired over a highly variable topography which is shown in Figure 4.9. Although there are significant bursts of abnormally high amplitude and serious static problems due to the rough topography and near surface velocity heterogeneity, overall this line exhibits good signal quality. From the perspective of applying the reverse-time migration technique, the traces in the original gathers are nevertheless sparsely sampled, and also somewhat irregularly distributed along the survey line, and are thus not ideal for the direct application.

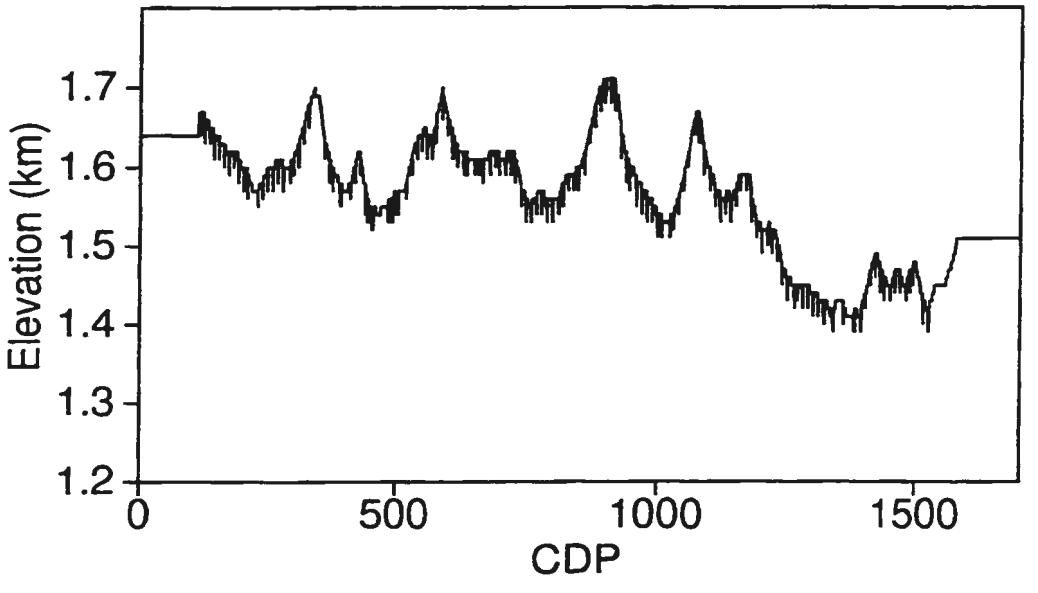

Figure 4.9: Topography of the Husky–Alberta foothills line. The highlighted part of the topography is where the acquisition was completed.

To investigate the interpolation mechanism implicit in the reverse-time migration for the real data, consider a specific shot gather, record 142. It is edited for noisy

traces, low-pass filtered, and shown in Figure 4.10 with most traces 20 m apart. Using a velocity model with 10 m by 10 m grid spacing which is iteratively built based upon structural information and migration velocity analysis, this shot gather is reverse-time migrated. Figure 4.11 shows six snapshots during the reverse-time migration of the shot. At an extrapolation time of 2.954 s (Figure 4.11a), just immediately after the initialization of the migration, the snapshot basically reflects the fact that the recorded traces are simultaneously exciting the mesh at the recording topography. At time 2.584 s (Figure 4.11b), the wavefront shown in the first panel has propagated to a greater depth while the recordings are still actively exciting the topography. From that stage on, we can see that propagated waves form quite understandable patterns due to the interference of waves propagating from different sources.

It is commonly assumed that the reverse-time migration procedure of a single experiment will simulate the wave propagation patterns that occur in the corresponding forward problem. This is usually true in the case of stacked data. However, this is not the case for shot gather migrations, as we can not expect to have these patterns of wavefields in the corresponding snapshots in forward modeling the data with the single source. Furthermore, these patterns are very different from what we have observed in the Marmousi case. The complicated patterns of the wavefields in the Marmousi example are mainly due to the velocity model complexity, especially its steep faults and the salt creep while the relatively identifiable patterns in the current case arise from the relatively gently dipping nature of the Earth. With time marching further backward, waves propagate into deeper parts of the Earth, with all wave propagation phenomena occurring simultaneously. One striking feature in all the snapshots is the continuous action of the recorded traces as distributed sources on the topography. In

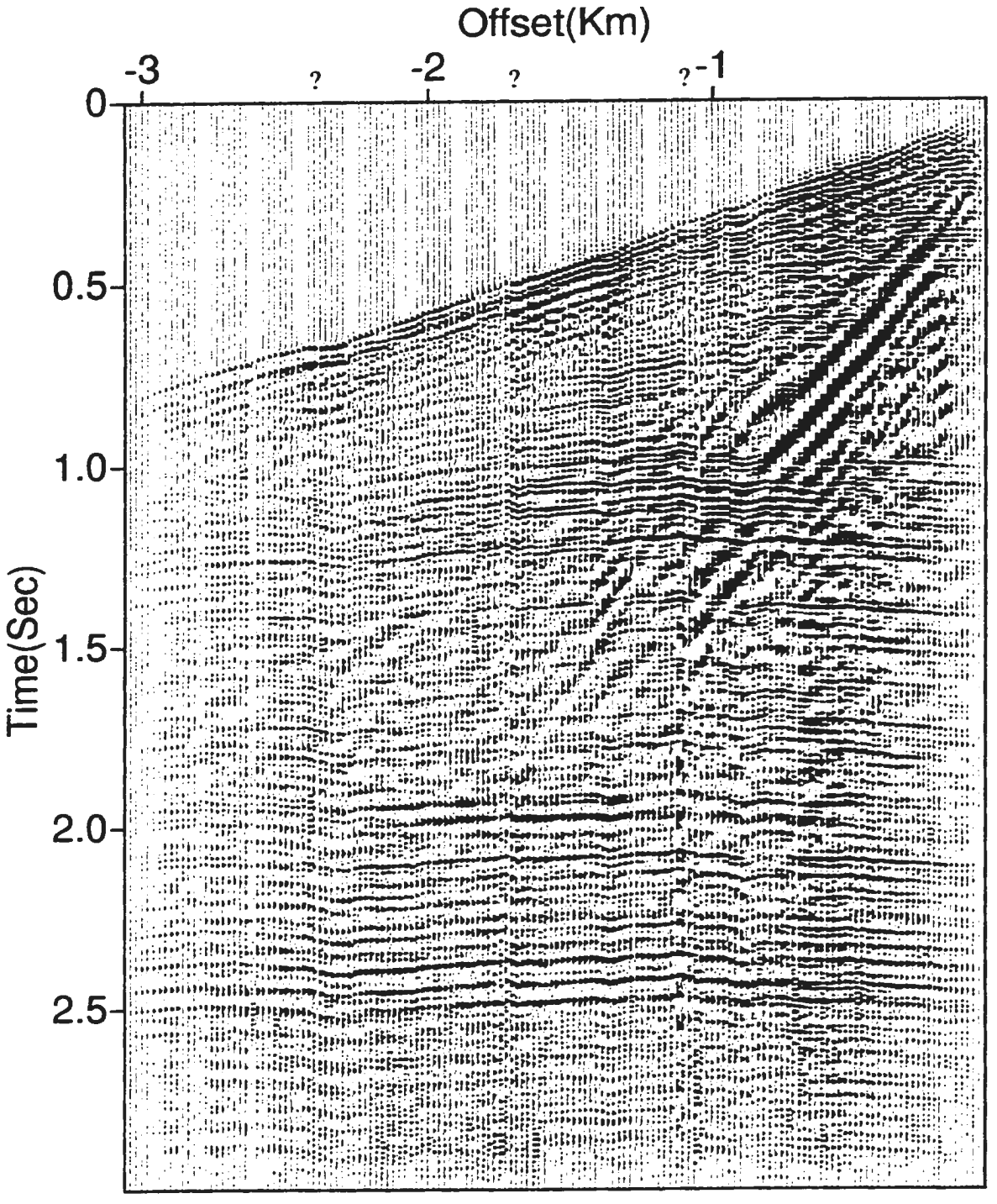

Figure 4.10: The conditioned original shot record No.142 of the Husky–Alberta foothills data set. This record is near the end of the line corresponding to high CDP numbers shown in Figure 4.9. The question marks identify the areas where problems such as amplitude variation exists.

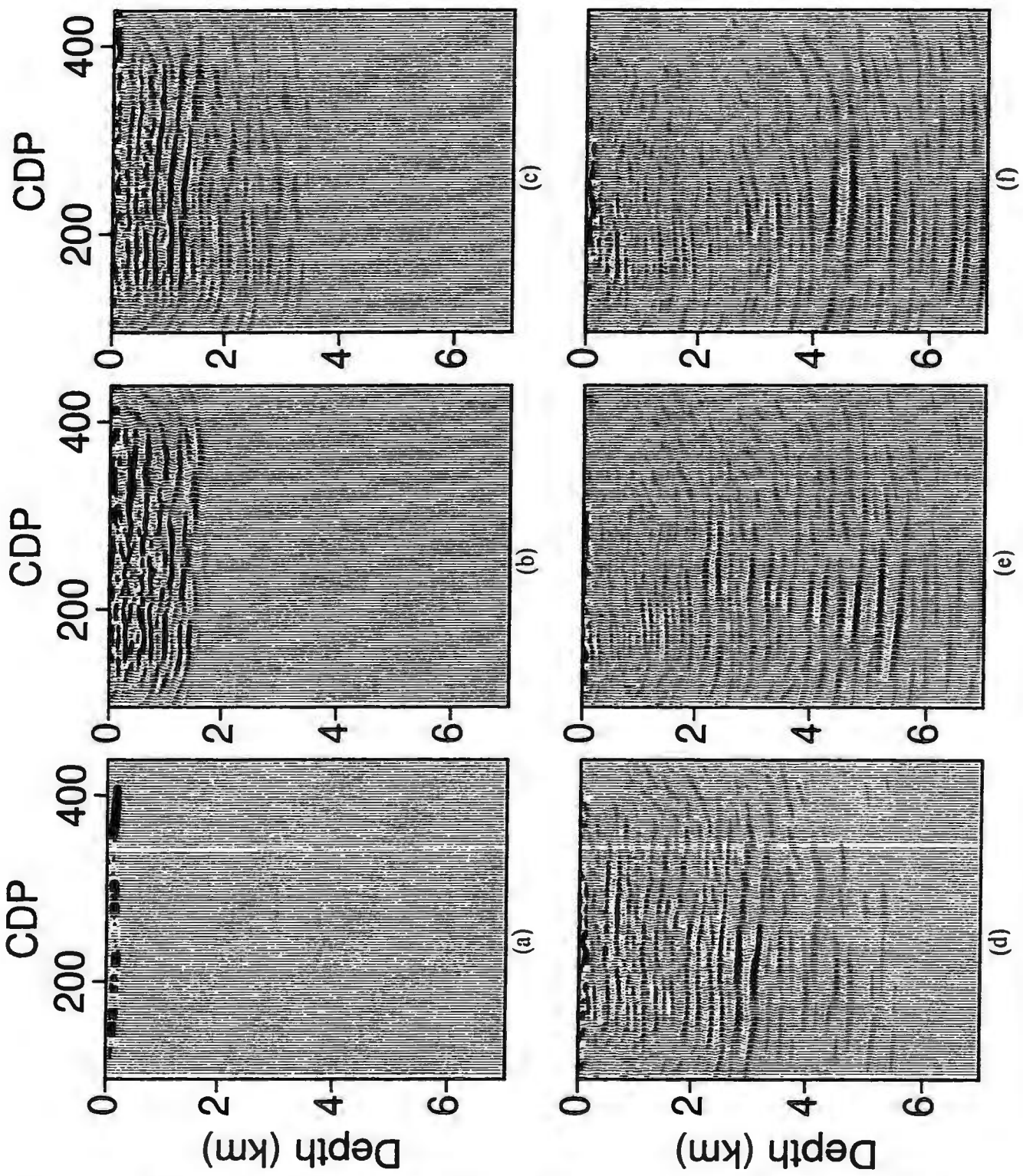

Figure 4.11: Snapshots during the reverse-time migration of the record shown in Figure 4.10. The snapshots are sequentially taken at time of 2.954 s (a), 2.584 s (b), 2.215 s (c), 1.846 s (d), 1.477 s (e), and 1.108 s (f).

fact, these observed wavefield patterns are basically similar to those produced by a forward modeling procedure with a spatially limited source distribution located on the topography. The only difference from the modeling problem is that the sources are acting continuously during the observation time.

In Figure 4.12 I show the corresponding shot migration image. As shown by Zhu and Lines (1996), this result is basically similar to that obtained by the prestack Kirchhoff depth migration algorithm which I discussed in the last chapter. In this migration, the shallow dipping formations are properly imaged. An interface is clearly imaged in this single shot migration as a good reflector at a depth of 2.8 km to 3.4 km. This interface expresses itself as a relatively gentle boundary in the left part, then as a right dipping refracting boundary because of its high acoustic contrast. This good imaging at least confirms the fact that the reverse-time migration algorithm can migrate an unevenly and sparsely spaced shot record with the resulting migration image similar to that obtained with prestack Kirchhoff migration. That is to say, reverse-time migration is directly applicable to shot records which were previously considered to be too sparse and irregular. In fact reverse-time migration tries to recover the nature of wave propagation from the source using the recorded shot gather. This is obvious by noticing the overall similarity between the interpolated shot gather which is shown is Figure 4.13, created during the reverse-time extrapolation procedure, and the original gather, Figure 4.10. The traces in Figure 4.13 are now evenly spaced on the recording topography with trace spacing of 10 m. Despite the overall similarity, there are still differences between the interpolated and the original. In the area before first breaks, there is noise in the interpolated gather due to the limited recording aperture and the approximation of the wave equation

by finite differences. In addition, there are several places labeled by question marks where the interpolation procedure does not seem to work well. My explanation of this phenomenon is that there exist problems in the original record. As we can see, there exist abrupt amplitude changes between neighboring traces, in addition to the noisy nature of the original record, as shown in Figure 4.10. These are not what we expect from a physical point of view. This variability between traces introduces additional sources of noise during the reverse-time extrapolation procedure. These problems can be largely reduced by balancing the shot gathers before migration, if the true amplitude is not critical in the final migration results.

The above tests clearly demonstrate that there are interpolation mechanisms implicit in the prestack reverse-time depth migration procedure. In fact, such mechanisms work equally well for stacked data. They are also valid in 3D. Figure 4.14 is a salt intrusion velocity model (courtesy of Phil Bording, University of Texas at Austin). Figure 4.15 shows a synthetic zero offset seismic section from this salt model. The trace spacing of the synthetic data is 40 m. Figure 4.16 shows the reverse-time migrated section with a grid spacing of 40 m using only every second trace of the stacked section. This would not be able to be directly migrated from the previous viewpoint of reverse-time migration. Nevertheless, this migration still provides a sharply defined image of the salt body. In fact, there is little difference noticeable between this result and the corresponding reverse-time migrated section, shown in Figure 4.17, using the whole stacked data. Thus, this migration (Figure 4.16) of half the stacked data set, though sparse compared to the computational finite-difference grid, still gives a reasonable recovery of the subsurface model, in both the lower part and the upper part of the model.

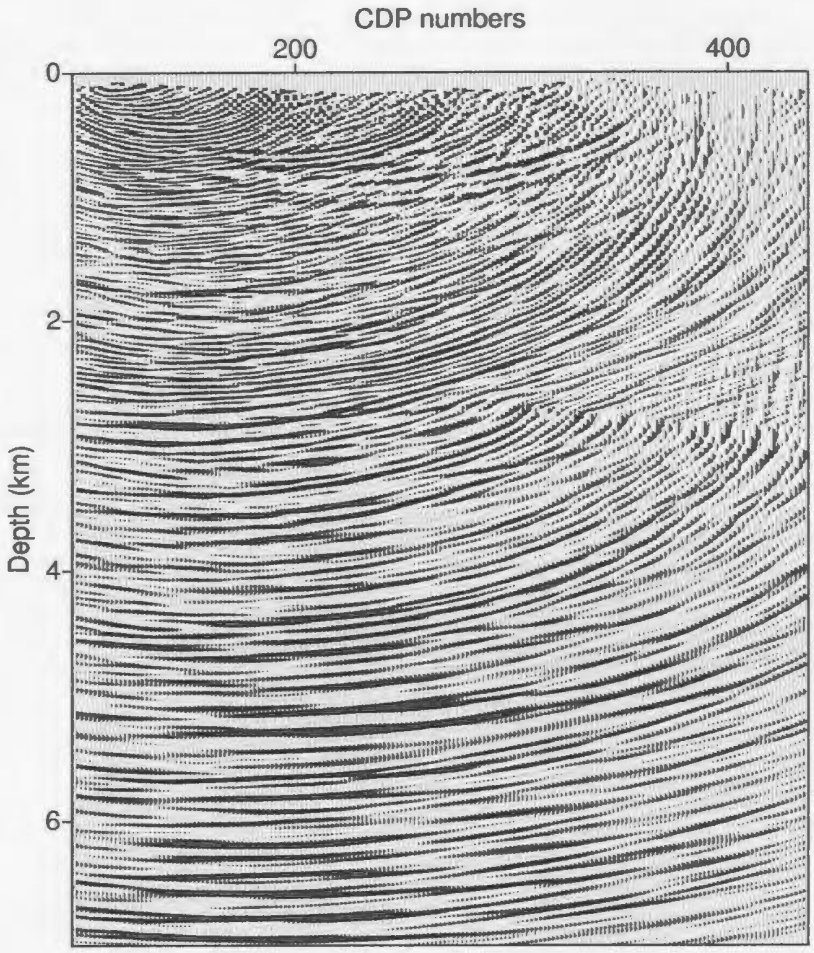

Figure 4.12: Migration image of the shot No.142 of the Husky–Alberta foothills line.

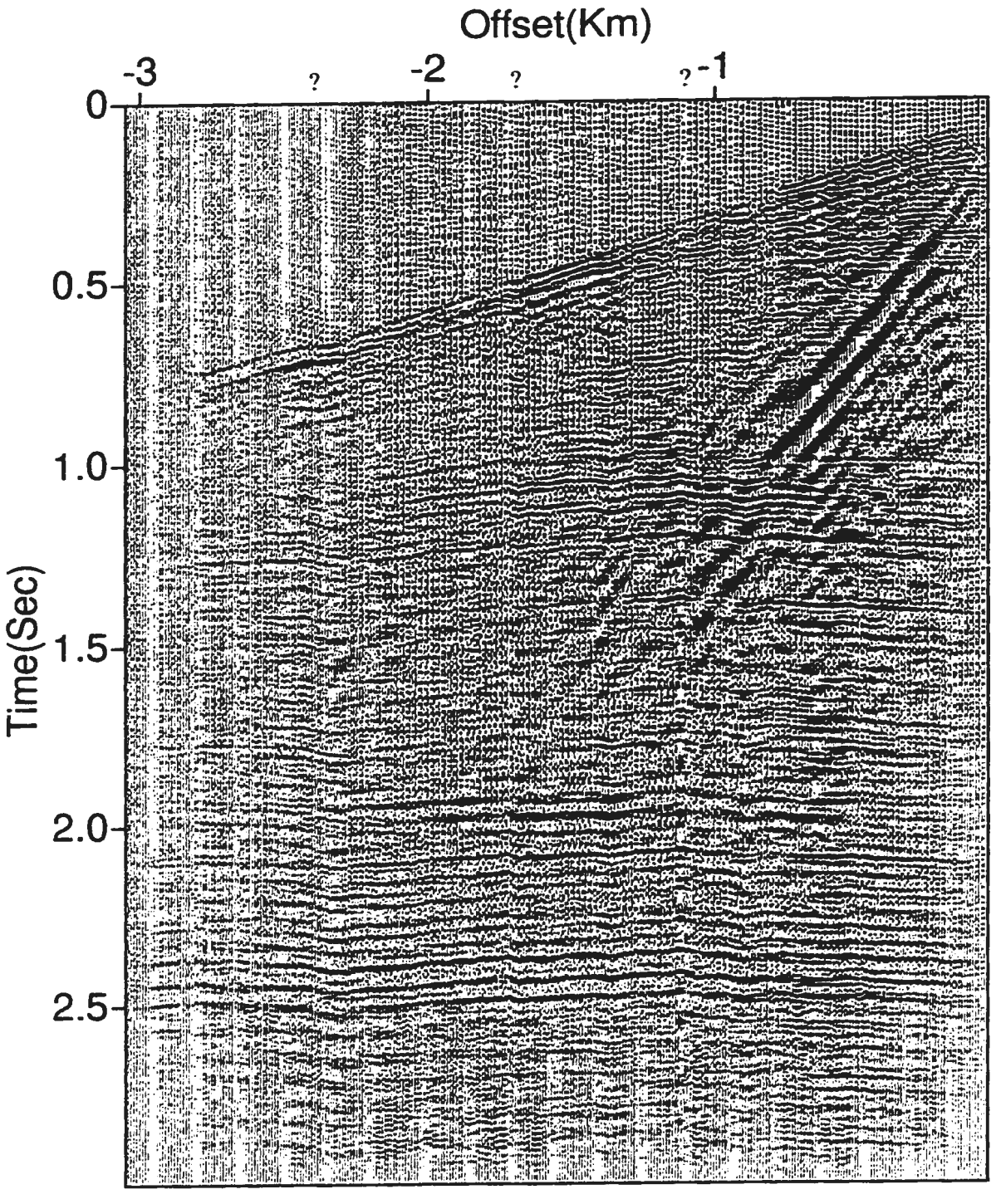

Figure 4.13: Interpolated shot record No.142 of the Husky–Alberta foothills line. Compared to the original shown in Figure 4.10, there is extra noise introduced in the record, especially around places labeled with question marks.

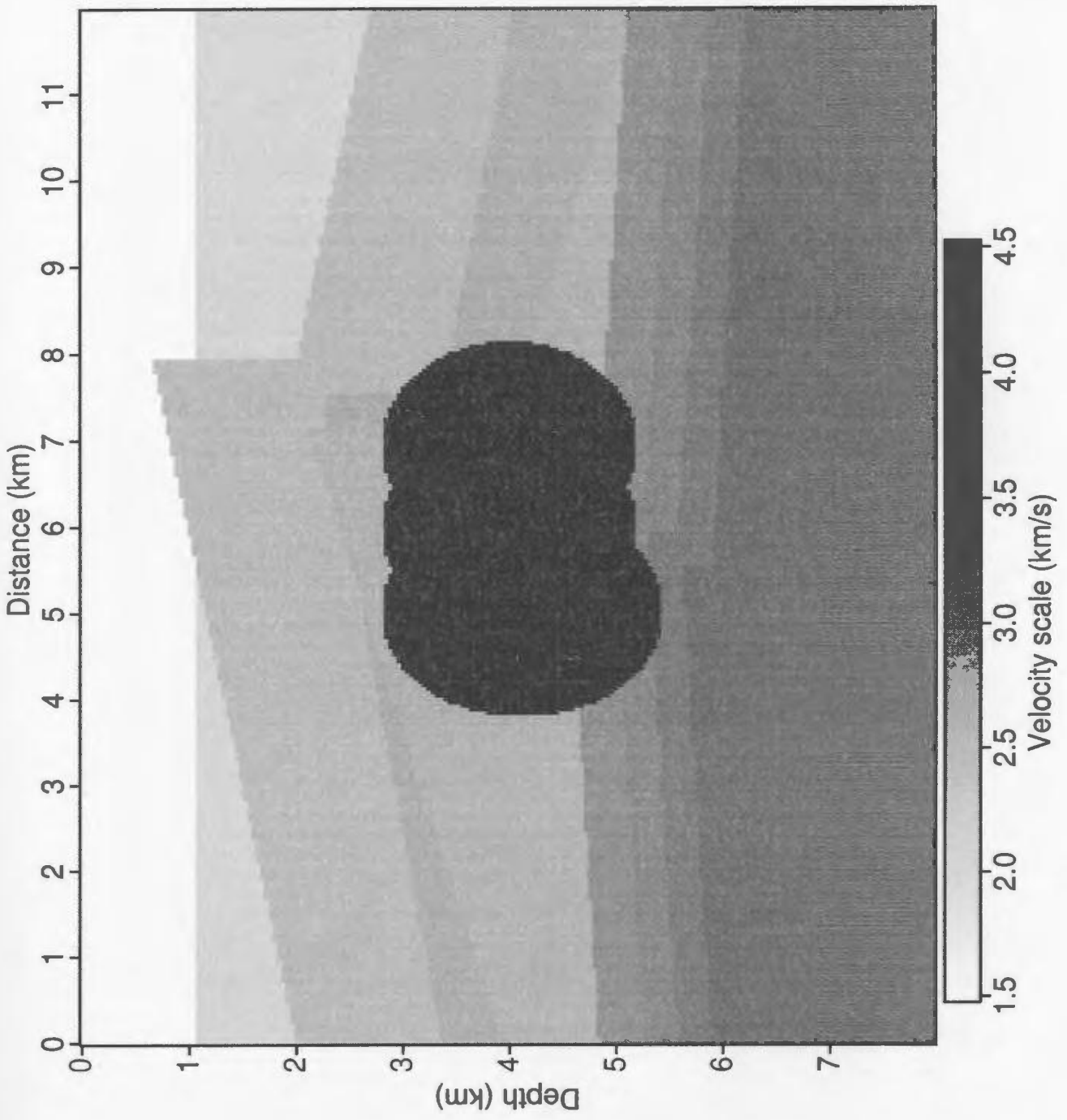

Figure 4.14: Salt intrusion velocity model with grid size of 40 m by 40 m.

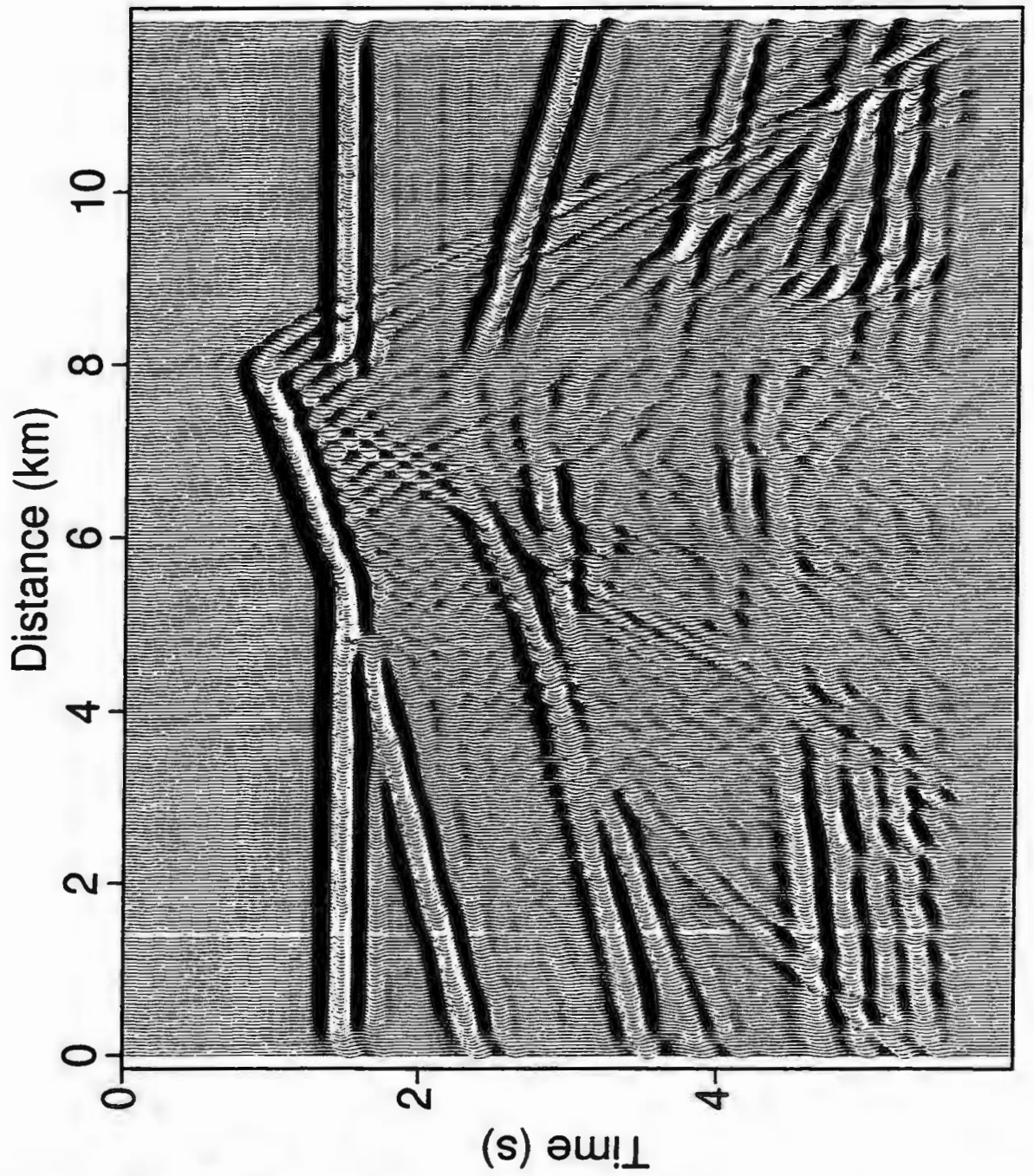

Figure 4.15: Zero offset section from the salt intrusion model shown in Figure 4.14. The CDP spacing is 40 m. This simulated stacked section has little resemblance to the salt model.

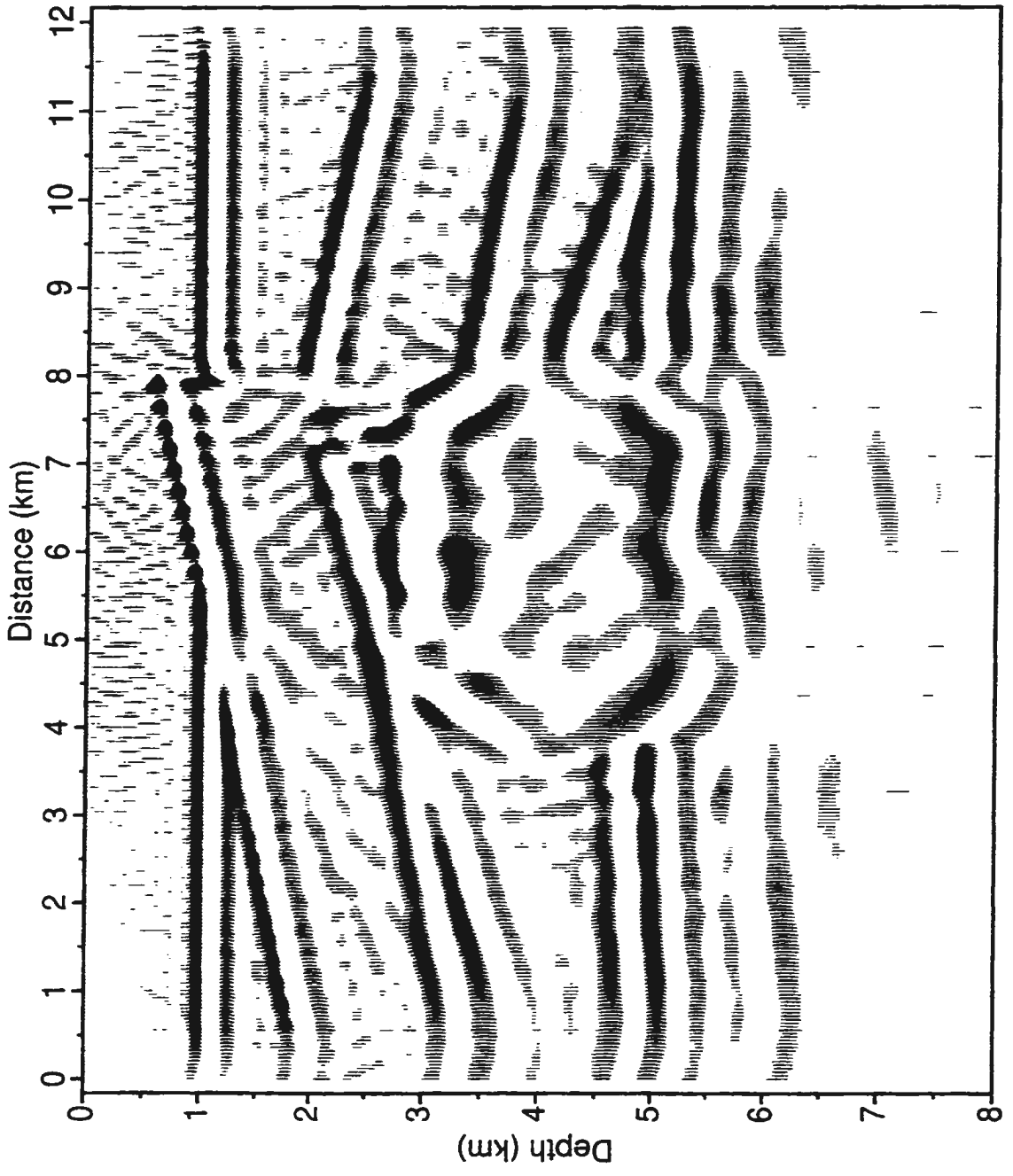

Figure 4.16: Reverse-time migration of the salt intrusion synthetic section with a computational grid of 40 m by 40m. Only half of the CDP traces are used in migration. Thus, there is one trace missing at every second surface position.

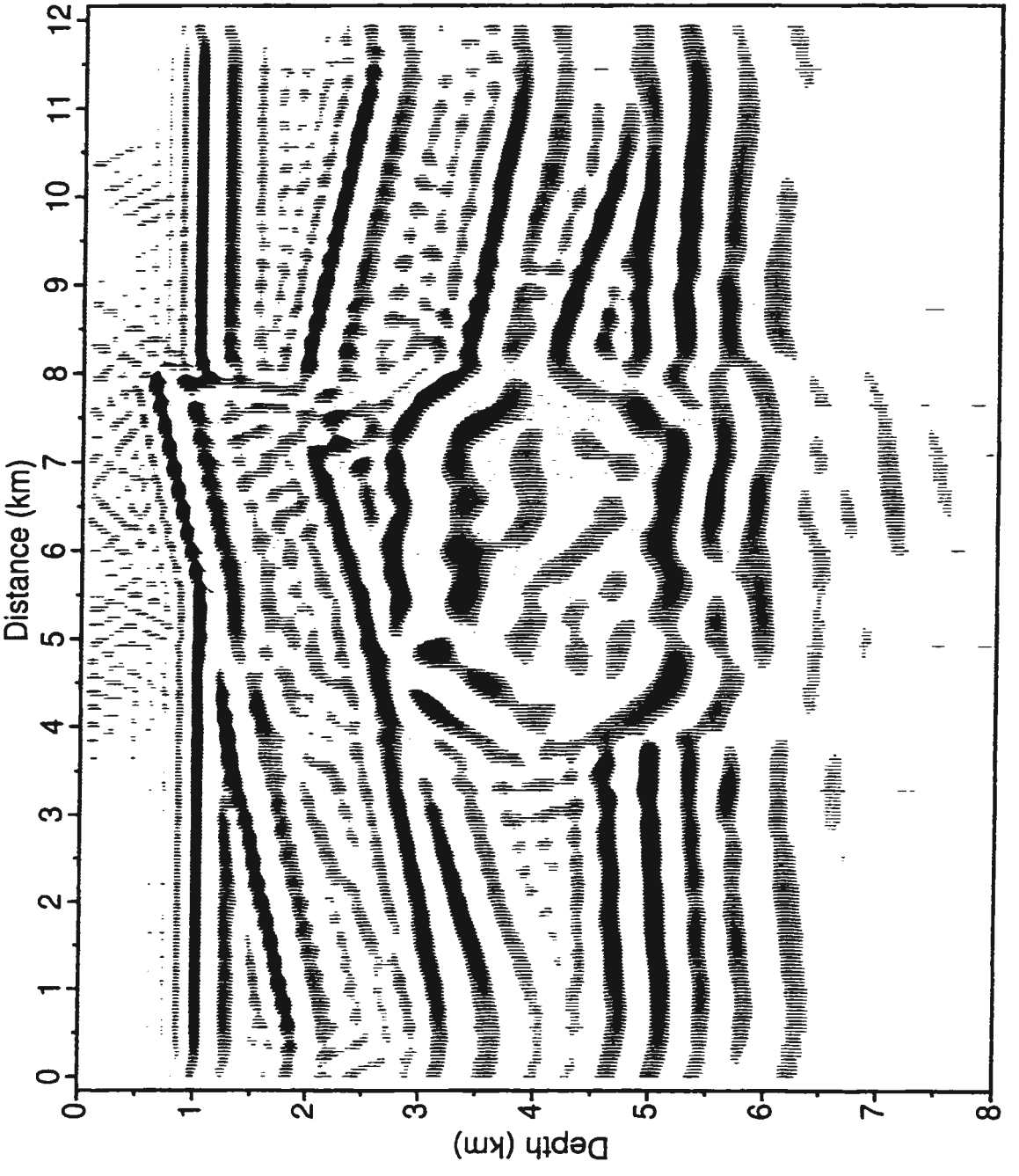

Figure 4.17: Reverse-time migration of the salt intrusion synthetic section with a computational grid of 40 m by 40m. All the CDP traces are used in migration.

This example again demonstrates that reverse-time migration of sparse stacked sections relative to the fine finite-difference grid works equally well as if the missing traces had already been interpolated from the original traces. This implicit interpolation of the reverse-time migration is essentially based upon the ability of the wavefield to heal itself during its propagation (Zhu and Lines, 1997). Thus, in such cases, the interpolation of missing traces can often be bypassed without much sacrifice of the accuracy of the final migration results.

4.3. Prestack reverse-time migration without interpolation — the Marmousi model example

In the last section, I have shown that reverse-time migration can be directly applied to spatially sparse and irregular data sets without a priori interpolation of the missing traces. These missing traces are implicitly interpolated during the reverse-time extrapolation procedure with unaliased irregular input records. The interpolation is essentially based on the ability of the wavefield to "heal itself" during propagation. I have also shown that this mechanism applies equally well to 2D, 3D, post-stack or prestack migrations. In this section, I will demonstrate the effectiveness of this treatment on migration of the Marmousi model data.

As discussed before, the Marmousi data set consists of 240 shots with every shot record consisting of 96 traces. The data set models a marine seismic line with group

intervals of 25 m, and shot spacing of 25 m. The traces are thus uniformly distributed at the water surface. Figure 4.18 shows some selected shot gathers from this model data. The shots contains many non-hyperbolic reflections and back-scattered energy. This is one good indicator of the necessity for prestack depth migration to correctly image the data. This acquisition geometry results in a CDP spacing of 12.5 m, the distance between sampled subsurface points. Ideally, migration should match this spatial resolution. Hence, a velocity model of 12.5 m grid spacing is used in migration. With such a fine gridded velocity model, the original model data are sparse, though regular, as there is one trace missing at every second surface grid point. Nevertheless, each shot record, is directly migrated without a priori interpolation, using the reverse-time migration algorithm by taking the traces as distributed sources on the surface. Figure 4.19 shows some migrated shots which correspond to the gathers in Figure 4.18. The imaged traces in each migrated shot are now equally spaced with distance identical to the CDP spacing.

Figure 4.20 shows the final migrated section of the Marmousi model data obtained by the reverse-time migration of the shot gathers. In this migration, almost all the main features of the model have been imaged properly: the dipping layers are correctly positioned with respect to their true spatial locations; the steep fault planes are very well imaged; and the subsalt anticline is reasonably well resolved. This result is comparable to other published results (Versteeg, 1993; Gray and May, 1994: Nichols, 1996) and also to the results in the last chapter. This successful imaging of the Marmousi data indicate that reverse-time migration could be directly applied to sparsely sampled seismic records, as long as the original records are not spatially aliased.

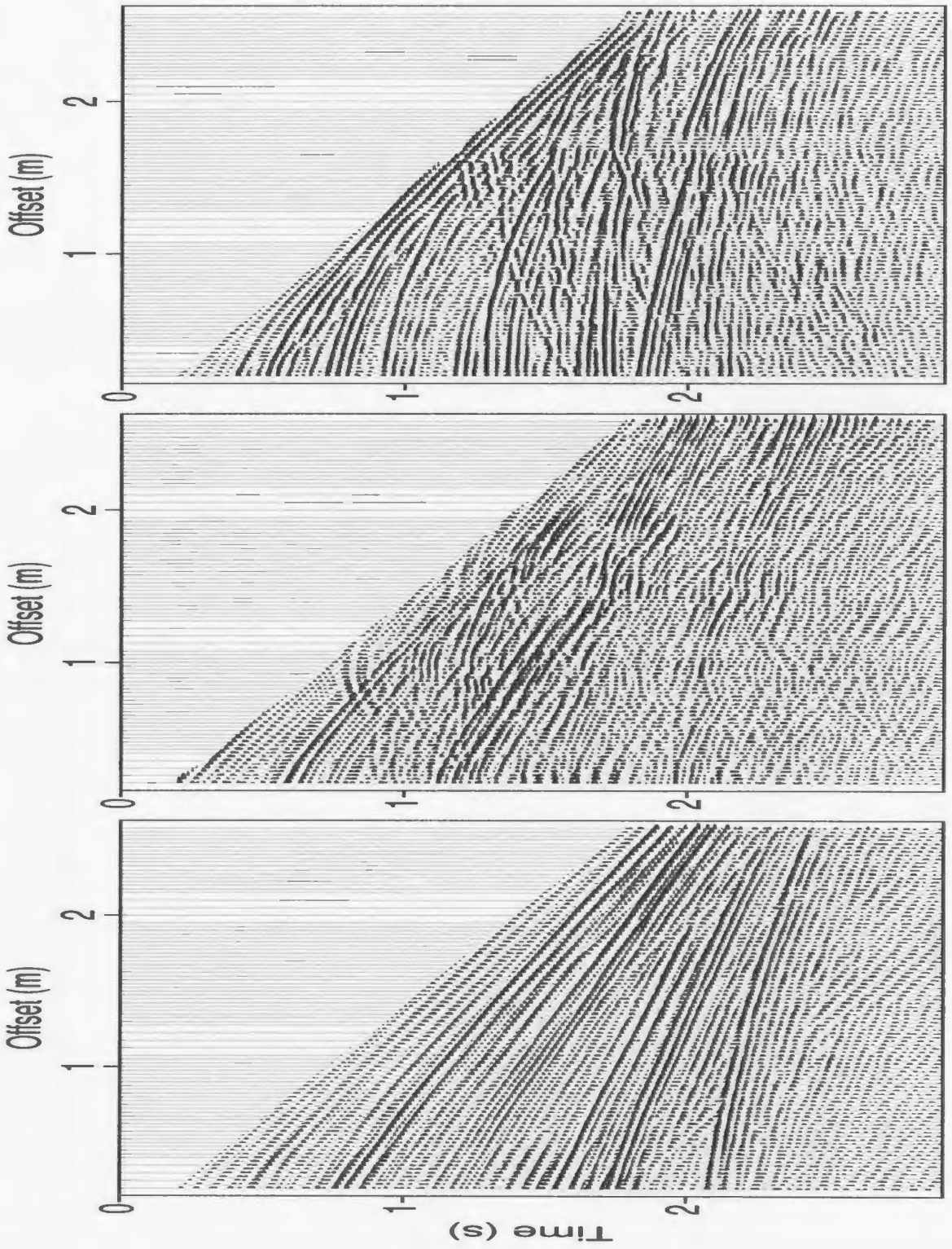

Figure 4.18: Selected shot gathers from the Marmousi model data.

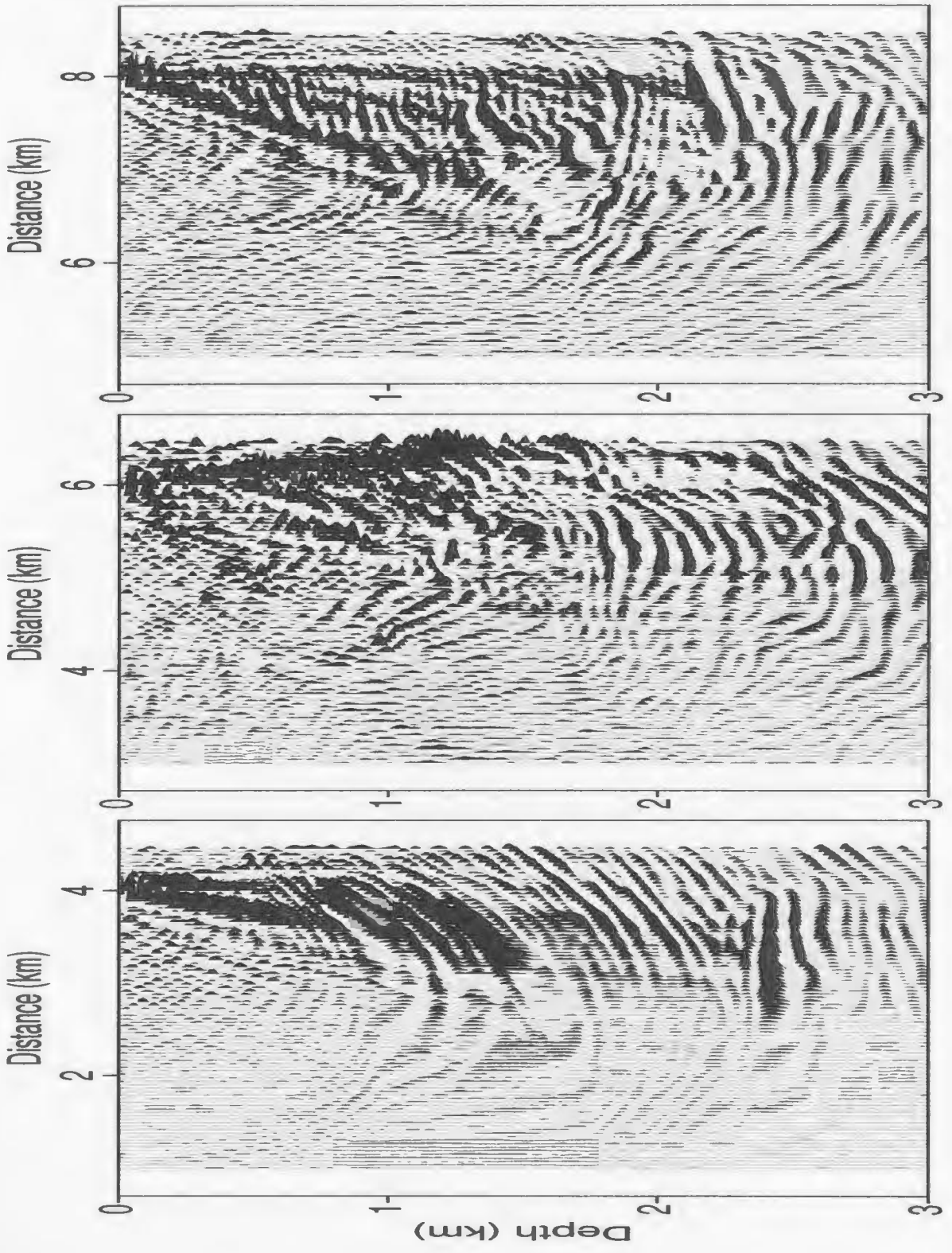

Figure 4.19: Selected migration shots of the Marmousi model data by prestack reverse-time migration.

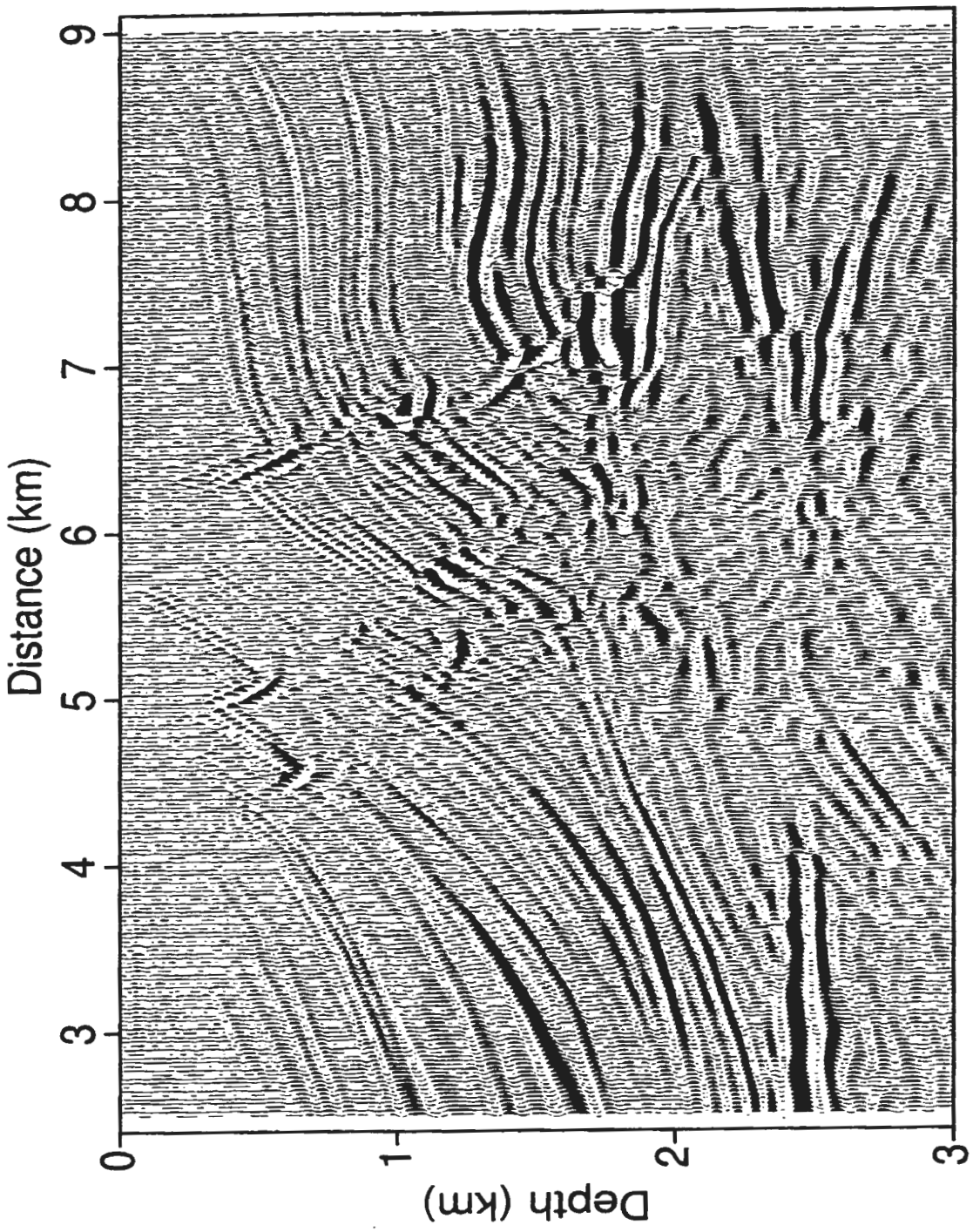

Figure 4.20: The final migrated section of the Marmousi model data by prestack reverse-time migration.

4.4. Prestack reverse-time migration without interpolation — the Husky–Alberta foothills example

In this section, the reverse-time migration will be applied to the Husky data set from the Alberta foothills. In this foothills line, there are 143 shots. The shot spacing is variable because of the difficulties of properly locating the shot holes in the rough mountainous terrain. The normal shot spacing is 100 m with a maximum of about 300 m (Figure 4.21). For this acquisition, there are nominally 300 traces per shot. At the start of the line, the spread rolls into the live station range so that the number of traces per shot gather increases from 150 to 300. At the end of the line, the spread remains stationary while the shot rolls out. Figure 4.22 shows the trace numbers in each shot. Compared to the shot spacings, the receiver groups are generally spaced regularly with little variation. Figure 4.23 is a plot of the group spacing of a representative shot. Thus, this acquisition would sample the subsurface with a CDP spacing of 10 m. However, the subsurface is not uniformly sampled. Figure 4.24 shows this nonuniform nature of the stacking fold.

To achieve image resolution at the CDP spacing, a velocity model with a grid size of 10 m by 10 m (Figure 4.25) is used to migrate the whole seismic line. The velocity model is built through an interpretive imaging process which consists of iterative prestack depth migration, velocity analysis and geologic interpretation. Though the traces are sparsely and irregularly distributed in space with respect to the grid, the reverse-time migration is performed directly using the raw records as distributed

sources. Figure 4.26 shows one representative shot from the original line. It is basically a split spread experiment. Two traces are edited as dead because of the signal quality. Overall the record exhibits relatively good quality. The reverse-time migration of this record is displayed in Figure 4.27.

This shot migration is quite complicated and is much more difficult to interpret on its own. This is because each shot only illuminates part of the Earth, and its illumination extent is not easily definable. Its interpretation would be relatively easier by combining with the final migrated section which is shown in Figure 4.28. Although we have run many tests on this foothills line at MUSIC (Wu et al., 1996; Lines et al., 1996; Zhu and Lines, 1996, 1997), Figure 4.28, produced by reverse-time migration without a priori interpolation is essentially identical to the best previous result. Because at this final stage of imaging this data, the migrated section and velocity model are geologically consistent in many respects, the geological interpretation of this imaging is essentially the same as the velocity model (Wu et al., 1996)

The successful migration of this complicated foothills line using the reverse-time migration clearly demonstrates that trace interpolation can be by-passed in many applications. In fact, as I have shown in this chapter, these missing traces are implicitly interpolated during the reverse-time extrapolation procedure. The interpolation is nevertheless essentially based upon the self-healing mechanism of the wavefield by interference during backward extrapolation (Zhu and Lines, 1997).

4.5. Summary

In this chapter, I have developed another implementation of reverse-time migration by treating the recordings as sources. I have also illustrated that reverse-time wave equation migration has the capability of implicitly interpolating missing traces whenever the unaliased input gathers are sparsely and irregularly sampled. The implicit interpolation was shown to be due to the wavefield self-healing mechanism through constructive interference of propagating wavefields. This new implementation of reverse-time migration was applied to migrate prestack seismic data from the Marmousi model, and the Husky–Alberta foothills line. Both the synthetic and the real data applications demonstrated that this prestack reverse-time migration technique was directly applicable to sparsely and irregularly sampled seismic records without the need of prior interpolation of missing traces as long as the recordings are not aliased.

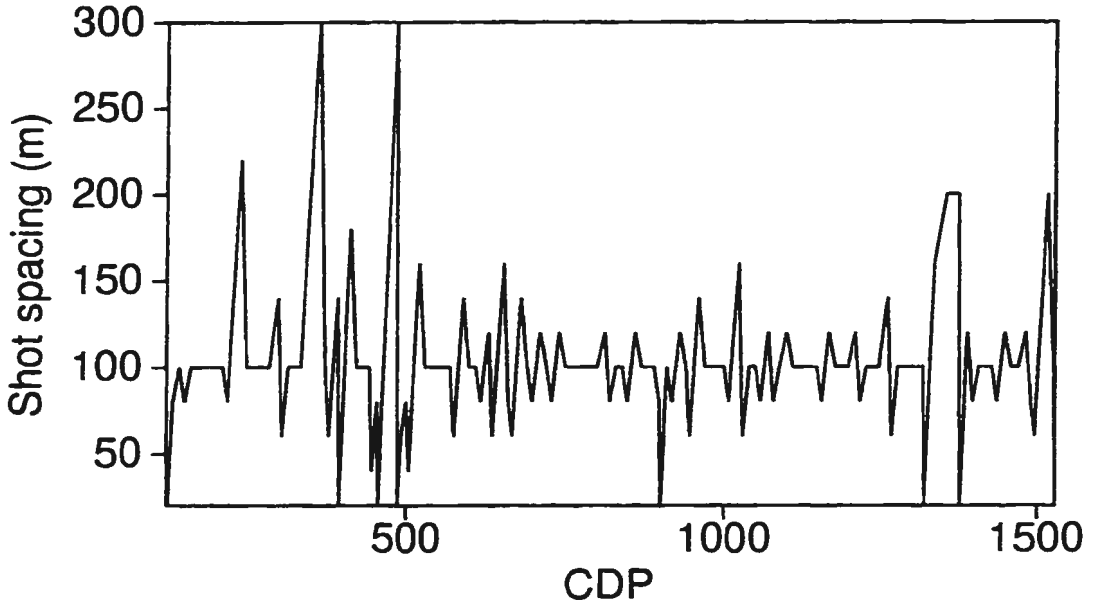

Figure 4.21: Shot spacing of the Husky–Alberta foothills line is varied. The largest spacing is about 300 m.

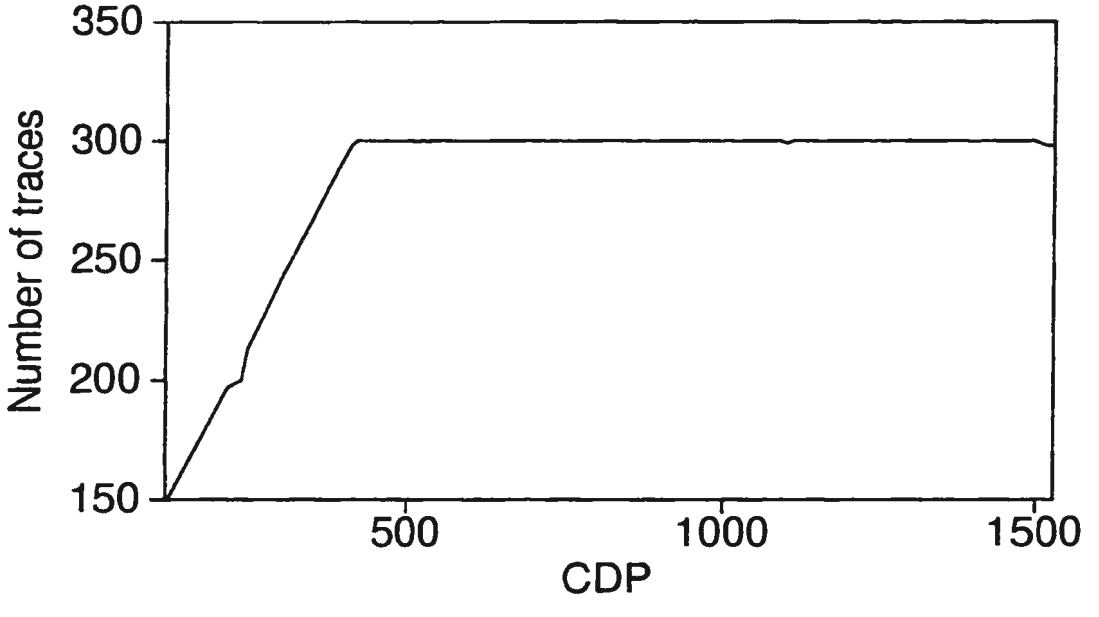

Figure 4.22: The number of traces in each shot in the Husky–Alberta foothills line. Every shot has almost the same number of geophone groups except at the beginning of the line.

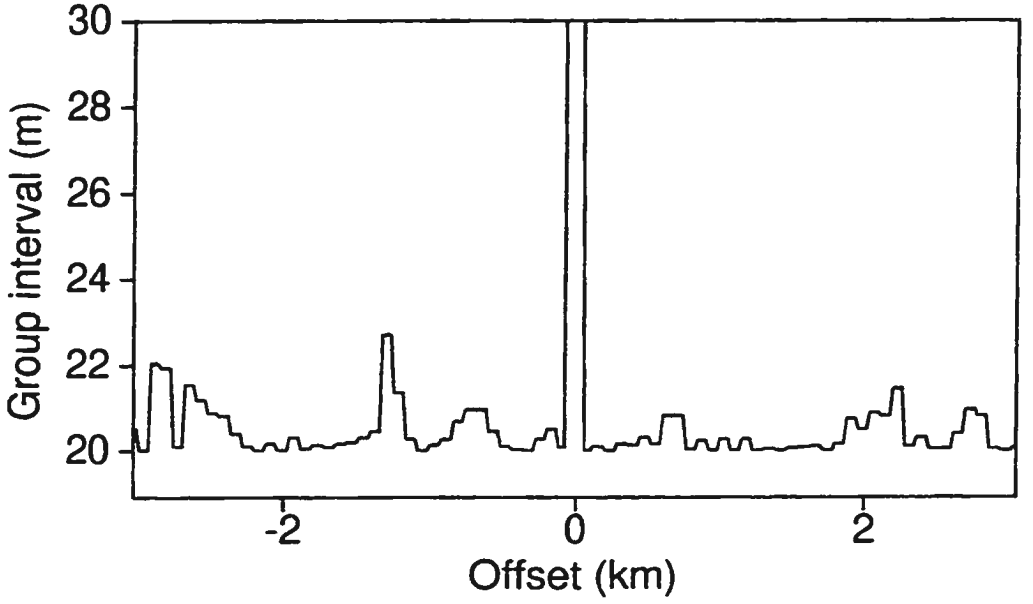

Figure 4.23: A representative display of the group intervals in a single shot. The group interval is kept at its normal value of 20 m very well considering the rough topography of the area.

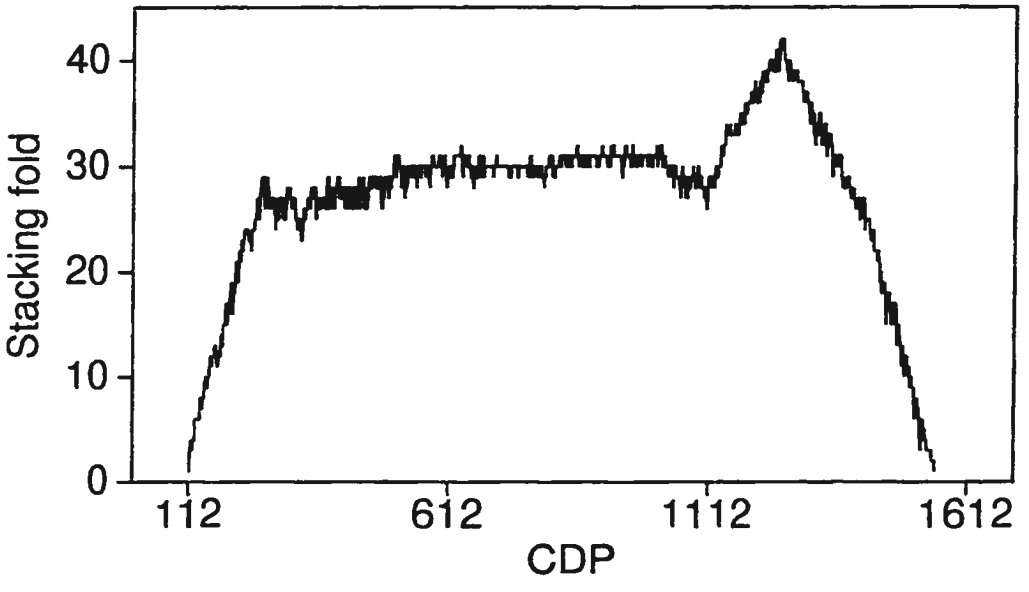

Figure 4.24: The CDP stacking fold of the Husky–Alberta foothills line. The subsurface is non-uniformly sampled as shown by the reasonable variation of the stacking fold.

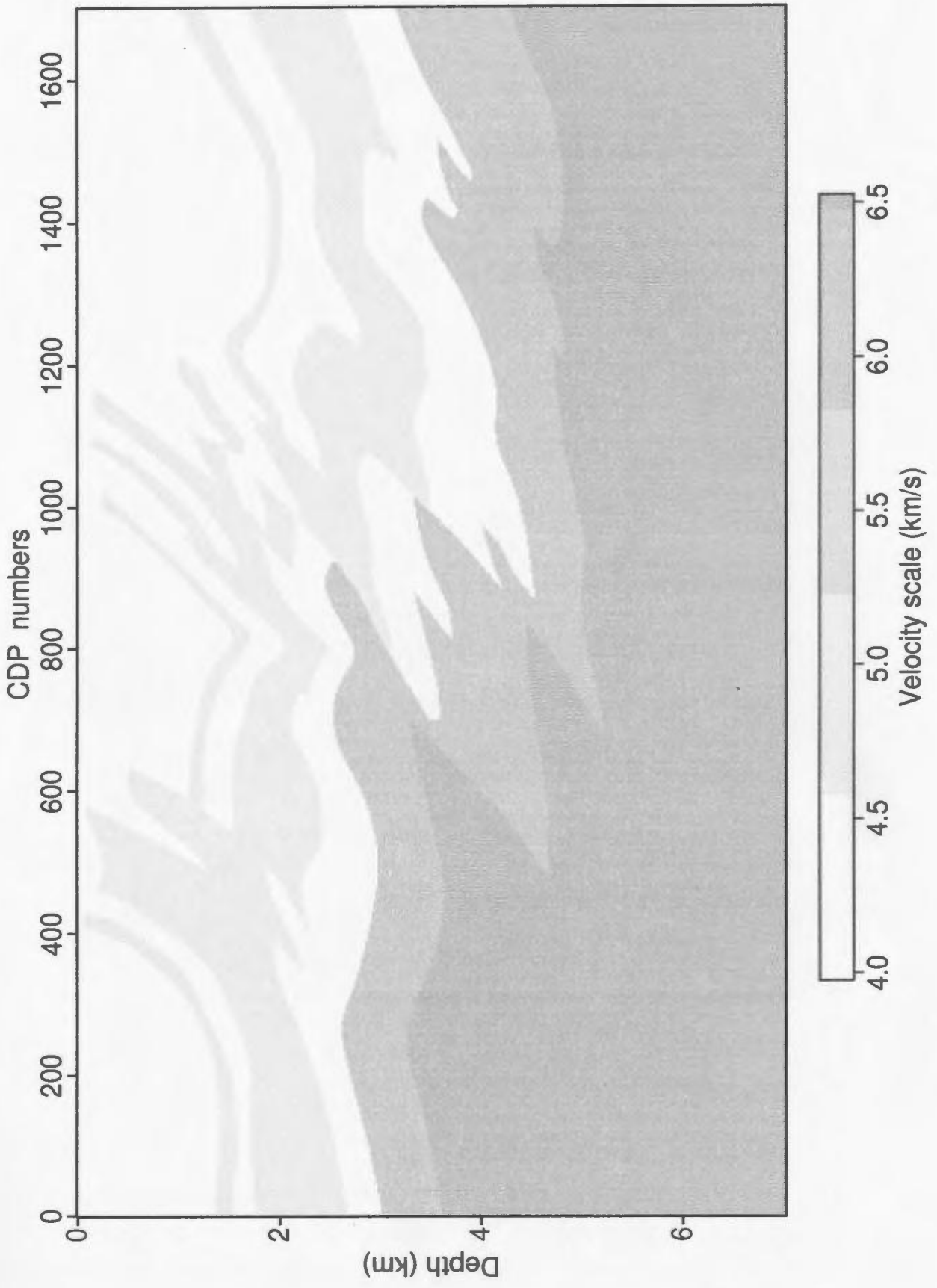

Figure 4.25: Velocity model of the Husky–Alberta foothills line.

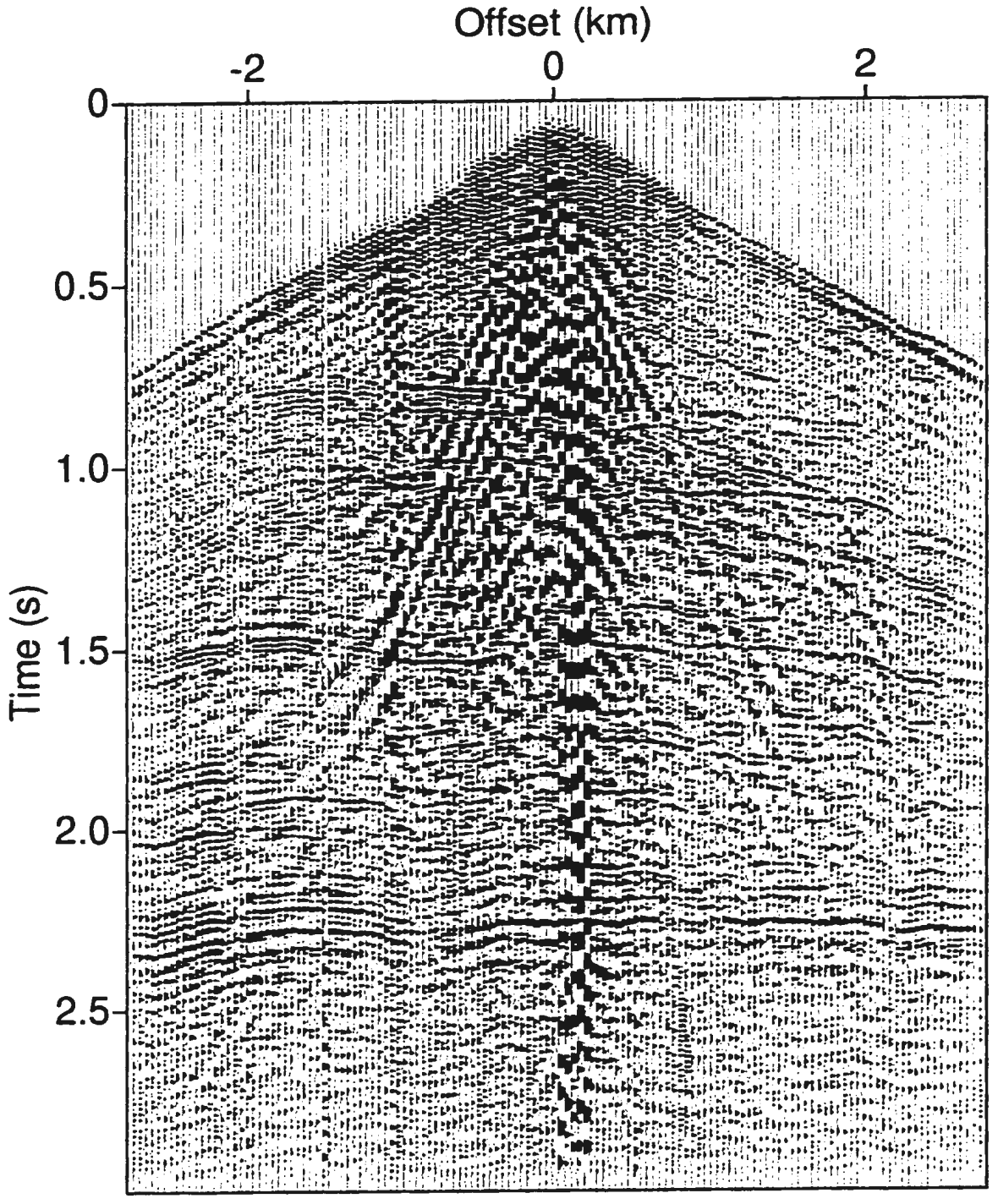

Figure 4.26: A representative shot gather from the Husky–Alberta foothills line.

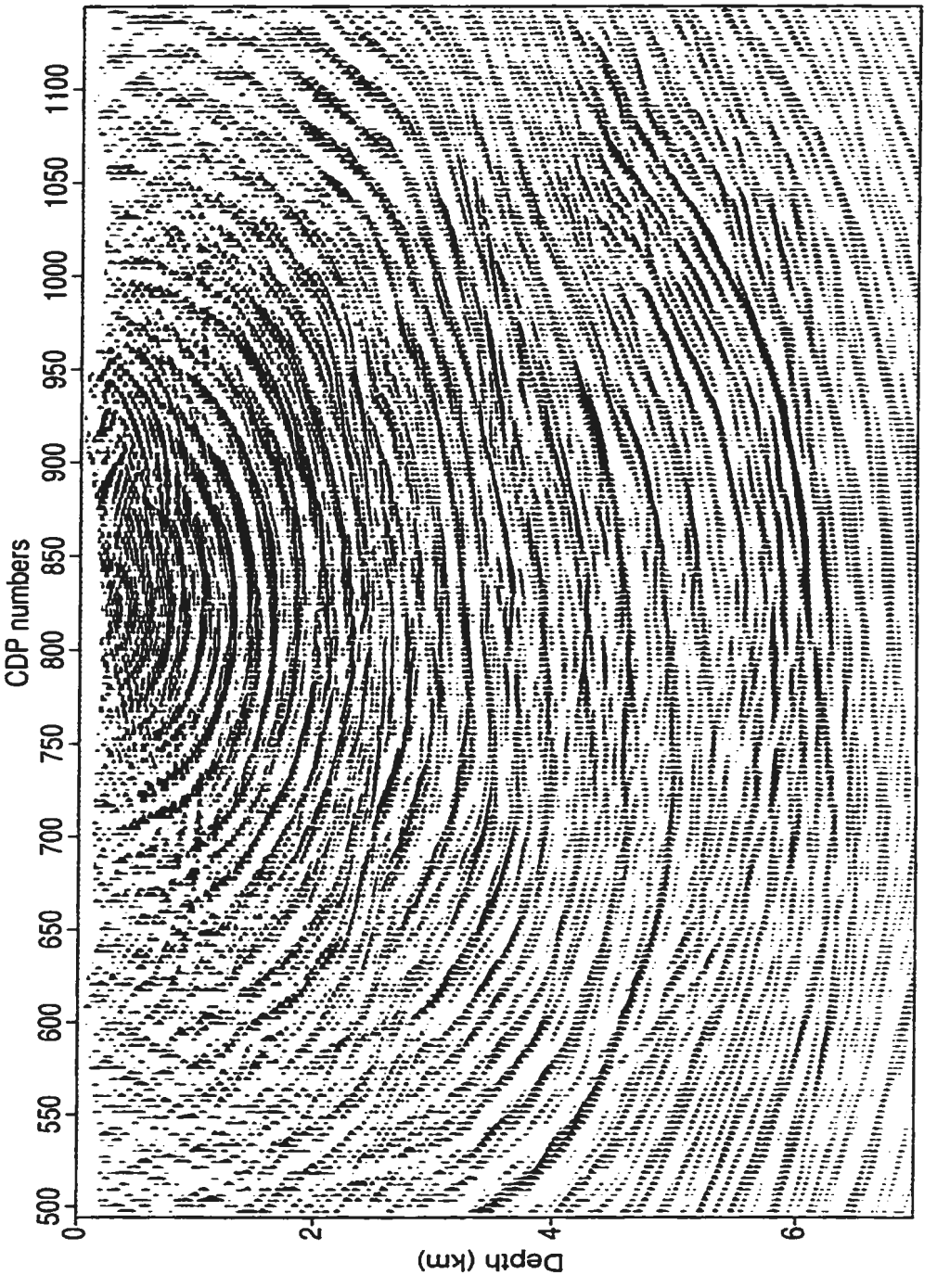

Figure 4.27: A representative shot migration from the Husky–Alberta foothills line using reverse-time migration.

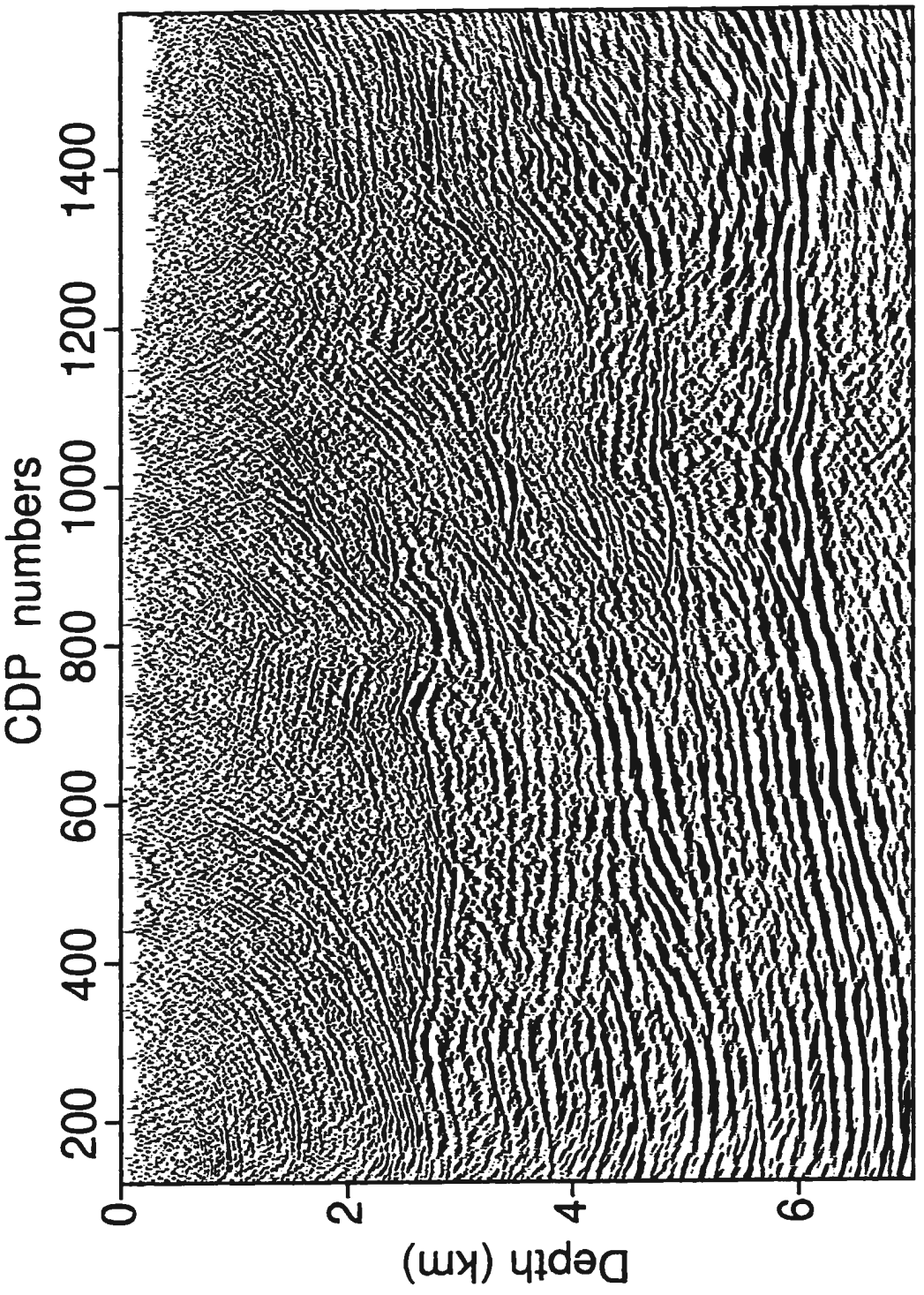

Figure 4.28: The final migrated section of the Husky–Alberta foothills line using reverse-time migration.

Chapter 5. An imaging strategy for complex geological settings

Seismic imaging plays a key role in the petroleum industry as it reconstructs the proper geological structures from the seismic recordings. Nevertheless, imaging does not simply mean migration; it is often accomplished by an iterative procedure consisting of initial velocity model building, migration, geological interpretation, and iterative velocity analysis. In complex geological areas where both strong vertical and lateral velocity variations exist, prestack depth migration has to be pursued.

In this chapter, I will first pursue a comparison of Kirchhoff and reverse-time migrations, two of the most widely used depth migration methods, especially with their application to prestack depth imaging of complex geology. These comparisons, in addition to our theoretical insights on both methods, will expose the advantages and disadvantages of either method. They might be used as a template for geophysicists to choose a proper method in different stages of the imaging problem. Following these comparisons, I will address the problem of determining interval velocities. I will illustrate that prestack depth migration is very sensitive to velocity errors, and common image gathers (CIGs) or common surface point gathers can be effectively used for velocity analysis. However, ample attention should be paid to the interpretation of such CIGs. I propose to use tomographic inversion to set up a near surface velocity

structure, in order to speed up the determination procedure. It is often of great help to use as many parallel means as available to analyze the velocity information.

In the last section of this chapter, I will develop a practical imaging strategy for complex structures. This strategy is basically an interpretive imaging procedure which consists of early cycles of prestack Kirchhoff depth migration, geological interpretation and velocity analysis, and the final application of reverse-time migration to refine the Kirchhoff integral migration result with the hope of providing a more accurate image of the earth.

5.1. Comparison of prestack Kirchhoff and reverse-time depth migration methods

I have demonstrated in the last two chapters that the Kirchhoff integral and reverse-time migrations are two of the most widely used depth migration techniques. Both are among the methods utilized in x-t domain. Both methods are soundly based on the wave equation, the mathematical description of seismic wave phenomena. However, the Kirchhoff method handles high frequency approximations to the wave equation, while the reverse-time migration works better for low frequencies, or equivalently longer wavelengths. Theoretically they both are capable of migrating steep dip reflections. Thus far, both the Kirchhoff integral and reverse-time migrations have been applied to real seismic data, even in the case of 3D with some degree

of success. However, there are few publications on data sets where both Kirchhoff and reverse-time migration methods are applied to prestack depth imaging of complex geology. Larner and Hatton (1990) give a very objective comparison of the Kirchhoff integral and finite-difference migrations in the case of stacked data, concluding that both methods produce comparable migration accuracy, though their finite-difference migration is based on a one-way wave equation. Whitmore at el. (1988) obtain similar conclusions in a comprehensive survey of poststack depth migration methods. Here, as I focus on prestack depth migration, however, I presume that the Kirchhoff integral and reverse-time migrations could possibly perform differently in some aspects.

This section provides a comparison of the Kirchhoff integral and reverse-time migration methods. I will focus discussions on algorithm evaluation, accuracy or migration effectiveness, and computation performance.

5.1.1. Integral vs finite-difference solutions

As I have discussed in Chapter 3, Kirchhoff migration of a single shot can be generally expressed by the surface integral,

$$R(\vec{x};\vec{x_s}) = \int_{\Sigma} \vec{n}\cdot\nabla\tau_r(\vec{x_r};\vec{x})A(\vec{x_r};\vec{x};\vec{x_s})u^m(\vec{x_r},\tau_s(\vec{x};\vec{x_s})+\tau_r(\vec{x_r};\vec{x});\vec{x_s})d\vec{x_r}, \qquad (5.1)$$

where Σ is the recording surface, τ_s and τ_r are the traveltimes from the source point $\vec{x_s}$ to the subsurface position $\vec{x}$, and from $\vec{x}$ to the receiver at $\vec{x_r}$ respectively. $\vec{n}$ is the outward normal of the surface Σ. Here u^m denotes the time derivative of the recorded traces. For the 2D case, $m = \frac{1}{2}$. The term $A(\vec{x_r};\vec{x};\vec{x_s})$ is the geometrical spreading term which functions here as an amplitude modulator to the recording traces. Using a far-field approximation, migration by using equation (5.1) is basically

a weighted summation of the derivative traces along the presumed diffraction trajectory $t = \tau_s + \tau_r$. The weight of each sample is appropriately determined by velocity, the distance traveled, and the obliquity of the emergent ray at the recording surface. Thus the determination of both τ_s and τ_r plays a key role in the calculation of the integral. These are traditionally evaluated by ray tracing. For the sake of economy, the obliquity of the emerging ray is not properly treated in our present implementation. This would not be a problem for the deeper part of the earth where rays will finally reach surface at relatively small angles. The shallow steep reflectors, on the other hand, could suffer some accuracy deterioration. In addition to the far-field approximation, this approximation further deteriorates the migration accuracy. As observed by Kelly et al. (1982), a general amplitude with a correct knowledge of the arrival time is often adequate for structural interpretation purpose. Thus it is expected that the approximations made to the Kirchhoff method would not affect the final migration image too much. In fact, as we will see in the comparison of the Husky–Alberta foothills line, the final migrated section of the line by the Kirchhoff method is very similar to that of the theoretically accurate reverse-time migration. This therefore indicates that the approximations would generally be acceptable in the real world.

In essence, the prestack Kirchhoff depth migration is performed non-recursively. It simply operates on the data trace by trace. A single trace is migrated by distributing the recorded energy along aplanatic curves with the amplitudes modulated by some geometrical functions. Figure 5.2 shows the Kirchhoff migration impulses of a single trace at a surface position of 3 km based on a faulted block velocity model (Figure 5.1). In this migration result for a single trace consisting of 6 events, the geometrical

distributions of the possible scatterers suggested by these events are correctly imaged. The migration amplitudes are also properly computed except at the two zones where refraction takes place. These refraction zones need to be specially treated if migration amplitudes are to be preserved. Such treatment generally requires extra computations.

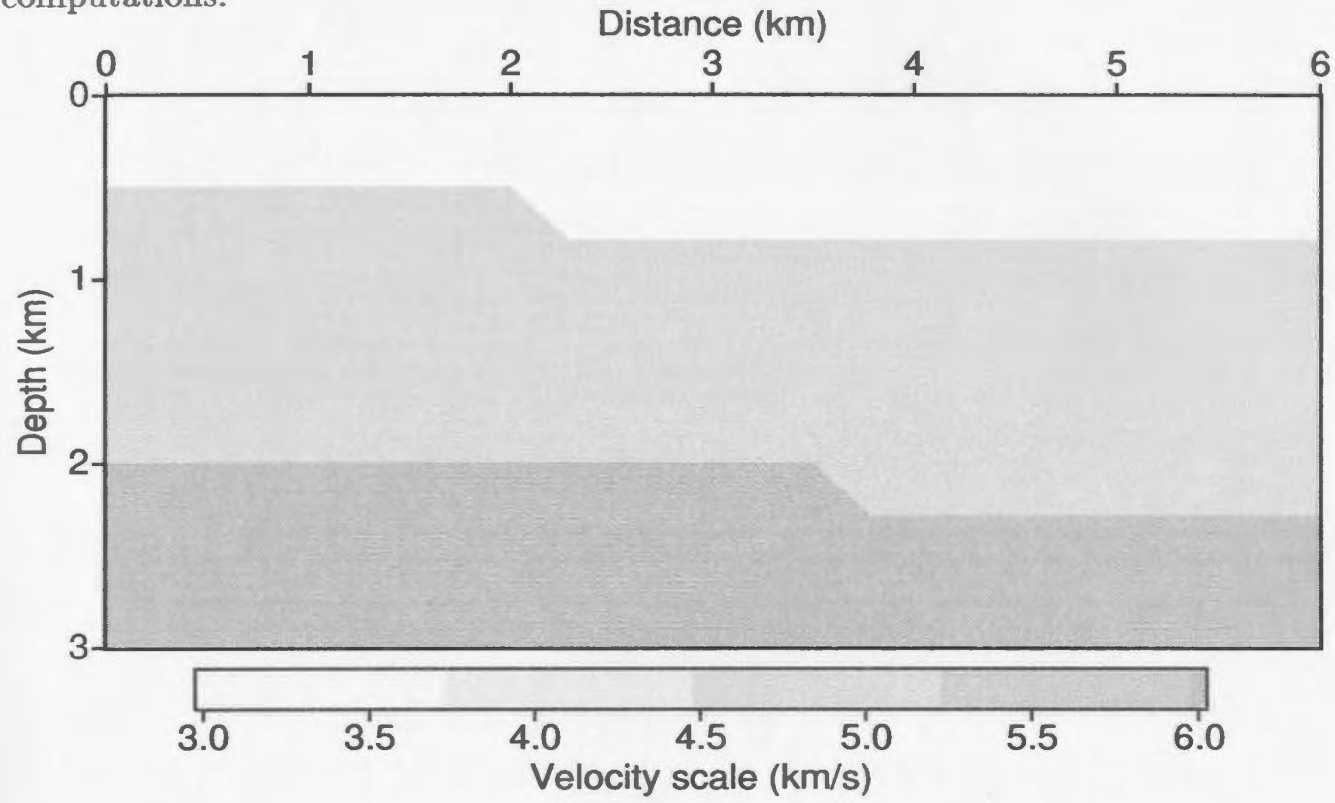

Figure 5.1: Faulted velocity model. A normal fault is developed throughout the depth range. The velocity in each block linearly increases with depth.

In contrast to the Kirchhoff method, reverse-time migration uses the finite-difference solution of the wave equation to extrapolate the recorded wavefields backward. As discussed in Chapter 4, by treating the recorded traces as distributed sources, the wavefields can be effectively extrapolated by the following finite-difference scheme in

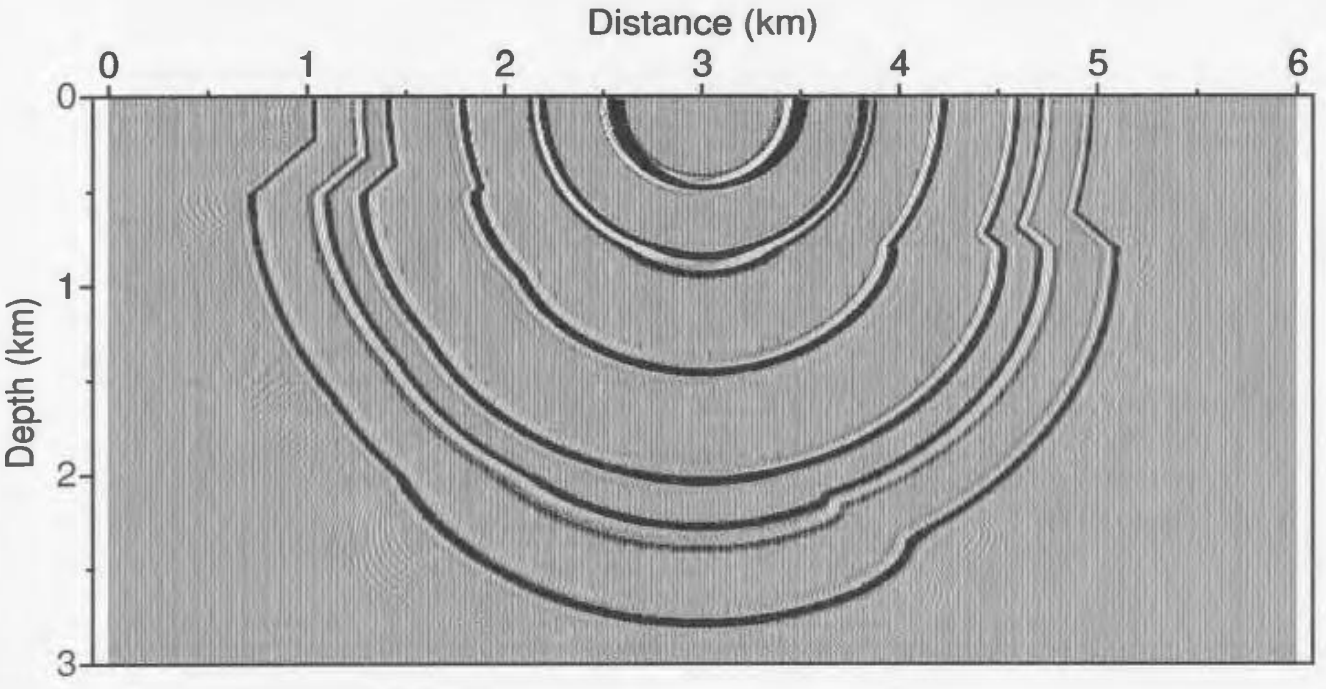

Figure 5.2: Kirchhoff migration impulses. This is the migration of a single trace at a surface position of 3 km based on a faulted velocity model shown in Figure 5.1.

reverse-time order:

$$u_{i,j}^{k-1} = A + 2u_{i,j}^{k} - u_{i,j}^{k+1} + s_{i,j}^{k-1}, \tag{5.2}$$

where s represents recorded traces, A is the finite-difference approximation of the Laplacian operation on the wavefield, and i, j, k are indexes for x, z and t respectively. The effect of A is basically a 2D spatial filtering on the present (t_k) wavefield.

Implementation of reverse-time migration can be summarized in four steps: determine the excitation-time imaging condition by solving the eikonal equation; extrapolate recorded wavefields backward in time using equation (5.2); apply the imaging condition; and then sum the individual migrated shots to produce a final stacked image. The first three steps are basically the same as described by Chang and McMechan (1986) and are essentially a shot record migration. Figure 5.3 shows the reverse-time

migration impulses with the same input data as used by Figure 5.2. Compared to the Kirchhoff migration impulses, this result accurately recovers not only the geometrical shapes but also the amplitudes. As expected, the critically refraction areas are migrated of small amplitude arrivals. It also clearly indicates that migration reflections will occur at the geological interfaces if the full wave equation is used and the velocity model is not properly smoothed (Loewenthal et al., 1987). Migration reflections refer to those reflected at model interfaces during time backward propagation of the wavefield due to impedance changes. Such migration reflections can also be significantly reduced by use of the non-reflecting wave equations by introducing a density function inversely proportional to the velocity function (Baysal et al., 1984; Zhu and Lines, 1994).

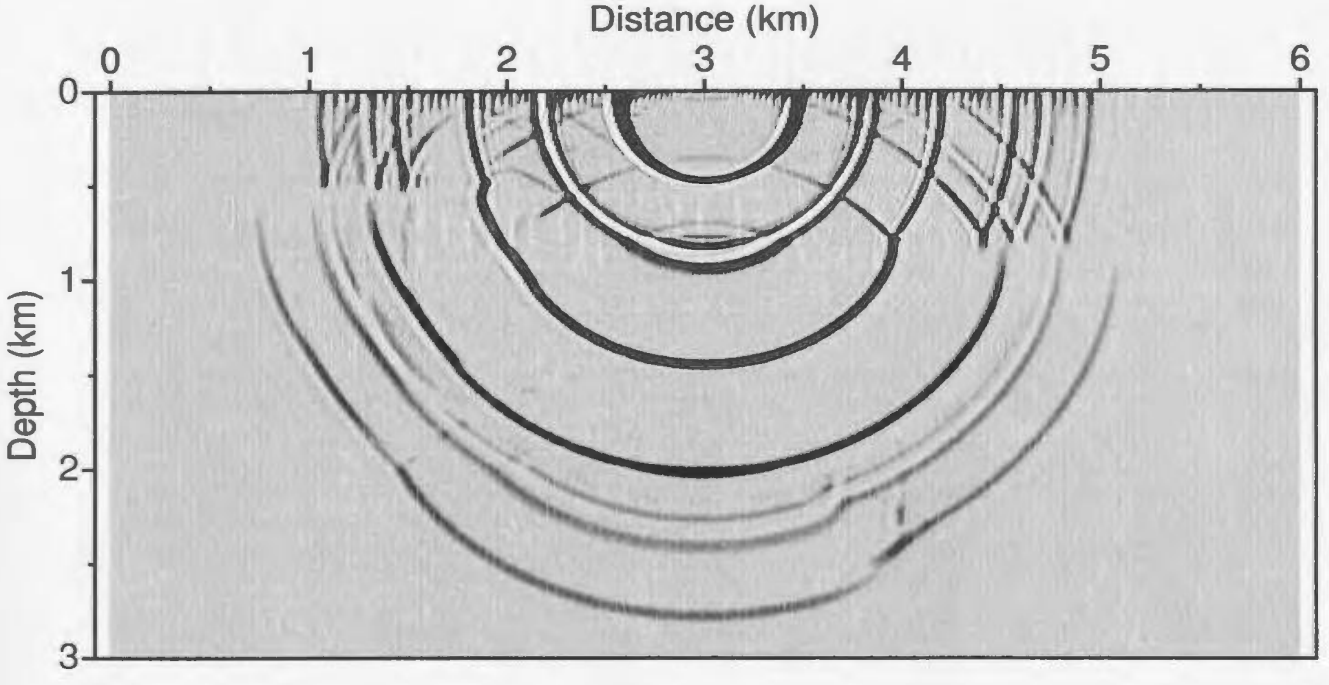

Figure 5.3: Reverse-time migration impulses. The migration is based on the same input data and the same velocity model as used in Figure 5.2.

5.1.2. Performance evaluations

Kirchhoff migration can be performed both recursively and non-recursively. My choice of the non-recursive method is largely based on the ability to accurately calculate the traveltimes. This eliminates the need of extrapolating the wavefields from depth to depth without sacrificing accuracy, thereby reducing the computation significantly. The enhancement in computational efficiency is worth the loss of extrapolated snapshots.

Generally, for a model of N_x by N_z grid points, migrating one shot with N traces, the Kirchhoff integral method will take $O(N_x' \cdot N_z \cdot N)$ operations (Table 5.1). In most cases, the migration aperture N_x' is much smaller than the model lateral extent N_x. It is seen from this expression that the computation is directly dependent on the number of traces in the gather. For example, the special case of migrating a single trace gather, as shown in Figure 5.2, only takes 24 s on a SPARC station 10/30. Of this, 17 s are due to the overall preparation for the migration. The computation of traveltimes takes about 40% of the total computations. This number is somewhat dependent on the complicated nature of the model which arises from the search of computing wavefronts in traveltime calculation. However, the number can be much reduced by setting up time tables before the integration procedure if there is enough memory available. In addition, Kirchhoff migration used here is accurate to the extent that both the far-field approximation and the neglect of the obliquity are acceptable. This presumption certainly is in error near the surface of the earth.

One of the most important attributes of the Kirchhoff method is that it can use selective shots and traces to image some prespecified targets as it is trace based

Table 5.1: Differences between Kirchhoff and reverse-time migrations for shot gathers. N is the number of traces in a shot. N_x and N_z are grid point numbers of the model laterally and vertically. N'_x is the shot migration aperture. N_t is the sample numbers of the trace, and N'_t is the time extrapolation steps.

	Kirchhoff	RT
recursive	no	yes
selective	yes	no
accuracy	very good*	excellent
desirable frequency	high f	low f
inclusion of topography	easy	reasonably easy
computation cost	$O(N'_x \cdot N_z \cdot N)$	$O(N'_x \cdot N_z \cdot N'_t)$
cost & frequency	$\propto f \sim f^2$	$\propto f^3$
vectorization	good	excellent
parallelization	excellent	excellent
data preparation	easy	with some effort

*except near surface.

(Gray and May, 1994; van der Schoot et al., 1989). This also makes the Kirchhoff method easy to use in areas with rough topography. Thus, near surface topographic corrections can be easily included in the Kirchhoff shot migration (Gray and Marfurt, 1995; Lines et al., 1996). Furthermore, the preparation of the model and data in the Kirchhoff migration is much simpler than for other methods. The selectivity of the data, high computational efficiency, plus the easy preparation of data sets render Kirchhoff migration as the preferred method, especially for the process of recursive migration and velocity analysis (Jervis et al., 1996).

Reverse-time migration is recursive in time and represents a general wave equation based method. It can be a very accurate method as the only possible error other

than that due to the velocity model is the discretization error which occurs when differentials are approximated by finite differences. Its high accuracy is nevertheless traded off against its very intensive computations. For a model of N_x by N_z, reverse-time migrating a single shot of N traces with each consisting of N_t samples, will take $O(N'_x \cdot N_z \cdot N'_t)$ operations. N'_x is generally chosen as in the Kirchhoff case, depending on the nature of the earth model and the recorded wavefields. N'_t is the number of extrapolation time steps. It is often much larger than the value of N_t, as N'_t is determined by the stability condition of the finite-difference scheme. Compared to the $O(N'_x \cdot N_z \cdot N)$ operations involved in the Kirchhoff scheme, reverse-time migration will generally require many more computations, as N'_t would be much larger than N in most cases. It is apparent from this estimation that the computations involved in reverse-time migration are independent of the number of traces in each shot, which is definitely in contrast to Kirchhoff method. So reverse-time migration for a gather of a single trace is computationally just the same as migration of a gather with many traces. Thus, it is hoped that reverse-time migration can use this advantage to achieve its high accuracy for migration of seismic data acquired with a large number of channels, which is currently the industry tendency. As a special example, the migration of Figure 5.3 which is on a gather of only one trace, takes 41 minutes on the same SPARC station 10/30. This estimation also implies that when the grid size is halved for a given two-dimensional model, the computation time will increase to 8 times the original for the reverse-time migration, and 4 times the original for the Kirchhoff method. Moreover, the preprocessing for reverse-time migration used to be considered as being more complicated. Our recent study, however, indicates that interpolation of missing traces, which is very difficult in complicated areas, can

be bypassed in many cases, since wavefields are capable of healing themselves by interference during the reverse-time extrapolation procedure (Zhu and Lines, 1997).

Despite the highly demanding computations, reverse-time migrations tend to have wider applicability. This is a reflection of geophysicists' endless pursuit of higher accuracy. Compared to the Kirchhoff method, its independence of accuracy and computations on the complexity of the geological model is also an advantage. These characteristics, in addition to the implicit ability to perform statics corrections, filtering, and self-healing of wavefields make reverse-time migration a very powerful method for imaging geologically complex areas (McMechan and Chen, 1990; McMechan and Sun, 1991; Reshef, 1991; Lines et al., 1996).

In addition to the differences we discuss above, Table 5.1 gives a more compete summary of performance comparisons between the two migration techniques.

5.1.3. Migration comparison for the Marmousi data

Both the prestack Kirchhoff and the reverse-time migration algorithms described in the last section have been extensively tested on this model. Figure 5.4 shows 3 selected migration shots using the prestack Kirchhoff integral scheme. In contrast, Figure 5.5 shows the corresponding shot migrations produced using the reverse-time migration technique. Both sets of migrations cover basically the same geological zones. However, there are still noticeable differences between them. The most obvious difference probably is around the sources where the Kirchhoff result lacks detail in the migration shots compared to the reverse-time migration result. This is partly due to the far field approximation made in the Kirchhoff method. In addition, in the reverse-time migration shots, it seems that the direct waves have masked the images

somewhat. This reflects the fact that the reverse-time migration uses the complete recorded wavefields while the Kirchhoff method essentially deals with reflections and diffractions. Though there exist other striking differences between these two sets, it is still not evident which method provides the better image except the near source zone. Figure 5.6 shows the whole migration image with the Kirchhoff integral method when a 12.5 m grid size is used. This migration takes about 2.44 hours of CPU time on Memorial University's campus computer DEC Alpha Server 1000 with a clock frequency of 200 MHz. Figure 5.7, on the other hand, shows the migrated stacked section with the reverse-time migration algorithm using the same gridded velocity model as in the Kirchhoff migration. However, this migration takes 21.43 hours of CPU on the same machine. These two plots are displayed with the same plotting parameters, so a direct comparison should be applicable. It is apparent that both methods have fairly well restored the geological features of the model despite the striking differences in the migration shots. Nevertheless, as we notice, there are several places where the two images are different. The left and the middle faults in the Kirchhoff result are not as sharply defined as in the reverse-time migration image. The reverse-time migrated section presents a sharp image of the right fault while the integral result smears the image of the fault around a depth of 1.5 km. In addition, reverse-time migration provides a slightly more continuous definition of the subsalt anticline structure than the Kirchhoff method. These differences are mainly due to the algorithm details involved in the two methods, especially the neglect of the obliquity and the use of first arrival times in the Kirchhoff method (Nichols, 1996).

Thus, in the example of the Marmousi data, the reverse-time migration gives a more accurate migration image than the Kirchhoff method. Its higher accuracy is

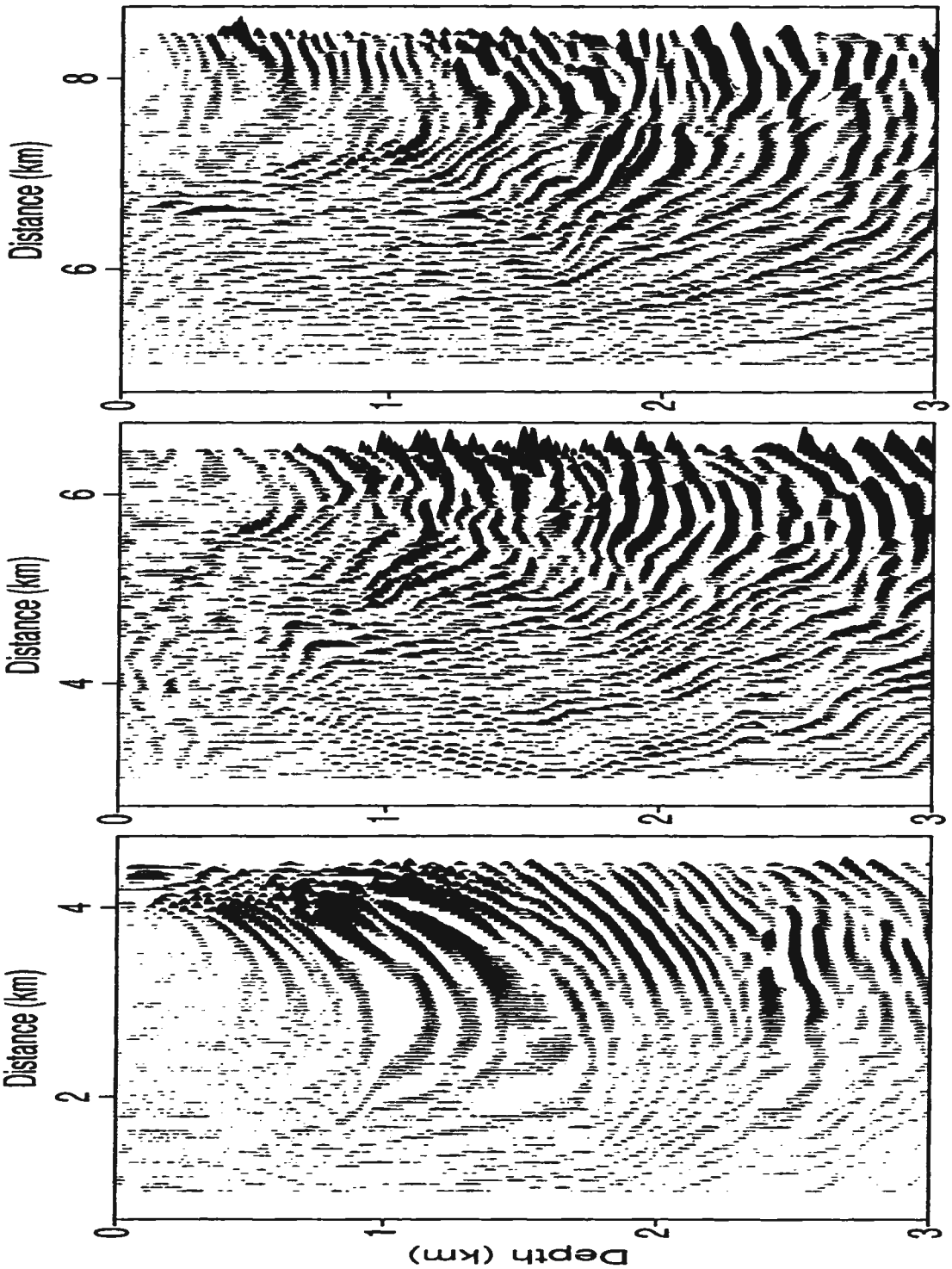

Figure 5.4: Selected migration of shot records from the Marmousi model data produced by the Kirchhoff integral method. A velocity model with 12.5 m of grid spacing is used in the migration.

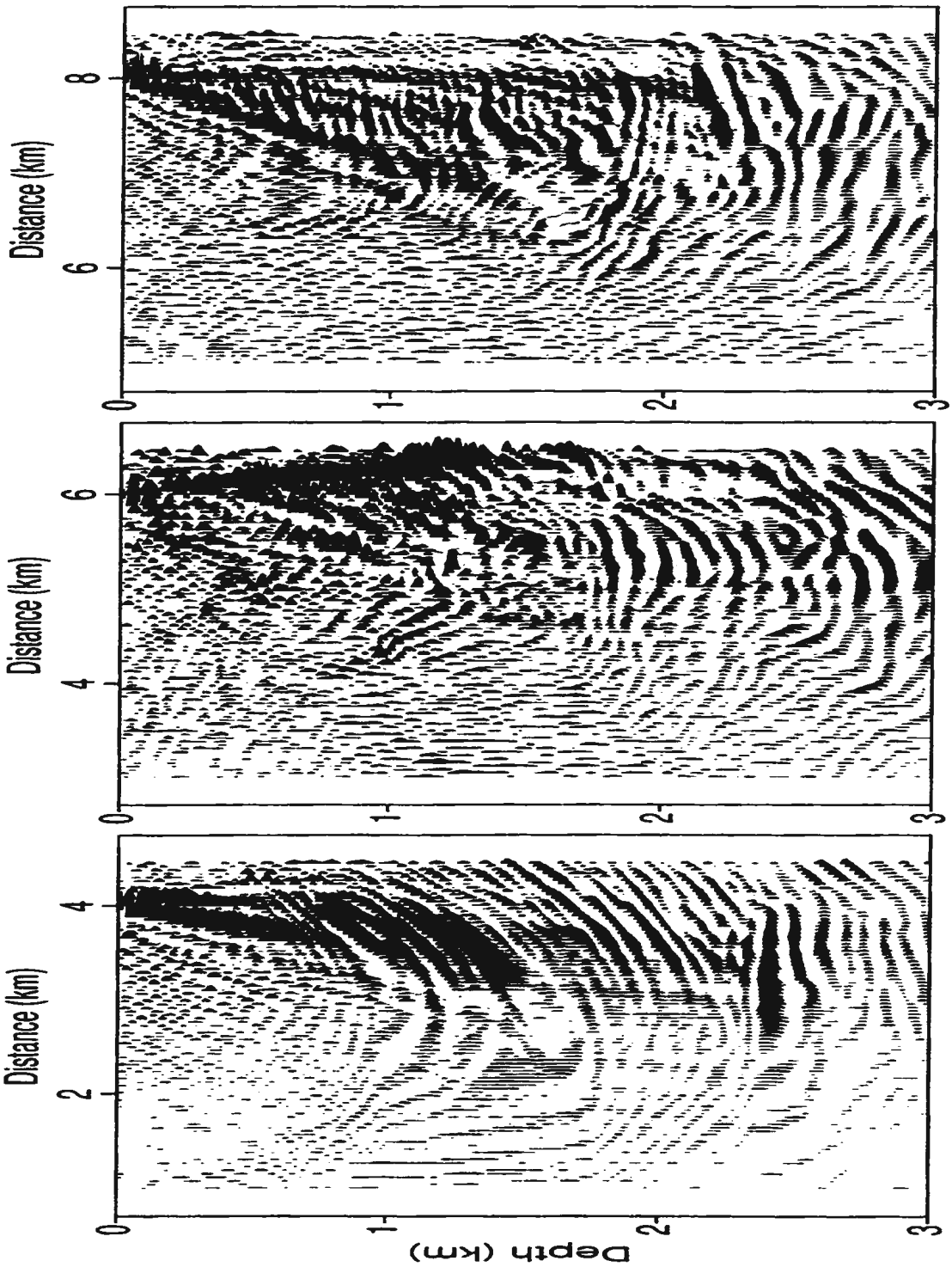

Figure 5.5: Selected migration of shot records from the Marmousi model set produced by the reverse-time migration method. A velocity model with 12.5 m of grid spacing is used in the migration.

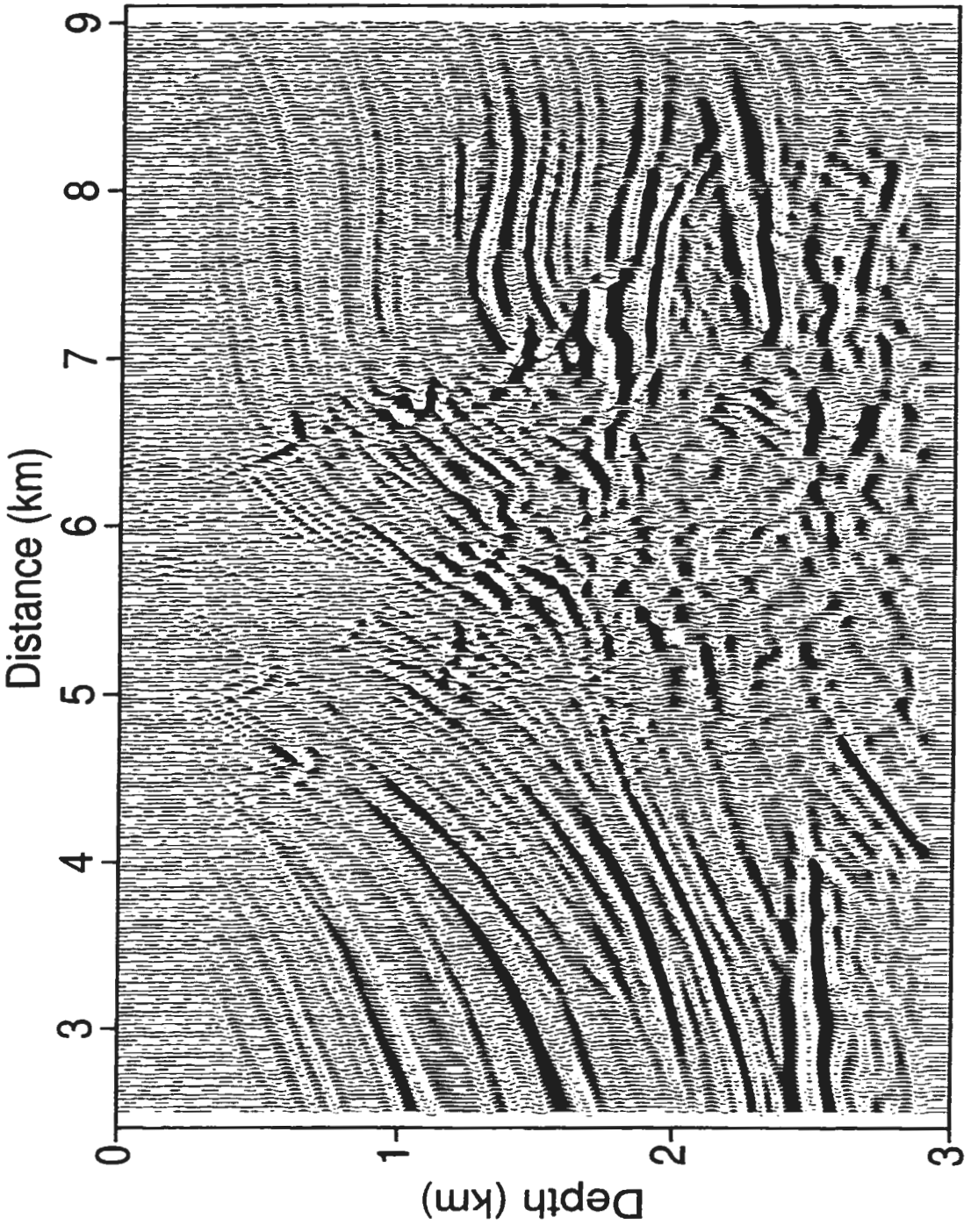

Figure 5.6: The final migrated section of the Marmousi model data set produced by the Kirchhoff integral method.

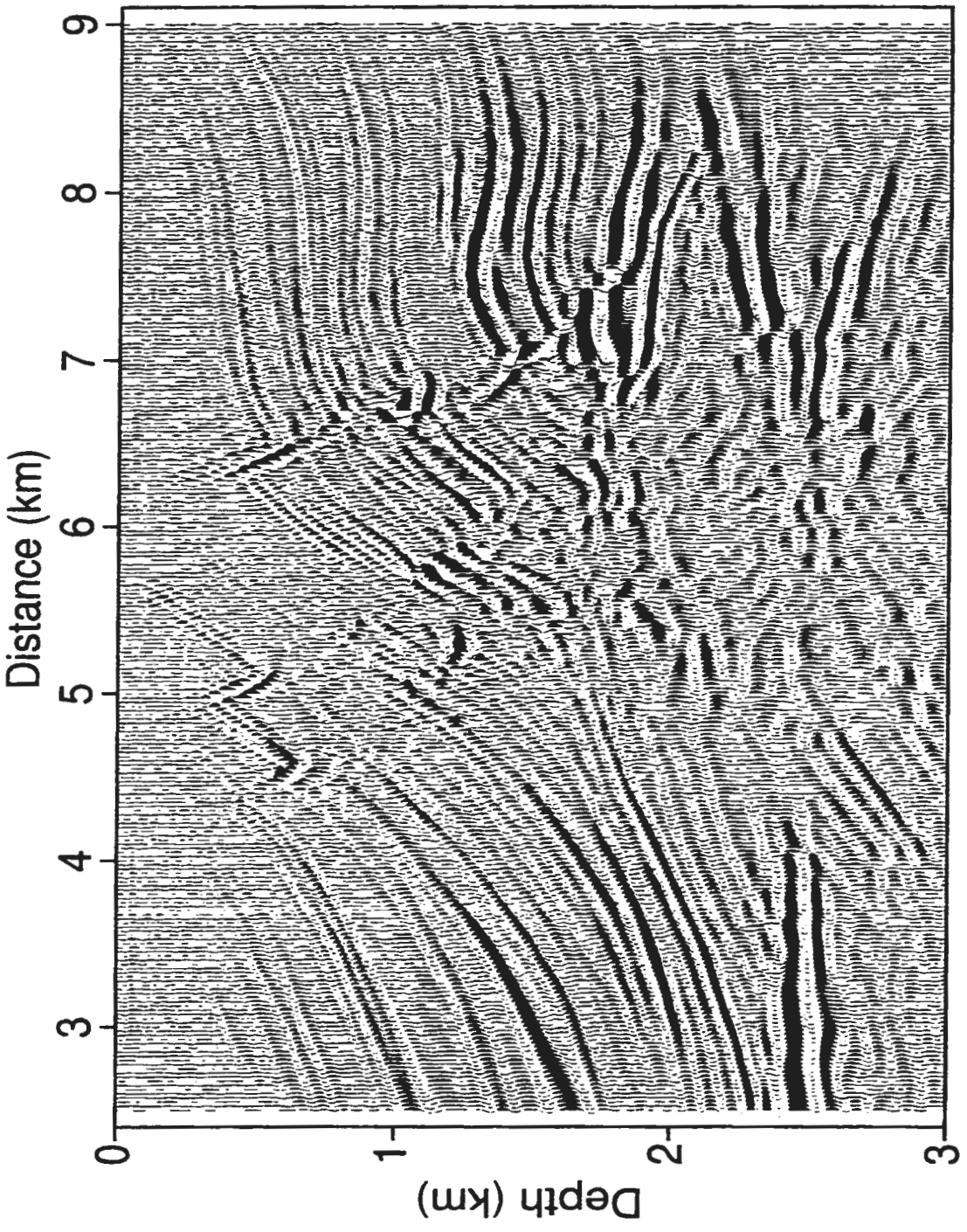

Figure 5.7: The final migration section of the Marmousi model data set produced by the reverse-time migration.

nevertheless based on the use of the true velocity model and is traded off against a much higher amount of computational time.

5.1.4. Migration comparison of the Husky–Alberta foothills data

The Husky–Alberta foothills line presents a challenging imaging case as there is no known answer due to its being real data. I use this foothills data set to evaluate the accuracy and effectiveness of both the Kirchhoff and reverse-time migration methods in a real case where only an approximate model is available.

Figure 5.8 shows a comparison of migration shot No.142 produced by Kirchhoff integral and reverse-time migrations when a 10 m by 10 m gridded velocity model is used. The velocity model is originally created based on structural geological information and the stacked section. The nearby well log information provides good constraints to the velocity model. The model is then updated by an interpretive imaging procedure consisting of iterative prestack depth migration, migration velocity analysis, and geological interpretation. Both results image the shallow dipping layers very well. They are very similar in many respects, especially considering the fact that they are only based on a single shot gather. Nevertheless, there are differences identifiable between the two shot migrations. As in the Marmousi example, the zone of the greatest contrast lies near the source area.

Figure 5.9 shows the final Kirchhoff migrated section. In this migration image, the shallow dipping formations at the upper left side of the section are clearly seen to be detached from the underlying gentle formations at about the depth of 2600 m. Two main thrust faults are well defined around CDP numbers of 580 and 810 respectively. Overall, this migration result offers a very encouraging result which is relatively easy

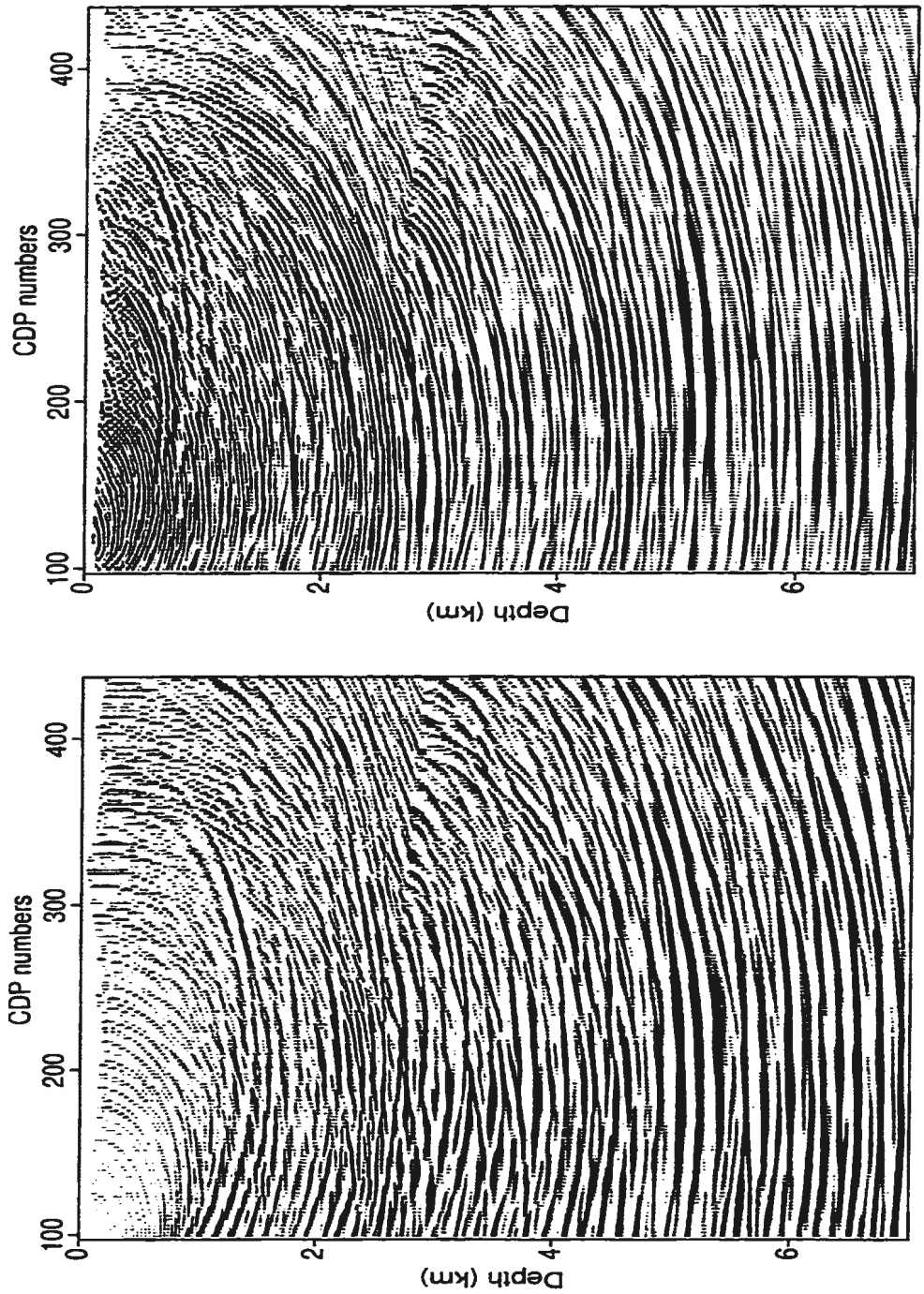

Figure 5.8: A comparison of a representative migration shot from the Husky–Alberta foothills line. The left corresponds to the Kirchhoff result. The right is the reverse-time migration result.

to interpret. The migration of this foothills line, however, takes about 22.91 hours of CPU time (Table 5.2). In fact, in the early stages of studying this line, the migration was done on a much coarser grid (20 m by 20 m). In that case, the Kirchhoff migration takes only about 5.61 hours of CPU time with quite similar results. My impression of the difference is that the coarser grid lacks a bit of continuity at the shallow parts of the earth model. From the table of CPU times, it is seen that use of a grid which is twice as dense will increase the CPU time by about 4.2 times, which is near to our theoretical estimate of 4 times, considering the overhead of computations involved in the migration.

Table 5.2: Computation cost examples of Kirchhoff and reverse-time depth migrations.

	Marmousi data		Husky–Alberta foothills line	
	h=25.0 m	h=12.5 m	h=20 m	h=10 m
Kirchhoff	37.28 minutes	2.44 hrs	5.61 hrs	22.91 hrs
RT	2.41 hrs	21.31 hrs	13.59 hrs	135.65 hrs

Note: based on a DEC Alpha Server 1000 with a clock frequency of 200 MHz.

In contrast, Figure 5.10 shows the reverse-time migrated section. It is based on the same velocity model as used in Figure 5.9. It essentially reveals the same salient features of the geology as Figure 5.9 with a little improvement in the triangle zone around CDP 800-1200. In the enlarged view of the migration image which corresponds to the upper left portion of the whole, as shown in Figure 5.11 and Figure 5.12, it is still difficult to tell one from the other. However, the production of this image with the reverse-time migration method requires about 135.65 hours of CPU time! This is definitely a significant increase in computer time compared

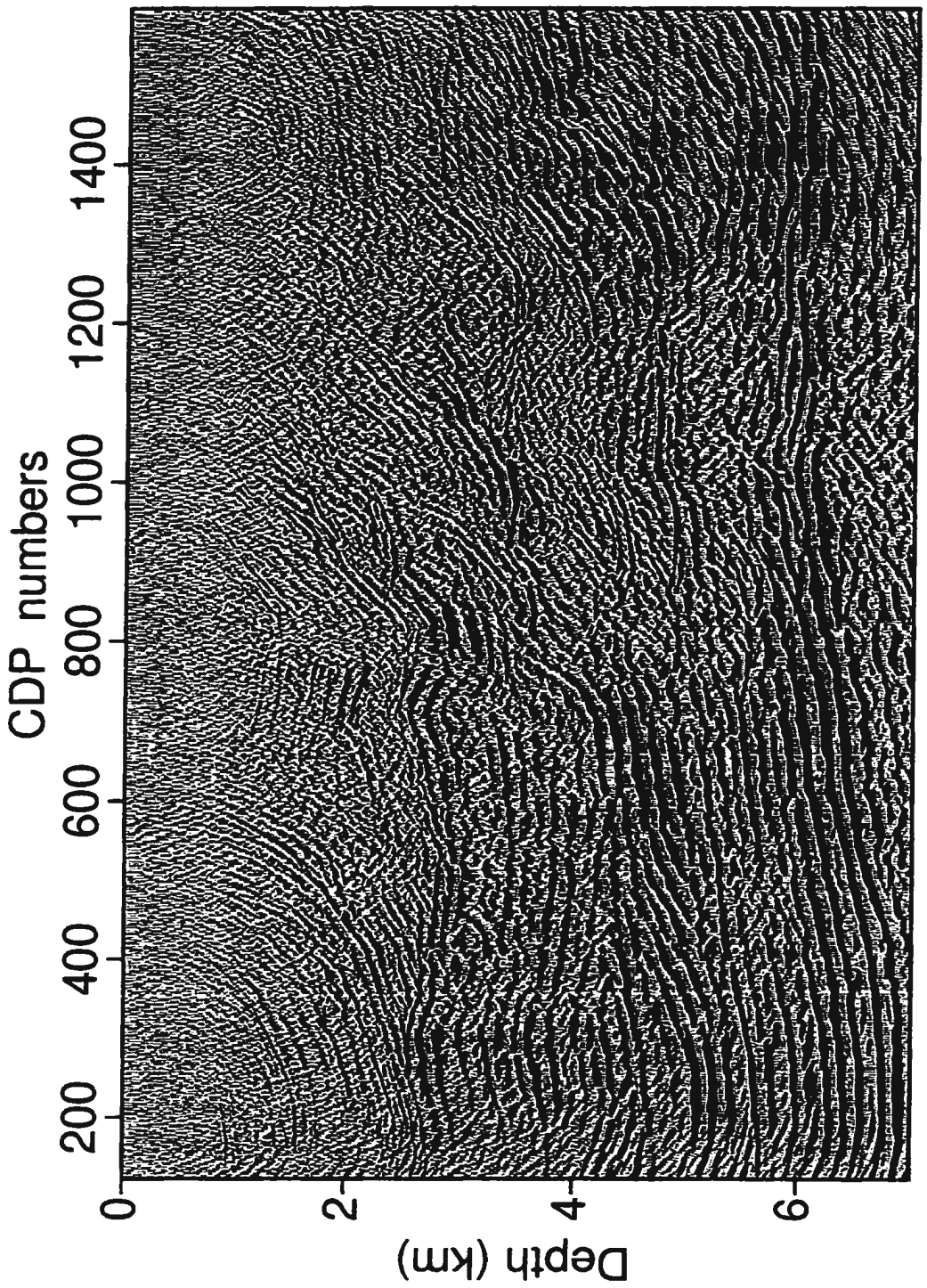

Figure 5.9: The final migrated section of the Husky–Alberta foothills line produced by the Kirchhoff integral technique.

to the 22.91 hours taken by the Kirchhoff method. For comparison purposes, we have also tested the reverse-time migration technique on this line using a coarser gridded velocity model of 20 m by 20 m. In that case, it takes 13.59 hours of CPU time. Thus, for the reverse-time migration in the case of this foothills line, when the model grid is twice as fine, the computation time nearly increases by a factor of 10 which is a bit higher than our theoretical estimate of a factor of 8. This possibly is due to the fact that a larger proportion of CPU time has been involved in swapping data as the digital model gets larger. The similarity of the two migrated sections of this foothills line, from application perspective, supports the adequacy of the the approximations made in the Kirchhoff integral method. Nevertheless, the similarity of the migration results between the Kirchhoff and reverse-time migration methods does not necessarily indicate that the Kirchhoff method is as accurate as the reverse-time method. It probably implies that there are still errors in the estimated velocity model. Due to these errors, it is not evident which method works better in achieving migration accuracy. Thus, both methods are similar in performance for real data where only an estimated velocity model is available.

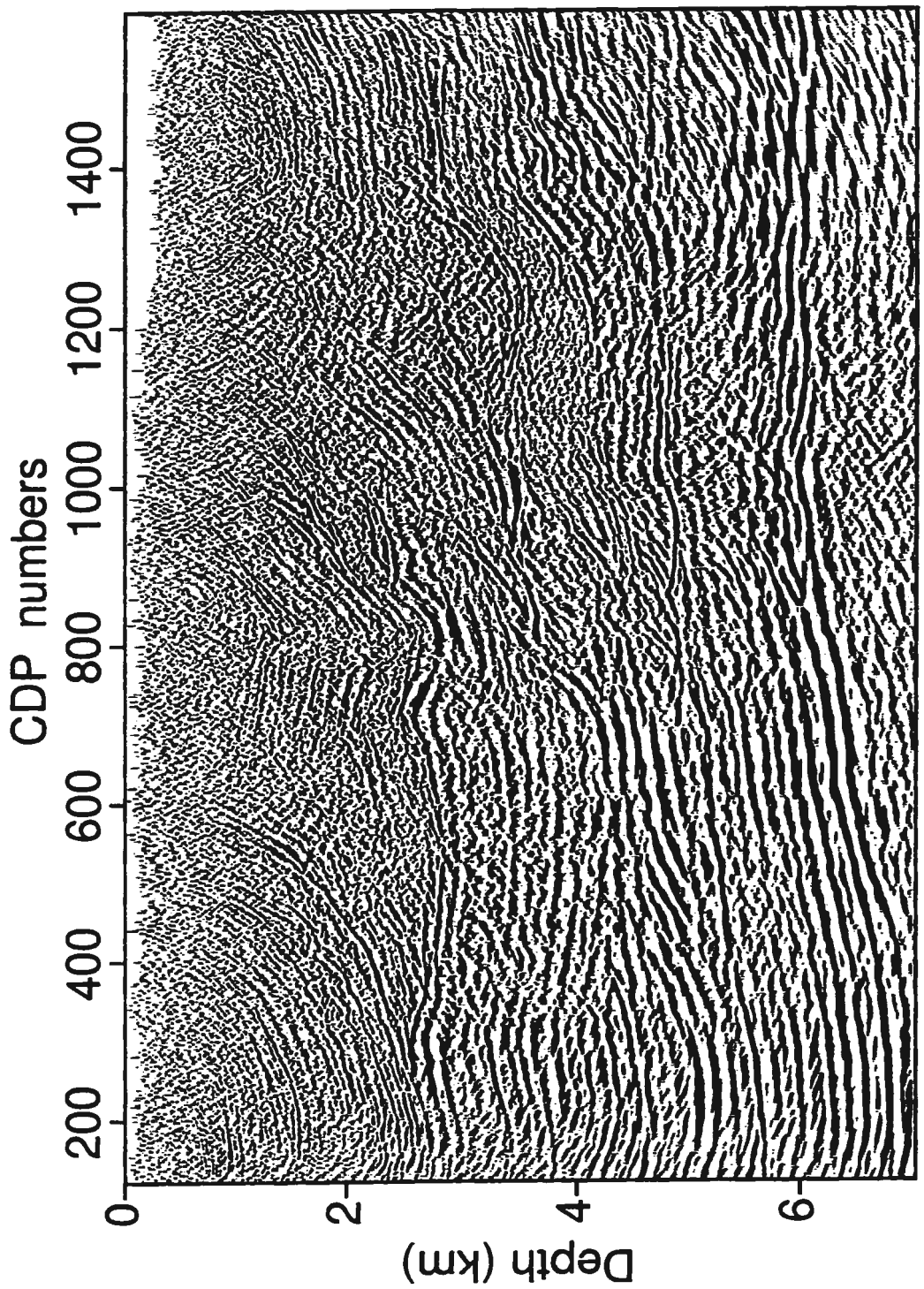

Figure 5.10: The final migration section of the Husky–Alberta foothills line produced by the reverse-time migration technique.

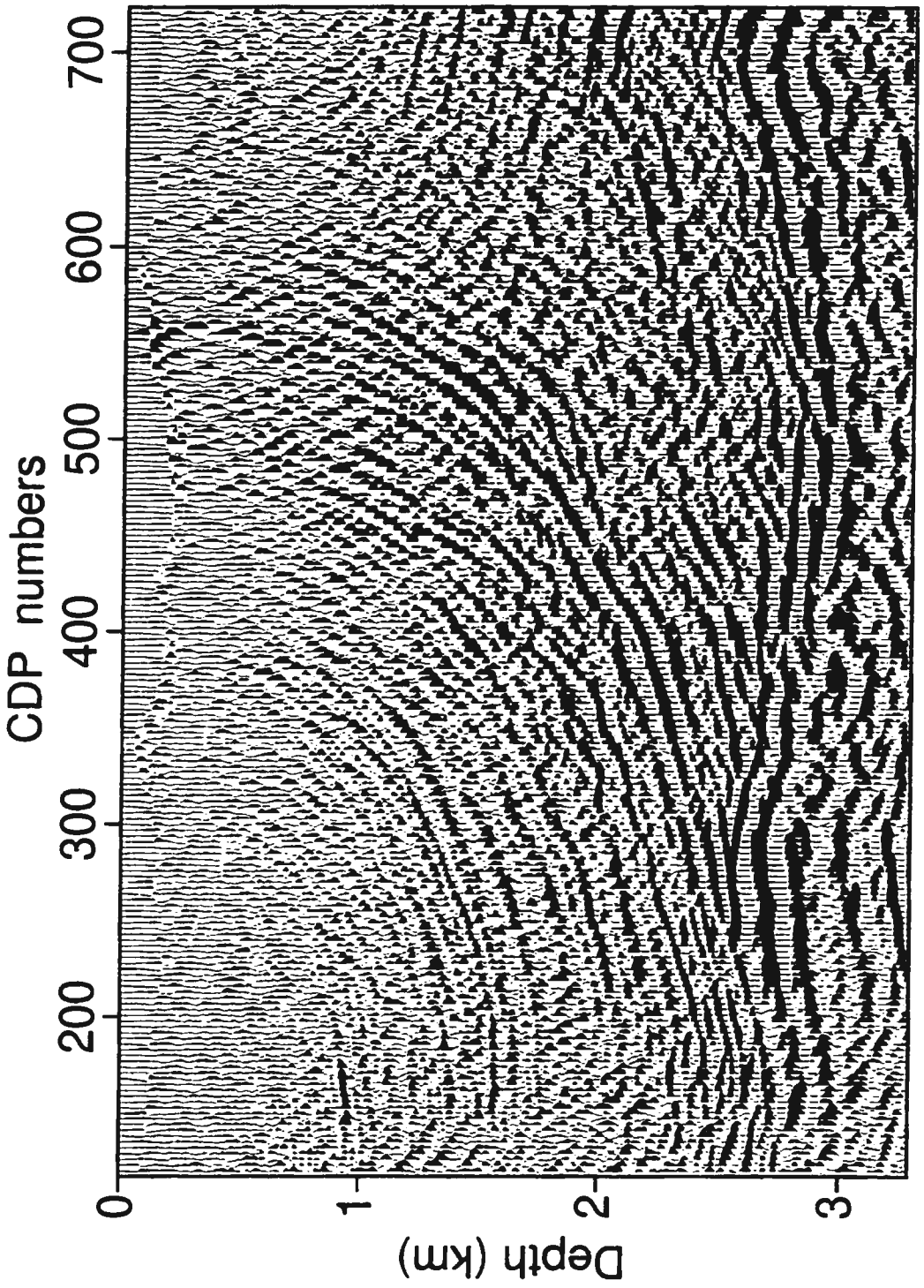

Figure 5.11: The enlarged view of the final migrated section of the Husky–Alberta foothills line produced by the Kirchhoff integral technique.

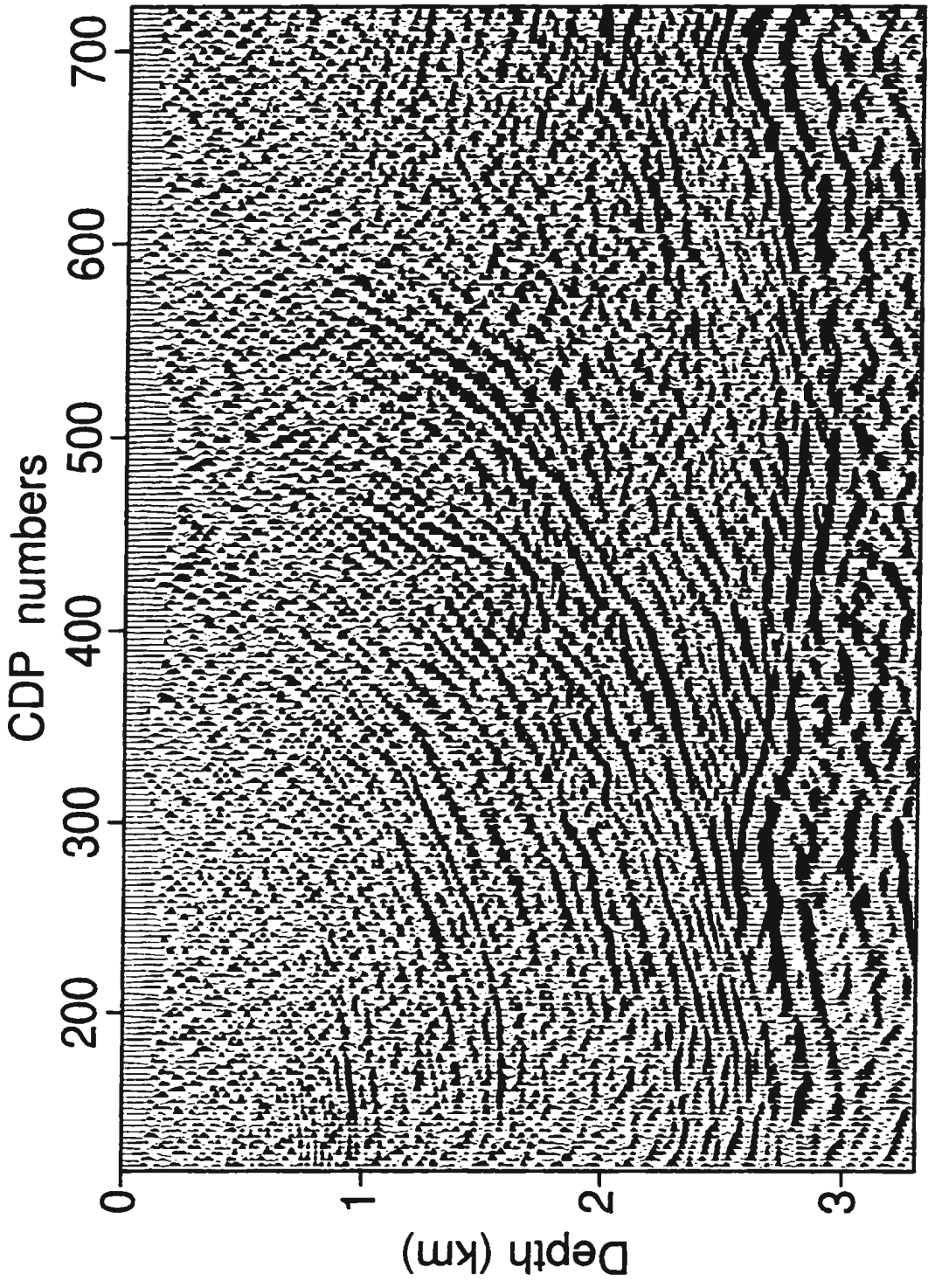

Figure 5.12: The enlarged view of the final migrated section of the Husky–Alberta foothills line produced by the reverse-time migration technique.

5.2. Fundamentals of interval velocity analysis with prestack migration moveout

In this thesis, I have extensively examined the physical and mathematical aspects of the seismic migration problems with the focus on the evaluation of two of the most widely used and accurate schemes, the Kirchhoff integral and the reverse-time migrations. I have shown that both are theoretically based on the wave equation, the mathematical expression of wave propagation phenomena. Both can accurately image reflections and diffractions without dip restriction if a reasonable approximation of the velocity field is available. Thus, the velocity model becomes the key component in these migration applications. As I pointed out in the introduction chapter, many alternatives exist for velocity analysis. In this section, I will address the basic theories in interval velocity analysis utilizing prestack migration moveout.

Consider the general subsurface structure and recording geometry as shown in Figure 5.13a. P denotes the arbitrary scattering point in the earth's interior. S and R are a source-receiver pair illuminating P. D is the surface image of P. Assuming that the average velocity above P is $\bar{v}$, and that the diffraction received at R due to a source wavelet from S and then diffracted at P never travels beneath P, then its arrival time can be expressed as:

$$t = \frac{1}{\bar{v}} \left(\overline{SP} + \overline{RP} \right). \tag{5.3}$$

When an average velocity $\bar{v}_m$ is used for migration, the diffraction signal received from P will be migrated to an incorrect point P'. P' generally has both vertical and lateral

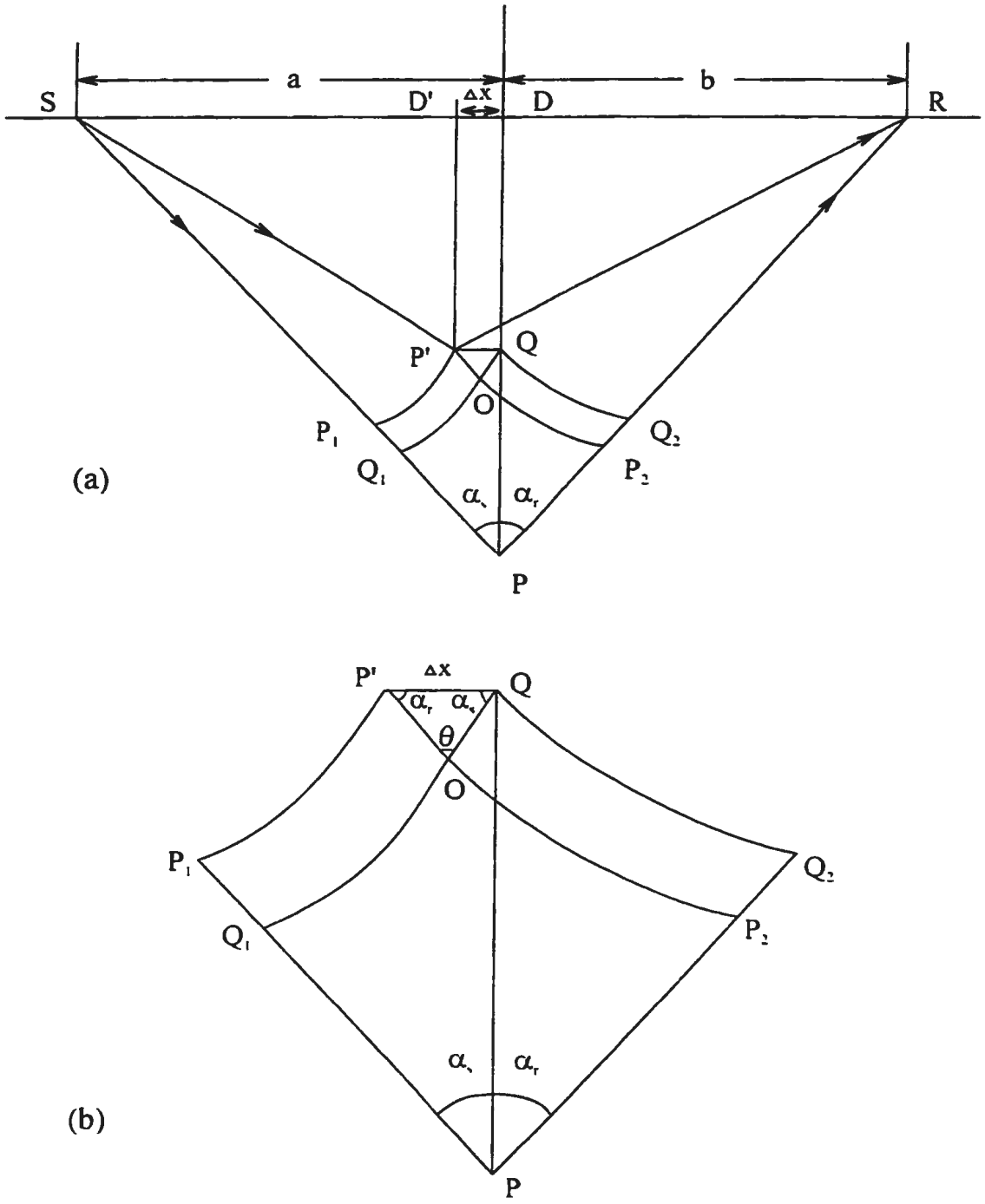

Figure 5.13: Migration depth-velocity relationship diagram in a general subsurface structure. (a) A wrong velocity migrates the reflection to a position P' which has a lateral displacement Δx in addition to a vertical displacement Δz. (b) is an enlarged view of the lower part of (a).

displacements from the true position P. I denote these displacements with $\Delta x = \overline{P'Q}$ and $\Delta z = \overline{QP}$. In this case, the traveltime will be,

$$\begin{aligned} t &= \frac{1}{\bar{v}_m}\left[\overline{SP'} + \overline{P'R}\right] = \frac{1}{\bar{v}_m}\left[(\overline{SP} - \overline{P_1P}) + (\overline{RP} - \overline{P_2P})\right] \\ &= \frac{1}{\bar{v}_m}\left[(\overline{SP} - \overline{Q_1P}) + (\overline{RP} - \overline{Q_2P})\right] + \frac{1}{\bar{v}_m}(\overline{P_2Q_2} - \overline{P_1Q_1}). \end{aligned} \tag{5.4}$$

From Figure 1.13b, the following relationship holds in the triangle $\Delta P'QO$,

$$\frac{\sin\alpha_s}{\overline{P'O}} = \frac{\sin\alpha_r}{\overline{QO}} = \frac{\sin\theta}{\overline{\Delta x}}. \tag{5.5}$$

Thus, we have,

$$\begin{aligned} \overline{P_2Q_2} - \overline{P_1Q_1} &\simeq \overline{QO} - \overline{P'O} \\ &= \frac{\Delta x}{\sin\theta}\sin\alpha_r - \frac{\Delta x}{\sin\theta}\sin\alpha_s \\ &= \frac{\Delta x}{\sin\theta}(\sin\alpha_r - \sin\alpha_s) \\ &= \frac{\Delta x}{\cos(\theta/2)}\sin\frac{\alpha_r - \alpha_s}{2}. \end{aligned} \tag{5.6}$$

In the derivation of the last equation above, I have used the following relationships $\alpha_r + \alpha_s + \theta = 180^0$; $\sin\theta = 2\sin\frac{\theta}{2}\cos\frac{\theta}{2}$; and $\sin\alpha_r - \sin\alpha_s = 2\cos\frac{\alpha_r+\alpha_s}{2}\sin\frac{\alpha_r-\alpha_s}{2}$. Therefore, the distance part of the last term of (5.4) would be an order smaller than Δx as long as $|\sin(\alpha_s - \alpha_r)/2)| < 0.10$ and θ is not close to 180^0. The latter condition generally holds, as α_s and α_r would not be zero for most cases. The first condition is equivalent to $|\alpha_s - \alpha_r| < 12^0$, i.e., the difference between the two illuminating angles being less than 12^0. As $|\alpha_s - \alpha_r| = 2\alpha$ where α is the structural dip at P, the above inequality thus only holds for structures of gentle dip. In such cases. (5.4) can be properly approximated by

$$t = \frac{1}{\bar{v}_m}\left[(\overline{SP} - \overline{Q_1P}) + (\overline{RP} - \overline{Q_2P})\right]. \tag{5.7}$$

This equation is physically equivalent to the assumption that the lateral displacement Δx is negligible compared to the vertical one. Eliminating t from equations (5.3) and (5.7), I obtain,

$$(1-\beta)(\overline{SP}+\overline{RP}\Big) = \overline{Q_1P}+\overline{Q_2P}, \tag{5.8}$$

where $\beta = \frac{\bar{v}_m}{\bar{v}}$. From Figure 5.13, the following general relations hold,

$$\overline{SP} = z \;/\cos\alpha_s; \qquad \overline{Q_1P} = -\Delta z\cos\alpha_s;$$

$$\overline{RP} = z \;/\cos\alpha_r; \qquad \overline{Q_2P} = -\Delta z\cos\alpha_r.$$

Substituting these relations into (5.8) leads to,

$$\Delta z = (\beta-1)\frac{z}{\cos\alpha_s\cos\alpha_r}. \tag{5.9}$$

In the case of zero offset source-receiver pair just at D, $\alpha_s = \alpha_r = 0$, I obtain,

$$\Delta z = (\beta-1)z. \tag{5.10}$$

This implies that the migration depth z will be shallower than the true depth z if a smaller than the true velocity ($\bar{v}_m < \bar{v}$) is used for migration, while deeper if a higher velocity ($\bar{v}_m > \bar{v}$) is used. Only when $\beta = 1$, i.e., the true medium velocity is used for migration, will the diffractor be properly located. By denoting $\Delta z_0 = (\beta-1)z$, (5.9) can be rewritten as,

$$\Delta z(\alpha_s,\alpha_r) = \frac{\Delta z_0}{\cos\alpha_s\cos\alpha_r}. \tag{5.11}$$

Now let's consider the following three categories.

a. Migration velocity less than the true velocity ($\bar{v}_m < \bar{v}$). In this case, $\beta < 1$, $\Delta z_0 < 0$, and $\Delta z(\alpha_s,\alpha_r) < \Delta z_0$. Generally the following relation also holds,

$$\Delta z(\alpha_s+\epsilon_1,\alpha_r+\epsilon_2) < \Delta z(\alpha_s,\alpha_r), \tag{5.12}$$

for any α_s, α_r and any nonnegative values of ϵ_1, ϵ_2. This relation indicates that the migration image of P will form a smile which curves upward on a common image gather (CIG) which is a display of migration traces versus the source-receiver offset corresponding to a fixed surface point.

b. Migration velocity greater than the true velocity ($\bar{v}_m > \bar{v}$). In this case, $\beta > 1$, $\Delta z_0 > 0$, and $\Delta z(\alpha_s, \alpha_r) > \Delta z_0$. Similar to (5.12) we have,

$$\Delta z(\alpha_s + \epsilon_1, \alpha_r + \epsilon_2) > \Delta z(\alpha_s, \alpha_r). \tag{5.13}$$

This relation indicates that the migration image of P forms a frown which curves downward on a CIG.

c. Migration velocity equal to the true velocity ($\bar{v}_m = \bar{v}$). In this special case, $\beta = 1$, $\Delta z_0 = 0$, thus,

$$\Delta z(\alpha_s, \alpha_r) = 0 \tag{5.14}$$

for any source-receiver pair. This simply means that when the true velocity is used for migration ($\bar{v}_m = \bar{v}$), the migration images of the diffractor point P will be at the exact depth regardless of source-receiver offset. So. its images form a horizontal segment on the CIG displays.

Therefore, the velocity error in migration is very well expressed on the migration common image gathers. I will use a point diffractor model to illustrate the above theoretical observations. Suppose two point diffractors lie in middle of a uniform medium with velocity v = 4000 m/s. The depths of the diffractors are 600 m and 800 m respectively. 81 shot gathers are theoretically simulated, with each consisting of 60 traces. Figure 5.14 shows the CIGs for surface position x = 1.0 km when different velocities are used in migration. It clearly demonstrates that only when the true

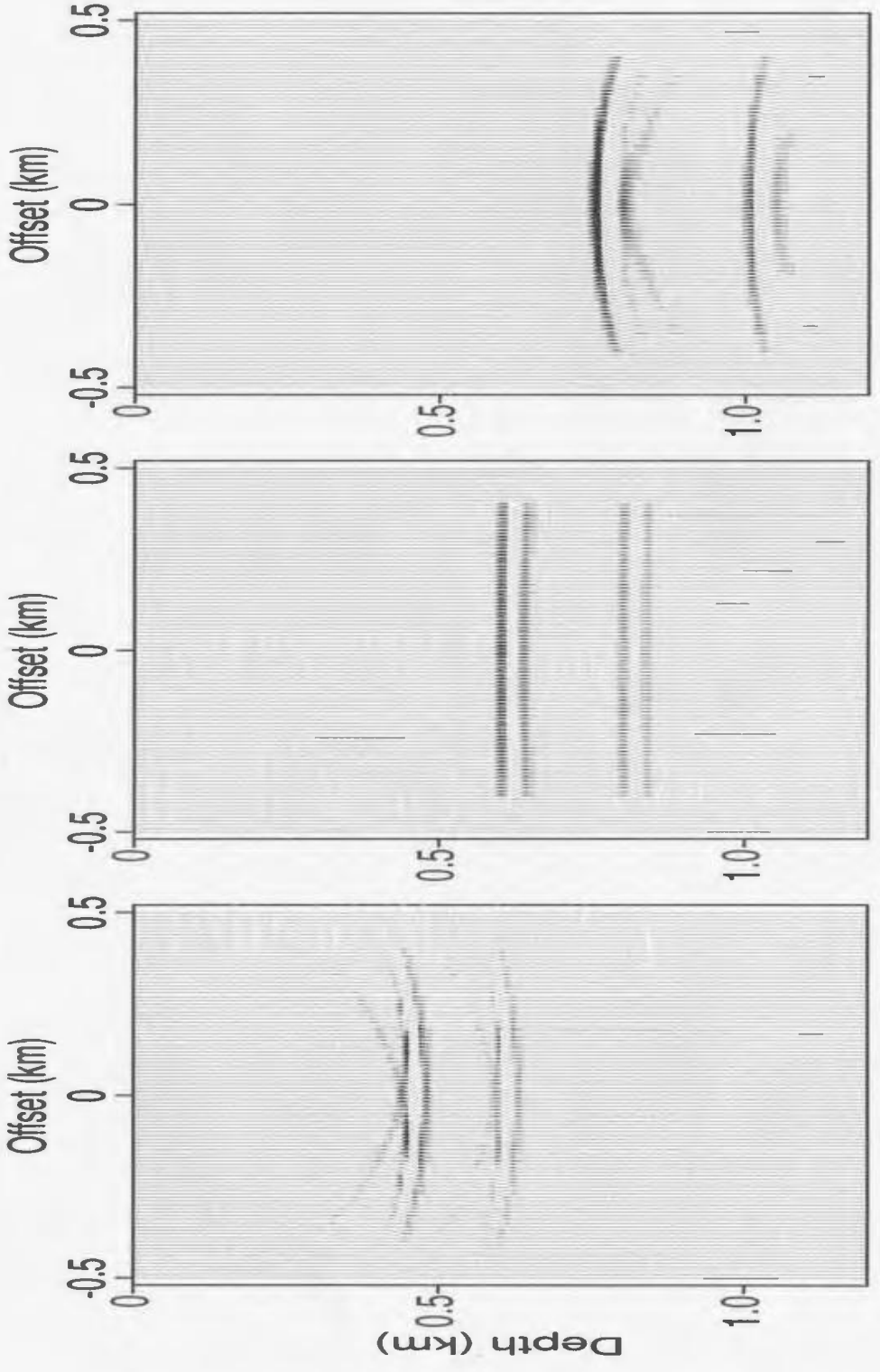

Figure 5.14: Common image gathers for a two point diffractors model. The CIG is at surface position of x = 1.0 km. A migration velocity lower than, equal to, or higher than the true velocity produces smiles (left), flat events (centre) or frowns (right) respectively.

velocity is used, will the migration images of diffractors be independent on the source-receiver offset. When the velocity is lower than the true velocity ($v_m = 3000\ m/s$), the diffractor images form smiles at a depth shallower than the true depth. This is totally in agreement with equation (5.12). In contrast, when the velocity is higher than the true velocity ($v_m = 5000\ m/s$), the diffractors will be expressed as frowns on a CIG at a depth greater than the true depth. This is just what has been predicted by the mathematical expression (5.13).

In addition to the expressions on CIGs, the velocity error is also well documented on the final migration sections, essentially the sum of depth migrations for various shots. Interestingly enough, the CIG gathers show shallow smiles for low velocities and deep frowns for high velocities (Lines et al., 1993), whereas the final depth migrated sections show shallow frowns for low velocities and deep smiles for high velocities (Yilmaz, 1987). Figure 5.15 shows prestack depth migrated sections which correspond to cases of velocity lower than, equal to, and higher than the true medium velocity. A too low migration velocity ($v_m = 3000\ m/s$) results in frown-type images, which indicates under-migration of the diffractions. This is basically the result of insufficient collapse of diffractions. In contrast, using a higher than real velocity ($v_m = 5000\ m/s$) in migration results in smile-type images, implying over-migration of the recorded diffractions. In either of the above two cases, the migration images of the diffractors are not properly focused. A smaller velocity results in image shallowing while a larger velocity leads to image deepening. Only when the true velocity is used, will the diffractions completely collapse to their true positions.

If we further take a careful look at Figures 5.14 and 5.15, it is seen that the curvatures of the shallow smiles/frowns are generally larger than the deep ones.

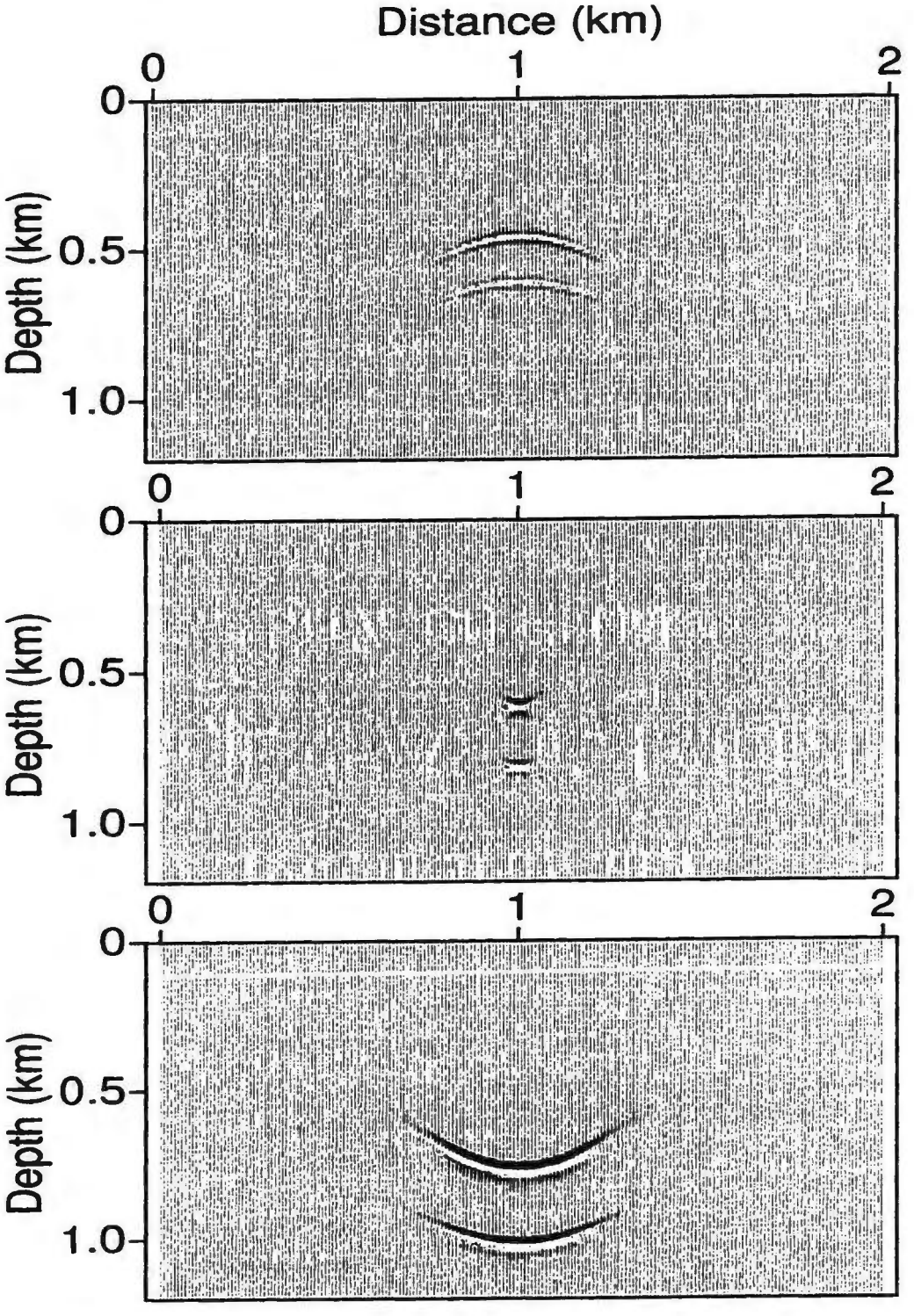

Figure 5.15: Migration of a two point diffractors model. A migration velocity smaller than, equal to, and larger than the true velocity is used for the top, middle, and bottom images respectively.

This indicates that velocity errors are more pronounced on shallow reflections and thus are more easily detected. This is also in agreement with the general observation that sufficient offset/depth ratio should be kept in order to properly analyze the velocity errors (Lines. 1993). Luckily we often have more constraints available on the shallow parts of the earth. such as well logging and geological exposures. We can also more effectively use techniques such as first break tomography to constrain the near surface velocity estimation. With respect to the deeper structure. we generally have to accept that it is coarsely defined and more ambiguous.

Though the diffractor model is over simplified. it is of vital significance in migration and velocity analysis theory. as any complicated structures can be considered as a continuum of diffractors. The following example comes from the Marmousi model data. Figure 5.16 displays selective CIGs from this model data set when a velocity model systematically 10% lower than the true model is used in migration. Here we only see half smiles in CIGs as the data is of one sided shooting. Almost all the events in CIGs curve upward with offset which increases from right to left. When the true velocity model is used in migration. the CIGs basically consist of horizontally aligned events (Figure 5.17). However. if migration velocity is systematically 10% higher than the actual velocity. the CIGs will look like those shown in Figure 5.18. It is seen that the amplitudes in Figure 5.18 are very different from those in Figure 5.16 and Figure 5.17. This is because the calculated imaging time with a higher migration velocity for each grid point is much smaller than the arrival time of the real source wavelet. resulting in a smaller image amplitude. This again indicates that a larger migration velocity often does more harm than a smaller one. In these CIGs. images form half branch of frowns which trends downward towards left edge of each CIG panel.

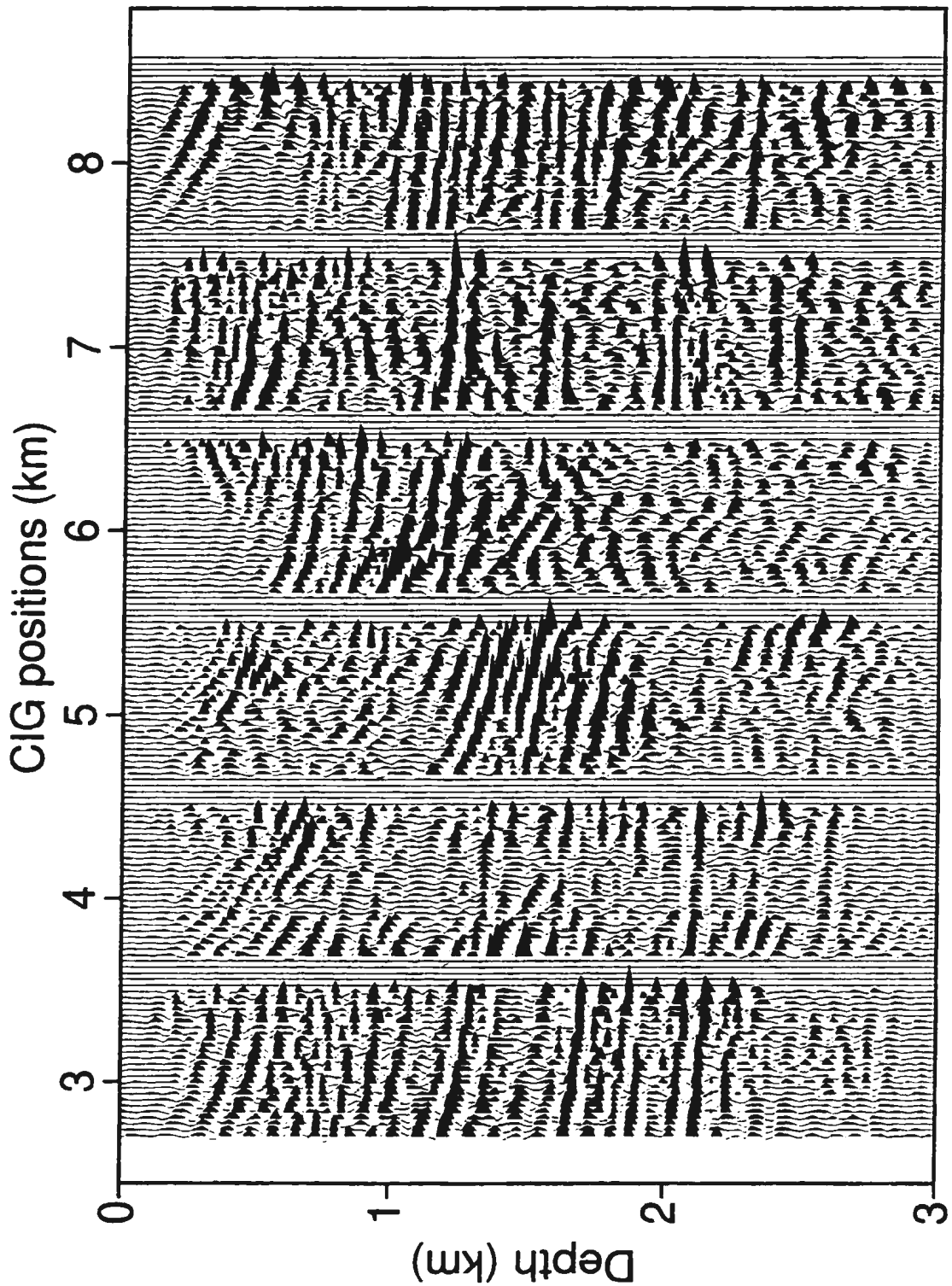

Figure 5.16: CIGs for the Marmousi model with smaller velocities. The migration velocity is systematically 10 % lower than the true values. Offset increases from right to left.

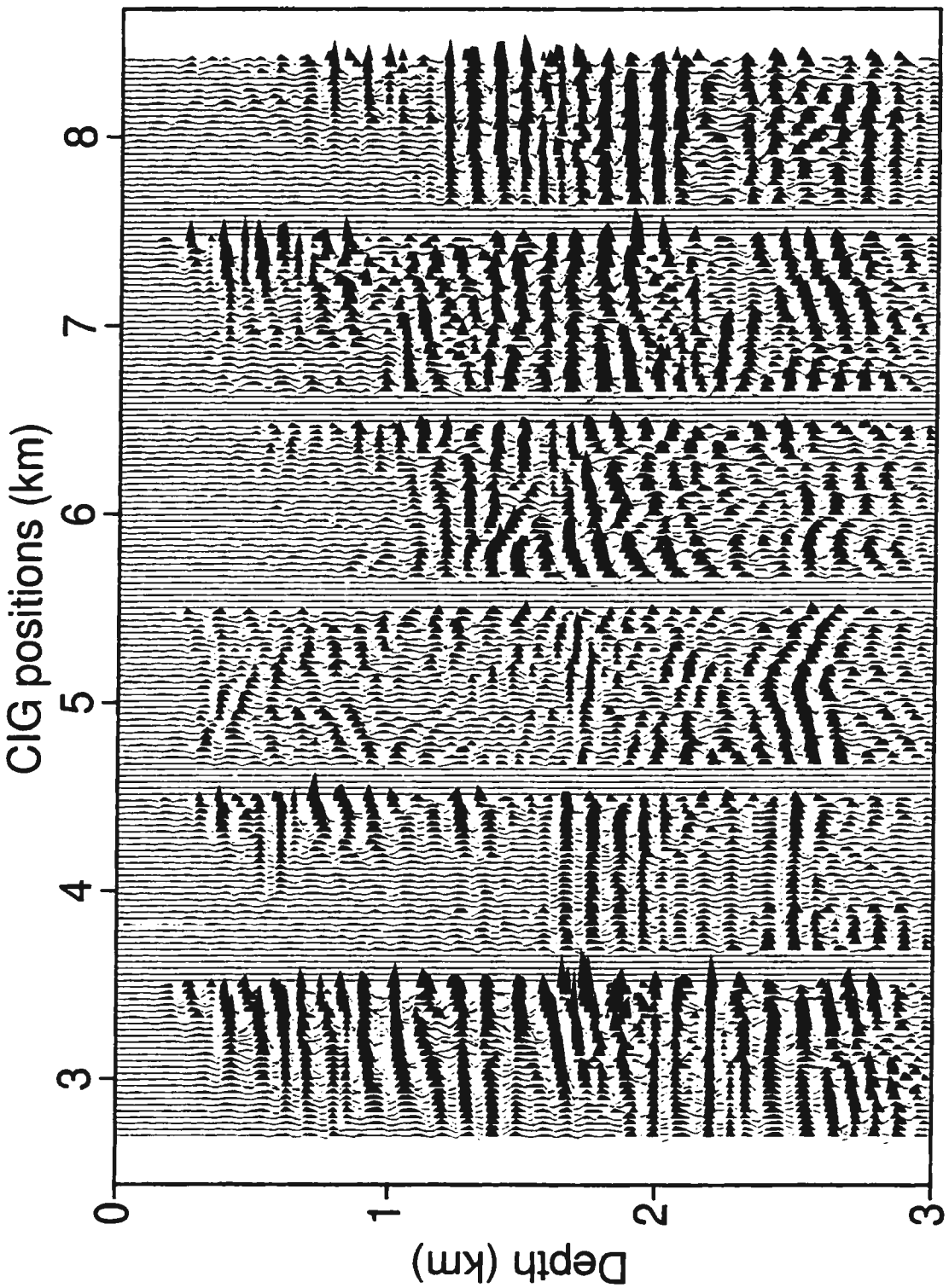

Figure 5.17: CIGs for the Marmousi model with true velocities. Offset increases from right to left.

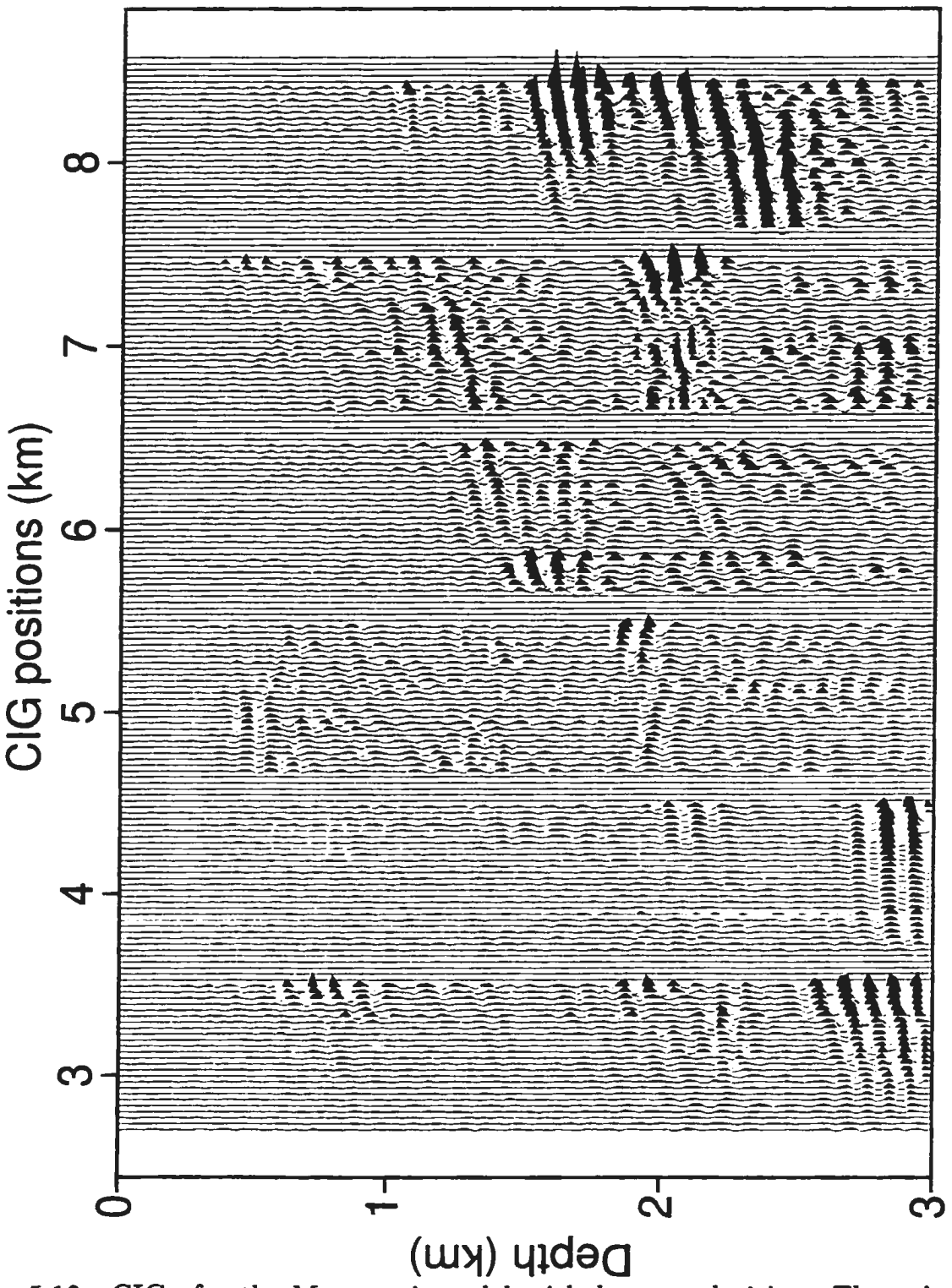

Figure 5.18: CIGs for the Marmousi model with larger velocities. The migration velocity is systematically 10 % higher than the true values. Offset increases from right to left.

Compared to the simple diffractor model. it is relatively more difficult to identify the smiles and frowns in this complicated model example. Thus. it is often required to quantify the migration velocity errors. One can measure the event curvatures in CIG panels. At each depth. a set of curves are defined by a range of $\beta's$ in equation (5.9). And migrated amplitudes are summed along every such defined curve. The final sum is displayed as a function of β and depth z. The normalized maximum sum at depth corresponds to that β matching the curvature. This velocity analysis is thus based on the migration moveout in depth which is quite similar to stacking velocity analysis by maximizing the stacking power or semblance after normal moveout correction in time (Taner and Koehler. 1969). Following Taner and Koehler (1969). if the migration amplitude is denoted as $u(x. z_m)$. with $z_m = z + \Delta z$. the summation along any curvature can be expressed.

$$g(z. \beta) = \frac{\left[\Sigma_x u(x. z_m = z + (\beta - 1)z/\cos\alpha_s \cos\alpha_r)\right]^2}{\Sigma_x u^2(x. z_m = z + (\beta - 1)z/\cos\alpha_s \cos\alpha_r)}. \qquad (5.15)$$

This is a very general expression independent of subsurface structure. However. the information about angles $\alpha_s. \alpha_r$ would require expensive computations by ray tracing. Thus. for economic purposes. summation trajectories are often analytically determined using a layered earth model assumption. Al-Yahya (1989) observed that the depth error due to such a simple structure assumption is quite small once we approach a reasonably good estimate of the velocity field. Al-Yahya (1989) also illustrated an example of such an interval velocity analysis method by extending the velocity spectrum of CMP gathers to the case of migrated CIG gathers.

Once we have picked up the β values at the maximum summation amplitude locations. a new estimate of the average velocity function can be estimated from the

migration velocity,

$$\bar{v} = \bar{v}_m \beta. \tag{5.16}$$

If we know the interval velocity at the surface layer, v_1, (5.16) allows iterative update of the deeper layer velocities,

$$v_i = i\bar{v}_i - (i-1)\bar{v}_{i-1}, \qquad i = 2, 3, ...N \tag{5.17}$$

where N is the total layer numbers of interest.

Though the above quantitative velocity update formulations are based on horizontal reflector assumptions, they work well in moderately complex structural areas. In such cases, the equations are not exact. However, we know that when we have horizontally aligned the images in common image gathers, we have no velocity error in the migration velocity model. This principle is independent of structure (Al-Yahya, 1989).

5.3. Iterative interpretive imaging

Prestack depth migration has proven to be a viable technique in imaging complex subsurface structures. Its success depends on the availability of a correct interval velocity model. Nevertheless, the determination of the interval velocity model in such complicated geological areas is often very difficult. Velocity analysis with prestack migration moveout as I described in the last section provides one measure to analyze and quantitatively update the velocity field. It essentially consists of two steps: estimating the average velocity and updating the interval velocity model. The first step can be automatically implemented by computers just as the determination of stacking velocity by stacking after normal moveout analysis (Taner and Koehler, 1969). However, the second step can not be completed without the input of the geological understanding of a geoscientist. Otherwise, significant errors will be introduced due to the erroneous division of geological formations. The importance of identifying the geological formations in this process is similar to the determination of interval velocities from RMS velocities using the Dix formula (Dix, 1955). Thus, the interval velocity field can not be automatically determined by analysis of migration moveout using prestack depth migration. The velocities should be interactively determined with the geologist's input.

In contrast to the above migration moveout analysis, tomography is generally implemented without the need of geological input. Often first break tomography is used to set up a near surface velocity structure. Such an inverted near surface velocity field is often reasonably accurate as first breaks are the most obvious and thus most

reliable events to pick. Based on this relatively reliable near surface model, reflection tomography can be used to further derive a more detailed velocity model by picking reflection events on either shot gathers or common offset sections. Generally shot gathers are a good candidate for identifying first breaks as these events are often linear or quasi-linear in this domain. For reflection picking, common offset sections are a preferred domain as reflection events approximately follow the shape of the reflectors. There are a couple of issues in tomographic inversion, however. First, there are often millions of readings to be picked which could be a prohibitive factor for processors to use the technology. Such a large amount of picking naturally results in inversion of a huge matrix. Then, there also exist cases where events are very difficult to identify and pick. In such cases significant picking errors will occur which will cause errors in the cell velocities, as the picked travel times are the primary data in tomographic inversion. Constrained tomography using such information as well logging can only improve the accuracy a little bit, though it can significantly improve the convergence rate of the inversion. Thus, though tomography can be done in a geologically independent way, the inverted velocity often lacks accuracy in addition to its low resolution limit.

Despite such concerns as tedious picking and reading errors, and accuracy and resolution limitations, tomography can in many cases be effective in obtaining a smoothed interval velocity field. This is particularly attractive in early stages of imaging a given data set as it can be done by the processor directly. This traveltime inversion velocity field provides a quantitative estimate of the velocity at every point of the interest area. It often contains zones where velocities are significantly in error due to insufficient coverage. The structural knowledge of a geologist will be highly

valuable in identifying such erroneous occurrences of the inverted velocity. Thus an interpreted tomographic velocity field can generally serve as a reasonable starting model for prestack depth migration and interval velocity determination with migration moveout analysis. After migration, the migrated section will be interpreted by a structural geologist. At the same time, common image gathers will be examined to analyze the correctness of the average velocity field at some prespecified controlling positions. If any significant errors are found by either method, a revised structure of the area will be proposed, and the velocity values will be adjusted by the computed new velocity value based on equation (5.17) combined with the knowledge of the area. Using this revised velocity field, another loop of prestack depth migration and velocity analysis will be pursued. This iterative interpretive imaging procedure will continue until no significant errors are detected both geologically by the geologist on the migrated section and geophysically on CIGs.

The above proposed imaging strategy is schematically outlined in Figure 5.19. This is a more complete version of the procedure previously presented (Zhu and Lines, 1995). From section 5.1, we know that Kirchhoff migration performs reasonably well even in very complex areas. So for economical purposes, it is suggested that the prestack depth migration will essentially be a Kirchhoff integral scheme until the last loop of the iterations. At the final stage of imaging, reverse-time migration will be employed to complement the Kirchhoff integral migrated section. This additional migration by the reverse-time technique serves two purposes: providing a possibly more accurate image of the earth and providing confidence to geological interpreters. Theoretically all the components of the flowchart should be implemented for a more accurate definition of the complex nature of the subsurface illuminated by the seis-

mic data. In practice, some simplified version can often be effectively employed to properly image complex areas taking account of the availability of geological expertise. Our experience with the Husky-Alberta foothills line indicates that even in the Alberta foothills where very complicated thrust sheets spread over young sediments, an interpretive imaging procedure without the application of reflection tomography produces a very encouraging result (Wu et al., 1996).

5.4. Summary

Theoretical comparisons of Kirchhoff integral and reverse-time migration methods showed that reverse-time migration is more accurate in imaging complex geological structures. Both methods were shown to be directly applicable to migrating from rough topography. However, Kirchhoff migration can be used to migrate seismic data selectively to image a prespecified target because it is a trace based processing. In contrast, reverse-time migration is computationally independent of trace numbers of shot gathers, which could be used to achieve its high accuracy for migrating seismic data acquired with a large number of channels. The application of both migration methods to the Marmousi model data demonstrated that prestack reverse-time migration was more accurate in imaging the steep dip faults than the prestack Kirchhoff method with nearly 8 times more computational cost. However in the case of the Husky-Alberta foothills line, the prestack Kirchhoff migration result

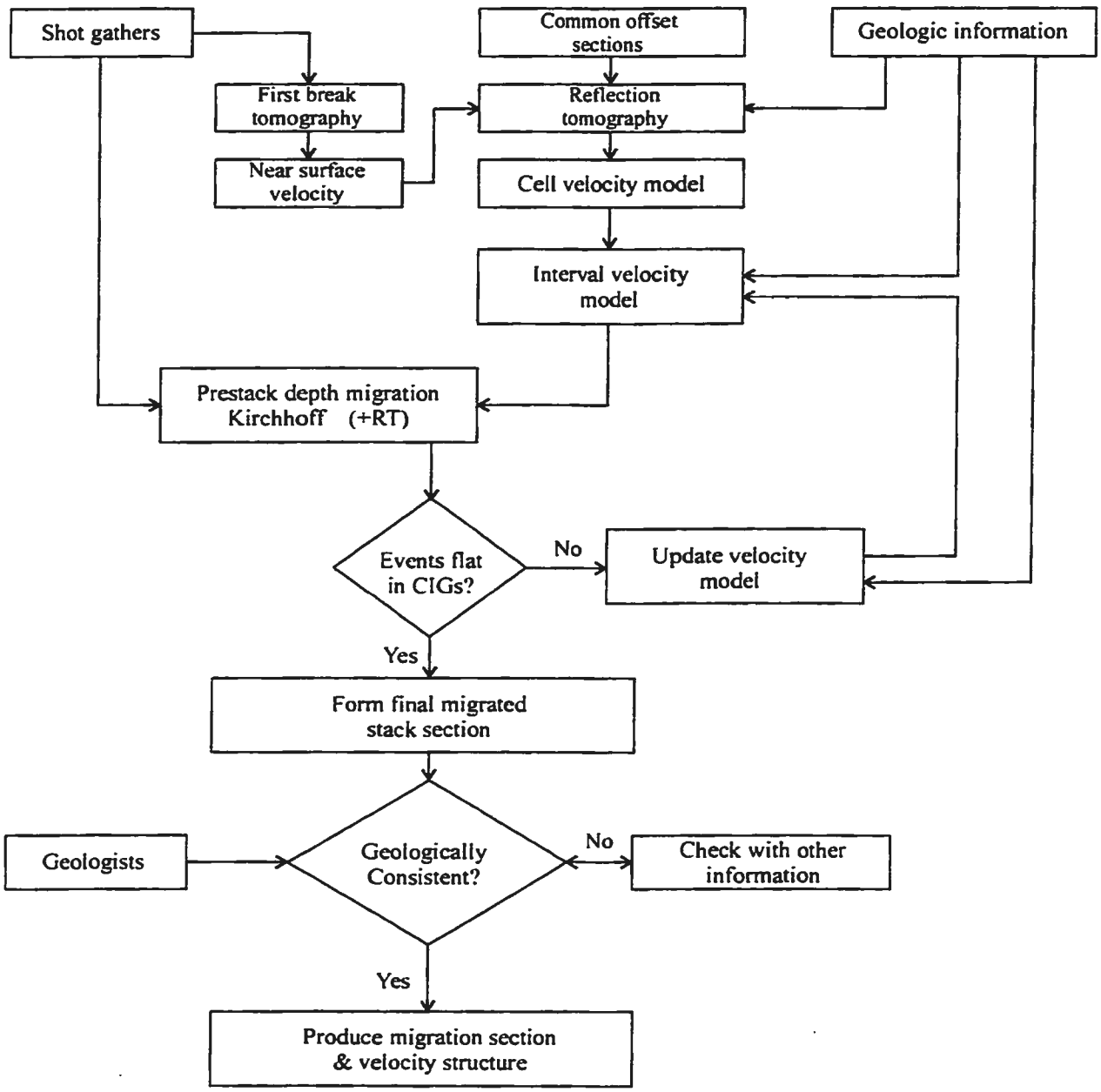

Figure 5.19: Interpretive imaging flowchart.

was very similar in many respects to that of the reverse-time migration with a much cheaper computational cost. I explained this similarity to be related to the inaccuracy of the velocity model used. Based on these comparisons, I concluded that the Kirchhoff migration should be the primary migration technique in the early stages of prestack depth imaging of complex structures.

In this chapter, I also discussed the problem of interval velocity determination. I illustrated that prestack depth migration is very sensitive to migration velocity errors and common image gathers (CIGs) could be effectively used for velocity analysis. For accurate and efficient velocity analysis, I proposed to use as many different means as possible. The image problem of geologically complex structures was finally proposed to be gradually solved through an iterative interpretive imaging procedure. This procedure was shown to be composed of initial velocity model setup, iterative prestack depth migration, geological interpretation of the migrated section and velocity model analysis.

Chapter 6. Conclusions

Seismic imaging aims to recover the true subsurface structure utilizing recorded signals along a seismic survey. Based on the concept of the common midpoint (CMP), the well-developed processing procedures of static corrections, NMO, DMO, and post-stack migration prove effective in areas without lateral and strong vertical velocity variations. In complicated geological provinces with strong vertical and lateral heterogeneities, including rugged topography, such a CMP-based strategy of imaging often fails, mainly due to the breakdown of the assumptions in the procedure. In such cases, the most important value of such a CMP processing system, is to provide a geologically meaningful approximate velocity model as a starting point for the prestack depth imaging procedure.

Prestack depth migration promises to fulfill the geophysicist's goal of producing a correct subsurface depth image with the premise that a good estimate of the low wavenumber part of the subsurface velocity model is attainable. This imaging processing is no longer based on concepts such as common midpoints and the exploding reflector model; it is solely based on wave equation solutions of wave propagation in true physical processes. The price for this gain is that prestack depth imaging is computationally highly intensive. The ultimate objective of this thesis research is thus to develop an accurate imaging strategy for seismic data acquired from very complex geological areas using prestack depth migrations with reasonably inexpensive

computations.

In this dissertation, I have developed two prestack depth migration methods. The first is the Kirchhoff integral scheme which is based on the integral solution of the acoustic wave equation. The other is the prestack reverse-time migration which is based on the finite-difference solution of the wave equation. The determination of the integral surfaces, or equivalently the loci of the aplanatics is carried out by tracing wavefronts. The tracing method is essentially completed by a combination of a finite-difference solution of the eikonal equation, excitation of Huygens' secondary wavelets, and application of Fermat's principle. This is a very general algorithm for computing first arrival traveltimes. It can even be directly used to calculate traveltimes of plane waves. Numerical tests and application examples of this wavefront tracing demonstrate that the method is very robust and accurate in calculating first arrival traveltimes in complex geological areas with very high velocity contrasts.

The migration integral equations I developed are based on the WKBJ approximation to the Green's function of the acoustic wave equation. These Kirchhoff integrals are shown to be a simple summation of amplitudes of differential traces along some integral surfaces with different amplitude modulators. The simplest approximate implementation of these integrals is the general summation method along diffraction curves or the general superposition scheme of aplanatic surfaces. As an efficient imaging technique, the integral method is capable of selectively migrating shots and traces to focus on some prespecified target.

In contrast to the Kirchhoff method, reverse-time migration is theoretically more accurate since it utilizes the full wave equation rather than its high frequency approximation. In addition to its merits of implicit static corrections and velocity filtering,

I found that it is also capable of interpolating missing traces during the reverse-time extrapolation of unaliased seismic data. Such interpolating mechanisms are based on the self-healing ability of wavefield by constructive interference of propagating waves. Such a self-healing mechanism of the wavefield allows migration of sparsely and irregularly spaced unaliased data directly without prior interpolation of missing traces. This is especially important in migration of prestack data where there is seldom one trace per surface grid point when a velocity model with grids as fine as CDP bins is used. As in the Kirchhoff method, I have also shown that reverse-time migration can directly migrate seismic data acquired over rough topography by using the true source and receiver coordinates. Despite these merits, the implementation of prestack reverse-time migration is computationally very intensive.

In this study, I demonstrated that imaging of complex geological structures generally requires an iterative interpretive imaging strategy. The imaging procedure developed consists of initial velocity model setup and iterative prestack depth migration, geological interpretation and velocity model updates. I have formulated a very general velocity analysis method using prestack depth migrated seismic data. The effectiveness of the velocity analysis method was demonstrated through both simple and complex examples.

Throughout the dissertation, I have applied the prestack depth imaging techniques developed to various data sets. The imaging of the Marmousi model data demonstrated that reverse-time migration was much more accurate than the Kirchhoff method in imaging the steeply dipping faults, although its computational cost is much greater. Nevertheless, the application of both methods to the Husky–Alberta foothills line produced quite similar results. Both methods successfully imaged the

shallow dipping interfaces. The thrust faults were well defined in both migration images. However, for imaging this foothills data set, the Kirchhoff method took less than a day of CPU time while the reverse-time migration took nearly a week. Based on the comprehensive comparison of Kirchhoff and reverse-time migrations, especially through their applications to seismic data from very complex geological areas, I conclude that the Kirchhoff method should at present be the primary prestack migration technique for seismic data from complex areas, although from theoretical calculations it is expected that the reverse-time migration will become preferred to achieve higher accuracy with possibly even fewer computations in migrating seismic records acquired with large numbers of channels. For the time being, the Kirchhoff method nevertheless constitutes the core element of the iterative interpretive imaging strategy.

References

Aki, K., and Richards, P. G., 1980, Quantitative seismology: Theory and methods, Vol.1: W.H. Freeman, San Francisco, 932 pp.

Al-Yahya, K., 1989, Velocity analysis by iterative profile migration: Geophysics, **54**, 718-729.

Alford, R.M., Kelly, K.R., and Boore, D.M., 1974, Accuracy of finite-difference modeling of the acoustic wave equation: Geophysics, **39**, 834-842.

Baysal, E., Kosloff, D.D., and Sherwood, J.W.C., 1983, Reverse time migration: Geophysics, **48**, 1514-1524.

Baysal, E., Kosloff, D.D., and Sherwood, J.W.C., 1984, A two-way non-reflecting wave equation: Geophysics, **49**, 132-141.

Berkhout, A.J., 1982, Seismic migration — Imaging of acoustic energy by wave field extrapolation: A. Theoretical aspects, Elsevier, Amsterdam, 445 pp.

Berkhout, A.J., 1984, Seismic migration—Imaging of acoustic energy by wave field extrapolation: B. Practical aspects, Elsevier, Amsterdam, 274 pp.

Bevc, D., 1997, Imaging complex structures with semirecursive Kirchhoff migration: Geophysics, **62**, 577-588.

Beydoun W. B., and Keho, T. H., 1987, The paraxial ray method: Fast computations of Green's functions for inverse scattering: Geophysics, **52**, 1639-1653.

Bleistein, N., 1984, Mathematical methods for wave phenomena: Academic Press Inc., Orlando, 341 pp.

Bleistein, N., 1986, Two-and-half dimensional in-plane wave propagation: Geophysical Prospecting, **34**, 686-703

Bording, R.P., and Lines, L.R., 1996, Wave equation methods for modeling and imaging: SEG course notes, Society of Exploration Geophysicists, Tulsa, 98 pp.

Cerveny, V., 1987, Ray tracing algorithms in three-dimensional laterally varying structures, in Nolet, G., Ed., Seismic tomography: with applications in global seismology and exploration geophysics: D. Reidel Publishing Co., Dordrecht, Holland. 99-133.

Chang, W.F., and McMechan, G.A., 1986, Reverse-time migration of offset vertical seismic profiling data using the excitation-time imaging condition: Geophysics, **51**, 67-84.

Chang, W.F., and McMechan, G.A., 1990, 3D acoustic prestack reverse-time migration: Geophysical Prospecting, **38**, 737-755.

Claerbout, J.F., 1971, Toward a unified theory of reflection mapping: Geophysics, **36**, 467-581.

Claerbout, J.F., 1976, Fundamentals of geophysical data processing: McGraw-Hill Book Co., New York, 274 pp.

Claerbout, J.F.,1985, Imaging the earth's interior: Blackwell Scientific Publ., Oxford, England, 398 pp.

Claerbout, J.F., and Nichols, D., 1991, Interpolation beyond aliasing by $\tau - x$ domain PEP's: **53**rd Meeting, European Association of Exploration Geophysicists, Abstract, 2-3.

Claerbout. J.F.. 1992. Earth soundings analysis: Processing versus inversion: Blackwell Scientific Publ.. Boston. 304 pp.

Dablain. M.A.. 1986. The application of high-order differencing to the scalar wave equation: Geophysics. **51**. 54-66.

Deregowski. S. M.. 1982. Dip-moveout and reflector point dispersal: Geophysical Prospecting: **30**. 318-322.

Deregowski. S. M.. 1986. What is DMO?: First Break. **4**. No.7. 7-24.

Dix. C.H.. 1955. Seismic velocities from surface measurements: Geophysics. **20**. 68-86.

Docherty. P. C. 1991. A brief comparison of some Kirchhoff integral formulas for migration and inversion: Geophysics. **56**. 1164-1169.

French. W.S.. 1975. Computer migration of oblique seismic reflection profiles: Geophysics. **40**. 961-980.

Geoltrain. S.. and Brac. J.. 1993. Can we image complex structures with first-arrival traveltimes?: Geophysics. **58**. 564-575.

Goodman. J. W.. 1968. Introduction to Fourier optics: McGraw-Hill Book Co.. San Francisco. 287 pp.

Gray. S.H.. 1986. Efficient traveltime calculation for Kirchhoff migration: Geophysics. **51**. 1685-1688.

Gray. S.H.. and May. W.P.. 1994. Kirchhoff migration using eikonal equation traveltimes: Geophysics. **59**. 810-817.

Gray. S.H.. and Marfurt. K.J.. 1995. Migration from topography: improving the near-surface image: Canadian Journal of Exploration Geophysicists. **31**. 18-24.

Hagedoorn. J. G.. 1954. A process of seismic reflection interpretation: Geophysical

Prospecting, **2**, 85-127.

Hale, D., 1984, Dip moveout by Fourier transform: Geophysics, **49**, 741-757.

Hemon, C., 1978, Equations d'onde et modeles: Geophysical Prospecting, **26**, 790-821.

Jervis, M., Sen, M., and Stoffa, P.L., 1996, Prestack migration velocity estimation using nonlinear methods: Geophysics, **61**, 138-150.

Keho, T. H., and Beydoun, W. B., 1988, Paraxial ray Kirchhoff migration: Geophysics, **53**, 1540-1546.

Kelly, K. R., Word, R. W., Treitel, S., and Alford, R. M., 1976, Synthetic seismograms: A finite-difference approach: Geophysics, **41**, 2-27.

Kelly, K. R., Alford, R. M., and Whitmore, N. D., 1982, Modeling — The forward method, in Jain, K. C., and deFigueiredo, Eds., Concepts and techniques in oil and gas exploration: Society of Exploration Geophysicists, Tulsa, 91-114.

Langan, R. T., Lerche, I., and Cutler, R. T., 1985, Tracing of rays through heterogeneous media: An accurate and efficient procedure: Geophysics, **50**, 1456-1465.

Larner, K., and Hatton, L., 1990, Wave equation migration: two approaches: First Break, **8**, 433-448.

Levin, F. K., 1971, Apparent velocity from dipping interfaces: Geophysics, **36**, 510-516.

Levin, S.A., 1984, Principle of reverse-time migration: Geophysics, **49**, 581-583.

Lines, L.R., 1993, Ambiguity in analysis of velocity and depth: Geophysics, **58**, 596-597.

Lines, L. R., Rahimian, F. and Kelly, K. R., 1993, A model-based comparison of modern velocity analysis methods: The Leading Edge, **12**, 750-754.

Lines, L.R., Wu, W., Lu, H., Burton, A., and Zhu. J., 1996, Migration from topography: Experience with an Alberta Foothills data set: Canadian Journal of Exploration Geophysicists, **32**, 24-30.

Loewenthal, D., and Mufti, I.R., 1983, Reversed time migration in spatial frequency domain: Geophysics, **48**, 627-635.

Loewenthal, D., Stoffa, P.L., and Faria, E.L., 1987, Suppressing the unwanted reflections of the full wave equation: Geophysics, **52**, 1007-1012.

McMechan, G.A., 1983, Migration by extrapolation of time-dependent boundary values: Geophysical Prospecting, **31**, 413-420.

McMechan, G.A., 1989, A review of seismic acoustic imaging by reverse-time migration: International Journal of Imaging Systems and Technology, **1**, 18-21.

McMechan, G.A., and Chen, H.W., 1990, Implicit static corrections in prestack migration of common-source data: Geophysics, **55**, 757-760.

McMechan, G.A., and Sun, R., 1991, Depth filtering of first breaks and ground roll: Geophysics, **56**, 390-396.

Mufti, I.R., Pita, J.A., and Huntley, R.W., 1996, Finite-difference depth migration of exploration-scale 3-D seismic data: Geophysics, **61**, 776-794.

Nichols, D.E., 1996, Maximum energy traveltimes calculated in the seismic frequency band: Geophysics, **61**, 253-263.

Nickerson, B., 1994, Depth migration based on fast generation of aplanatic surface using an eikonal equation solver: 1994 Annual MUSIC report, Memorial University of Newfoundland, 26-54.

Podvin, P., and Lecomte,I., 1991, Finite-difference computation of traveltimes in very contrasted velocity models: A massively parallel approach and its associated

tools: Geophysical Journal International, **105**, 271-284.

Qin, F., Luo, Y., Olsen, K. B., Cai, W., and Schuster, G. T., 1992, Finite-difference solution of the eikonal equation along expanding wavefronts: Geophysics, **57**, 478-487.

Rajasekaran, S. and McMechan, G.A., 1995, Prestack processing of land data with complex topography: Geophysics, **60**, 1875-1886.

Ratcliff, D.W., Gray, S.H., and Whitmore, N.D., 1992, Seismic imaging of salt structures in the Gulf of Mexico: The Leading Edge, **11**, 15-31.

Reshef, M. and Kosloff, D.D., 1986, Migration of common-shot gathers: Geophysics, **51**, 324-331.

Reshef, M., 1991, Depth migration from irregular surfaces with depth extrapolation methods: Geophysics, **56**, 119-122.

Robinson, E.A. and Treitel, S., 1980, Geophysical signal analysis: Prentice-Hall, Inc., Englewood Cliffs, New Jersey, 466 pp.

Schneider, W.A., 1971, Developments in seismic data processing and analysis (1968-1970): Geophysics: **36**, 1043-1073.

Schneider, W.A., 1978, Integral formulation for migration in two and three dimensions:Geophysics: **43**, 49-76.

Schneider, W.A., Jr., Ranzinger, K. A., Balch, A. H., and Kruse, C., 1992, A dynamic programming approach to first arrival traveltime computation in media with arbitrary distributed velocities: Geophysics, **57**, 39-50.

Sheriff, R. E., 1991, Encyclopedic dictionary of exploration geophysics: Society of Exploration Geophysicists, Tulsa, 376 pp.

Skuce, A., 1995, Seismic imaging in the Canadian Rocky Mountain Foothills: Paper presented at the 1995 SEG workshop #6, Houston, Texas.

Slotnick, M. M., 1974, Lessons in seismic computing: Society of Exploration Geophysicists, Tulsa, 268 pp.

Spitz, S., 1991, Seismic trace interpolation in the F-X domain: Geophysics, **56**, 785-794.

Stork, C., Welsh, C., and Skuce, A., 1995, Demonstration of processing and model building methods on a real complex structure data set: proceedings from 1995 SEG workshop #6, Houston, Texas.

Taner, M. T. and Koehler, F., 1969, Velocity spectra—digital computer derivation and applications of velocity functions: Geophysics, **34**, 859-881.

van der Schoot, A., Romijn, R., Larson, D.E., and Berkhout, A.J., 1989, Prestack migration by shot record inversion and common depth point stacking: a case study: First Break, **7**, 293-304.

Versteeg, R., 1993, Sensitivity of prestack depth migration to the velocity model: Geophysics, **58**, 873-882.

Vidale, J.E., 1988, Finite-difference calculation of travel times: Bulletin of the Seismological Society of America, **78**, 2062-2076.

Vidale, J.E., 1990, Finite-difference calculation of traveltimes in three dimensions: Geophysics, **55**, 521-526.

Vidale, J.E. and Houston, H., 1990, Rapid calculation of seismic amplitudes: Geophysics, **55**, 1504-1507.

Wapenaar, C. P. A., and Berkhout, A. J., 1989, Elastic wave field extrapolation: Redatuming of single- and multi-component seismic data: Elsevier, Amsterdam, 468 pp.

Whitmore, N.D., 1983, Iterative depth migration by backward time propagation:

Presented at the **53rd** Annual Meeting, Society of Exploration Geophysicists, Expanded Abstracts, 827-830.

Whitmore, N.D., Gray, S.H., and Gersztenkorn, A., 1988, Two-dimensional post-stack depth migration: a survey of methods: First Break, **6**, 189-197.

Whitmore, N.D., 1995, An imaging hierarchy for common–angle plane wave seismograms: Ph.D. thesis, The University of Tulsa, Tulsa, 118 pp.

Wu, W.J., Lines, L.R., Burton, A., Lu, H.X., Jamison, W., Zhu, J., and Bording, R. P., 1996, Prestack depth migration of an Alberta foothills data set — the Husky experience: **66**th Annual Meeting, Society of Exploration Geophysicists, Expanded Abstracts, 559-561.

Yilmaz, 1987, Seismic data processing: Society of Exploration Geophysicists, Tulsa, 526 pp.

Zhu, J., and Lines, L.R., 1994, Imaging of complex subsurface structures by VSP migration: Canadian Journal of Exploration Geophysicists, **30**, 73-83.

Zhu, J., and Lines, L.R., 1995, Subsurface imaging with prestack depth migration and velocity analysis: **22**nd Annual Meeting, Canadian Society of Exploration Geophysicists, Expanded Abstract, 5-6.

Zhu, J., and Lines, L.R., 1996, Comparison of Kirchhoff and Reverse-time migration methods with applications to prestack depth imaging of complex Structures: **66**th Annual Meeting, Society of Exploration Geophysicists, Expanded Abstracts, 539-542.

Zhu, J., and Lines, L.R., 1997, Implicit interpolation in reverse-time migration: Geophysics, **62**, 906-917.